University of Southampton

Faculty of Engineering and Physical Sciences

Institute of Sound and Vibration Research

Wave Propagation in Non-Uniform Waveguides

Angelis Karlos

Thesis for the Degree of Doctor of Philosophy

January 2020

University of Southampton

Abstract

Faculty of Engineering and Physical Sciences

Institute of Sound and Vibration Research

Thesis for the Degree of Doctor of Philosophy

Wave Propagation in Non-Uniform Waveguides

by Angelis Karlos

Non-uniform waveguides in which the waves slow down as they propagate have a variety of uses. First, the attenuation within the waveguide is enhanced as the waves slow down, which can be used for absorption of flexural or acoustic waves without excessive use of damping material in so-called 'acoustic black holes'. Second, the position of the peak response along the waveguide can vary with frequency, allowing for spatial frequency analysis, as occurs in the cochlea and also in recent 'rainbow' sensors.

In this thesis, four different examples of such non-uniform waveguides are studied using both analytical and numerical methods. The reflection from elastic wedges of different thickness profiles is first analysed using the WKB method, and the results are compared with those calculated with the Finite Element method. It is shown that higher orders of WKB approximation are required to capture the details of the frequency variation of the reflection coefficient, and that an exponential wedge presents the least reflection among the studied profiles. For an acoustic waveguide with fitted rings of tapered inner radius, the reflection coefficient is then calculated with a Transfer Function method and compared with experimental results in the literature.

A one-dimensional 'box model' of the cochlea with passive micromechanics is also analysed, using both the WKB method and the Finite Difference method. The dependence of the coupled cochlear response to a number of non-dimensional parameters is studied, and it is found that one such parameter, which has previously been used to define the overall phase shift, also determines the symmetry of the frequency response of the system. The design of an acoustic 'rainbow' sensor is discussed and shown to involve a trade-off between the selectivity of the response and the number of elements. The new design is then described, consisting of a main duct with Helmholtz-Resonator side branches of varying dimensions, in which the damping is optimised so that its main characteristics are similar to those of the cochlea, to give a tonotopic mapping and a smooth frequency response.

Table of Contents

List of Figures

List of Tables

List of Accompanying Material

Dataset containing the MATLAB figure files (.fig) of the plots
(DOI: https://doi.org/10.5258/SOTON/D1195)

Declaration of Authorship

I, Angelis Karlos, declare that the thesis titled 'Wave Propagation in Non-Uniform Waveguides' and the work presented in it are my own work, and have been generated by me as the result of my own original research. I confirm that:

1. This work was done wholly or mainly while in candidature for a research degree at this University;

2. Where any part of this thesis has previously been submitted for a degree or any other qualification at this University or any other institution, this has been clearly stated;

3. Where I have consulted the published work of others, this is always clearly attributed;

4. Where I have quoted from the work of others, the source is always given. With the exception of such quotations, this thesis is entirely my own work;

5. I have acknowledged all main sources of help;

6. Where the thesis is based on work done by myself jointly with others, I have made clear exactly what was done by others and what I have contributed myself;

7. Parts of this work have been published as:

   A. Karlos, D. Vignali, B. Lineton and S. Elliott. Quasi-linear modelling of the coupled cochlea using the WKB method. In *Mechanics of Hearing 2017*, volume 1965, 030004, American Institute of Physics, 2018. https://doi.org/10.1063/1.5038457

   A. Karlos, S. Elliott and J. Cheer. Reflection from elastic wedges of different thickness profiles. In *ISMA2018 and USD2018*, pages 4571-4584, 2018.

   A. Karlos, S. J. Elliott and J. Cheer. Higher-order WKB analysis of reflection from tapered elastic wedges. *Journal of Sound and Vibration*, 449:368-388, 2019. https://doi.org/10.1016/j.jsv.2019.02.041

   A. Karlos and S. J. Elliott. Reflection from a non-uniform acoustic waveguide with fitted rigid rings using a Transfer Function method. In *26th International Congress on Sound and Vibration, July 2019.*

Signature: Date:

Στην μητέρα μου και στο πνεύμα του πατέρα μου
(To my mother and to my father's spirit)

Acknowledgements

This PhD has primarily been a lonesome journey in terms of the research work, although illuminated by the ever-glowing guidance of Steve Elliott, whose contribution as a supervisor has been fundamental for the outcome of this work. I have learned a lot from his approach on science, but even more importantly, I have been inspired by his attitude towards the various issues that arose during the course of the PhD. In particular, I want to thank Steve for his positive stance on shifting the focus of the research during the first year of the programme.

Beyond my collaboration with Steve, many people contributed to my PhD in various ways. I owe special thanks to Jordan Cheer, the collaboration with whom resulted in a journal publication. I would also like to thank the following people, many of whom are my friends, who explicitly helped me with issues in my PhD: Felipe Vásquez, Ander Biguri, Kristian Hook, Charlie House, Chung Kwan Lai, Michał Kalkowski, Nikos Kournoutos, Thanasis Papaioannou, Reuben Lindroos, Dario Vignali and Francesco D'Amore.

I am also grateful to my friends that did not specifically help me with the research, but accompanied me during this journey: Raman Bhatia, Jana Tichoňová, Eirini Tzouka, Elena Perdomo, Irantzu Pérez, Orestis Vryonis, Angélica Hernández, Miika Pursiainen, Noel Castro, Xavi Garcia, Ronan Serre, Vyom Verma, Julia Kääriäinen, Dorotea Belcheva, Boni Hima and Emilien Valat. I would also like to thank my office mates Krithika Anil, Yushan Gao, Joe Milton and David Slater. I am particularly grateful to Theophilos Gkinis, who encouraged me to do a PhD in the United Kingdom.

I wish to thank my mother and my siblings whose love is a source of motivation in my life. Finally, I would like to thank my father, to whom I owe a great part of my intellectual development.

List of Symbols

a	Neck radius of a Helmholtz Resonator (m)
A	Absorption coefficient
C	Acoustic compliance ($\mathrm{m}^4 \cdot \mathrm{s}^2 \cdot \mathrm{kg}^{-1}$)
c_{gr}	Group velocity ($\mathrm{m} \cdot \mathrm{s}^{-1}$)
c_p	Quasi-longitudinal wave velocity ($\mathrm{m} \cdot \mathrm{s}^{-1}$)
c_{ph}	Phase velocity ($\mathrm{m} \cdot \mathrm{s}^{-1}$)
d	Decay length (m)
D	Bending stiffness of a plate ($\mathrm{Pa} \cdot \mathrm{m}^3$)
E	Young's modulus (Pa); scaling parameter in the designed 'rainbow' sensor
f	Frequency (Hz)
f_n	Natural frequency (Hz)
F_n, F_{ch}	Normalised frequency
h	Wedge thickness (m); effective cochlear chamber height (m)
H	Thickness ratio; scaling parameter of Helmholtz Resonator cavities
h_0	Wedge thickness at the junction (m)
k	Wavenumber (m^{-1})
k_{eff}	Effective wavenumber of a waveguide with fitted rings (m^{-1})
l	Characteristic length (m)
L	Acoustic inertance ($\mathrm{kg} \cdot \mathrm{m}^{-4}$); length of the cochlea (m)
l_0	Ideal length of a waveguide with fitted rings (m)
l_1	Actual length of a waveguide with fitted rings (m)
l_{tr}	Truncation length of a waveguide with fitted rings (m)
l_{eff}	Effective length (m)
L_{eff}	Normalised effective length
m	Loaded basilar membrane mass per unit area ($\mathrm{kg} \cdot \mathrm{m}^{-2}$)
n_{eff}	Effective number of elements
N_{eff}	Normalised effective number of elements
N_c	Phase-shift parameter
p	Acoustic pressure (Pa); pressure difference between the cochlear chambers (Pa)
P	Normalised pressure difference between the cochlear chambers
Pr	Prandtl number
Q, Q_0	3-dB quality factor
Q_c	3-dB coupled quality factor

r	Radius (m); Basilar membrane resistance per unit area ($\mathrm{kg \cdot s^{-1} \cdot m^{-2}}$)
R	Reflection coefficient; acoustic resistance ($\mathrm{kg \cdot m^{-4} s^{-1}}$)
R_p	Power reflection coefficient
R_{end}	End reflection coefficient
R_{jun}	Junction reflection coefficient
R_{tot}	Total reflection coefficient
s	Basilar membrane stiffness per unit area ($\mathrm{kg \cdot s^{-2} \cdot m^{-2}}$)
S	Cross-sectional area ($\mathrm{m^2}$)
SWR	Standing Wave Ratio
t	Time (s)
T	Transmission coefficient
$\mathbf{T}$	Transfer Matrix
T_{ij}	Elements of the Transfer Matrix
T_p	Power transmission coefficient
u	Longitudinal fluid velocity ($\mathrm{m \cdot s^{-1}}$)
u_{st}	Stapes velocity ($\mathrm{m \cdot s^{-1}}$)
V	volume ($\mathrm{m^3}$)
v_{bm}	Basilar membrane transverse velocity ($\mathrm{m \cdot s^{-1}}$)
V_{bm}	Normalised basilar membrane transverse velocity
w	Transverse displacement of the midsurface of a wedge (m)
x	Longitudinal position (m)
X_n, X_{ch}	Normalised position
x_0	Ideal wedge length (m)
x_1	Actual wedge length (m)
y	Specific acoustic admittance ($\mathrm{m^2 \cdot s \cdot kg^{-1}}$)
Y	Acoustic admittance ($\mathrm{m^4 \cdot s \cdot kg^{-1}}$)
Y_0	Characteristic acoustic admittance ($\mathrm{m^4 \cdot s \cdot kg^{-1}}$)
Y_{in}	Input acoustic admittance ($\mathrm{m^4 \cdot s \cdot kg^{-1}}$)
Y_{bm}	Basilar membrane admittance ($\mathrm{m^2 \cdot s \cdot kg^{-1}}$)
z	Specific acoustic impedance ($\mathrm{kg \cdot m^{-2} \cdot s^{-1}}$)
Z	Acoustic impedance ($\mathrm{kg \cdot m^{-4} \cdot s^{-1}}$)
z_0	Specific characteristic acoustic impedance ($\mathrm{kg \cdot m^{-2} \cdot s^{-1}}$)
Z_0	Characteristic acoustic impedance ($\mathrm{kg \cdot m^{-4} \cdot s^{-1}}$)
Z_{in}	Input acoustic impedance ($\mathrm{kg \cdot m^{-4} \cdot s^{-1}}$)

α	Loss coefficient in an acoustic 'rainbow' sensor (m^{-1})
δ	Viscous boundary layer thickness (m)
Δ	Element length in the Finite Difference cochlear model (m)
η	Damping loss factor; dynamic viscosity ($\mathrm{Pa} \cdot \mathrm{s}$)
κ	Bulk modulus (Pa)
λ	Wavelength (m)
Λ	Discretisation ratio
μ	Mass ratio; loss coefficient in a waveguide with fitted rings
ρ	mass density ($\mathrm{kg} \cdot \mathrm{m}^{-3}$)
σ	Poisson's ratio
ϕ_0	Total phase shift inside a wedge (rad)
ω	Angular frequency ($\mathrm{rad} \cdot \mathrm{s}^{-1}$)
ω_n	Natural angular frequency ($\mathrm{rad} \cdot \mathrm{s}^{-1}$)

Chapter 1

Introduction

1.1 Non-uniform waveguides

The propagation of waves depends on the properties of the medium in which the waves are transmitted. In this thesis, a number of different mechanical waves are studied, which always require a medium with mass, that is, they cannot propagate in vacuum, in contrast to electromagnetic waves.

In many cases, the medium of propagation can be treated as being unbounded, such as in acoustic waves in free space. There is, however, an abundance of physical systems where the medium of propagation is localised, either explicitly defined by exact spatial boundaries or limited to a more or less arbitrary region of space. In such systems, the term 'waveguide' is often used. Although it is possible for multiple types of waves to propagate in such systems, this thesis will focus on those in which only one type of wave is dominant.

In nature, the properties of a system supporting wave propagation may generally vary, either spatially or temporally. In the research presented in this thesis, only waveguides whose properties are independent of time are considered. According to whether their properties are constant or varying with respect to space, waveguides are divided into 'uniform' and 'non-uniform', respectively, although such systems can also be described as 'homogeneous' and 'inhomogeneous'.

Uniform waveguides have been studied for a large variety of waves and are well understood, including acoustic waves in uniform ducts and flexural waves in uniform plates and beams. Travelling waves in uniform waveguides propagate with constant velocity and constant amplitude. In non-uniform waveguides, however, whose properties vary with position, the propagation velocity varies along the direction of propagation. Accordingly, the amplitude of travelling waves also varies with position, to ensure energy conservation [5].

The modelling procedure of physical systems, either naturally occurring or manufactured, constitutes a transform from the actual physical plane to their mathematical representation. This procedure involves a compromise between accuracy and validity on one side, and clarity

and simplicity on the other. The modeller is free to define the balancing point of compromise, given the properties of the system that are essential to a particular problem.

In the simplest case, non-uniform waveguides are described by a single equation, as, for example, for an acoustic duct with varying cross-sectional area [6]. For more complicated systems, however, different equations have to be used for different regions of the system, and their solutions have to be coupled. In such cases, it is often not possible to derive an analytical solution for the problem. Even for the case where the system is described by a single equation, it is often not possible to find exact analytical solutions. Therefore, methods that provide approximate solutions need to be used. These can be either numerical methods, such as the Transmission Line method and the Finite Element method, or approximate analytical methods, such as the WKB method. The choice of method depends on the equations describing a given system and on the desired accuracy, with different methods having different limitations of accuracy.

Non-uniform waveguides can be divided into two main categories with respect to their behaviour in terms of reflection or absorption. The first category consists of waveguides which cause incident waves to be reflected, or scattered. An example of such waveguides is acoustic horns, which cause incident waves below a cut-off frequency to be reflected, where the cut-off frequency depends on the flare of the horn. This category of non-uniform waveguides is not considered in the main body of the thesis, although a brief description of acoustic horns is presented in Appendix A, since they were initially considered before the thesis became more focused.

The second category includes waveguides which cause incident waves to be focused at a localised spatial region, where they may be absorbed to some extent. The level of absorption and the position of the focus where absorption takes place generally depend on frequency. This thesis is concerned with such non-uniform waveguides with focusing and absorbing properties.

1.2 Examples of non-uniform waveguides with absorbing properties

In this section, the general characteristics of the types of non-uniform waveguides that are considered in the main chapters of the thesis are briefly presented.

1.2.1 Elastic wedges

It was first proposed in [7] that a plate whose thickness is tapered down to zero at its free end according to a power-law can completely absorb incident bending waves. This is accomplished by a corresponding decrease of the propagation velocity, which becomes zero at the vanishing tip, so that waves halt there and are not reflected from the end boundary. This phenomenon

has come to be known the 'Acoustic Black Hole' effect, despite the fact that the waves are not acoustic.

It was also shown in [7] that even small truncations, which inevitably occur in practice, leading to non-zero end thickness and accordingly to non-zero end velocity, cause considerable reflection. A way to overcome this defficiency was proposed in [8], where it was theoretically predicted that the addition of thin layers of viscoelastic material significantly reduces reflection. Such a tapered structure, either in the form of a plate or of a beam with constant width, resembles a wedge, a term that is used in the literature as well as in this thesis. Practical applications of the tapered elastic wedge may include light-weight vibration dampers in the automotive and aerospace industry and energy harvesters, as reviewed in [9], as well as terminations of vibrating parts of industrial machinery.

For many practical applications, a wedge will form the termination of a uniform waveguide, as depicted in Figure 1.1a. Therefore, the reflection coefficient evaluated at the uniform waveguide, denoted by R_1 in Figure 1.1a, is of particular interest, as it represents the overall reflective behaviour of the system. Figure 1.1b shows the modulus of this reflection coefficient for a uniform beam with four different termination configurations, plotted against frequency [10]. The uppermost line of the graph corresponds to a termination consisting of a uniform beam covered with a thick layer of absorbing material, shown for reference. It can be seen that very little absorption takes place in this case, as the reflection coefficient retains a value close to one throughout the considered spectrum.

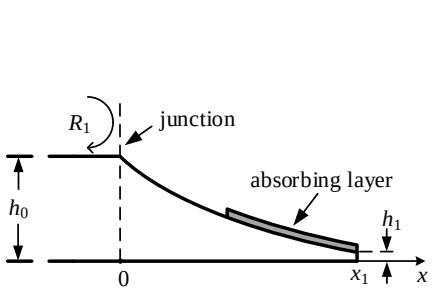

(a)

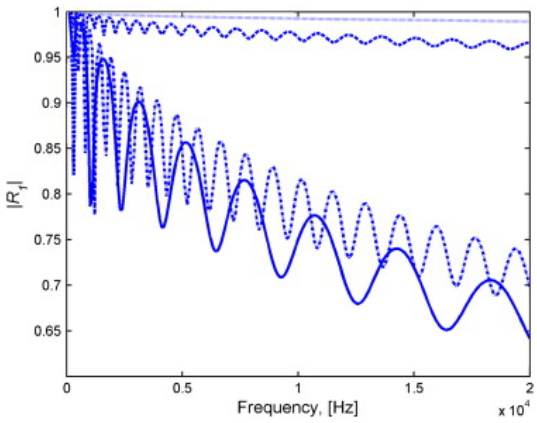

(b)

Figure 1.1. (a) Schematic of an elastic wedge of length x_1 and constant width, tapered down to thickness h_1, terminating a semi-infinite uniform beam of the same width, and thickness h_0. The thinner part of the wedge is covered by a layer of absorbing material. The schematic is based on the general characteristics of Figure 1 in [10]. (b) Modulus of the reflection coefficient seen from the uniform beam. The plotted lines from top to bottom correspond to a termination consisting of a uniform beam covered with a thick damping layer, a wedge without a damping layer, a wedge covered with a thin damping layer, and a wedge covered with a thick damping layer. The image is taken from Figure 4 in [10] with permission.

The three lower lines in Figure 1.1b correspond to the uniform beam terminated by a truncated wedge. The uppermost among these lines corresponds to a wedge without a damping layer, and the two lower lines correspond to wedges covered with damping layers, with the

lowermost line corresponding to a thick damping layer and the line which is slightly higher corresponding to a thin damping layer. It can be seen that the wedge causes fluctuations in the reflection coefficient, due to the interaction between waves reflected from the end and waves reflected from the junction of the uniform and non-uniform parts. It can also be seen that the termination with a truncated wedge, without using an absorbing layer, provides little absorption, with the resultant reflection coefficient having high values. When even a thin absorbing layer is added, however, the reflection coefficient is significantly reduced.

It is apparent from Figure 1.1b that a combination of the tapered geometry and the use of absorbing layers is required to achieve significant levels of absorption. In Chapter 2, an analysis of the reflection from elastic wedges is carried out, focusing on the relation between their reflective behaviour and their geometrical characteristics.

1.2.2 Absorbing non-uniform acoustic waveguides

A system with similar absorption properties as those of a tapered elastic wedge was proposed in [11] for an acoustic duct. The design of the proposed system comprises fitted thin rigid rings of tapered inner radius, as depicted in Figure 1.2a. Such a system can be approximated by a waveguide with a tapered radius corresponding to the ring inner radius, and the cavities formed between consecutive rings can be approximately modelled as an equivalent continuous wall admittance, which varies along the waveguide. It was shown in [11] that the propagation velocity vanishes at the end, where the equivalent continuous radius vanishes, so that waves are not reflected. Instead, they are completely absorbed due to thermal and viscous losses in the boundaries of the cavities. Exact analytical solutions can be found for this equivalent continuous model.

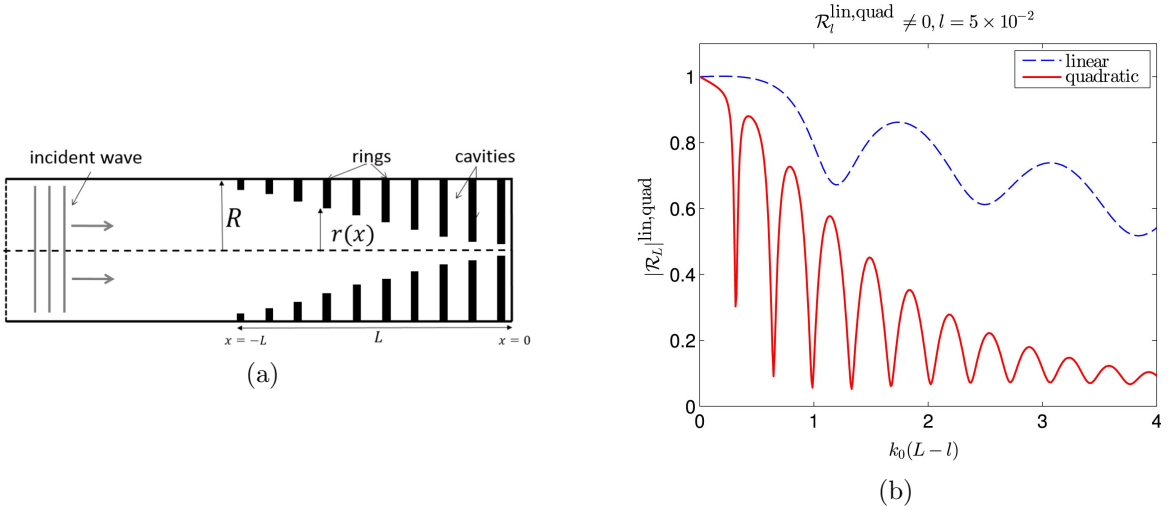

Figure 1.2. (a) Schematic of a cross section of a rigidly terminated circular tube with a series of fitted thin rigid rings of tapered inner radius. The image is taken from Figure 1 in [12] with permission. (b) Modulus of the reflection coefficient of a tube with fitted rings, either with linear or with quadratic ring inner-radius variation, plotted against normalised wavenumber; L is the length of the non-uniform termination, as shown in (a), and l is the length of truncation from the position where the equivalent continuous inner radius vanishes. The image is taken from Figure 3d in [12] with permission.

As in the case of elastic wedges, in practice it is not possible to realise a waveguide with vanishing propagation velocity. For a duct with fitted rings, it is not realisable to have a vanishing inner radius, especially because a discrete number of rings has to be used. This leads to non-zero velocity at the end of the waveguide, which in turn results in reflection. Therefore, it is assumed that the waveguides are truncated at a position before the vanishing point of the ring inner radius.

Power-law inner-radius variations of order one, that is, linear, and two, that is, quadratic, where considered in [12]. The reflection coefficient of a waveguide with fitted rings, calculated with an approximate continuous model as described above, is plotted in Figure 1.2b against normalised wavenumber, for both linear and quadratic inner-radius variation [12]. It can be seen that the frequency response of the reflection coefficient has similar fluctuations as in the case of elastic wedges, shown in Figure 1.1b. The modulus of the reflection coefficient of the quadratic waveguide plotted in Figure 1.2b is seen to be much smaller than that of the linear waveguide, which is also due to the fact that for the same truncation length, the quadratic waveguide has a much smaller ring inner radius towards the end compared to the linear waveguide.

Waveguides with fitted rigid rings are analysed in Chapter 3, for linear and quadratic ring inner-radius variation. Apart from the continuous analytical model, the reflection coefficient is also calculated with a Transfer Function method, and results from simulations are also compared with experimental results from the literature.

1.2.3 The cochlea as a non-uniform waveguide

The cochlea is a coil-shaped organ of the inner ear, where the mechanical vibrations induced from external acoustic waves are transduced into neural signals that travel to the brain. The coiling is not thought to play a significant role in wave propagation. A simplified model of the uncoiled cochlea is shown in Figure 1.3a. This model comprises two fluid-filled chambers, scala vestibuli and scala tympani, which are separated by the flexible cochlear partition and are connected through a small opening, the helicotrema, at the apical end of the cochlea. The basilar membrane is the main flexible component of the cochlear partition. Waves are generated by the interaction of the mass of the fluid in the chambers and the stiffness of the basilar membrane. The stiffness of the basilar membrane decreases along the cochlear length, causing the waves to slow down.

The input of the cochlea is the vibration of the stapes, which drives the fluid in the chambers into motion. The coupling of the motion of the fluid in the chambers with the transverse vibration of the cochlear partition results in a wave travelling along the cochlea, giving rise to a pressure difference across the cochlear partition and a transverse velocity of the cochlear partition. The modulus and phase of the cochlear partition velocity are plotted for single frequency excitation as a function of position along the cochlea in Figures 1.3b and 1.3d,

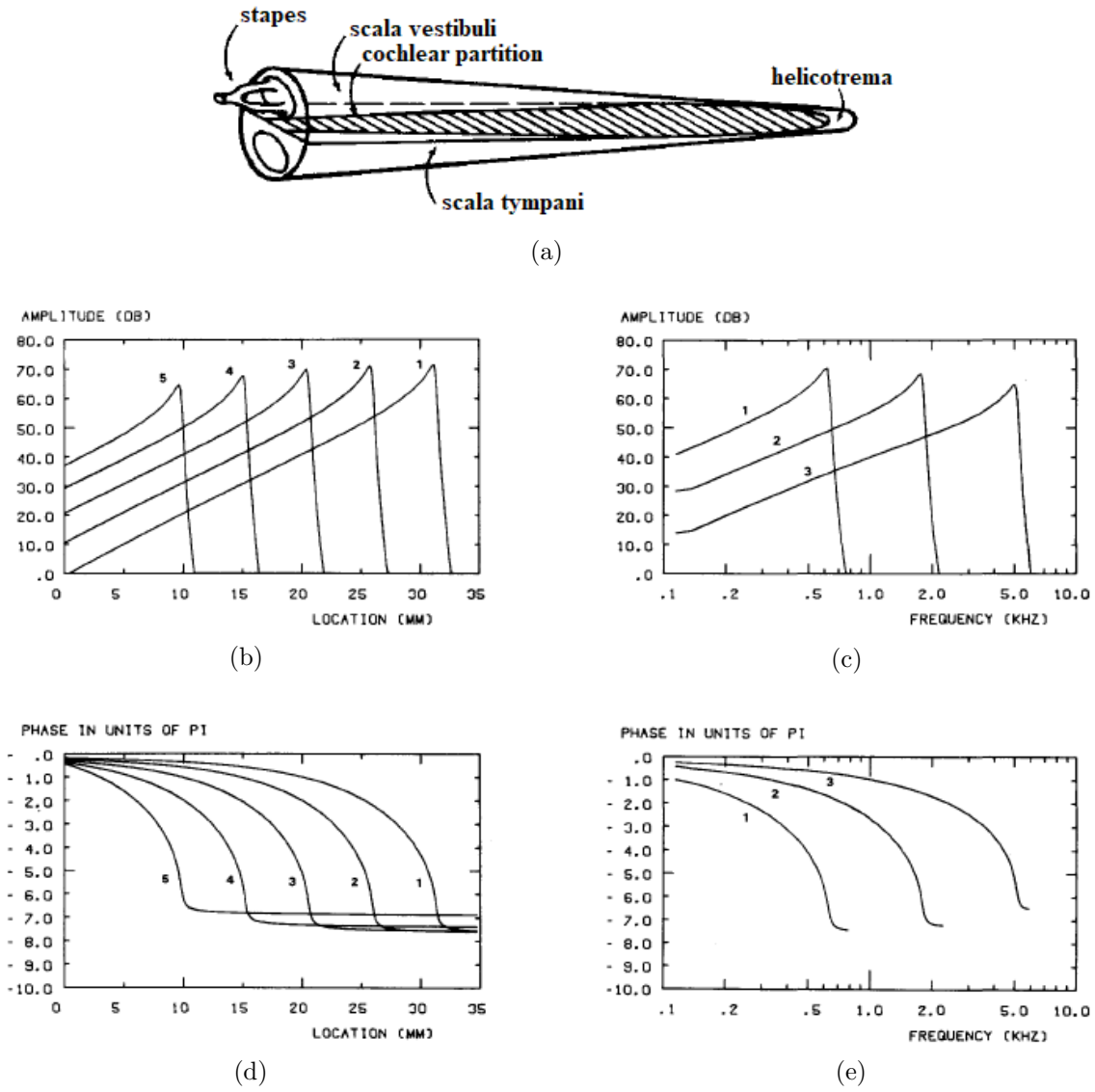

Figure 1.3. (a) Uncoiled model of the cochlea showing the stapes, the two fluid-filled chambers, that is, scala vestibuli and scala tympani, the cochlear partition and the helicotrema. The image is taken from Figure 5.1c in [13] with permission. (b) Modulus and (c) phase of the cochlear partition velocity response plotted against position along the cochlea for five different excitation frequencies; the curves denoted by numbers 1 to 5 correspond to different frequencies, starting from the lowest. The images in (b) and (c) are taken from Figure 6.7 in [13] with permission. (d) Modulus and (e) phase of the cochlear partition velocity response plotted against frequency for three different positions; the curves denoted by numbers 1 to 3 correspond to different positions, starting from further from the stapes. The images of (d) and (e) are taken from Figure 6.8 in [13] with permission.

respectively, for five different frequencies [13]. It can be seen that the amplitude of the cochlear partition velocity increases and peaks at a specific position along the cochlear length, which is different for different frequencies, due to the non-uniformity of the waveguide. Lower frequencies peak at positions closer to the helicotrema and higher frequencies peak at positions closer to the stapes. Beyond the peak position, the wave amplitude rapidly decreases. Accordingly, the phase accumulates up to the point of peak response, beyond which it is reasonably uniform.

A similar coupled response variation occurs at a given position along the cochlea if the response is plotted against logarithmic frequency, as seen in Figures 1.3c and 1.3e in terms of modulus and phase, respectively. At a given position, the modulus of the cochlear partition

velocity increases and peaks at a certain frequency, beyond which it rapidly decays. This characteristic frequency is different for different positions along the cochlea. The phase in Figure 1.3e also varies in a similar way to the one against position plotted in Figure 1.3c.

The correspondence of peak frequency response and position in the cochlea is called the tonotopic mapping, with different frequency components being localised at different positions. The sensory cells at those positions are thus excited at different frequencies and the corresponding signals are sent to the auditory nerve [13]. The cochlea thus functions as a spatial spectrum analyser. Additionally, the cochlea presents practically no reflection to excitation at the stapes [13], thus absorbing the input vibrations of the stapes over its working frequency spectrum.

The wave-based functioning of the cochlea as a spectrum analyser is more efficient than conventional spectral analysis methods, requiring less processing power, as has been discussed in [14]. There has therefore been research interest in designing and implementing systems with similar functioning principles within various physical contexts. An analysis of a simple cochlear model is carried out in Chapter 4, focusing on the dependence of the coupled cochlear response to the variation of certain model parameters.

1.2.4 Acoustic 'rainbow' sensors

Acoustic 'rainbow' sensors are systems that focus different frequency components of acoustic waves to different positions, similarly to the observed cochlear coupled response. They originated in optical sensors with the same function [2], hence their name. Apart from their potential application as broadband absorbers, as presented for example in [1], acoustic 'rainbow' sensors could also be used as efficient signal analysers, having the spectral analysis advantages present in the cochlea.

An example of an acoustic 'rainbow' sensor is depicted in Figure 1.4a, consisting of a series of grooves of varying depth separated by rigid plates, as proposed in [15]. The input of the system is an acoustic source at the left side of the structure, not shown here, and the main direction of propagation is along the z axis. The grooves act as quarter-wave resonators, with an acoustic stiffness that decreases along the length of the waveguide, which generates a wave by interaction with the mass of the surrounding fluid.

The acoustic intensity in the grooves is plotted against longitudinal position, z, in Figure 1.4b. It can be seen that different frequencies peak at different positions along the structure, beyond which the response rapidly decays, similarly to what is observed in the cochlea. However, fluctuations of the acoustic intensity are observed along the longitudinal direction, which are indicative of standing waves due to reflections. The slightly smaller peaks occurring in positions before the highest peak and the non-smooth variation of the response imply that the different frequency components are not well localised, thus compromising the

functioning of the system as a spatial spectrum analyser.

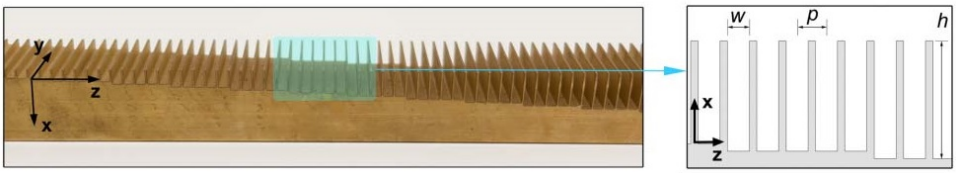

(a)

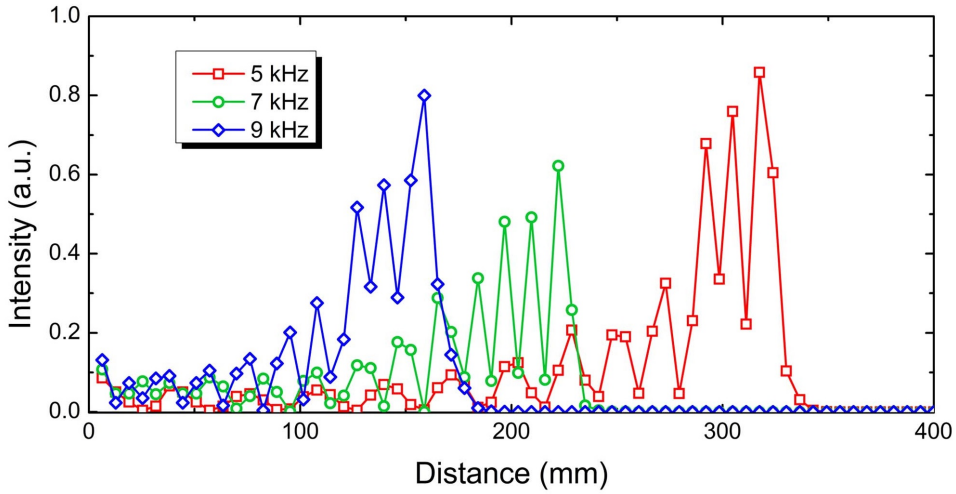

(b)

Figure 1.4. (a) Three-dimensional schematic of an acoustic waveguide with grooves of increasing height. The image is taken from Figure 1a in [15]. (b) Normalised acoustic intensity in the grooves for the structure presented in (a) plotted against distance for three different excitation frequencies. The image is taken from Figure 2c in [15]. The article from which both images are taken is published in open access under a Creative Commons Attribution-NonCommercial-NoDerivs 3.0 Unported License, https://creativecommons.org/licenses/by-nc-nd/3.0/.

A different acoustic system inspired by the functioning of the cochlea was presented in [2], consisting of a main duct with a series of Helmholtz-Resonator side branches, whose properties vary along the length of the structure. Figures 1.5a to 1.5d show the normalised acoustic pressure modulus in an example of such a system for excitation frequencies of 1, 2, 3 and 4 kHz, respectively. The low frequency propagates throughout the length of the system, whereas the higher frequencies reach different positions where they peak, beyond which they rapidly decay, in a way similar to that observed for the system of Figure 1.4a and to what is observed in the cochlea. It can again be seen, however, in Figures 1.5a to 1.5d that the response fluctuates along the longitudinal direction, as can be seen from the longitudinal variation of the colours in the resonators prior to the resonator with the highest response for a given frequency.

A two-dimensional colour map of the acoustic response of the system is given in Figure 1.5e, showing the variation against both frequency and position. It can again be seen that the response fluctuates with frequency for a given position, as implied by the interchanging light and dark blue regions, up to a certain frequency beyond which it decays. If each Helmholtz Resonator is regarded as a pass band filter around the frequency of peak response, its non-smooth

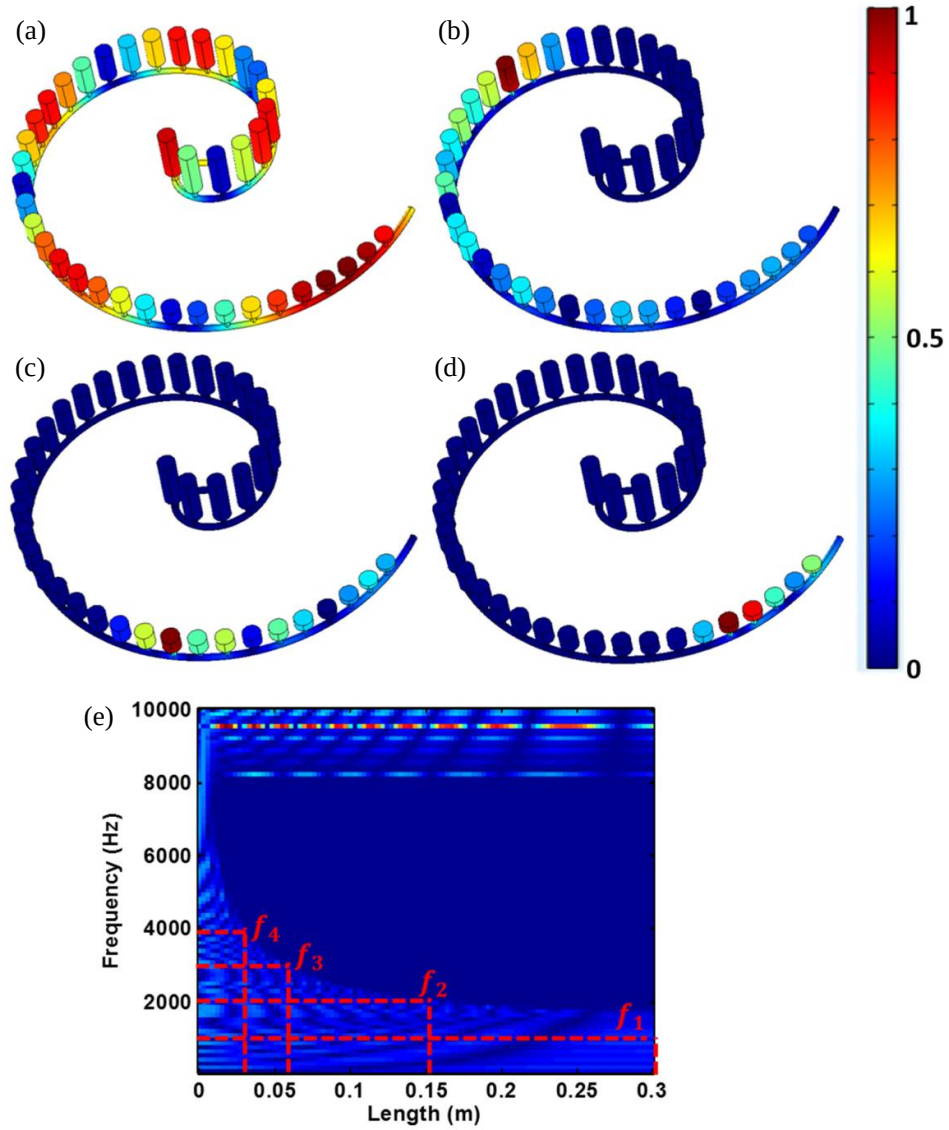

Figure 1.5. (a)-(d) Normalised modulus of the acoustic pressure in a system consisting of a circular duct with an array of Helmholtz-Resonator side branches [2], for excitation frequencies of 1, 2, 3 and 4 kHz, respectively. (e) Normalised modulus of the acoustic pressure along the axis of the duct of the system shown in (a)-(d) plotted against position and frequency; the noted frequencies are $f_1 = 1$ kHz, $f_2 = 2$ kHz, $f_3 = 3$ kHz $f_4 = 4$ kHz. All the images are taken from Figure 3 in [2], which is published in open access under a Creative Commons Attribution 4.0 International License, https://creativecommons.org/licenses/by/4.0/.

fluctuating frequency response deteriorates its use as a filter.

A system of a duct with a series of Helmholtz Resonator side branches, similar to the one shown in Figure 1.5, is presented in Chapter 5. The design of the system, however, is based on the values of a number of non-dimensional parameters for the cochlea. Simulations show that such a system can produce a smooth spatial and spectral response, so that it can be used as a more effective acoustic 'rainbow' sensor.

1.3 Outline of the thesis

In Chapter 2, an elastic wedge is considered, acting as a termination to a uniform plate. A method based on the WKB approximation for the various wave components is presented, where the system of equations of the boundary conditions is solved by matrix inversion. Thus the reflection coefficients of the system, namely, the total, junction and end reflection coefficients, are obtained. Apart from the first-order WKB approximation, which is most commonly used in the literature, higher-order approximations are also derived. The total reflection coefficient is also calculated with the Finite Element method. An analysis is carried out of the relation of the various reflection coefficients, specifically on how the reflection coefficients due to the junction and due to the truncated end affect the form of the total reflection coefficient. The validity of the WKB method with different orders of approximation is assessed by comparing the results for the modulus of the total reflection coefficient with those obtained with the Finite Element method. Apart from the typically used power-law thickness variation, different thickness profiles with similar absorbing properties are also considered.

In Chapter 3, an acoustic duct termination consisting of fitted thin rigid rings is considered. Similarly to an elastic wedge, such a system causes waves to slow down and considerable absorption takes place towards the end of the waveguide. A general analysis of the system is carried out based on a continuous analytical model. A Transfer Function method is formulated, also implemented with a geometrical variation compared to how it is implemented in the literature. A Transmission Line approximation to the Transfer Function method is also assessed. Results from numerical simulations are compared with experimental ones taken from the literature.

In Chapter 4, a one-dimensional single-degree-of-freedom 'box model' of the passive cochlea is used to calculate the coupled cochlear response. The wave equation is solved both with the WKB method and with the Finite Difference method. The main characteristics of the cochlear functioning are presented, based on the variation of the wavenumber, the propagation velocity and the coupled response. A parametric analysis is also carried out, where the dependence of the form of the coupled response on a set of non-dimensional parameters is studied.

In Chapter 5, an acoustic system consisting of a main duct with side branches of Helmholtz Resonators is studied. A system with identical Helmholtz resonators is first considered, and its general characteristics are presented. Two systems of acoustic 'rainbow' sensors from the literature are then analysed. The design of a system with Helmholtz Resonators whose properties vary along its length is then presented, with parameter values based on corresponding ones for the cochlea. The response is calculated with a Transfer Matrix method and with a Transmission Line approximation. The performance of the system as a 'rainbow' sensor is assessed. The behaviour of the system as an acoustic absorber is also examined.

The conclusions drawn in the thesis are summarised in Chapter 6. Similarities and

differences between the considered systems are further discussed. The main body of the thesis closes with suggestions for future work on the studied subjects.

1.4 Research objectives and contributions of the thesis

A fundamental objective of the thesis is the extension of scientific knowledge and understanding of wave-focusing absorbing waveguides, whose absorptive behaviour is induced by their non-uniform features rather than by the use of absorptive material. The motivation for this research objective stems from the extended potential for applications using such systems, for example for vibration and acoustic absorbers or for 'rainbow' sensors. The similarities and differences of non-uniform absorbing systems within different physical contexts, for example for bending plates and for acoustic ducts, are also highlighted.

The assessment of different analysis methods for the different systems forms another objective traversing the analysis of the thesis. Therefore, two or more calculation methods are used for each different type of system examined and the corresponding results are compared. Special interest is drawn to the strengths and the limitations of the WKB approximation method.

In terms of the cochlea, it is of interest to study the dependence of its coupled response to a set of non-dimensional parameters. The use of non-dimensional parameters can further facilitate the design of systems with similar response characteristics. Furthermore, including the cochlea in this study of non-uniform waveguides illustrates a general connection between naturally occurring and artificially designed systems. The design of an acoustic system that functions as a 'rainbow' sensor with smooth spatial and frequency response, similar to the coupled response of the cochlea, is the final main objective of this research.

The main contributions of the thesis are:

(i) A higher-order WKB analysis of the reflections from a tapered elastic wedge terminating a uniform plate, showing that the first-order WKB approximation that is usually employed is insufficient for predicting the details of the total reflection coefficient, whereas higher-order WKB approximations can provide good predictions above some frequency.

(ii) Analysis of reflection from different thickness profiles of the tapered elastic wedge along with the typically used power-law thickness profile. The exponential wedge in particular is found to have generally lower reflection than the wedges of different profiles. This analysis also illustrates the relation of the different sources of reflection for a wedge terminating a uniform plate with the overall reflective behaviour of the system, and helps identify the limitations of the applicability of the WKB method.

(iii) A non-dimensional parameter analysis of the passive cochlea, which illustrates the relation of the form of the coupled cochlear response with the physical characteristics of the

cochlea, especially with respect to the phase-shift parameter and the mass ratio. It is shown that changing the phase-shift parameter changes the symmetry of the coupled response, whereas changing only the mass ratio while keeping the phase-shift parameter intact does not change the form of the coupled response.

(iv) Analysis of acoustic 'rainbow' sensors to show that the damping in the resonators generates a trade-off between selectivity and the number of elements, leading to a new design based on parameter values of the cochlea, which has a smooth response both with respect to space and frequency, and which presents high absorption over its working spectrum.

(v) A comparative analysis of the different studied systems with focusing and absorbing properties, which provides insight into their general behaviour, and highlights the relation between the specific aspects of the different systems and their corresponding responses.

Parts of the work presented in this thesis have been published, including one journal article and three articles in conference proceedings, as follows:

A. Karlos, S. J. Elliott, and J. Cheer. Higher-order WKB analysis of reflection from tapered elastic wedges. *Journal of Sound and Vibration*, 449:368-388, 2019.

A. Karlos and S. J. Elliott. Reflection from a non-uniform acoustic waveguide with fitted rigid rings using a Transfer Function method. In *26th International Congress on Sound and Vibration*, Montreal, Canada, 7-11 July, 2019.

A. Karlos, S. Elliott, and J. Cheer. Reflection from elastic wedges of different thickness profiles. In *ISMA2018 and USD2018*, pages 4571-4584, Leuven, Belgium, 17-19 September, 2018.

A. Karlos, D. Vignali, B. Lineton, and S. Elliott. Quasi-linear modelling of the coupled cochlea using the WKB method. In *Mechanics of Hearing*, Brock University, Canada, 19-24 June, 2017, volume 1965, American Institute of Physics.

The conference article listed last concerns work that is not included in the main body of the thesis, but the extended Appendix B contains the relevant work.

Chapter 2

Tapered elastic wedges

2.1 Introduction

Flexural vibrations affect the behaviour of a variety of mechanical systems, from small machinery parts to vehicles, aircraft and buildings. It is often desired that flexural vibrations are reduced, as higher amplitude vibrations can cause fatigue [16], leading to higher demands in maintenance. Flexural vibrations are also the main cause of sound radiation [16], so that their damping is crucial for noise reduction.

The vibration of an elastic structure under bending with given boundaries can be thought of as resulting from the constructive interference of incident and reflected bending waves between the structure boundaries along the direction, or directions, of wave propagation. Therefore, one way to damp vibrations is by reducing the reflection from the boundaries. It was proposed by Mironov in [7] that reflections of flexural waves from the free boundary of a thin plate could be reduced by tapering the plate thickness, ideally to zero, according to a power-law profile variation, resulting in a wedge-like structure. The behaviour of a thin plate under bending along its longitudinal direction is similar to that of a thin beam of constant width, so that conclusions drawn for a non-uniform plate can be extended to beams.

It was theoretically predicted in [7] that, for the case of quadratic tapering, the propagation velocity decreases along the tapered plate and it becomes zero at its vanishing edge. Therefore, incident waves slow down and halt at the tip, so that they do not reach the boundary and are thus not reflected; an arbitrarily small amount of structural damping is sufficient to absorb all the incident energy at the vicinity of the edge. Similar results were obtained in [17] for the general case of power-law thickness variation of power larger or equal to two. This phenomenon has come to be known as the 'Acoustic Black Hole' effect, even though it applies to flexural rather than acoustic waves; the term 'Vibrational Black Hole' has also been used alternatively [18].

It was demonstrated in [7], however, that even a very small truncation at the tip of the wedge, which inevitably occurs in practice, leads to significant reflection. A way to overcome this was proposed by Krylov and Tilman in [8], were it was predicted by simulations that

adding thin layers of viscoelastic material on the wedge surface dramatically improves the absorptive performance of the structure, giving significantly less reflection. This result was also experimentally confirmed in [19]. Two-dimensional indentations of power-law variation in plate surfaces have also been used with similar results, as has been shown both theoretically [20] and experimentally [21].

A measure for the performance of the elastic wedge as a vibration absorber that has been widely used in the literature is the modulus of the reflection coefficient, as was done for example in [7] and [8]. A number of different methods have been used for the calculation of the reflection coefficient. The WKB approximation method, which provides approximate analytical solutions of different orders of approximation to differential equations, was implictly used in [7] to obtain the analytical form of the wavenumber. In [8], the first-order WKB approximation was used, also called the geometrical acoustics approximation.

In both [7] and [8], only the reflection from the truncated edge was considered, which corresponds to assuming a semi-infinite tapered wedge with the incident wave originating within the wedge and no reflection occurring from the direction of incidence. The modulus of the reflection coefficient at a given distance from the edge was calculated using the wavenumber, which is also provided by the zeroth-order WKB approximation. The varying wave amplitude provided by the first-order WKB approximation is not required for this calculation, due to the amplitude terms of the incident and reflected waves cancelling out at the position where the reflection coefficient is calculated, so that the analysis in [7] and [8] is equivalent to a zeroth-order WKB approximation.

For practical applications, it is useful to consider the tapered wedge as forming a termination to a uniform plate, as shown in Figure 2.1. Such a system has been analysed in the literature using various methods. In [10] and in [22, 23], a numerical method based on the Impedance Matrix was used. A parametric study for the optimisation of various geometrical parameters was carried out in [24] using Finite Element modelling. In [25], a wavelet decomposition was used, giving good agreement both with Finite Element simulations and with experiments.

A system consisting of a wedge terminating a uniform rectangular plate was considered in [26]. A two-dimensional solution based on the first-order WKB approximation was formed, accounting also for oblique incidence, and the transfer mobility was calculated; experiments were also conducted. Some correspondence was observed between the calculated and the measured responses in terms of general characteristics over a part of the spectrum, but the calculated response failed to capture the details of the experimental one. These discrepancies between simulations and experiment were attributed to the use of different boundary conditions in the two cases.

The validity of the WKB method relies on the satisfaction of a set of conditions, the most

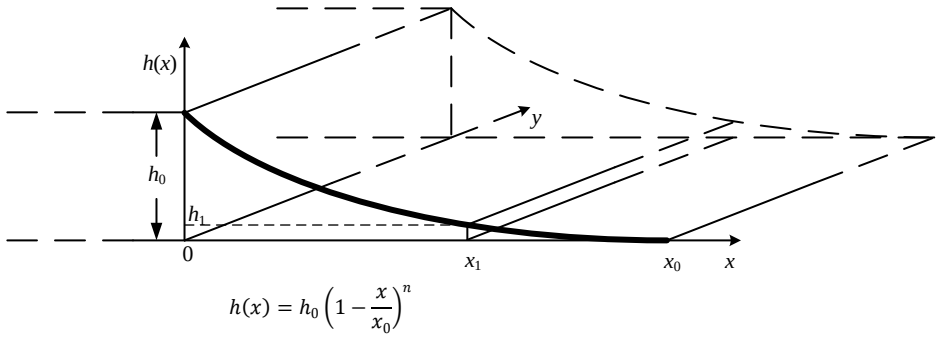

Figure 2.1. Schematic of a power-law wedge, either ideally tapered down to zero thickness at the ideal length, x_0, or truncated at length x_1, terminating a semi-infinite uniform plate. The thickness at the junction of the uniform plate and the wedge, h_0, the thickness at the end of the truncated wedge, h_1, and the mathematical expression of the thickness variation, $h(x)$, are shown.

common of which is expressed mathematically as [8]

$$\left|\frac{k'}{k^2}\right| \ll 1, \tag{2.1}$$

where k is the wavenumber and the prime denotes differentiation with respect to the spatial variable. This condition expresses the requirement that the spatial rate of change of the wavelength should be negligible. According to the formal derivation of the WKB approximation, further validity conditions also need to be satisfied, as is presented for example in [27, 28], but only the condition of Equation (2.1) is typically used in the engineering literature. In [29], the reflective behaviour of a tapered beam connected to a uniform beam was assessed by relating Finite Element results for the reflection coefficient with the quantity of the left side of Equation (2.1).

WKB approximations of order higher than one were used in [30] for the calculation of the natural frequencies of a non-uniform beam and results were compared with ones from Finite Element simulations. Significant improvement of the predicted frequencies was provided by using higher-order WKB approximations. It would therefore be expected that higher-order WKB approximations could also provide considerable improvement in predicting the reflection coefficient of a wedge terminating a uniform plate, compared to the first-order WKB approximation, which was used in [26].

In this chapter, a wedge terminating a thin uniform plate is analysed using WKB approximations of order up to three. The boundary conditions of the system, expressed in terms of the WKB approximations of the different wave components, are formulated into a matrix equation, which is solved numerically by inversion. Apart from the usually considered power-law thickness variation profile, other thickness profiles are also examined, namely, an exponential, a power-cosine, a Gaussian and a compound power-law profile. The results from

the different orders of WKB approximation are compared with those from Finite Element models for the different profiles.

Apart from the total reflection coefficient, defined as the ratio of the reflected wave to the incident wave, both evaluated in the uniform plate, the reflection coefficient due to the discontinuity at the junction of the uniform plate and the wedge and the reflection coefficient due to the truncated edge are also obtained. The latter corresponds to the reflection coefficient calculated in [7] and [8]. The relation of the junction and end reflection coefficients with the characteristics of the total reflection coefficient is discussed.

In Section 2.2, the wave equation for harmonic flexural waves on a thin plate is presented, and the WKB solutions of order of approximation up to three are derived. The effective length for a truncated wedge is also introduced, defined as the length of an equivalent uniform plate in terms of travel time of a wave pulse. A zeroth-order WKB analysis for the calculation of the reflection coefficient for a truncated wedge driven internally is first carried out in Section 2.3. The reflection coefficients involved in the system of a wedge terminating a uniform plate are then presented, namely, the total, junction and end reflection coefficients. Subsequently, a method for the calculation of the different reflection coefficients, as well as the related transmission coefficients, is introduced, based on the solution of the system of equations of the boundary conditions. A Finite Element model for the calculation of the modulus of the total reflection coefficient is also presented.

An analysis on reflection from a quadratic wedge is given in Section 2.4, where the total, junction and end reflection coefficients calculated with the analytical method using different orders of WKB approximation are compared; the total reflection coefficient is also compared with results from Finite Element simulations. The relation of the magnitude of the junction and end reflection coefficients with the form of the total reflection coefficient is discussed. An analysis on the validity of the WKB approximations in relation to the validity condition of Equation (2.1) is included.

The reflection coefficients of different thickness profiles are presented in Section 2.5, where the total reflection coefficient is calculated with Finite Element models and the junction and end reflection coefficients are calculated with the analytical method involving WKB approximations. The characteristics of the total reflection coefficient in relation to the junction and end reflection coefficients are discussed for the different profiles, especially regarding the general level of reflection, the magnitude of fluctuations in the total reflection coefficient, the frequency of the first dip and the bandwidth between consecutive dips.

A comparison of results for the total reflection coefficient calculated with different orders of WKB approximation with ones from Finite Element simulations for wedges of different thickness profiles is given in Section 2.6. The limitations of the WKB approximation for the different profiles are highlighted, also with respect to the WKB validity condition. Conclusions are summarised in Section 2.7.

A major part of the work on reflection from tapered elastic wedges has been published in the Journal of Sound and Vibration [31], and, therefore, the analysis presented in this chapter is heavily based on that article. Part of the work was also presented in the ISMA 2018 international conference [32].

2.2 The WKB approximation method for an elastic wedge

2.2.1 The wave equation for flexural waves on a non-uniform thin plate

An elastic wedge is considered whose width is infinite along the y direction, as shown in Figure 2.1, so that the system variables vary only along the x direction. One-dimensional harmonic flexural plane waves on a thin plate with varying thickness $h(x)$ are described by the fourth-order differential equation [16]

$$\left[D(x)w''(x,\omega)\right]'' - \omega^2\rho h(x)w(x,\omega) = 0, \tag{2.2}$$

where $w(x,\omega)$ is the complex transverse displacement amplitude of the midsurface of the plate, ω is the angular frequency, ρ is the density of the material of the plate, $D(x) = \rho c_p^2 h^3(x)/12 = Eh^3(x)/\left(12(1-\sigma^2)\right)$ is the bending stiffness, or flexural rigidity, E is the Young's modulus, σ is the Poisson's ratio, and c_p is the propagation velocity of quasi-longitudinal waves on a thin plate, given by $c_p = \left[E/\left(\rho\left(1-\sigma^2\right)\right)\right]^{1/2}$. The independent variable of the differential equation is the spatial coordinate x, and differentiation with respect to x is denoted by primes. The convention for the time variation of the harmonic displacement is $\mathrm{e}^{\mathrm{i}\omega t}$, where i is the imaginary unit.

The corresponding equation for the flexural vibrations of a thin beam is [16]

$$\left[B(x)w''(x,\omega)\right]'' - \omega^2\rho A_{cs}(x)w(x,\omega) = 0, \tag{2.3}$$

where $B(x) = EI(x)$ is the bending stiffness of the beam, where $I(x)$ is the second moment of area, and $A_{cs}(x)$ is the cross-sectional area. The second moment of area and the cross-sectional area are given, respectively, by $I(x) = bh^3(x)/12$ and $A_{cs}(x) = bh(x)$, where b is the width of the beam. It should be noted that the bending stiffness of the plate, D, is measured in N·m, while the bending stiffness of the beam is measured in N·m^2. If the width of the beam, b, is constant, it cancels out, and Equation (2.3) becomes

$$\left[\frac{Eh^3(x)}{12}w''(x,\omega)\right]'' - \omega^2\rho h(x)w(x) = 0, \tag{2.4}$$

which is equivalent to Equation (2.2), apart from a constant factor of $1/\left(1-\sigma^2\right)$ in the bending stiffness of the plate. Therefore, all the following analysis can also be applied to a beam of

constant width, if the correction factor for the plate involving Poisson's ratio is accounted for.

Equation (2.2) is an ordinary differential equation, since only differentiation with respect to the spatial coordinate is involved. In the consequent analysis, the dependence on frequency and on position are often omitted for notational convenience. It should be mentioned that exact analytical solutions to Equation (2.4), were recently found for power-law thickness variation of order greater or equal to two [33], that is, for the thickness profile which is most typically used in the literature.

2.2.2 WKB solutions to the wave equation

The WKB method provides analytical solutions of different orders of approximation to differential equations. A more general presentation of the method is given in Appendix C. For Equation (2.2), the first-order WKB approximation was derived by Pierce in [5], based on considerations on the conservation of energy. A more general approach is followed here, based on perturbation analysis, similar to that presented in [34], which facilitates the derivation of higher-order approximations.

A perturbation factor, defined by $\epsilon = \omega^{-1/2}$, may be included in Equation (2.2), so that it takes the form

$$\epsilon^4 \left(Dw''\right)'' - \rho h w = 0. \tag{2.5}$$

A trial solution for the transverse displacement may be applied, in the form of an infinite exponential power series,

$$w = A\mathrm{e}^{\epsilon^{-1} \sum_{n=0}^{\infty} S_n \epsilon^n}, \epsilon \to 0, \tag{2.6}$$

where the functions S_n vary both with position and frequency, and A is an arbitrary complex constant with dimensions of displacement. In strict mathematical notation, the sign of equality should be replaced by $\sim$, to express the fact that this formula asymptotes to the solution of Equation (2.5) as the perturbation factor tends to zero, that is, as the frequency tends to infinity. Here a looser mathematical notation using equalities is followed, in accordance with the engineering literature.

The requirement that the perturbation factor tend to zero for the solution to be accurate implies that the WKB method should provide good results at higher frequencies, and the validity of the method is expected to deteriorate at low frequencies, where the perturbation factor becomes large. It should be pointed out, however, that since Equation (2.5) corresponds to thin plate theory, it is descriptive of the flexural vibrations only up to frequencies for which the rotational inertia and the effect of shear are negligible, and for which only the fundamental mode is present [35]. Therefore, the solutions provided by the WKB method are only valid in a limited bandwidth within which the frequency is high enough for the WKB solution to be valid and low enough so that the rotational inertia and the shear deformation are insignificant, and

only plane waves are present. Similar limitations for the WKB method were pointed out in [30] for the case of thin beams.

If the trial solution given by Equation (2.6) is substituted into Equation (2.5), and after dividing all terms by the exponential, the resulting equation may be rearranged as a polynomial equation of ϵ. This equation must be valid for all values of ϵ, so that an infinite set of differential equations is obtained. The first four of these equations are

$$\epsilon^0 : S_0'^4 = \frac{\rho h}{D} = \frac{12}{c_p^2 h^2}, \tag{2.7}$$

$$\epsilon^1 : S_1' = -\frac{3}{2}\frac{S_0''}{S_0'} - \frac{1}{2}\frac{D'}{D}, \tag{2.8}$$

$$\epsilon^2 : S_2' = -\frac{3}{2}\frac{S_1'^2}{S_0'} - \frac{3}{2}\frac{S_1''}{S_0'} - 3\frac{S_0''S_1'}{S_0'^2} - \frac{S_0'''}{S_0'^2} - \frac{3}{4}\frac{S_0''^2}{S_0'^3} - \frac{3}{2}\frac{D'}{D}\frac{S_1'}{S_0'} - \frac{1}{4}\frac{D''}{D}\frac{1}{S_0'} - \frac{3}{2}\frac{D'}{D}\frac{S_0''}{S_0'^2} \tag{2.9}$$

and

$$\begin{aligned}\epsilon^3 : S_3' = &-\frac{S_1'^3}{S_0'^2} - \frac{3}{2}\frac{D'}{D}\frac{S_1'^2}{S_0'^2} - 3\frac{S_1'S_2'}{S_0'} - \frac{3}{2}\frac{D'}{D}\frac{S_2'}{S_0'} - \frac{3}{2}\frac{S_2''}{S_0'} - \frac{S_1'''}{S_0'^2} - \frac{1}{4}\frac{S_0''''}{S_0'^3} - \frac{1}{2}\frac{D''}{D}\frac{S_1'}{S_0'^2} - 3\frac{S_1'S_1''}{S_0'^2} - \\ &\frac{3}{2}\frac{D'}{D}\frac{S_1''}{S_0'^2} - \frac{S_0'''S_1'}{S_0'^3} - \frac{1}{2}\frac{D'}{D}\frac{S_0'''}{S_0'^3} - \frac{3}{2}\frac{S_0''S_1''}{S_0'^3} - \frac{1}{4}\frac{D''}{D}\frac{S_0''}{S_0'^3} - 3\frac{S_0''S_2'}{S_0'^2} - \frac{3}{2}\frac{S_0''S_1'^2}{S_0'^3} - \frac{3}{2}\frac{D'}{D}\frac{S_0''S_1'}{S_0'^3}.\end{aligned} \tag{2.10}$$

The WKB approximation of order N for the transverse displacement can be written as

$$w = A\mathrm{e}^{\epsilon^{-1}\sum_{n=0}^{N} S_n\epsilon^n}, \tag{2.11}$$

so that the first $N+1$ terms for S_n' have to be solved sequentially, starting from the zeroth-order one, given by Equation (2.7).

Equation (2.7), which is called the eikonal equation, has four algebraic roots,

$$S_0' = j\left(\frac{12^{1/2}}{c_p h}\right)^{1/2}, \tag{2.12}$$

where the factor $j = \pm 1, \pm \mathrm{i}$ determines the different roots. By integrating Equation (2.12) with respect to x and multiplying by ϵ^{-1}, the first term in the exponent of the solution (2.11) is obtained,

$$\epsilon^{-1}S_0 = j\int_0^x k(\tilde{x})\mathrm{d}\tilde{x}, \tag{2.13}$$

where the lower limit of integration has been set to be at the coordinate origin for convenience, and

$$k = \left(\frac{12^{1/2}\omega}{c_p h}\right)^{1/2} \tag{2.14}$$

is the wavenumber in the non-uniform plate.

Structural damping may be included in the modelled system through a complex Young's modulus, which leads to a complex quasi-longitudinal velocity and, in turn, to a complex wavenumber. The corresponding real and complex quantities, without and with damping, respectively, starting with the Young's modulus, are as follows,

$$E \to E(1+\mathrm{i}\eta) \Rightarrow c_p \to c_p(1+\mathrm{i}\eta)^{1/2} \Rightarrow k \to \frac{k}{(1+\mathrm{i}\eta)^{1/4}}, \tag{2.15}$$

where η is the damping loss factor. In most cases, the loss factor is much smaller than one, so that the complex wavenumber may be simplified as

$$k = \left(\frac{12^{1/2}\omega}{c_p h}\right)^{1/2} \left(1 - \mathrm{i}\frac{\eta}{4}\right). \tag{2.16}$$

It should be noted that once the effect of damping is explicitly included in the expression for the wavenumber through the imaginary part, as in Equation (2.16), the quasi-longitudinal velocity in this equation has to be purely real.

The second term in the exponent of the WKB solution, given by Equation (2.11), is the solution of Equation (2.8), which is

$$S_1 = \frac{3}{4}\ln\left(\frac{h_0}{h}\right), \tag{2.17}$$

where h_0 is the thickness at $x = 0$. It should be noted that S_1 is the same for all four functions of Equation (2.12), as the factor j cancels out in Equation (2.8). Including only the $n = 0$ and $n = 1$ terms in the solution gives the first-order WKB approximation,

$$w_1 = A\left(\frac{h_0}{h}\right)^{3/4} \mathrm{e}^{j\int_0^x k(\tilde{x})\mathrm{d}\tilde{x}}, \tag{2.18}$$

where A is an arbitrary complex constant with dimensions of displacement. The first-order WKB approximation is most typically used in the literature and it is often referred to simply as the WKB approximation. In the fields of acoustics and vibration, it is also called the geometrical acoustics approximation [8].

Higher-orders of approximation may be obtained by including more terms in the exponent of Equation (2.11). Specifically, the second- and third-order WKB approximations may be written as

$$w_2 = A\left(\frac{h_0}{h}\right)^{3/4} \mathrm{e}^{j\int_0^x k(\tilde{x})\mathrm{d}\tilde{x} + \omega^{-1/2}S_{2,j}} \tag{2.19}$$

and

$$w_3 = A\left(\frac{h_0}{h}\right)^{3/4} \mathrm{e}^{j\int_0^x k(\tilde{x})\mathrm{d}\tilde{x} + \omega^{-1/2}S_{2,j} + \omega^{-1}S_{3,j}}, \tag{2.20}$$

respectively, where the subscript j also denotes the different S_2 and S_3 functions corresponding to the four roots of the eikonal equation. The higher-order functions S_2 and S_3 are obtained

by integrating Equations (2.9) and (2.10), respectively, which are in general not integrable analytically, so that numerical integration has to be employed. It should be noted that Equation (2.5) can also be transformed into a system of four first-order differential equations, which can then be solved numerically. However, such a solution lacks the insightful analytical form provided by the WKB method.

The one-dimensional wave equation (2.2) only accounts for normal incidence. Oblique incidence could be accounted for by using the two-dimensional wave equation for flexural waves in thin plates, given for example in [26]. This would result in an additional exponential factor in the WKB solutions with a wavenumber for propagation in the direction parallel to the edge, that is, along the y axis in Figure 2.1, as was done for the first-order WKB approximation in [26]. Such an analysis, however, is beyond the scope of this thesis.

As mentioned in the introduction, the validity of the WKB method relies on the satisfaction of certain validity conditions, the most common of which is given in Equation (2.1). By substitution of the wavenumber given by Equation (2.16) into Equation (2.1) it can be verified that, in general, the latter is violated at low frequencies and satisfied at higher frequencies, regardless of the thickness variation. This result is predominant in defining the limitations of applicability of the WKB method. An analysis on the validity condition given in Equation (2.1) in relation to the performance of the WKB approximations is presented in Section 2.4 for a quadratic wedge and in Section 2.6.1 for different thickness profiles. An analysis of additional WKB validity conditions is given in Appendix C.3.2.

2.2.3 Effective length of a truncated wedge

The novel concept of the effective length for a truncated wedge can be defined as the length of an equivalent uniform plate whose thickness, h_0, is the same as the maximum thickness of a given wedge, in which a wave takes the same time to travel from its input boundary to its end as it takes for a wave to travel from the junction to the truncated edge in the wedge. The time it takes for a narrowband flexural wave pulse to travel from the junction to the truncated end is given by

$$t_w = \int_0^{x_1} \frac{\mathrm{d}x}{c_{gr}(x)}, \tag{2.21}$$

where c_{gr} is the group velocity, defined by $c_{gr} = \mathrm{d}\omega/\mathrm{d}(\mathrm{Re}\{k\})$, where Re{} denotes the real part of the quantity in curly brackets. The corresponding time for an equivalent uniform plate is

$$t_u = \frac{l_{eff}}{c_{gr,u}}, \tag{2.22}$$

where l_{eff} is the length of the equivalent uniform plate, which coincides with the effective length of the wedge as defined above, and $c_{gr,u}$ is the flexural group velocity in the uniform plate, defined by the same formula as for the wedge. The group velocity in the uniform plate is

constant along its length, since the wavenumber there, given by Equation (2.16) with $h = h_0$, is also constant. Requiring that the two travel times are equal gives

$$l_{eff} = c_{gr,u} \int_0^{x_1} \frac{\mathrm{d}x}{c_{gr}(x)}. \tag{2.23}$$

Using the wavenumber of Equation (2.16), the group velocities for the wedge and the equivalent uniform plate are written, respectively, as

$$c_{gr}(x) = 2\left(\frac{c_p h(x)\omega}{12^{1/2}}\right)^{1/2} \tag{2.24}$$

and

$$c_{gr,u} = 2\left(\frac{c_p h_0 \omega}{12^{1/2}}\right)^{1/2}. \tag{2.25}$$

Therefore, the effective length of the wedge can be expressed as

$$l_{eff} = h_0^{1/2} \int_0^{x_1} \frac{\mathrm{d}x}{h^{1/2}(x)}, \tag{2.26}$$

or as

$$l_{eff} = \frac{1}{\mathrm{Re}\{k_0\}} \int_0^{x_1} \mathrm{Re}\{k(x)\}\mathrm{d}x, \tag{2.27}$$

where $k_0 = k(0)$ and its real part is given by

$$\mathrm{Re}\{k_0\} = \left(\frac{12^{1/2}\omega}{c_p h_0}\right)^{1/2}. \tag{2.28}$$

It is apparent from Equation (2.26) that the effective length of the wedge is independent of frequency. A normalised effective length with respect to the length of the truncated wedge can be defined as

$$L_{eff} = \frac{l_{eff}}{x_1}. \tag{2.29}$$

The phase velocity in the wedge, defined by $c_{ph} = \omega/\mathrm{Re}\{k\}$, is written as

$$c_{ph}(x) = \left(\frac{c_p h(x)\omega}{12^{1/2}}\right)^{1/2}. \tag{2.30}$$

It can be seen by comparing Equations (2.24) and (2.30) that the group velocity is double the phase velocity; the same holds for a flexural wave in a uniform plate. The wavelength in the wedge, defined by $2\pi/\mathrm{Re}\{k\}$, takes the form

$$\lambda(x) = 2\pi\left(\frac{c_p h(x)}{12^{1/2}\omega}\right)^{1/2}. \tag{2.31}$$

2.3 Reflection coefficients for an elastic wedge

2.3.1 Zeroth-order WKB approximation for the end reflection coefficient

A truncated wedge driven internally is first considered, such as the one depicted in Figure 2.2. The incident wave originates inside the wedge at $x = 0$, so that this system is similar to the one in the original paper by Mironov [7]. The displacement in the wedge is written as

$$w = w_i + w_r + w_{rn}, \tag{2.32}$$

where w_i is the incident wave, w_r is the reflected travelling wave and w_{rn} is the reflected nearfield wave. In Equation (2.32), no nearfield positive-x wave is considered, since no boundary is considered on the left side of the wedge. By defining the end reflection coefficient and the nearfield reflection coefficient as $R_{end} = w_r(0)/w_i(0)$ and $R_n = w_{rn}(0)/w_i(0)$, respectively, and expressing the wave components as WKB approximations, $w_a = \mathrm{e}^{\psi_a}$, where the subscript a can be either i, r or rn, the total displacement takes the form

$$w = A\left(\mathrm{e}^{\psi_i} + R_{end}\mathrm{e}^{\psi_r} + R_n\mathrm{e}^{\psi_{rn}}\right). \tag{2.33}$$

Furthermore, the complex constant amplitude of the incident wave, A, is assumed to be equal to 1 m for convenience, since this is crossed out in the following analysis.

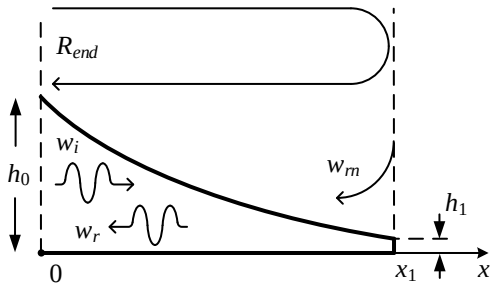

Figure 2.2. Truncated elastic wedge driven internally. The incident travelling wave, w_i, reflected travelling wave, w_r, and reflected nearfield wave, w_{rn}, are shown, as well as the end reflection coefficient,R_{end}.

The boundary conditions at the free end can be written as $w''(x_1) = 0$ and $w'''(x_1) = 0$ [36]. The zeroth-order ψ function for the various wave components in Equation (2.33) has the form

$$\psi_a = j\int_0^x \frac{12^{1/4}\omega^{1/2}}{c_p^{1/2}h^{1/2}}\left(1 - \mathrm{i}\frac{\eta}{4}\right)\mathrm{d}\tilde{x}, \tag{2.34}$$

where $j = -\mathrm{i}$ for ψ_i, $j = \mathrm{i}$ for ψ_r and $j = 1$ for ψ_{rn}. Once the appropriate ψ functions of Equation (2.34) are substituted into Equation (2.33) and the derivatives of the displacement

of order up to three are calculated, the system of the two boundary conditions can be solved, giving for the end reflection coefficient the solution

$$R_{end} = \frac{\left(3\left(\frac{k'}{k^2}\right)^2 - \frac{k''}{k^2}\right)(1-\mathrm{i}) - 2\frac{k'}{k^2} - 1 - \mathrm{i}}{\left(3\left(\frac{k'}{k^2}\right)^2 - \frac{k''}{k^2}\right)(-1-\mathrm{i}) - 2\frac{k'}{k^2} + 1 - \mathrm{i}} \mathrm{e}^{-2\mathrm{i}\int_0^{x_1} k(x)\mathrm{d}x}. \tag{2.35}$$

This expression may be simplified by assuming that the validity condition of Equation (2.1) holds, which complies with the zeroth-order approximation, and also by neglecting the second-order terms, thus yielding

$$R_{end,0} = -\mathrm{i}\mathrm{e}^{-2\mathrm{i}\int_0^{x_1} k(x)\mathrm{d}x}. \tag{2.36}$$

The same result as in Equation (2.36) can be obtained by assuming that the reflection coefficient due to the truncated edge, that is, the ratio of the travelling reflected wave over the incident wave both evaluated at $x = x_1$, is approximately equal to that of a uniform plate, which is equal to $-\mathrm{i}$, as shown in Appendix D. The end reflection coefficient evaluated at the origin can then be calculated by incorporating the exponential as in Equation (2.36), which accounts both for the phase shift due to the wave travelling from $x = 0$ to $x = x_1$ and back, and for the decay due to damping, through the integrated real and imaginary parts of the wavenumber, respectively.

From Equation (2.36), the modulus and phase of the end reflection coefficient can be calculated, giving, respectively,

$$|R_{end,0}| = \mathrm{e}^{2\int_0^{x_1} \mathrm{Im}\{k(x)\}\mathrm{d}x}, \tag{2.37}$$

where, according to Equations (2.16) and (2.24),

$$\mathrm{Im}\{k\} = -\frac{\eta}{4}\left(\frac{12^{1/2}\omega}{c_p h}\right)^{1/2} = -\frac{\eta\omega}{2c_{gr}}, \tag{2.38}$$

and

$$\angle R_{end,0} = -\frac{\pi}{2} - 2\int_0^{x_1} \mathrm{Re}\{k(x)\}\mathrm{d}x, \tag{2.39}$$

where

$$\mathrm{Re}\{k\} = \left(\frac{12^{1/2}\omega}{c_p h}\right)^{1/2} = 2\frac{\omega}{c_{gr}}. \tag{2.40}$$

The expression of Equation (2.37) is equivalent to the one given in [7]. It can be seen from the form of the imaginary part of the wavenumber given in Equation (2.38) that the imaginary part of the wavenumber, and, therefore, the absorption, increases in absolute terms as the thickness decreases. Especially close to the tip, the absorption becomes very large. This can be explained by the fact that the group velocity, and the phase velocity, for which $c_{ph} = c_{gr}/2$, becomes very

small there and the wave is concentrated close to the tip, where it is greatly absorbed.

The integral of the imaginary part of the wavenumber defines the modulus of the end reflection coefficient, as can be seen in Equation (2.37). Since the imaginary part of the wavenumber becomes absolutely very large towards the tip, its spatial integral is dominated by the thickness variation close to the edge. The relation for the modulus of the end reflection coefficient given in Equation (2.37) can also be written explicitly with respect to either the thickness variation, the group velocity or the effective length as

$$|R_{end,0}| = \mathrm{e}^{-\frac{\eta}{2}\left(\frac{12^{1/2}\omega}{c_p}\right)^{1/2}\int_0^{x_1}\frac{\mathrm{d}x}{h^{1/2}(x)}} = \mathrm{e}^{-\eta\omega\int_0^{x_1}\frac{\mathrm{d}x}{c_{gr}(x)}} = \mathrm{e}^{-\eta\mathrm{Re}\{k_0\}l_{eff}}, \tag{2.41}$$

where k_0 is the wavenumber at the input, whose real part is given by Equation (2.28), and l_{eff} is the effective length given by either of Equations (2.26) and (2.27). Accordingly, it can be seen that the modulus of the end reflection coefficient is dominated by the thickness close to the tip, with smaller thickness giving smaller group velocity there and, therefore, less end reflection. Equivalently, the modulus of the end reflection coefficient varies according to the effective length, with larger effective lengths giving more absorption and thus less reflection.

The relation for the phase given in Equation (2.39) can be written as

$$\angle R_{end,0} = -\frac{\pi}{2} - 2l_{eff}\left(\frac{12^{1/2}\omega}{c_p h_0}\right)^{1/2}, \tag{2.42}$$

where Equations (2.27) and (2.28) have also been used. It can be seen from Equation (2.42) that the phase of the end reflection coefficient decreases according to the square root of the frequency. It can also be seen that the phase of the end reflection coefficient is determined by the effective length of the wedge, with larger effective lengths producing faster phase shift with frequency.

2.3.2 Reflection coefficients for a wedge terminating a uniform plate

The cross section of a wedge terminating a uniform plate of thickness h_0 is illustrated in Figure 2.3, either truncated at length x_1, with edge thickness h_1, or ideally tapered down to zero thickness at length x_0. In this analysis, the principal quantity characterising the reflective behaviour of the system of a wedge terminating a uniform plate is the total reflection coefficient, R_{tot}, shown in Figure 2.3, which is defined as the ratio of the reflected wave, w_r, which travels backwards in the uniform plate, over the incident wave, w_i, both evaluated at the junction of the uniform and tapered parts,

$$R_{tot} = \frac{w_r(0)}{w_i(0)}. \tag{2.43}$$

It should be noted that longitudinal waves may also be excited as the flexural waves travel along the system, due to the asymmetry of the wedge geometry with respect to the midplane, as seen

in Figure 2.3. Such coupling effects could be avoided by implementing a symmetric wedge with the same thickness variation; the analysis in Section 2.2 would still hold, as it only accounts for the thickness variation, regardless of the exact geometry of the wedge.

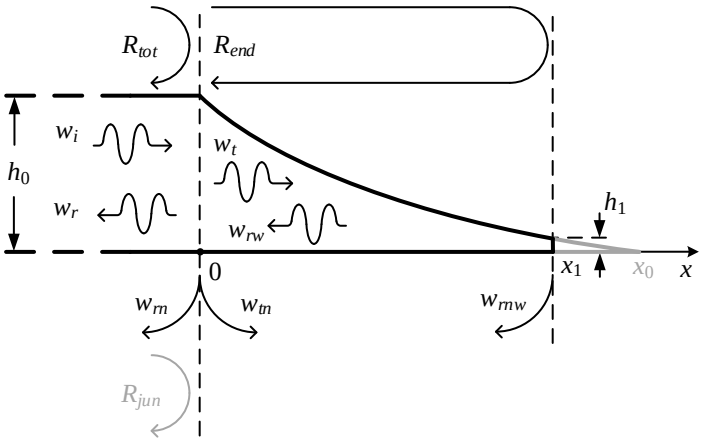

Figure 2.3. Schematic of a cross section of a wedge terminating a semi-infinite uniform plate. The various wave components are shown, namely, the incident travelling wave, w_i, the reflected travelling wave, w_r, and the reflected nearfield wave, w_{rn}, in the uniform part, and the transmitted travelling wave, w_t, the reflected travelling wave, w_{rw}, the transmitted nearfield wave, w_{tn}, and the reflected nearfield wave, w_{rnw}, in the wedge. The thickness of the uniform plate, h_0, and the thickness at the end of the truncated wedge, h_1, corresponding to length x_1, are shown, along with the total reflection coefficient, R_{tot}, and the end reflection coefficient, R_{end}. The ideal termination at length x_0 and the junction reflection coefficient, R_{jun}, are drawn in grey. The latter is equivalent to the total reflection coefficient of an ideally tapered wedge.

For the calculation of the total reflection coefficient, the various boundary conditions of the system must first be defined. There are two continuity and two equilibrium conditions at the junction, and two boundary conditions at the truncated edge. The conditions at the junction are the continuity of displacement, w, and its slope, $\theta = w'$, and the equilibrium of the bending moment, $M = Dw''$, and the shear force, $V = -M'$, as presented for example in [16], which may be expressed, respectively, as

$$w_u(0) = w_w(0),\ w'_u(0) = w'_w(0),\ w''_u(0) = w''_w(0),\ w'''_u(0) = \frac{3h'(0)}{h_0}w''_w(0) + w'''_w(0), \tag{2.44}$$

where w_u is the total displacement in the uniform plate and w_w is the total displacement in the wedge. The boundary conditions at the free truncated edge are the vanishing of the bending moment and the shear force [36], which result, respectively, in the equations

$$w''_w(x_1) = 0,\ w'''_w(x_1) = 0, \tag{2.45}$$

where x_1 is the coordinate of the truncated edge.

The total displacement in the uniform plate is given by

$$w_u = w_i + w_r + w_{rn}, \tag{2.46}$$

and the total displacement in the wedge is given by

$$w_w = w_t + w_{tn} + w_{rw} + w_{rnw}. \tag{2.47}$$

The subscript n in the wave components designates the nearfield components, r designates the reflected, t the transmitted and w the components in the wedge; the latter subscript is used in order to differentiate reflected waves in the wedge from those in the uniform plate. Components that do not have the letter n in the subscript are travelling waves.

It should be noted that the slope of the thickness is discontinuous at the junction, since its limits approaching from negative and positive x are different. The limit when approaching from the uniform part is zero, $\lim_{x\to 0_-} h'(x) = 0$, while the limit when approaching from the wedge, $\lim_{x\to 0_+} h'(x)$, is in general not zero. Therefore, $h'(0)$, which is used in the last of Equations (2.44), cannot be defined. However, since this slope results from considerations for the wedge, the limit of the slope as the junction is approached from the wedge is used, that is, $h'(0) = \lim_{x\to 0_+} h'(x)$.

The various travelling and nearfield wave components may be written in analytical form. The components inside the wedge are written as WKB solutions of a certain order of approximation; for first-, second- and third-order approximations, Equations (2.18), (2.19) and (2.20), respectively, have to be used. The appropriate value for the factor j also has to be chosen: $-$i corresponds to a wave travelling towards the positive$-x$ direction, $+$i to a wave travelling towards the negative$-x$ direction, -1 to a nearfield wave decaying towards the positive$-x$ direction and $+1$ to a nearfield wave decaying towards the negative$-x$ direction.

In compound form, the components in the wedge may be written as

$$w_a = A\mathrm{e}^{\psi_a}, \tag{2.48}$$

where a can be t, tn, rw or rnw, the functions ψ_a correspond to the exponent in Equation (2.11) and A is a complex constant. It should be noted, however, that introducing the complex wavenumber given by Equation (2.16) cancels the correspondence of the various terms to travelling and nearfield waves, since all the exponents in the WKB solutions given in Equations (2.18), (2.19) and (2.20) are complex and, therefore, all terms have both travelling and decaying terms. Nevertheless, since the loss factor is generally much smaller than one, the imaginary part of the wavenumber is much smaller than its real part, and the terms with $j = \pm$i are still predominantly travelling, while the terms with $j = \pm 1$ are predominantly nearfield, at least for the first-order WKB approximation given by Equation (2.18). The wave components in the uniform part are expressed as

$$w_a = A\mathrm{e}^{jk_u x}, \tag{2.49}$$

where, in this case, a can be i, r or rn, the factor j again defines the type of wave, as explained above, and k_u is the spatially constant wavenumber in the uniform plate, given by Equation (2.16) with $h = h_0$.

It is useful at this point to define reflection and transmission coefficients whose role will become apparent below. These are defined as ratios of the wave components evaluated at the junction,

$$R_n = \frac{w_{rn}(0)}{w_i(0)},\ T = \frac{w_t(0)}{w_i(0)},\ T_n = \frac{w_{tn}(0)}{w_i(0)},\ \tilde{R}_{end} = \frac{w_{rw}(0)}{w_i(0)},\ R_{nw} = \frac{w_{rnw}(0)}{w_i(0)}. \tag{2.50}$$

It should be noted that all of these coefficients, along with the total reflection coefficient defined in Equation (2.43), are ratios of wave components with respect to the incident wave. The end reflection coefficient, defined as the ratio of the reflected travelling wave in the wedge to the transmitted travelling wave, both evaluated at the junction, is of special interest, and can be expressed as

$$R_{end} = \frac{w_{rw}(0)}{w_t(0)} = \frac{\tilde{R}_{end}}{T}. \tag{2.51}$$

This coefficient coincides with the reflection coefficient calculated in [7] and in Section 2.3.1, with the difference that in the analysis presented here, nearfield waves are also accounted for.

The total displacements, given by Equations (2.46) and (2.47), can be expressed using Equations (2.49) and (2.48), respectively, along with the coefficients of Equations (2.50) and the total reflection coefficient defined in (2.43), as

$$w_u = w_i(0)\left(\mathrm{e}^{-ik_u x} + R_{tot}\mathrm{e}^{ik_u x} + R_n\mathrm{e}^{k_u x}\right) \tag{2.52}$$

and

$$w_w = w_i(0)\left(T\mathrm{e}^{\psi_t} + T_n\mathrm{e}^{\psi_{tn}} + \tilde{R}_{end}\mathrm{e}^{\psi_{rw}} + R_{nw}\mathrm{e}^{\psi_{rnw}}\right). \tag{2.53}$$

In order to clarify the above expressions, it should be pointed out that the ψ functions are zero at the junction, where $x = 0$, since all the S functions in the exponent of the WKB solution, given in Equation (2.11), emerge from integration over the spatial coordinate. Thus the complex amplitudes of the various components coincide with reflection and transmission coefficients, which are all evaluated at the junction, multiplied by the input amplitude of the incident wave.

It should be noted that the application of boundary conditions only at the junction and at the edge, as in Equations (2.44) and (2.45), assumes that the wedge variables vary smoothly enough within the wedge, so that no reflection occurs apart from at the junction and at the edge. Therefore, this approach does not account for reflections along the wedge away from the junction and the edge.

2.3.3 Matrix formulation of the boundary conditions

By calculating up to the third derivatives of the total displacements in Equations (2.52) and (2.53), which involve up to the third derivatives of the ψ functions, and substituting these into the boundary conditions of Equations (2.44) and (2.45), a six-by-six system of equations is obtained, where the unknowns are the reflection and transmission coefficients. In matrix form, this system of equations can be expressed as

$$\mathbf{Mr} = \mathbf{b}, \tag{2.54}$$

where $\mathbf{M}$ is the system matrix, whose elements are given in Appendix E, $\mathbf{r}$ is the vector of the unknown coefficients, given by

$$\mathbf{r} = [R_{tot} \quad R_n \quad T \quad T_n \quad \tilde{R}_{end} \quad R_{nw}]^{\mathrm{T}}, \tag{2.55}$$

and $\mathbf{b}$ is the vector of constant terms, given by

$$\mathbf{b} = [0 \quad 0 \quad -1 \quad \mathrm{i}k_u \quad k_u^2 \quad -\mathrm{i}k_u^3]^{\mathrm{T}}. \tag{2.56}$$

Solving the matrix equation (2.54) by matrix inversion for a given frequency gives the reflection and transmission coefficients. Although the matrix inversion has poor conditioning properties at higher frequencies, the final results calculated using MATLAB [37] were indistinguishable from the results obtained using higher precision floating-point arithmetic. It should be noted that the amplitude of the incident wave, $w_i(0)$, is cancelled out from all of the equations, as can be seen in Appendix E, which is expected due to the assumed linearity of the system, so that the various coefficients are independent of the amplitude of excitation.

A similar analysis as the one presented for the truncated wedge may be carried out for a wedge which is ideally tapered to zero thickness, either driven from the uniform part or from inside the wedge, as shown in Figures 2.4a and 2.4b, respectively. The junction reflection coefficient for an ideally tapered wedge driven from the uniform part is denoted by $R_{jun,f}$, where the subscript f stands for forward, and for an ideally tapered wedge driven from inside the wedge it is denoted by $R_{jun,r}$, where the subscript r stands for reverse. In the former case, the negative$-x$ travelling and nearfield waves are absent in the wedge, since no reflection occurs at the ideally tapered edge, while in the latter case, the positive$-x$ wave in the uniform plate is absent, since the plate is infinite towards negative$-x$, and also no negative$-x$ nearfield wave is present in the wedge, again due to the absence of reflection at the edge.

Either when the ideal wedge is driven from the uniform part or from inside the wedge, only the four conditions at the junction are applied, given in Equation (2.44), which leads to two four-by-four systems of equations for the respective reflection and transmission coefficients

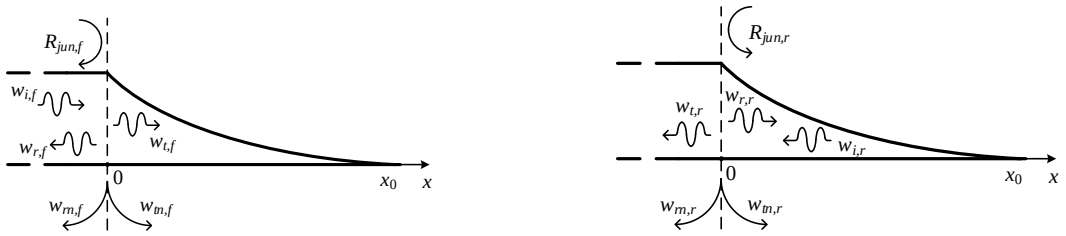

(a) (b)

Figure 2.4. Schematics of a cross section of an ideally tapered wedge, (a) driven from the uniform plate, and (b) driven from inside the wedge. The corresponding junction reflection coefficients are shown, along with the corresponding travelling and nearfield wave components. The subscripts f and r in (a) and (b), respectively, denote forward and reverse incidence.

at the junction. The corresponding matrix equations are presented in detail in Appendix E. Calculations showed that it makes little difference to the modulus of the junction reflection coefficient whether the wedge is driven from the direction of the uniform plate or from the wedge; therefore, this is simply denoted by $|R_{jun}|$ for the most part of the following analysis.

2.3.4 Total reflection coefficient calculated using Finite Element modelling

A numerical method that is used extensively for the solution of problems in a wide variety of scientific fields is the Finite Element method. Its main concept is based on the quantisation of a spatial continuum into a finite number of elements, so that the equations of a corresponding physical problem are solved for the specified elements [38, 39]. The method is known to give accurate results, provided that the spatial mesh of the elements is fine enough to accurately represent a specific problem.

In high-frequency applications where the wavelength becomes smaller, meshing requirements rise, since a minimum number of elements need to fall within a wavelength to capture the spatial variations of the physical variables. A commonly used lower limit is six elements per wavelength [40]. The need for a greater number of elements in high frequencies leads to a significant increase in computation time, which, in increasingly complex systems, may form a restricting factor for the application of the Finite Element method.

The modulus of the total reflection coefficient defined by Equation (2.43) can be calculated using the Finite Element method. Figure 2.5 illustrates the geometry of a Finite Element model, implemented in COMSOL [41]. The model comprises two-dimensional solid elements on the plane of the figure, so that it is equivalent to the model of a plate with infinite width in the direction perpendicular to the plane of the figure. In the results from Finite Element simulations presented in the following sections, the uniform part of the plate is set to have a length of 5.1 m, and the wedge has a length of 0.3 m. 14456 two-dimensional solid elements are used for the uniform part and 3345 to 8325 two-dimensional solid elements are used for the wedge, where a different number of elements is used for the different profiles presented in

Section 2.5. The thinner the thickness profile becomes near the edge, the greater the number of elements required. For the quadratic wedge, presented in Section 2.4, 3939 two-dimensional solid elements were used.

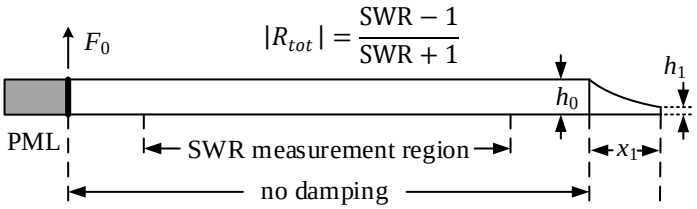

Figure 2.5. Geometry of the Finite Element model used for the calculation of the modulus of the total reflection coefficient by measuring the Standing Wave Ratio (SWR). The system is driven by a harmonic transverse force of constant amplitude, F_0. A Perfectly Matched Layer (PML) is applied in order to model the uniform plate as semi-infinite.

The aim of the Finite Element model is to estimate the modulus of the total reflection coefficient using the Standing Wave Ratio (SWR) in the uniform plate. The SWR is the ratio of the minimum over the maximum modulus of the field variable. From the SWR, the modulus of the total reflection coefficient can be calculated as [42]

$$|R_{tot}| = \frac{\text{SWR} - 1}{\text{SWR} + 1}. \tag{2.57}$$

The junction and end reflection coefficients cannot be calculated with the Finite Element model shown in Figure 2.5, but if the total reflection coefficient calculated with the WKB method can be validated against the Finite Element model, then the individual components may be reliably calculated using the WKB method.

The Finite Element model is excited by a harmonic transverse force of constant amplitude at the left end of the uniform plate; a Perfectly Matched Layer is also attached to the left of the excitation line to prevent reflections from that side, so that the uniform plate becomes semi-infinite. Some damping is included in the wedge using the loss factor described in Section 2.2, but the uniform part is modelled as lossless, so that the wave does not decay along the uniform plate and the SWR can be measured accurately. Furthermore, the SWR is measured within a region that is away from sources of nearfield waves, these being the excitation point and the junction. This region has to be sufficiently long such that at least one half-wavelength at the lowest frequency of interest can be accommodated, so that the minima and maxima of the displacement are included.

2.4 Reflection from a quadratic wedge

In this section, results for the various reflection coefficients of a quadratic wedge, that is, with its thickness varying as $h = h_0(1 - x/x_0)^2$, are presented using the WKB method, in order to illustrate some general properties of these coefficients, both individually and in relation to each other. Wedges with a power-law profile of power larger than 2 have been analysed in [8]. The total reflection coefficient calculated with a Finite Element model is used as a reference for the assessment of the analytical results. The geometrical and material property values of Table 2.1 are used. The length of the ideal, untruncated, wedge is calculated from the actual length using the thickness variation as

$$x_0 = \frac{x_1}{1 - H^{1/2}}, \tag{2.58}$$

where H is the ratio of the thickness at the truncated end to the thickness at the junction,

$$H = \frac{h_1}{h_0}. \tag{2.59}$$

Geometrical property	Value	Material property	Value
Length of wedge (x_1)	30 cm	Young's modulus (E)	$70 \cdot 10^9$ Pa
Thickness at junction (h_0)	1 cm	Density (ρ)	2700 kg·m^{-3}
Thickness at edge (h_1)	0.01 cm	Poisson's ratio (σ)	0.33
		Loss factor (η)	0.01

Table 2.1. Assumed geometrical and material properties of the truncated wedge.

The moduli of its end, junction and total reflection coefficients, calculated with the first-, second- and third-order WKB approximations, are plotted in Figures 2.6a, 2.6b and 2.6c, from 10 Hz to 10 kHz. In Figure 2.6c, the modulus of the total reflection coefficient calculated with the Finite Element model is also plotted and is used as a reference result with which the analytical ones can be compared. It can be seen from the plots in Figure 2.6 that, over the frequency range plotted, the second- and third-order WKB approximations give the same results for all the reflection coefficients of the quadratic wedge. The first-order and higher-order approximations also appear to converge at higher frequencies, as expected due to the increasing validity of the WKB method there.

In Figure 2.6a, the end reflection coefficient calculated with the higher-order approximations starts from a value of around 0.95 at 10 Hz, and then increases slightly and starts decreasing above about 100 Hz, although this detail is not clearly distinguishable on the scale of the plot. The end reflection is related to the amount of dissipation taking place in the wedge, which becomes greater as the wavelength becomes smaller. The wavelength is given by Equation (2.31), so that dissipation becomes greater as the frequency increases. Therefore, it would be expected that the end reflection should decrease monotonically with increasing frequency throughout the spectrum, contrary to the observed analytical result from the WKB

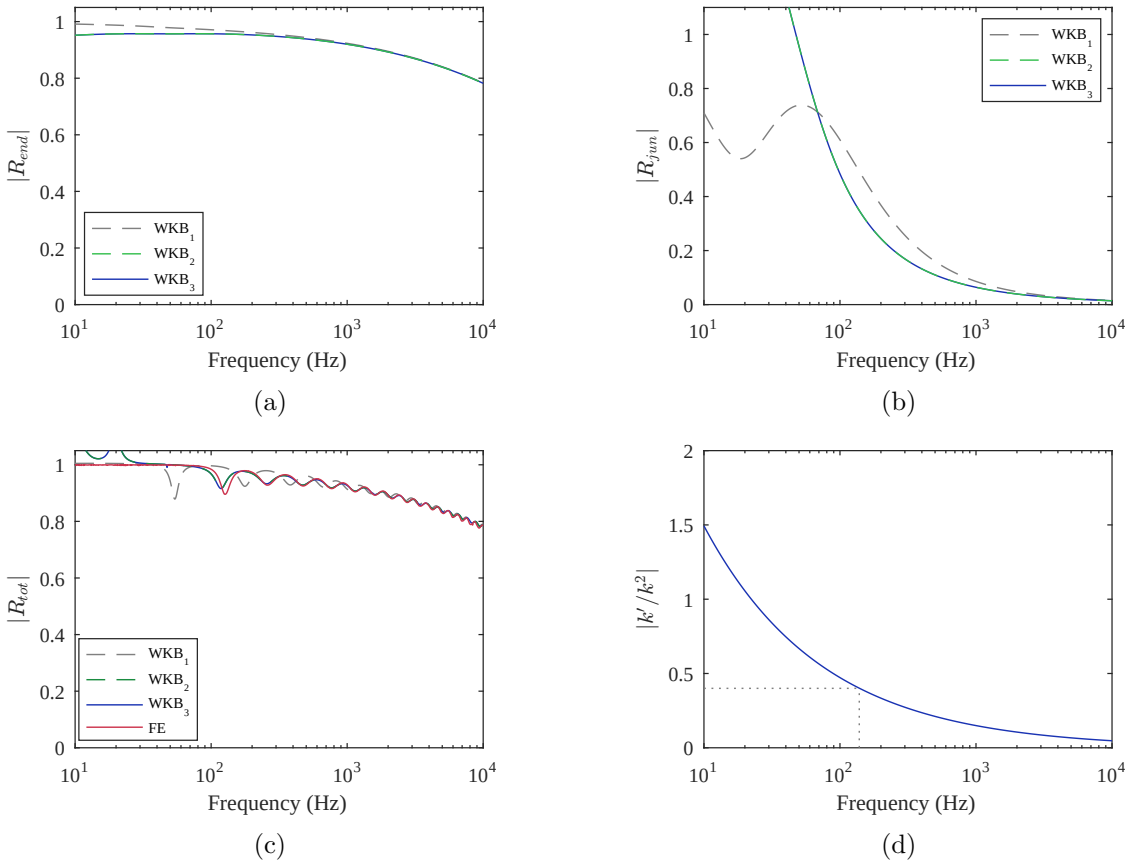

Figure 2.6. Frequency variation of the modulus of the reflection coefficients of the quadratic wedge with the properties given in Table 2.1, calculated with the first-, second- and third order WKB approximations: (a) end reflection coefficient, R_{end}, (b) junction reflection coefficient, R_{jun}, and (c) total reflection coefficient, R_{tot}, along with the one calculated with Finite Elements. (d) WKB validity condition term for the quadratic wedge against frequency; the frequency where the validity term has a value of 0.4 is noted with dotted lines. The second- and third-order coefficients for the quadratic wedge, shown in plots (a), (b) and (c), coincide.

analysis at low frequencies.

The first-order junction reflection coefficient, plotted in Figure 2.6b, also has a peak at about 50 Hz. However, the discontinuity at the junction is expected to produce more reflection at lower frequencies, where the wavelength is larger and the discontinuity is seen as more abrupt, and less reflection at higher frequencies, where the wavelength becomes shorter and the wave is more efficient at following the discontinuity. Therefore, the junction reflection coefficient would be expected to decrease monotonically with increasing frequency, as seen for the higher-order WKB solutions. Furthermore, the junction and total reflection coefficients, plotted in Figures 2.6b and 2.6c, respectively, give values greater than one at low frequencies when calculated with higher-order WKB approximations, a result which violates energy conservation. All these inaccuracies can be attributed to the deteriorating validity of the WKB method with decreasing frequency.

Despite the discrepancies at lower frequencies, inspection of Figure 2.6c illustrates that there is very good agreement between the total reflection coefficient calculated with the second-order WKB approximation and that calculated with the Finite Element model above about 150 Hz;

fairly good correspondence is seen at frequencies as low as 40 Hz. The first-order approximation, on the other hand, fails, in general, to predict the fluctuations of the total reflection coefficient with frequency, apart from at higher frequencies, even though it still predicts the general level of reflection. Consequently, the second-order WKB appears to be a good approximation for the quadratic wedge over most of its functional spectrum.

The WKB validity condition, given in Equation (2.1), is plotted in Figure 2.6d, for the quadratic wedge. Exceptionally for the quadratic wedge, the validity term, that is, the left-hand side of Equation (2.1), is independent of position, as has been previously stated in [7] and [8]. Although, in principle, the validity condition requires that the validity term be much smaller than one, a value of 0.4 has previously been used as a practically acceptable limit [43]. The WKB method is thus expected to give fairly accurate results above about 150 Hz, as noted by the dotted lines in Figure 2.6d, a result which complies with the correspondence of the second-order WKB approximation with the Finite Element results. It should be pointed out, however, that satisfaction of the validity condition of Equation (2.1) does not appear to ensure good results for the first-order approximation, as can be seen in Figure 2.6c. This may be linked to the fact that the first-order approximation also needs to satisfy a condition which limits the magnitude of the second-order WKB term, which is truncated in the first-order solution; similar validity conditions need to be satisfied for any order of WKB approximation [27].

The case of two quadratic wedges with very small and very large damping, respectively, is also considered to illustrate the general behaviour of the wedge as an absorber. The modulus of the total reflection coefficient for $\eta = 0.005$ and $\eta = 0.5$ is plotted in Figure 2.7a, calculated with the second-order WKB approximation. It can be seen that in the case of very little damping, the total reflection coefficient has a high value throughout the considered spectrum, and, therefore, the waves are primarily reflected. When a large damping factor is used, reflection is greatly decreased.

The modulus of the displacement in the wedge, calculated with Equation (2.53) with the second-order WKB approximation, normalised with respect to the thickness, is plotted against position in Figure 2.7b, at frequency $f = 808$ Hz, for an incident displacement amplitude of $w_i(0) = 10^{-6}$ m. The specific frequency corresponds to the dashed vertical line in Figure 2.7a, and is chosen to correspond to a dip of very low reflection for the high damping case. In both cases, the displacement presents an increasing trend as the wedge gets thinner. In the case of low damping, the displacement appears to have nodal points, which is indicative of nearly total reflection from the end of the wedge. In the case of high damping, however, the displacement presents little fluctuation along the length of the wedge, which implies that the displacement in the wedge primarily consists of a forward-travelling wave, which in turn suggests that little reflection occurs at the truncated end.

It can also be seen from Figure 2.7b that for the given thickness variation and input amplitude, the displacement at the tip in the case of low damping has a magnitude similar

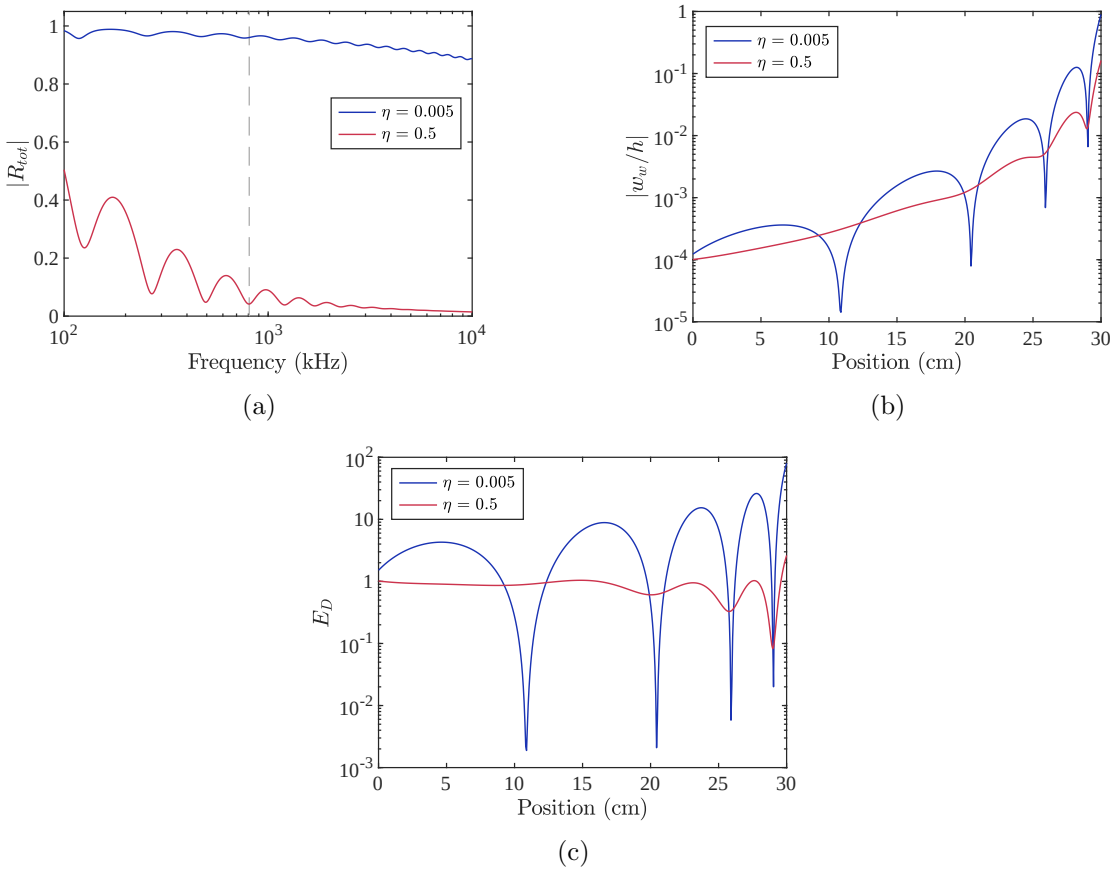

Figure 2.7. (a) Modulus of the total reflection coefficient of a quadratic wedge for two different values of damping, plotted against frequency. (b) Modulus of the displacement normalised with respect to the thickness at frequency 808 Hz, for two different values of damping, plotted against position. (c) Modulus of the energy density normalised with respect to the input energy density at frequency 808 Hz, for two different values of damping, plotted against position. Results are calculated with the second-order WKB approximation for a wedge with the properties given in Table 2.1 for an incident displacement amplitude of $w_i(0) = 10^{-6}$ m. The vertical line in (a) corresponds to $f = 808$ Hz.

to the thickness; for high damping, the relative displacement is one order of magnitude smaller. For higher input displacements, however, the displacement at the tip will become much larger. For example, it will be about a thousand times larger than the thickness there for an input amplitude of 1 mm in the case of high damping, thus invalidating the underlying linearity assumption of the calculation method presented in Section 2.2. Additionally, for thinner wedges, and in particular for wedges with smaller truncation thickness, h_1, for a given junction thickness, h_0, the displacement towards the tip will also become larger, as can be deduced from Equation (2.18). Therefore, for relatively low damping, the validity of the calculation method is limited by the input displacement amplitude and by the thickness ratio.

A periodic shift takes place in the vibrating elastic wedge between kinetic and potential energy [16]. The magnitude of the energy density per unit area can be calculated as the maximum of the kinetic energy density within a cycle of vibration, which is given by

$$E_d = \frac{1}{2}\rho h \left|u\right|^2 = \frac{1}{2}\rho h \omega^2 \left|w_w\right|^2, \tag{2.60}$$

where $u = \mathrm{i}\omega w_w$ is the velocity of harmonic flexural vibration. The normalised energy density with respect to the input energy density can then be written as

$$E_D = \frac{E_d}{E_{d,i}} = \frac{h}{h_0}\left|\frac{w_w}{w_i(0)}\right|^2, \tag{2.61}$$

where $E_{d,i}$ is the incident energy density. The constant loss factor, η, corresponds to the proportion of the energy that is dissipated [16], so that the dissipation is proportional to the energy density expressed by Equation (2.60). The normalised energy density given in Equation (2.61) is plotted against position in Figure 2.7c. It can be seen that the energy density becomes largest at the tip of the wedge, so that most of the absorption takes place there.

2.4.1 Interrelation of the different reflection coefficients

The end, total and junction reflection coefficients of the quadratic wedge with the properties given in Table 2.1, calculated using the second-order WKB approximation, are plotted together in Figure 2.8. The end and total reflection coefficients of a quadratic wedge with a very small truncation thickness, $h_1 = 1$ nm, are also plotted. The junction reflection coefficient of this 'thin' wedge is the same as that of the default wedge, whose truncation thickness is $h_1 = 100$ µm, since the two wedges have the same ideal length, x_0, and the junction reflection coefficient is not affected by the length of truncation. A wedge with a truncation thickness of 1 nm is far too thin to manufacture but is used here to illustrate how the end reflection coefficient dominates that at the junction, especially at higher frequencies, even for an almost perfect wedge.

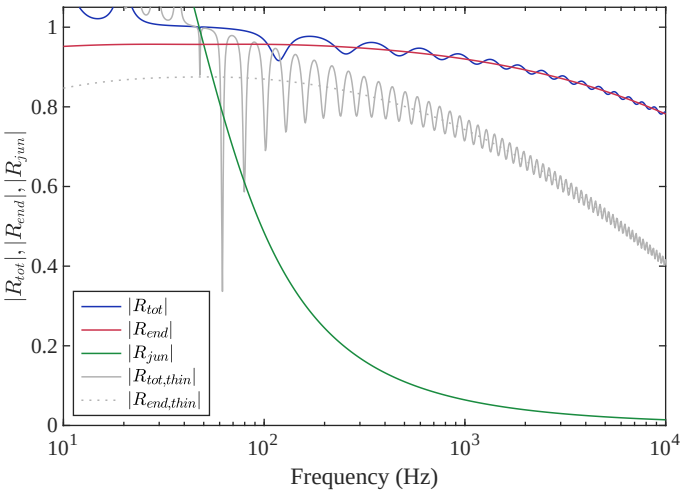

Figure 2.8. Moduli of the total, R_{tot}, end, R_{end}, and junction, R_{jun}, reflection coefficients of the quadratic wedge with the properties given in Table 2.1, using the second-order WKB approximation. The total and end reflection coefficients are also plotted for a quadratic wedge with the same ideal length, x_0, but with a very small truncation thickness, $h_1 = 1$ nm, denoted by the word 'thin' in the subscripts in the legend. The junction reflection coefficient for the two quadratic wedges is the same, since they have the same ideal length.

The junction reflection coefficient is equal to the total reflection coefficient of an ideally tapered wedge, that is, without truncation, and decreases to very small values with increasing frequency. When even a tiny truncation is introduced, such as that of a thickness of 1 nm, considerable reflection occurs, even at high frequencies, as can be seen in Figure 2.8. The end reflection coefficient thus provides the general level of reflection, around which the total reflection coefficient fluctuates with frequency. The ripples in the total reflection are due to interference between the two sources of reflection, namely, the junction and the truncation. The ripples are more pronounced for the 'thin' wedge since the magnitude of the reflection from the end is more similar to that from the junction. In [23], it was suggested that the ripples occur due to reflections away from the edge, although it was not clarified whether these occur at the junction or within the waveguide.

The relative magnitude of the end reflection coefficients of the 'thin' and the nominal wedge can also be related to their respective effective lengths. The effective length of the nominal wedge, calculated with Equation (2.26), is $l_{eff} = 0.78$ m, whereas for the 'thin' wedge, it is $l_{eff} = 2.7$ m. Therefore, according to Equation (2.41), the 'thin' wedge produces less end reflection, as observed in Figure 2.8.

2.4.2 Widening of the bandwidth between the dips

A novel analysis on the widening of the bandwidth between consecutive dips in the modulus of the total reflection coefficient with linear frequency is presented in this section. The total reflection coefficient of a quadratic wedge is plotted in blue in Figure 2.9 on a linear-frequency scale. In the same graph, the phase of the reverse junction reflection coefficient, $\angle R_{jun,r}$, and of the end reflection coefficient, $\angle R_{end}$, are also plotted, as green and black lines, respectively. The total phase shift is defined as the sum of these phases,

$$\phi_0 = \angle R_{jun,r} + \angle R_{end}, \tag{2.62}$$

and is plotted in red in Figure 2.9. The phase ϕ_0 is the total phase shift of a wave starting from $x = 0_+$, that is, inside the wedge, travelling towards positive x, getting reflected at the end, travelling back to the junction and getting reflected at the junction. All of the mentioned solid-line plots in Figure 2.9 are produced with the second-order WKB solution. The horizontal lines correspond to integer cycles of phase, and the vertical lines pass from the intersections of these lines with ϕ_0, that is, they are defined by the integer cycles of ϕ_0. It can be observed that the vertical lines pass from the dips of the total reflection coefficient, that is, the dips of the total reflection coefficient are defined by the integer cycles of the phase shift. Some small deviation of this correspondence occurs at lower frequencies, which is not visible in this linear-frequency graph.

Even though the dips in the total reflection coefficient appear to become denser with

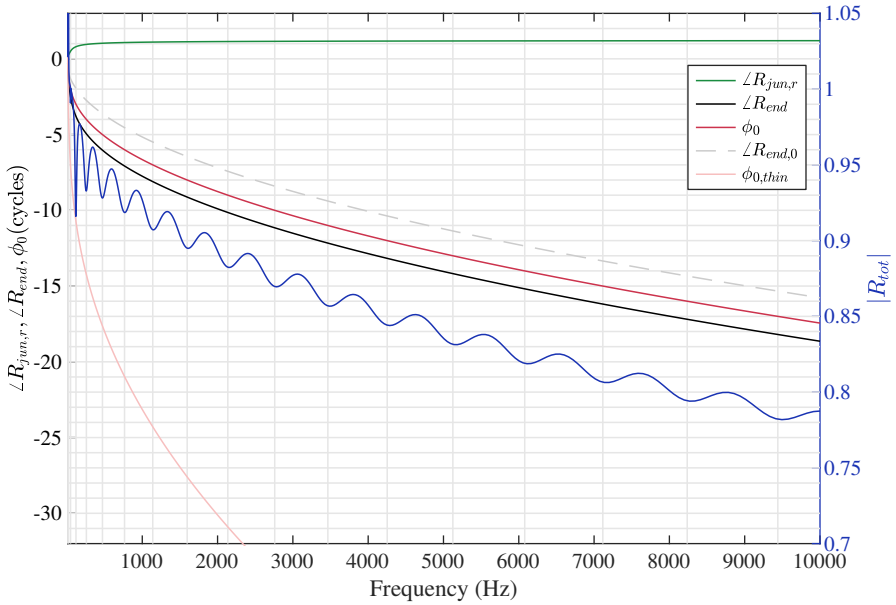

Figure 2.9. Linear-frequency plot of the modulus of the total reflection coefficient, $|R_{tot}|$, of a quadratic wedge, whose y axis is on the right side of the graph, along with the phase of the end reflection coefficient, $\angle R_{end}$, the phase of the reverse junction reflection coefficient, $\angle R_{jun,r}$, and the total phase shift, ϕ_0, whose y axis is on the left side of the graph, all calculated with the second-order WKB approximation. The phase of the zeroth-order WKB approximation of the end reflection coefficient, $\angle R_{end,0}$, and the total phase shift of a thin wedge with $h_1 = 1$ nm, calculated with the second-order WKB approximation, $\phi_{0,thin}$, are also plotted. The horizontal lines correspond to integer cycles of phase and the vertical lines pass from the integer-cycle crossings of ϕ_0.

increasing frequency in the logarithmic-frequency plots, as can be seen, for example, in Figure 2.8, they actually widen, as can be seen in the linear-frequency plot in Figure 2.9. Insight into the mechanism of the widening of the dips may be gained by use of the zeroth-order calculation of the end reflection coefficient, as presented in Section 2.3.1. The zeroth-order end reflection phase, given by Equation (2.42), is plotted as a dashed grey line in Figure 2.9. It can be seen from Equation (2.42) that the phase of the zeroth-order end reflection coefficient has a square-root dependency on the frequency, apart from a constant offset of $-\pi/2$. Therefore, as frequency increases, the absolute rate of change of $\angle R_{end,0}$ with frequency decreases, due to its square-root dependency, so that a phase shift between two consecutive cycles requires a greater bandwidth.

Moreover, the rate of change of the total phase shift, ϕ_0, with frequency is dominated by the change of the phase in the end reflection coefficient, $\angle R_{end}$, while the phase of the reverse junction reflection coefficient, $\angle R_{jun,r}$, varies little across the spectrum and mainly at lower frequencies, as can be seen in Figure 2.9. Therefore, the bandwidths between consecutive integer crossings of ϕ_0 are defined predominantly by the phase of R_{end}, even though the exact locations of the dips are defined by the phases of both R_{end} and $R_{jun,r}$. Finally, it can be seen in Figure 2.9 that the variation of $\angle R_{end}$, as calculated with the second-order WKB approximation, shown as a black solid line, is similar to the variation of $\angle R_{end,0}$, shown as a dashed grey line, apart mainly from an offset, so that the square-root frequency dependency of the latter may imply a

qualitatively similar spectral behaviour for the former, and, due to previous considerations, also for the total phase shift, ϕ_0. Thus the widening of the dips may be linked to the square-root dependency of the total phase shift with frequency.

It can be seen in Equation (2.42) that larger effective lengths give a steeper decrease in the phase of the end reflection coefficient. Since the latter dominates the total phase shift, ϕ_0, whose integer-cycle crossings determine the dips in the total reflection coefficient, it can also be concluded that larger effective lengths give denser dips of the total reflection coefficient. This is illustrated by the total phase of a 'thin' wedge, with $h_1 = 1$ nm, which is plotted in Figure 2.9 as a light red line, and whose integer-cycle crossings are much denser in the spectrum. In Figure 2.8, this is seen as dense ripples in the total reflection coefficient for the 'thin' wedge; the difference in the frequency scale of Figures 2.8 and 2.9 should be noted. An analytical relation for the total reflection coefficient with respect to the various reflection and transmission coefficients of the system is derived through an analysis of multiple reflections between the junction and the truncated end in Appendix F. The dependence of the modulus of the total reflection coefficient on ϕ_0 is also apparent in Equation (F.14), although it is not obvious how this defines the observed dips.

2.5 Reflection from wedges of different thickness profiles

Apart from the power-law wedge, other thickness variation profiles may be used, which also lead to zero phase and group velocity at the edge of an ideally tapered wedge, thus exhibiting similar absorbing properties. It was noted in [8], for example, that a sinusoidal thickness variation, raised to a power greater or equal to 2, may be used instead of a power-law in this context. In this analysis, a wedge varying according to a cosine raised to a power is considered. Furthermore, the exponential thickness variation forms the limit of a power-law profile with the same length and the same junction and edge thickness, as the order of power tends to infinity, as shown in Appendix G. For such an exponential thickness variation, the ideally tapered wedge would need to have infinite length, since the decaying exponential function vanishes at infinity. Despite this theoretical limitation, in practice truncation always occurs due to manufacturing restrictions, so that the truncated, finite-length exponential wedge may be considered. Similarly, simulations have shown that the Gaussian profile is the limit of the power-cosine profile as the order of power tends to infinity. Finally, a compound power-law profile is considered, which comprises a concave power-law part from its thick end up to half its ideal length and a convex power-law part from the midpoint up to the vanishing edge. The two parts of the profile are symmetric with respect to the point $(x_0/2, h_0/2)$.

The properties of the thickness profiles considered are summarised in Table 2.2. For each of them, the fact that the phase and group velocities vanish at the ideal edge can be shown by calculating the limits $\lim_{x\to x_0} c_{ph}$ and $\lim_{x\to x_0} c_{gr}$, respectively, where the phase velocity

and the group velocity are given by Equations (2.30) and (2.24), respectively. The exponential and Gaussian thickness variations can also be expressed as $h = h_0 H^{x/x_1}$ and $h = h_0 H^{(x/x_1)^2}$, respectively.

profile type	Thickness variation (h)	Length of ideal wedge (x_0)	Decay factor	Normalised effective length (L_{eff})
P-L	$h_0\left(1-\frac{x}{x_0}\right)^n,\ n>2$	$\frac{x_1}{1-H^{1/n}}$	-	$\frac{H^{\frac{1}{n}-\frac{1}{2}}-1}{\left(1-\sqrt{H}\right)\left(\frac{n}{2}-1\right)}$
Q	$h_0\left(1-\frac{x}{x_0}\right)^2$	$\frac{x_1}{1-\sqrt{H}}$	-	$\frac{\ln H}{2(\sqrt{H}-1)}$
Exp	$h_0 \mathrm{e}^{-\beta x}$	∞	$\beta = -\frac{\ln H}{x_1}$	$\frac{1-\frac{1}{H^2}}{2\ln H}$
P-C	$h_0 \cos^n\left(\frac{\pi x}{2x_0}\right),\ n \geq 2$	$\frac{\pi x_1}{2\arccos\left(H^{1/n}\right)}$	-	N/A
Gauss	$h_0 \mathrm{e}^{-\gamma x^2}$	∞	$\gamma = -\frac{\ln H}{x_1^2}$	$\frac{1}{2}\sqrt{-\frac{\pi}{\ln H}}\mathrm{erfi}\left(\sqrt{-\ln H}\right)$
CP-L	$\begin{cases} \frac{h_0}{2}\left(2-\left(\frac{2x}{x_0}\right)^n\right),\ 0 \leq x \leq \frac{x_0}{2} \\ \frac{h_0}{2}\left(2-\frac{2x}{x_0}\right)^n,\ \frac{x_0}{2} \leq x \leq x_0 \end{cases}$	$\frac{2x_1}{2-(2H)^{1/n}}$	-	N/A

Table 2.2. Formulas for different thickness profiles. The abbreviations for the profile types correspond, from top to bottom, to power-law for $n > 2$, quadratic, exponential, power-cosine for $n > 2$, Gaussian and compound power-law for $n > 2$. The normalised effective lengths for the power-cosine and compound power-law profiles have complicated forms, written with respect to special functions, and are not displayed here; they were calculated with the software Maple [44]. In the normalised effective length of the Gaussian profile, erfi denotes the imaginary error function.

In this analysis, the quadratic profile is used as a representative case of the power-law thickness variation. A seventh-order cosine is used as a representative case of the power-cosine profile, where the order of power has been chosen so that, for the geometrical properties given in Table 2.1, this wedge presents a similar general level of reflection as a quadratic wedge with the same geometrical properties. Furthermore, a compound power-law wedge of order four, that is, a compound quartic wedge is used. All the truncated wedges considered in this analysis have the same length and the same thickness at the junction and at the truncated edge. An analysis of wedges with the same junction and end thickness but different lengths is given in Appendix H. A plot of the thickness variation of the profiles is shown in Figure 2.10a. The thick dot indicates half the length of an ideally tapered compound quartic profile.

The phase velocity in the wedge is given by Equation (2.30). It can thus be seen that the phase velocity is proportional to the square root of the thickness and so all the profiles have the same phase velocity at the edge, since they have the same thickness there. The spatial variation of the phase velocity at 1 kHz for the different profiles is plotted in Figure 2.10b. The square root relation with the thickness becomes apparent by comparison of the corresponding plots for the quadratic profile, whose phase velocity decreases linearly along the wedge.

In Figure 2.10c, the normalised effective length, L_{eff}, defined by Equation (2.29), is plotted against the thickness ratio, H, which is defined by Equation (2.59); both axes are logarithmically scaled. Most of the different formulas of L_{eff} for the different thickness profiles are given in Table 2.2. It can be seen that the effective length decreases with increasing thickness ratio. This

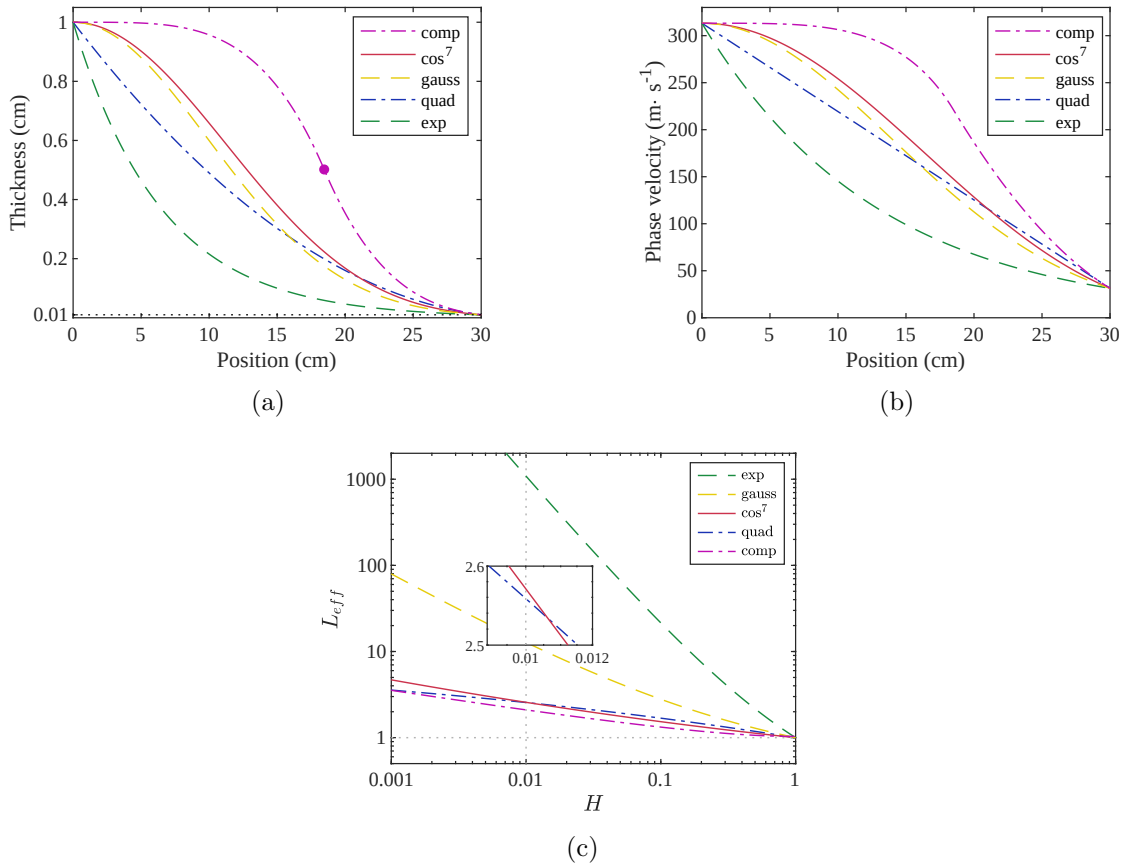

Figure 2.10. Properties of a quadratic, a seventh-order cosine, an exponential, a Gaussian and a compound quartic wedge: (a) thickness variation, from 1 cm to 0.1 mm over a length of 30 cm, (b) spatial variation of the phase velocity at 1 kHz. The dot in (a) corresponds to the ideal midpoint of the compound quartic profile, that is, to the point with coordinates $(x_0/2, h_0/2)$. (c) Normalised effective length of the wedges of different profiles, plotted on a logarithmic scale against logarithmic thickness ratio. The dotted vertical line passes from the value $H = 0.01$ and the dotted horizontal line passes from the value $L_{eff} = 1$. The small graph shows a detail for the quadratic and seventh-order cosine wedges at $H = 0.01$.

is expected, since larger H implies larger edge thickness for a given thickness at the junction, which in turn corresponds to less thickness variation along the wedge and, therefore, to less propagation velocity decrease. In the high limit where H tends to 1, all profiles tend to that of a uniform plate and the normalised effective length tends to 1, that is, the effective length coincides with the actual length.

The modulus of the total reflection coefficient for the wedges of different profiles is plotted in Figure 2.11, calculated with the Finite Element method, and the moduli of the junction and end reflection coefficients for the different profiles are plotted over a narrower frequency band in Figure 2.12, calculated with the third-order WKB approximation. It should be noted that the validity of the WKB results deteriorates below some frequency, which is different for the different profiles, as will be discussed in Section 2.6.1. Therefore, the plots in Figure 2.12 should not be used to obtain strict quantitative conclusions but rather approximate qualitative ones. It is mentioned here in advance that the WKB results for the compound quartic wedge are not valid throughout most of the considered spectrum. The moduli of the end reflection coefficients

for the different profiles, plotted in Figure 2.12, correspond to the general levels of the moduli of the total reflection coefficients in Figure 2.11.

A comparison of the moduli of the end reflection coefficients plotted in Figure 2.12 with the corresponding phase velocities of Figure 2.10b, or equivalently, the corresponding thickness variations of Figure 2.10a, helps explain the general levels of reflection for the various thickness profiles; differences in the general level of reflection are more prominent at high frequencies. It should be noted that most of the dissipation takes place near the tip, as was noted in Section 2.3.1. As a result, the seventh-order cosine and the quadratic profiles, which have a very similar variation in the phase velocity towards the tip of the wedge, present very similar general levels of reflection.

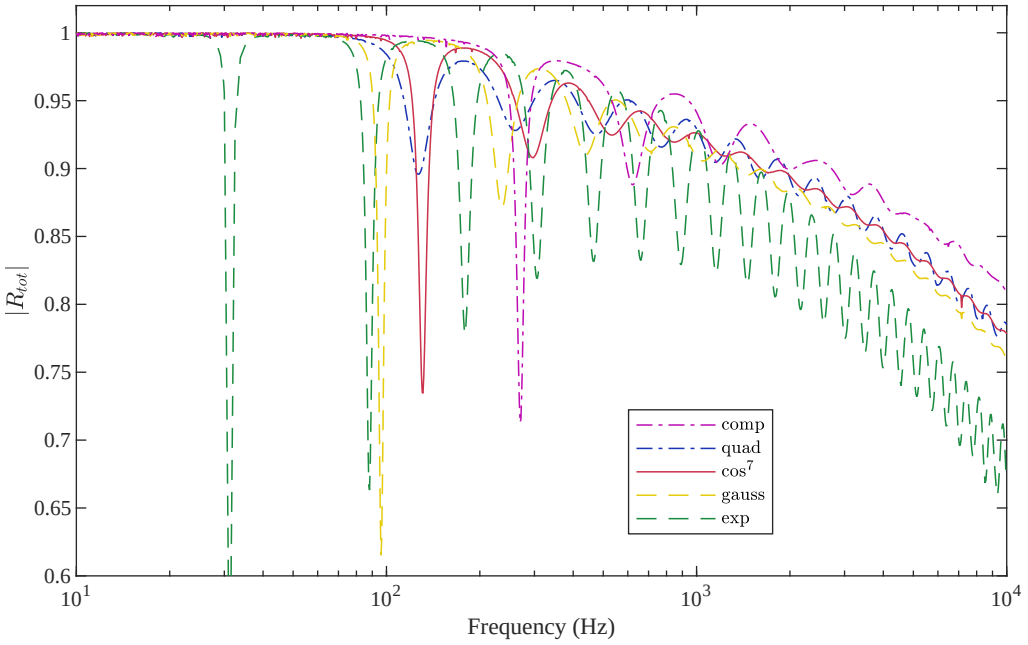

Figure 2.11. Variation in the modulus of the total reflection coefficient with frequency for a quadratic, a seventh-order cosine, an exponential, a Gaussian and a compound quartic wedge, calculated using the Finite Element method.

For the exponential profile, the phase velocity is smaller than that of the other profiles throughout the length of the wedge, so that the modulus of its end reflection coefficient, and, therefore, its general level of reflection, is also smaller. Since the exponential wedge is equivalent to a power-law wedge of infinite power, the fact that the general level of reflection of the exponential wedge is smaller than that of the quadratic one is in agreement with the finding that power-law wedges of increasing order present less end reflection, as was shown in [8], and is also proved mathematically in Appendix I. As for the compound quartic wedge, its phase velocity is larger than that of the rest of the profiles, and its general level of reflection is also comparatively larger.

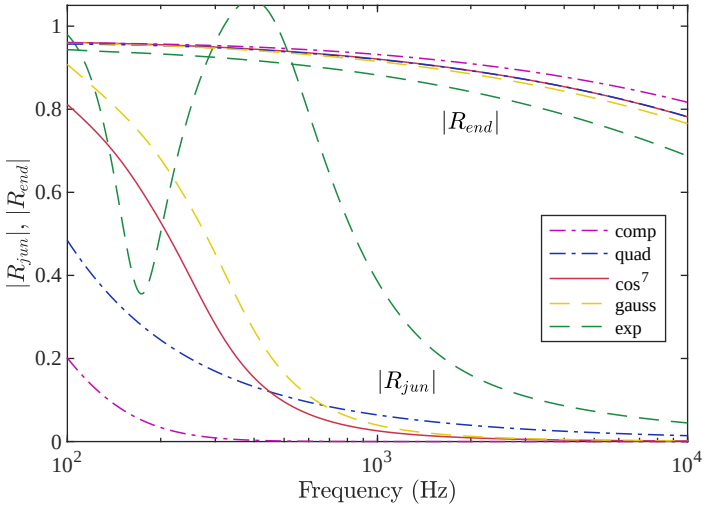

Figure 2.12. Modulus of the junction and end reflection coefficients for the different thickness profiles, calculated with the third-order WKB approximation, plotted over a smaller frequency band than in Figure 2.11. The lines at the lower part of the graph correspond to the junction reflection coefficient and the ones at the upper part of the graph correspond to the end reflection coefficient.

2.5.1 Reflection due to the junction for different profiles

The relation of the junction reflection coefficient with the slope of the discontinuity at the junction can provide new insight on the reflective behaviour of the wedge. Reflection from the junction would be expected to be less for wedges which are smoothly connected to the uniform plate in terms of slope, so that the discontinuity at the junction would have less effect, compared to ones where there is a discontinuity of slope at the junction. The fluctuations of the total reflection coefficient are also expected to be greater when the moduli of the end and junction reflection coefficients are closer in magnitude, as noted with respect to Figure 2.8 for the quadratic wedge.

For the quadratic, seventh-order cosine and Gaussian profiles, the modulus of the end reflection coefficient is of similar level, as can be seen in Figure 2.12. The reflection due to the junction for the two latter profiles, which have zero slope at the junction, would be expected to be less than for the quadratic one, which has a discontinuity of slope at the junction, and, therefore, the fluctuations of the total reflection coefficient would also be expected to be of smaller magnitude. Such behaviour is observed at higher frequencies in Figure 2.11, where the seventh-order cosine and the Gaussian profile present smaller fluctuations and therefore less reflection due to the junction compared to the quadratic one. These results are also in agreement with those for the moduli of the junction reflection coefficients plotted in Figure 2.12, where the junction reflection coefficient of the power-cosine and Gaussian wedges is smaller than that of the quadratic wedge at higher frequencies.

At lower frequencies, however, the fluctuations of the total reflection coefficient of the power-cosine and Gaussian profiles become greater than those of the quadratic. This result

complies with the observation that, below some frequency, the junction reflection coefficient of the former profiles becomes larger than that of the latter, as can be seen in Figure 2.12. For example, in the frequency band between 200 and 300 Hz, the junction reflection coefficients of the power-cosine and Gaussian wedges are larger than that of the quadratic wedge, and the fluctuations of the total reflection coefficient are respectively larger; the end reflection coefficients for these three profiles are almost identical in this frequency band.

The compound quartic wedge, which also has zero slope at the junction, presents smaller fluctuations than the quadratic only at higher frequencies, above about 2 kHz; at lower frequencies its reflection coefficient actually has much greater fluctuations. No conclusions can be drawn from the variation of the junction reflection coefficient for this profile, since the WKB method does not provide accurate results for this profile, as will be shown in Section 2.6. As for the exponential profile, its absolute slope at the junction is greater than that of the quadratic, and, therefore, the discontinuity is more abrupt, leading to larger reflection due to the junction, as can be seen in Figure 2.12; discrepancies at lower frequencies are due to the deteriorating validity of the WKB approximation there. Additionally, the modulus of the end reflection coefficient of the exponential profile is smaller than that of the quadratic one, and the modulus of its junction reflection coefficient is larger than that of the quadratic, so that its total reflection coefficient has greater fluctuations compared to the quadratic, as can be seen in Figure 2.11.

The fact that the reflection due to the junction for the power-cosine, Gaussian and compound power-law profiles becomes greater than that of the quadratic below some frequency, as is implied by the corresponding magnitude of the fluctuations of the total reflection coefficient, contradicts the simplistic consideration that reflection at the junction should be defined by the discontinuity of slope. Apparently, even when the slope at the junction is zero, the subsequent gradual change of thickness in the wedge causes reflection, especially at lower frequencies, where the wavelength is larger and the change in thickness, even a gradual one, is seen more as a discontinuity.

Although the WKB method does not account for reflections away from the junction and the edge, the analytical method involves the derivatives of order up to three of the WKB approximations of Equations (2.18) to (2.20), as can be seen from the boundary conditions given in Equations (2.44) and (2.45), which, in turn, involve higher-order derivatives of the thickness variation. Therefore, the 'variational trend' of the thickness near the junction is actually accounted for through the higher-order derivatives of the thickness there. The first derivative of the power-cosine and the Gaussian thickness variation at the junction is zero, but higher-order derivatives are non-zero there. This explains the non-zero junction reflection coefficients for these profiles plotted in Figure 2.12. For the compound quartic profile, the first, second and third derivatives of the thickness are zero at the junction, which may explain the predicted zero reflection at the junction from the WKB method over most of the spectrum

plotted in Figure 2.12.

2.5.2 Bandwidth between consecutive dips for different profiles

It is notable from Figure 2.11 that the first dip in the total reflection coefficient for the exponential wedge is at a lower frequency than that for the other profiles. This is due to the fact that the phase velocity, as plotted in Figure 2.10b, is significantly lower for the exponential than for the other profiles over most of the length, so that the phase accumulation required for the reflection from the end to interfere destructively with that from the junction occurs at a lower frequency. The plots of the normalised effective lengths of Figure 2.10c are more insightful in this respect. It can be seen that, for a given thickness ratio, H, the exponential wedge has the largest effective length, followed by the Gaussian, the quadratic and power-cosine, and the compound quartic wedge. Therefore, the first dip in the total reflection coefficient occurs at frequencies of the inverse order for the different profiles. The same order applies to the density of the dips along the spectrum, or, equivalently, to the bandwidth between consecutive dips, with the bandwidth between consecutive dips being the smallest among the considered profiles for the exponential profile and the largest for the compound quartic profile.

A small discrepancy can be observed in the case of the quadratic and power-cosine profiles, since the first dip of the quadratic profile occurs at a frequency very slightly smaller than that for the power-cosine wedge, as can be seen in Figure 2.11, whereas the respective effective length is very slightly smaller, as can be seen in the detail plot in Figure 2.10c for the value of the thickness ratio $H = 0.01$ used here. The effective length, defined by Equation (2.23), uses the group velocity defined as $\mathrm{d}\omega/\mathrm{d}\left(\mathrm{Re}\{k\}\right)$, and the wavenumber given by Equation (2.16) is used. It should be noted, however, that the real part of this form of the wavenumber is actually a first-order WKB approximation, since it corresponds to the spatial angular frequency only for the first-order WKB solution to the wave equation, given by Equation (2.18); it also corresponds to this physical quantity for the zeroth-order WKB approximation given in Equation (2.36). For higher orders of WKB approximation, the actual spatial angular frequency, that is, the actual wavenumber, corresponds to more complicated expressions, given by the real part of the integrand of the integral in the exponents of Equations (2.19) and (2.20). This observation, combined with the limitations of the validity of the WKB approximation, can account for this discrepancy.

Overall, the exponential profile gives the least general level of reflection, which is due to it being thinner than the other wedges over the whole length, which leads to greater energy dissipation. For a tuned system, where it may be desired that the reflection becomes small at specific frequencies, the exponential profile can also provide greater dips in the total reflection coefficient, particularly at higher frequencies.

2.6 Comparison of results from the WKB method with those from a Finite Element analysis

Figure 2.13 shows a comparison of the modulus of the total reflection coefficient calculated using WKB approximations of order up to three with numerical results from Finite Element models, for the different thickness profiles excluding the quadratic, the corresponding results for which have already been presented in Figure 2.6c. Firstly, it can again be seen that below some frequency, which is different for each profile, the reflection coefficient calculated with the analytical method has values greater than one, thus violating energy conservation, due to the WKB method being invalid at low frequencies. Additionally, it can be seen that the first-order WKB approximation gives good predictions for the overall level of reflection, but fails, in general, to predict the fluctuations in the reflection coefficient, apart from at the very high frequencies, as was also the case for the quadratic wedge.

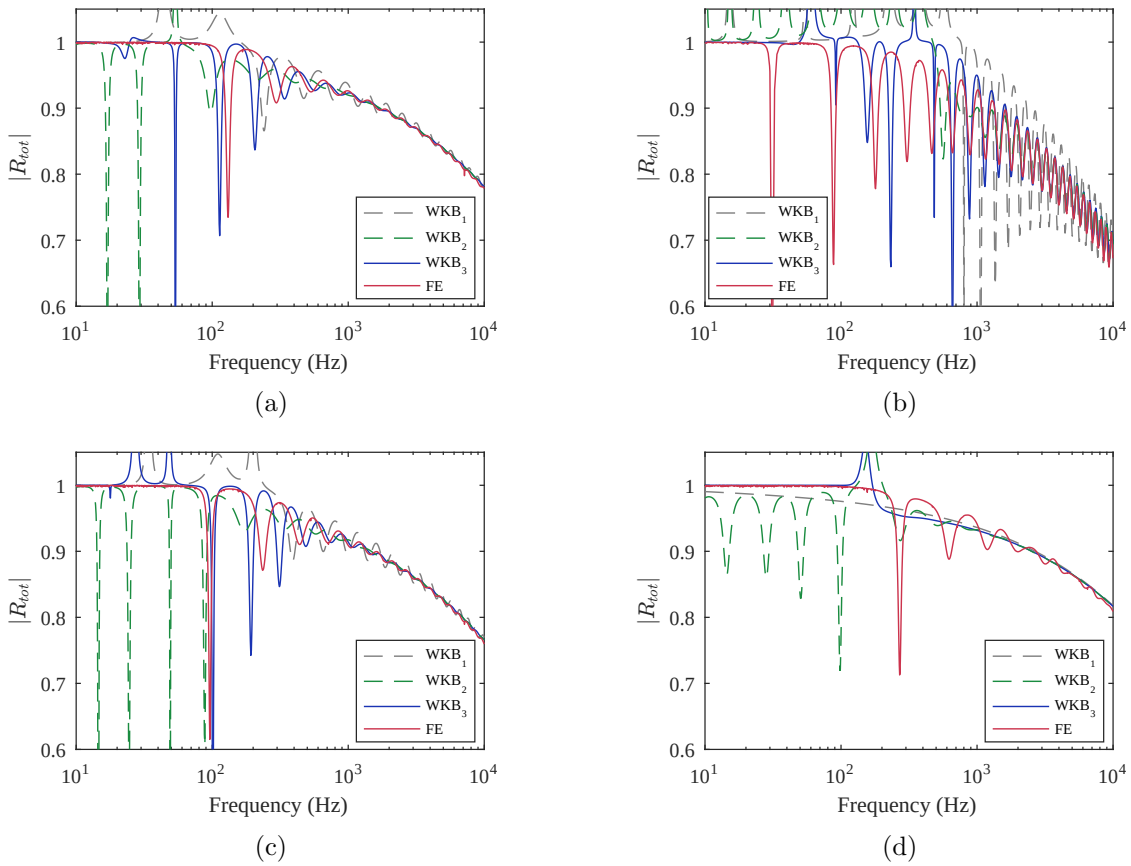

Figure 2.13. Modulus of the total reflection coefficient with first-, second- and third-order WKB approximations and with the Finite Element method, for (a) a seventh-order cosine, (b) an exponential, (c) a Gaussian and (d) a compound quartic wedge.

Higher-order approximations appear to improve the correspondence with numerical results, although this is not so obvious and requires detailed inspection. For the seventh-order cosine, results for which are shown in Figure 2.13a, the second-order approximation gives good matching above about 1 kHz, although this is mainly due to the fact that the fluctuations in the reflection

coefficient become very small with increasing frequency, so that any mismatch in the dips is not easily distinguishable. The third-order approximation provides some further improvement, since good correspondence with numerical results can be seen above about 500 Hz. The Gaussian wedge, results for which are plotted in Figure 2.13c, presents similar behaviour, where the corresponding frequencies above which different orders of approximation match well with numerical results are shifted slightly upwards.

In the case of the exponential wedge, whose total reflection coefficients are plotted in Figure 2.13b, the higher-order approximations match quite well with the Finite Element results above about 1500 Hz. Furthermore, the second-order approximation gives a good prediction of the frequencies at which the dips occur down to about 1 kHz, while the third-order approximation predicts the dip frequencies down to about 400 Hz. It should be noted, however, that the level of fluctuations in the reflection coefficient is not well predicted at some frequencies.

The presence of considerable ripples for the compound quartic wedge, as seen in the Finite Element solution of Figure 2.13d, cannot be satisfactorily explained by the WKB analysis, which assumes that reflections occur only at the junction and the edge. A quite abrupt change in the thickness takes place within the wedge away from the junction, more prominently around the region of the ideal midpoint, defined by the dot in Figure 2.10a. This transition appears to provide a distributed 'discontinuity' that causes reflection, both for the incident wave travelling from the uniform part and for the wave reflected from the edge, thus producing the first dip due to interference at a higher frequency than any of the other profiles. This is also illustrated in Figure 2.10, where the compound quartic profile is seen to have the smallest effective length. Therefore, the WKB method fails to predict the fluctuations of the total reflection coefficient, as can be seen in Figure 2.13d.

2.6.1 The WKB validity condition for different thickness profiles

To further investigate the performance of the analytical method for the various profiles, the validity term for the WKB method, given by the left-hand side of Equation (2.1), is plotted against frequency and position as a colour map in Figure 2.14. In the individual colour maps for the various profiles, the regions where the validity term is greater and smaller than 0.4 are separated by a curve. It can be seen that for the exponential wedge, Figure 2.14b, the WKB validity condition is more strongly violated at the junction, but it is satisfied here above about 1 kHz, which seems to agree, in general terms, with the frequency above which the correspondence of higher-order analytical results with numerical ones is observed in Figure 2.13b. For the other profiles, however, the results in Figure 2.14 show that the validity condition is satisfied at the origin but it is strongly violated in the central region of the wedges, where the slope of the taper profile is greatest. For the seventh-order cosine and Gaussian wedges, the validity condition is satisfied above about 300 Hz at this position, which forms a relatively good lower limit for the

correspondence of the higher-order analytical results with the numerical results, as shown in Figures 2.13a and 2.13c, respectively.

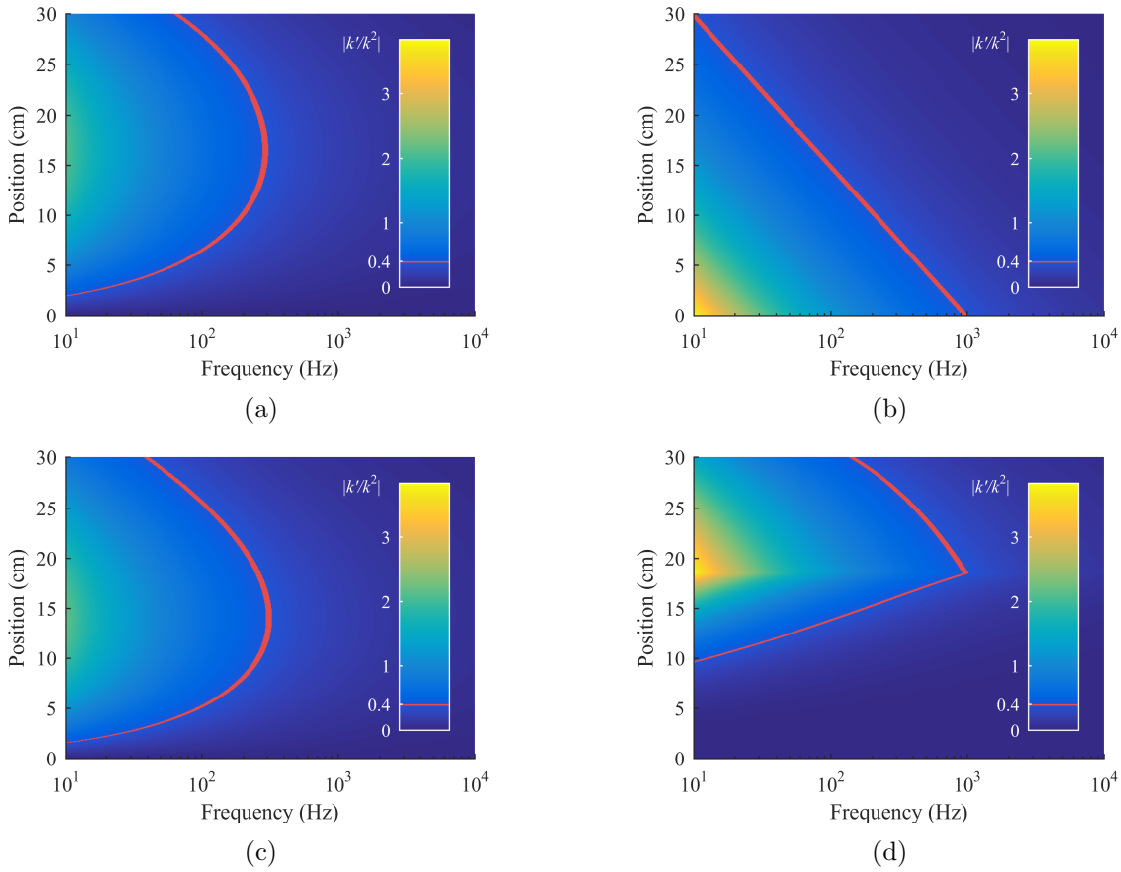

Figure 2.14. Colour map of the WKB validity condition term varying with frequency and position for (a) a seventh-order cosine, (b) an exponential, (c) a Gaussian and (d) a compound quartic wedge. The curve corresponding to the value $\left|k'/k^2\right| = 0.4$ is also plotted.

For the compound quartic wedge, shown in Figure 2.14d, the WKB validity term has its maximum value at its ideal midpoint, shown in Figure 2.10a, where the slope is greatest. It can be seen that even above 1 kHz, where the validity condition is sufficiently satisfied throughout the compound quartic wedge, the analytical results shown in Figure 2.13d fail to predict the fluctuations in the total reflection coefficient as calculated by the Finite Element method. These discrepancies may also be linked to the fact that the derivatives up to the third one of the thickness variation of the compound quartic profile are zero at the junction, which limits the efficiency of the analytical method in accounting for reflections close to the junction, as was mentioned in Section 2.5.1.

It should be pointed out that the validity condition of Equation (2.1) forms only one of the two conditions that the first-order WKB approximation needs to satisfy, as explained in [28]; the other condition is related to the magnitude of the first truncated higher-order term in the solution. WKB approximations of higher order, however, have to satisfy additional validity conditions, so that a thorough analysis of the validity of the WKB method would have to include these conditions [28].

The analytical method does not provide good results for thickness profiles whose thickness varies very little near the junction but varies a lot along the wedge, away from the junction. The analytical method also does not consider reflections within the wedge away from its boundaries, as was noted in Section 2.3.2. In [22], however, where an Impedance Matrix method is used, it is assumed that reflections occur throughout the wedge. Therefore, in systems where considerable internal reflections are expected, such as the wedges whose slope changes strongly away from the junction, the analytical method may be expected to provide inaccurate results.

Another important point is that the asymptotic power series in the exponent of the general WKB solution given in Equation (2.6) usually diverges [27]. In the case of the WKB approximation for the wedge, this means that, for a given frequency, there is a certain order of approximation up to which the solution improves, but above which the solution becomes worse, as explained for example in [45] and [46]. Therefore, even though the WKB approximations of order up to three, as used here, are found in general to improve with increasing order, it is expected that approximations of some even higher order will start giving worse results.

The deteriorating validity of the WKB method at lower frequencies imposes a lower limit to its applicability. Additionally, the analysis in this chapter is based on the flexural wave equation given in Equation (2.2) which applies to thin plates. This limitation requires that the thickness of the plate is much smaller than the flexural wavelength [16]. The ratio of the thickness over the local wavelength is given by

$$\frac{h}{\lambda} = \frac{1}{2\pi}\left(\frac{12^{1/2}\omega h}{c_p}\right)^{1/2}, \tag{2.63}$$

and it is plotted against frequency in Figure 2.15 at the two boundary positions of the wedge, that is, the junction and the truncated end, for the geometrical properties of Table 2.1. At all intermediate positions the ratio h/λ has values between the values at the boundaries. It can be seen that the thickness is much smaller than the local flexural wavelength over the considered spectrum, thus justifying the use of thin plate theory in the context of this study.

As a general comment, it should be pointed out that the analysis presented in this chapter is carried out for a frequency range starting from the very low frequency of 10 Hz, and that all frequency plots use a logarithmic scale, except for Figure 2.9. The lower frequency limit and the logarithmic representation were chosen especially to highlight the limitiations of a method that is expected to behave worse at low frequencies. The lower part of the frequency range is less important for absorbing elastic wedges in practice, since their absorbing character greatly deteriorates in this range. The total reflection coefficients presented in this chapter also generally have relatively high values, for the most part over about 0.65. It is well established in the literature that, in practice, a combination of appropriate thickness variation and application of thin absorbing layers gives lower reflection coefficients with practically useful levels of absorption, as reviewed in [47]. However, in the analysis presented here, a relatively

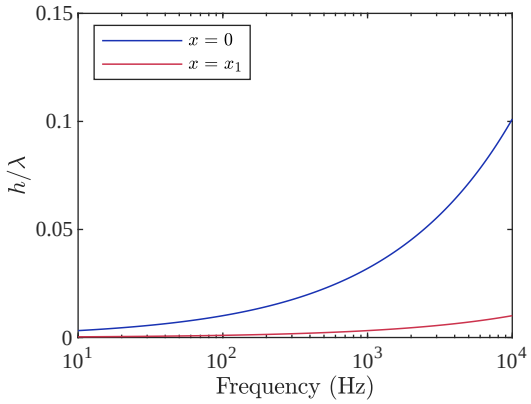

Figure 2.15. Ratio of the thickness over the local flexural wavelength plotted against frequency at the two limit positions, that is, at the junction, $x = 0$, and at the truncated end, $x = x_1$, for the geometrical properties of Table 2.1.

low level of internal damping was deliberately used to illustrate interference effects between reflections from the junction and the end of the wedge.

2.7 Summary and conclusions

A method for the calculation of the reflection coefficient of an elastic wedge terminating a uniform plate has been presented, based on analytical expressions of the flexural wave components using the WKB approximations of different orders. The boundary conditions were formed into a matrix equation and the reflection and transmission coefficients of the system were obtained by solution of this equation. These analytical results were compared with those from a Finite Element model. The analytical results were found to predict the Finite Element simulations better with increasing frequency, as predicted by the behaviour of the WKB validity condition.

The total reflection coefficient was found to fluctuate with frequency, due to interference between reflections primarily from the junction and the truncation at the end of the wedge, when the thickness of the wedge changes more rapidly close to the junction. The end reflection coefficient, which accounts only for reflection due to the truncation, defines the general level of reflection and thus dominates the overall reflection in the cases considered here. Fluctuations in the modulus of the total reflection coefficient are due to interference between the phases of the waves reflected from the junction and the end of the wedge. The distinct dips in the total reflection coefficient are more pronounced when the junction and end reflection coefficients are of similar magnitude, where the junction reflection coefficient is estimated using the WKB method by considering an ideally tapered wedge, for which no reflection occurs at its free edge.

An effective length for a truncated wedge has been introduced, which determines the frequency at which the first dip in the modulus of the total reflection coefficient occurs, as well as the bandwidth between consecutive dips. The larger the effective length, the lower the

frequency of the first dip and the narrower the bandwidth between consecutive dips. Among the profiles considered, the exponential wedge was found to have both a lower general level of reflection and to produce more pronounced fluctuations in the reflection coefficient over most of the spectrum. The density of the dips of the total reflection coefficient of the exponential wedge is also greater than for the other profiles, as it has the largest effective length.

The first-order WKB approximation, which is typically used in the literature, was found to predict the general level of reflection but fails, for the most part, to predict the dips in the total reflection coefficient. Second- and third-order approximations, on the other hand, generally provide good matching with results from Finite Elements above some frequency. This frequency, in general, decreases with increasing order of WKB approximation, thus improving the overall prediction.

It was also observed that the analytical method behaves differently for the various profiles. Analysis of a compound quartic wedge, for example, illustrated that the analytical method fails to predict the fluctuations of the overall reflection when the thickness does not change significantly at the junction but does so within the wedge, away from the junction. It is also implied by this analysis that it may not be feasible for a relatively short wedge to have a thickness profile that produces no reflection both at the junction and along its length, since the required smoothness at the junction would have to be compensated by a rapid change of thickness along its length.

Overall, the analytical method, using higher-order WKB approximations, can generally provide good results for different thickness profiles over the part of the spectrum where the tapered wedge is effective. In addition, it provides insights into the reflection due to the junction and that due to the truncation, which are not provided by the Finite Element model.

Chapter 3

Absorbing acoustic waveguides with fitted rings

3.1 Introduction

The idea of implementing a reflectionless waveguide based on its geometry was first proposed in [7], in the context of flexural waves in thin plates, as was presented in Chapter 2. It was theoretically shown in that article that a thin plate whose thickness has a power-law variation of order equal to or greater than two could completely absorb incident flexural waves if the waveguide is ideally tapered down to zero thickness. This would cause the waves to gradually slow down and eventually halt in the vanishing tip, where they would be attenuated through structural damping.

In an acoustic waveguide, however, where the waves propagate longitudinally in a fluid bounded by rigid walls, such as the acoustic horns discussed in Appendix A, the phase and group velocities at each point of the waveguide are related by [48]

$$c_{ph} c_{gr} = c_0^2, \tag{3.1}$$

where c_0 is the speed of sound in the fluid. Therefore, in this case, it is not possible to achieve both vanishing phase and group velocities only by smoothly tapering the boundaries, since if one vanishes the other becomes infinite. A way to implement an acoustic waveguide that manifests the 'Acoustic Black Hole' effect in the acoustic context was presented in [11], where rigid rings of varying inner radius are fitted inside a cylindrical waveguide, as shown in Figure 3.1. An analytical model for the wave propagation was used in that article, in which the compliances of the discrete cavities formed between consecutive rings were approximated by a continuous compliance of an equivalent wall admittance. Simulations in [11] predicted considerable absorption of incident waves.

Experimental results for absorbing waveguides of the form of Figure 3.1, for both linear

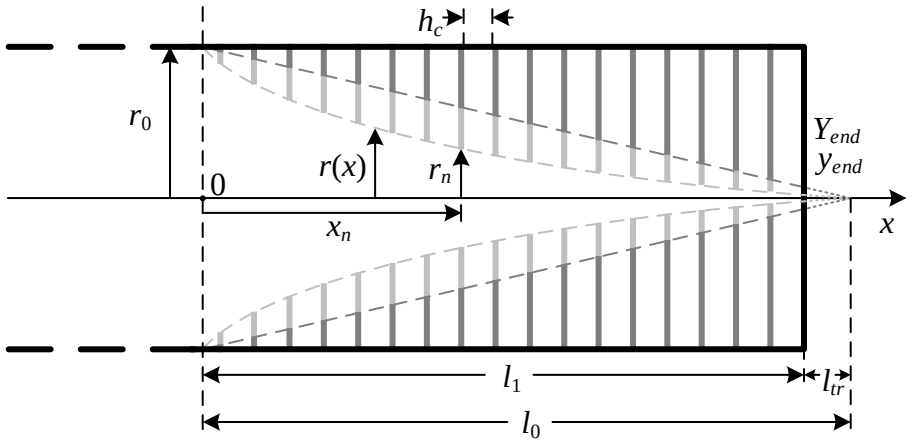

Figure 3.1. Schematic of a longitudinal section of the termination of a semi-infinite cylindrical tube of radius r_0 with fitted rigid rings of varying inner radius r_n at distances x_n from the input boundary of the non-uniform termination. The equivalent continuous radius of the analytical model, $r(x)$, is shown as a dark grey dashed line for the linear profile and as a light grey dashed line for the quadratic profile, starting from the input boundary of the non-uniform waveguide at $x = 0$, and reaching the tube axis at $x = l_0$. The waveguide is truncated by a length l_{tr}, thus having an actual length l_1. The length of a cavity formed by two consecutive rings, h_c, is shown, along with the longitudinal acoustic admittance, Y_{end}, and specific acoustic admittance, y_{end}, of the termination of the waveguide.

and quadratic variation of the inner radius of the rings and with varying distances between consecutive rings, were presented in [49] and [3]. The results showed considerable absorption in the frequency range of unimodal propagation, with a qualitatively similar pattern of fluctuation for the reflection coefficient as that predicted theoretically in [11]. The insertion of various absorbing materials was also tried, without, however, providing significantly more enhancement of the absorption of the system. The Transmission Matrix method was used in [12] for simulating absorbing waveguides of both linear and quadratic inner radius variation to evaluate the effect of varying the design features of the system. It was shown in that article that the results with the continuous analytical model proposed in [11] approach those with the Transmission Matrix method if a very large number of rings is used.

A model of a muffler was presented in [50], consisting of an infinite tube interrupted by a peripheral structure of rings forming cavities of varying radius, so that the cylindrical region of acoustic transmission is kept intact, but considerable absorption occurs due to the non-uniform peripheral structure. This system has a similar functioning principle as the one in [11], even though the waveguide is not terminated. Analytical and numerical simulations were presented in [50] and [51], and experimental measurements were presented [52].

In this chapter, a waveguide consisting of a tube with fitted rigid rings of tapered inner radius is studied. An analytical model using an equivalent wall admittance, [12], is presented in Section 3.2, with additional considerations on the propagation velocities and new results being presented for an effective length. A Transfer Function method is presented in Section 3.3,

which does not make the assumption of an equivalent wall admittance, and is used to calculate the reflection coefficient for comparing with the analytical results, although it cannot provide the acoustic pressure and volume velocity along the waveguide. A comparison of results using both methods of simulations is given in Section 3.4 and the simulations are compared with experimental results from the literature in Section 3.5. A summary and conclusions are given in Section 3.6. A summary of the results in this chapter was presented by the author in [53].

3.2 Analytical modelling

The propagation of acoustic plane waves in a waveguide with rigid walls and varying cross section is described by Webster's horn equation [6], as discussed in Appendix A. A generalised form of Webster's equation for a horn whose wall normal admittance is not zero and varies with position was derived in [11]. This is used to analyse the acoustic absorber in Figure 3.1 by assuming that the distance between consecutive cavities is small compared with the wavelength, so that the behaviour of the cavities can be represented by a continuous spatially varying normal admittance. For time-harmonic acoustic pressure varying as $p(x,\omega)\mathrm{e}^{\mathrm{i}\omega t}$, the generalised wave equation is written as [11]

$$p''(x,\omega) + (\ln S(x))' p'(x,\omega) + \left(k^2(\omega) - \frac{2\mathrm{i}\omega\rho y(x,\omega)}{r(x)}\right) p(x,\omega) = 0, \tag{3.2}$$

where S is the cross-sectional area, k is the wavenumber in free space, given by $k = \omega/c$, where ω is the angular frequency and c is the speed of sound in free space, ρ is the density of air, y is the radial wall specific admittance, r is the horn radius and the prime notation corresponds to differentiation with respect to the spatial coordinate, x. Henceforth, the dependence of variables to x and ω will be generally omitted for convenience. It should also be noted that, in the consequent analysis, specific acoustic impedances and admittances, which correspond to ratios involving acoustic pressure and particle velocity, are denoted by z and y, respectively, that is, with small letters, whereas Z and Y are used to denote acoustic impedances and admittances, that is, ratios involving acoustic pressure and volume velocity.

Losses in the system may be included through a complex speed of sound, expressed as $c = c_0(1+\mathrm{i}\mu)$, where c_0 is the lossless speed of sound in free space and μ is a loss parameter [11]. The losses are in turn incorporated into the wavenumber, which, for $\mu \ll 1$, can be approximated by $k = k_0(1-\mathrm{i}\mu)$, where $k_0 = \omega/c_0$ is the lossless wavenumber.

The system shown in Figure 3.1, which involves a number of discrete cavities between consecutive rings of varying radius r_n, may be approximated by a horn of tapered radius $r(x)$, where $r(x)$ is the continuous envelope passing from the discrete inner radii of the rings, and regarded as having a continuous wall admittance, calculated with a locally reacting compliance due to the compressibility of the fluid in the radial direction [11]. Two different radius variation

profiles are considered, that is, a linear and a quadratic one, as has also been done in the literature [12, 3]. These are shown with dashed lines of different shades of grey for the different profiles in Figure 3.1. For the continuous analytical model presented in this section, the continuous radius tapers down to zero beyond the terminating wall of the waveguide, so that the waveguide is truncated at a length $l_1 = l_0 - l_{tr}$, where l_0 is the length of ideal taper and l_{tr} is the truncation length, to avoid singularities in the analytical solution for the pressure.

Since plane-wave propagation within the duct is assumed, the depth of the cavities between consecutive rings is less than a quarter wavelength, and so their acoustic behaviour is dominated by their compliance. The specific acoustic admittance of the cavity between two consecutive rings is thus given by [54]

$$y_{cav,n} = \frac{\mathrm{i}k}{z_0}\frac{V_n}{S_{l,n}}, \tag{3.3}$$

where $z_0 = \rho c_0$ is the characteristic specific acoustic impedance of air, and V_n and $S_{l,n}$ are the volume and the area of the lateral surface of the n-th cavity, respectively. When the cavities become very short, their shape approaches that of the difference of two cylinders, one with radius r_0 and one with radius r_n. In the continuous limit, the radius r_n can be taken to be the continuous radius r, so that the volume and the area of the lateral surface are written, respectively, as

$$V = \pi h_c \left(r_0^2 - r^2\right) \tag{3.4}$$

and

$$S_l = 2\pi r h_c, \tag{3.5}$$

where h_c is the length of the cavity, as shown in Figure 3.1. The continuous specific admittance can then be written as

$$y = \frac{\mathrm{i}k}{z_0}\lim_{h_c\to 0}\frac{V}{S_l}, \tag{3.6}$$

which gives

$$y = \mathrm{i}\frac{k}{z_0}\frac{r_0^2 - r^2}{2r}. \tag{3.7}$$

Using Equation (3.7), Equation (3.2) can be written as [11, 12]

$$p'' + 2(\ln r)'p' + \left(\frac{kr_0}{r}\right)^2 p = 0. \tag{3.8}$$

The acoustic pressure in the uniform part of the system, that is, for $x \leq 0$, is expressed as

$$p_u = p_0\left(\mathrm{e}^{-\mathrm{i}kx} + R\mathrm{e}^{\mathrm{i}kx}\right), \tag{3.9}$$

which consists of an incident positive-x travelling wave, $p_u^+ = p_0\exp\{-\mathrm{i}kx\}$, and a reflected negative-x travelling wave, $p_u^- = p_0 R\exp\{\mathrm{i}kx\}$, where p_0 is the incident wave amplitude, which can be taken to be one, without loss of generality. The complex coefficient R represents the

reflection coefficient of the system, defined as

$$R = \frac{p_u^-(0)}{p_u^+(0)}. \tag{3.10}$$

Given an expression for the wall admittance, such as Equation (3.7), an effective wavenumber can be calculated from the analytical solution of Equation (3.8) [12]. Specific forms for the effective wavenumber are given for the linear and quadratic profiles in Sections 3.2.1 and 3.2.2, respectively. From this, the phase and group velocities can be calculated by $c_{ph} = \omega/\mathrm{Re}\{k_{eff}\}$ and $c_{gr} = \mathrm{d}\omega/\mathrm{d}(\mathrm{Re}\{k_{eff}\})$, respectively, where k_{eff} is the effective wavenumber.

The novel concept of the effective length can also be defined, corresponding to the length of an equivalent uniform tube for which the time for an incident wave to travel from its input to its end is the same as the time for an incident wave to travel from the input to the end of the non-uniform waveguide with fitted rings. The effective length is expected to be greater than the actual length of the waveguide, since waves slow down as they propagate along the waveguide, as will be shown below, and therefore it takes longer for them to reach the end. The time for a narrowband wave pulse to travel from the input to the end of the non-uniform waveguide can be calculated by

$$t_{nu} = \int_0^{l_1} \frac{\mathrm{d}x}{c_{gr}}, \tag{3.11}$$

while for a uniform tube, the travel time is

$$t_u = \frac{l_{eff}}{c_0}, \tag{3.12}$$

where l_{eff} is the effective length. By equating the two travel times, the effective length is expressed as

$$l_{eff} = c_0 \int_0^{l_1} \frac{\mathrm{d}x}{c_{gr}}. \tag{3.13}$$

A normalised effective length can also be defined, with respect to the actual length, as

$$L_{eff} = \frac{l_{eff}}{l_1}. \tag{3.14}$$

Three boundary conditions apply to the system: the continuity of pressure and the continuity of particle velocity at the boundary of the uniform and non-uniform parts at $x = 0$, and the termination of the waveguide at a given longitudinal specific admittance, y_{end}, at $x = l_1$. The boundary conditions are expressed, respectively, as

$$p_u(0) = p(0),\ u_u(0) = u(0) \text{ and } y_{end} = \frac{u(l_1)}{p(l_1)}, \tag{3.15}$$

where p is the acoustic pressure at the non-uniform part of the waveguide, and u_u and u are the particle velocities at the uniform and at the non-uniform part, respectively. It is helpful

for the subsequent analysis to introduce the reflection coefficient at the end of the waveguide, defined as

$$R_{end} = \frac{p^-(l_1)}{p^+(l_1)}, \tag{3.16}$$

where $p^+(l_1)$ and $p^-(l_1)$ are the positive-x and negative-x travelling waves in the non-uniform waveguide at $x = l_1$ in Figure 3.1.

3.2.1 Linear inner-radius variation

In the literature, two profiles of inner-radius variation have been considered: a linear and a quadratic one. In both cases, there exists an exact solution to Equation (3.8). In the linear case, the inner radius varies as $r = r_0(1-x/l_0)$, where l_0 is the ideal length of the waveguide if it were tapered down to zero radius, as shown in Figure 3.1, and the general solution to Equation (3.8) is [12]

$$p = A(x-l_0)^{-\frac{1}{2}+\mathrm{i}\frac{m}{2}} + B(x-l_0)^{-\frac{1}{2}-\mathrm{i}\frac{m}{2}}, \tag{3.17}$$

where $m = \sqrt{(2kl_0)^2 - 1}$, and A and B are complex, frequency-dependent coefficients to be defined by the boundary conditions. In Equation (3.17), the first term corresponds to a positive-x travelling wave and the second to a negative-x travelling wave. The use of the base $x - l_0$ of the exponential instead of x in [12] is due to the different system of coordinates used here compared with the coordinate system in [12].

An effective wavenumber for the waveguide can be obtained by expressing the phase accumulation in either the forward or the reverse pressure wave of Equation (3.17) in terms of a natural exponential. The forward pressure wave can thus be written as

$$A(x-l_0)^{-\frac{1}{2}}(x-l_0)^{\mathrm{i}\frac{m}{2}} = A(x-l_0)^{-\frac{1}{2}}\mathrm{e}^{-\mathrm{i}\int_0^x k_{eff}(\tilde{x})\mathrm{d}\tilde{x}}, \tag{3.18}$$

where k_{eff} is the effective wavenumber and $\tilde{x}$ is an auxiliary integration variable. By eliminating the common factors and then taking the natural logarithm of both parts and differentiating, the effective wavenumber is found to be [12]

$$k_{eff} = k\frac{\sqrt{1-\dfrac{1}{(2kl_0)^2}}}{1-\dfrac{x}{l_0}}. \tag{3.19}$$

Below a given frequency, the argument of the square root in Equation (3.19) becomes negative, however, and so the effective wavenumber becomes imaginary, that is, no propagation occurs and waves are evanescent. The condition for propagation is $2k_0l_0 > 0$, so that the cut-off frequency predicted by the analytical model for the linear waveguide is given by $f_{c,lin} = c_0/(4\pi l_0)$.

To calculate the phase and group velocities, losses can initially be neglected by setting $\mu = 0$, so that $c = c_0$ and $k = k_0$. Thus, the effective wavenumber becomes real, as long as the

expression under the square root is non-negative, and convenient analytical forms for the phase and group velocities can be obtained. The phase velocity is calculated by $c_{ph} = \omega/\mathrm{Re}\{k_{eff}\}$, which, for no losses, is equivalent to $c_{ph} = \omega/k_{eff}$, giving the explicit form

$$c_{ph} = c_0 \left(1 - \frac{x}{l_0}\right) \frac{1}{\sqrt{1 - \dfrac{1}{(2k_0 l_0)^2}}}. \tag{3.20}$$

The group velocity is calculated by $c_{gr} = \mathrm{d}\omega/\mathrm{d}(\mathrm{Re}\{k_{eff}\})$, which, for the effective wavenumber of Equation (3.19) and no losses, takes the form [12]

$$c_{gr} = c_0 \left(1 - \frac{x}{l_0}\right) \sqrt{1 - \frac{1}{(2k_0 l_0)^2}}. \tag{3.21}$$

It can be seen that the effective wavenumber is inversely proportional to $1 - x/l_0$, that is, it follows an inverse spatial variation compared to the inner radius, whereas the phase and group velocities decrease linearly along the waveguide, following the taper of the inner radius. At high frequencies, both velocities present the same variation,

$$\lim_{f\to\infty} c_{ph} = \lim_{f\to\infty} c_{gr} = c_0 \left(1 - \frac{x}{l_0}\right). \tag{3.22}$$

The effective length can be calculated by Equation (3.13) using Equation (3.21), yielding

$$l_{eff} = l_0 \frac{\ln \dfrac{l_0}{l_{tr}}}{\sqrt{1 - \dfrac{1}{(2k_0 l_0)^2}}}. \tag{3.23}$$

The normalised effective length, defined by Equation (3.14), is given by

$$L_{eff} = \left(1 + \frac{1}{L_{1,tr}}\right) \frac{\ln(1 + L_{1,tr})}{\sqrt{1 - \dfrac{1}{(2k_0 l_0)^2}}}. \tag{3.24}$$

where $L_{1,tr} = l_1/l_{tr}$, where $l_1 = l_0 - l_{tr}$ is the actual length. The limiting value of the normalised effective length at high frequencies is given by

$$\lim_{f\to\infty} L_{eff} = \left(1 + \frac{1}{L_{1,tr}}\right) \ln\left(1 + L_{1,tr}\right). \tag{3.25}$$

It is shown in Appendix J that the normalised effective length is larger than one, which implies that the effective length is larger than the actual length.

To calculate the reflection coefficient, the particle velocity in the non-uniform part is calculated by applying the principle of momentum conservation, $u = \mathrm{i}p'/\omega\rho$, to Equation (3.17),

giving

$$u = \frac{\mathrm{i}p_0}{2kz_0}\left[A(x-l_0)^{-\frac{3}{2}+\mathrm{i}\frac{m}{2}}(\mathrm{i}m-1) - B(x-l_0)^{-\frac{3}{2}-\mathrm{i}\frac{m}{2}}(\mathrm{i}m+1)\right]. \tag{3.26}$$

Similarly, the particle velocity in the uniform part may be calculated from the conservation of momentum applied to the pressure in the uniform part, given in Equation (3.9), giving

$$u_u = \frac{p_0}{kz_0}\left(\mathrm{e}^{-\mathrm{i}kx} - R\mathrm{e}^{\mathrm{i}kx}\right). \tag{3.27}$$

Using Equations (3.9), (3.17), (3.26) and (3.27), the boundary conditions given by Equations (3.15) are written as

$$1 + R = A(-l_0)^{-\frac{1}{2}-\mathrm{i}\frac{m}{2}} + B(-l_0)^{-\frac{1}{2}+\mathrm{i}\frac{m}{2}}, \tag{3.28}$$

$$1 - R = \frac{\mathrm{i}}{2k}\left[A(-l_0)^{-\frac{3}{2}+\mathrm{i}\frac{m}{2}}(-\mathrm{i}m+1) + B(-l_0)^{-\frac{3}{2}-\mathrm{i}\frac{m}{2}}(\mathrm{i}m+1)\right], \tag{3.29}$$

and

$$y_{end} = \frac{\mathrm{i}}{2kz_0l_{tr}}\frac{A(-\mathrm{i}m+1)(-l_{tr})^{\mathrm{i}m} + B(\mathrm{i}m+1)}{A(-l_{tr})^{-\mathrm{i}m} + B}. \tag{3.30}$$

The end reflection coefficient, defined in Equation (3.16), takes the form

$$R_{end} = \frac{B}{A}(-l_{tr})^{-\mathrm{i}m}. \tag{3.31}$$

Eliminating the ratio B/A from Equations (3.30) and (3.31), the end reflection coefficient may be expressed with respect to known quantities as

$$R_{end} = \frac{2kl_{tr}z_0y_{end} - \mathrm{i} - m}{-2kl_{tr}z_0y_{end} + \mathrm{i} - m}. \tag{3.32}$$

The two continuity conditions at the input boundary, that is, Equations (3.28) and (3.29), may be solved together with Equation (3.31), to give

$$R = \frac{R_{end}(-l_0)^{-\mathrm{i}m}(-l_{tr})^{\mathrm{i}m}(2\mathrm{i}kl_0 + \mathrm{i}m + 1) + 2\mathrm{i}kl_0 - \mathrm{i}m + 1}{R_{end}(-l_0)^{-\mathrm{i}m}(-l_{tr})^{\mathrm{i}m}(2\mathrm{i}kl_0 - \mathrm{i}m - 1) + 2\mathrm{i}kl_0 + \mathrm{i}m - 1}. \tag{3.33}$$

The reflection coefficient has also been derived in [11] and [12].

3.2.2 Quadratic inner-radius variation

For the quadratic waveguide, the inner radius varies as $r = r_0(1-x/l_0)^2$ and the general solution is [12]

$$p = A\left(-1 + \mathrm{i}\frac{kl_0^2}{x-l_0}\right)\mathrm{e}^{\mathrm{i}\frac{kl_0^2}{x-l_0}} + B\left(1 + \mathrm{i}\frac{kl_0^2}{x-l_0}\right)\mathrm{e}^{-\mathrm{i}\frac{kl_0^2}{x-l_0}}, \tag{3.34}$$

where A and B are complex constants. The first term of Equation (3.34) represents a positive-x travelling wave and the second term a negative-x travelling wave. These should be opposite to the forms in [12], due to the different convention of time dependence. The $x - l_0$ in the

denominators in Equation (3.34) instead of x in [12] is again due to the different coordinate system used, which leads to a different definition of the inner radius profile.

The effective wavenumber for the quadratic waveguide is given by [12]

$$k_{eff} = \frac{k}{\left(1-\frac{x}{l_0}\right)^2\left[1+\frac{\left(1-\frac{x}{l_0}\right)^2}{(kl_0)^2}\right]}. \tag{3.35}$$

Similarly to the linear case, it is assumed that losses can be neglected for the calculation of the propagation velocities and the effective length, so that $c = c_0$ and $k = k_0$. Thus, the phase velocity is written as

$$c_{ph} = c_0\left(1-\frac{x}{l_0}\right)^2\left[1+\frac{\left(1-\frac{x}{l_0}\right)^2}{(k_0l_0)^2}\right] \tag{3.36}$$

and the group velocity as [12]

$$c_{gr} = c_0\frac{\left(1-\frac{x}{l_0}\right)^2\left[1+\frac{\left(1-\frac{x}{l_0}\right)^2}{(k_0l_0)^2}\right]^2}{1+3\frac{\left(1-\frac{x}{l_0}\right)^2}{(k_0l_0)^2}}. \tag{3.37}$$

It can be seen that both the phase and group velocities have a fourth-order polynomial dependence on the spatial term $1 - x/l_0$. At high frequencies, however, the fourth-order term is suppressed, giving the limiting behaviour

$$\lim_{f\to\infty} c_{ph} = \lim_{f\to\infty} c_{gr} = c_0\left(1-\frac{x}{l_0}\right)^2, \tag{3.38}$$

which is proportional to the variation of the radius of the quadratic waveguide.

The effective length for the quadratic waveguide can be calculated by Equation (3.13) using Equation (3.37), and takes the form

$$l_{eff} = l_0\left\{\left[\frac{l_{tr}}{l_0}\left(1+\frac{\left(\frac{l_{tr}}{l_0}\right)^2}{(k_0l_0)^2}\right)\right]^{-1} - \left[1+\frac{1}{(k_0l_0)^2}\right]^{-1}\right\}, \tag{3.39}$$

and the normalised effective length, defined by Equation (3.14), is written as

$$L_{eff} = \left(1 + \frac{1}{L_{1,tr}}\right)\left\{\left[\frac{1}{1+L_{1,tr}}\left(1 + \frac{\frac{1}{(1+L_{1,tr})^2}}{(k_0 l_0)^2}\right)\right]^{-1} - \left[1 + \frac{1}{(k_0 l_0)^2}\right]^{-1}\right\}, \tag{3.40}$$

where $L_{1,tr} = l_1/l_{tr}$. The limiting value of the normalised effective length at high frequencies is given by

$$\lim_{f\to\infty} L_{eff} = L_{1,tr} + 1. \tag{3.41}$$

As in the linear case, it can be seen that this limiting value depends on the relation of the truncation length with the actual length of the waveguide and that it is larger than one, which means that the effective length is larger than the actual length at higher frequencies.

By applying the principle of momentum conservation, the particle velocity in the non-uniform part of the quadratic waveguide is found to be

$$u = \frac{\mathrm{i}kl_0^4}{(x-l_0)^3 z_0}\left(A\mathrm{e}^{\mathrm{i}\frac{kl_0^2}{x-l_0}} - B\mathrm{e}^{-\mathrm{i}\frac{kl_0^2}{x-l_0}}\right). \tag{3.42}$$

In the uniform part, the particle velocity is given by Equation (3.27). Using Equations (3.9), (3.27), (3.34) and (3.42), the boundary conditions expressed by Equations (3.15) are written as

$$1 + R = A(-1 - \mathrm{i}kl_0)\mathrm{e}^{-\mathrm{i}kl_0} + B(1 - \mathrm{i}kl_0)\mathrm{e}^{\mathrm{i}kl_0}, \tag{3.43}$$

$$1 - R = -\mathrm{i}kl_0\left(A\mathrm{e}^{-\mathrm{i}kl_0} - B\mathrm{e}^{\mathrm{i}kl_0}\right), \tag{3.44}$$

and

$$y_{end} = -\frac{\mathrm{i}kl_0^4}{l_{tr}^2 z_0}\frac{A\mathrm{e}^{-\mathrm{i}\frac{kl_0^2}{l_{tr}}} - B\mathrm{e}^{\mathrm{i}\frac{kl_0^2}{l_{tr}}}}{A(-l_{tr} - \mathrm{i}kl_0^2)\mathrm{e}^{-\mathrm{i}\frac{kl_0^2}{l_{tr}}} + B(l_{tr} - \mathrm{i}kl_0^2)\mathrm{e}^{\mathrm{i}\frac{kl_0^2}{l_{tr}}}}. \tag{3.45}$$

The end reflection coefficient, defined in Equation (3.16), for the quadratic waveguide is written as

$$R_{end} = \frac{B(l_{tr} - \mathrm{i}kl_0^2)}{A(-l_{tr} - \mathrm{i}kl_0^2)}\mathrm{e}^{\mathrm{i}2\frac{kl_0^2}{l_{tr}}}. \tag{3.46}$$

Eliminating the ratio B/A from Equations (3.45) and (3.46), the end reflection coefficient is written as

$$R_{end} = \frac{k^2(l_{tr}^2 l_0^4 z_0 y_{end} - l_0^6) - \mathrm{i}kl_{tr}l_0^4 + l_{tr}^4 z_0 y_{end}}{k^2(-l_{tr}^2 l_0^4 z_0 y_{end} - l_0^6) + \mathrm{i}kl_{tr}l_0^4 - l_{tr}^4 z_0 y_{end}}. \tag{3.47}$$

By solving the system of Equations (3.43), (3.44) and (3.46), the reflection coefficient at the

input boundary can be expressed with respect to the end reflection coefficient as

$$R = \frac{R_{end}(2k_0^2l_0^3 + \mathrm{i}kl_0^2 - 2\mathrm{i}kl_{tr}l_0 + l_{tr})\mathrm{e}^{-2\mathrm{i}\frac{kl_0^2}{l_{tr}}}\mathrm{e}^{\mathrm{i}kl_0} - (\mathrm{i}kl_0^2 - l_{tr})\mathrm{e}^{-\mathrm{i}kl_0}}{R_{end}(\mathrm{i}kl_0^2 + l_{tr})\mathrm{e}^{-2\mathrm{i}\frac{kl_0^2}{l_{tr}}}\mathrm{e}^{\mathrm{i}kl_0} + (2k_0^2l_0^3 - \mathrm{i}kl_0^2 + 2\mathrm{i}kl_{tr}l_0 + l_{tr})\mathrm{e}^{-\mathrm{i}kl_0}}. \tag{3.48}$$

The wavenumbers and effective lengths for a specific example of waveguide will be presented in Section 3.4, once the numerical method, used to compare with the analytical results, has been introduced.

3.3 The Transfer Function method

In this section, an alternative method of analysing the acoustic behaviour is discussed that takes into account the separate sections of the waveguide shown in Figure 3.1. This avoids the assumption of the analytical model in Section 3.2 that the effect of the sections is smeared out into a continuously varying wall admittance. A Transfer Function formulation is first derived using a simplification of the Transfer Matrix approach, which accounts for wave propagation within the sections, before a Transmission Line formulation is discussed, which assumes lumped-parameter elements. The results from these methods are then compared with those from the analytical method in the following section.

3.3.1 Transfer Function formulation

The reflection coefficient of the system may be calculated from the input admittance, which can be calculated from the admittance at the end boundary of the waveguide by iterative use of Transfer Functions. To illustrate this method, an element of the structure consisting of the region of a ring and its adjacent cavity is considered, as marked by the light grey region in Figure 3.2. The admittance at the input of the element, Y_n, can be related to the admittance at its output, Y_{n+1}, by use of Transfer Functions. A similar approach is presented in [12], where the pressure and volume velocity at the input of each element are related to the corresponding quantities at the input of the next element through Transmission Matrices. In the present analysis, however, since the reflection coefficient is the quantity of interest, which can be calculated from the input admittance, there is no need for explicit knowledge of the pressure and volume velocity, so that the simpler approach is taken, using only Transfer Functions.

There are three effects that have to be considered for the transition of the admittance from the output of a propagation element to its input [12]. First, the effect of the compressibility of the inter-ring cavity, which can be modelled as a lumped admittance, $Y_{c,n}$, which is parallel to the output admittance of the n-th element, or equivalently to the input admittance of the $(n+1)$-th element, Y_{n+1}, giving the combined admittance $\tilde{Y}_{c,n}$, as shown in Figure 3.2. Second, the propagation of the wave in the region of length $h_{c,n}$ between the two rings. Third, the

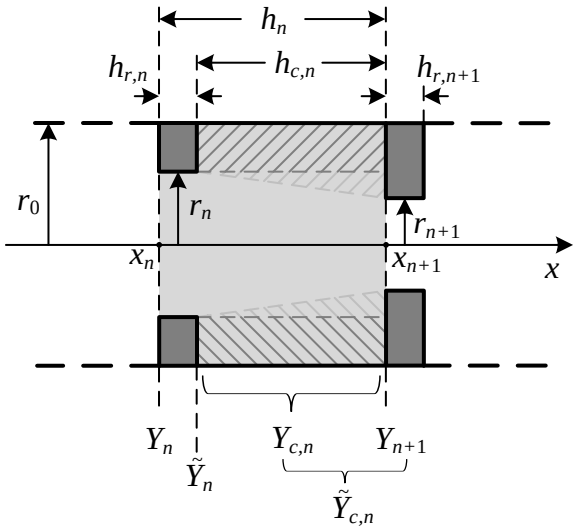

Figure 3.2. Schematic of a longitudinal cross section of an element region of the waveguide of length h_n, starting from the input boundary of the n-th ring and finishing at the input boundary of the next ring. The radii of the corresponding rings, r_n and r_{n+1}, are shown, along with the radius of the cylindrical tube, r_0, as well as the respective longitudinal distances of these rings from the origin of coordinates, x_n and x_{n+1}. The thickness of the n-th ring and the length of the n-th cavity are denoted by $h_{r,n}$ and $h_{c,n}$, respectively. The admittance at the input of the n-th ring and at the input of the $(n+1)$-th ring is denoted by Y_n and Y_{n+1}, respectively. The lined region corresponds to the lateral cavity, which provides the equivalent radial lumped admittance. This region can either be considered as the difference of a cylinder with radius r_0 and a truncated cone with end radii r_n and r_{n+1}, or the difference of two cylinders with radii r_0 and r_n, respectively. The lining for the two different geometrical approaches is coloured with different shades of grey. The radial lumped admittance, $Y_{c,n}$, due to the compressibility of the inter-ring cavity is also shown, along with intermediate admittances within the element: the combination of the output admittance and the cavity admittance, $\tilde{Y}_{c,n}$, and the admittance at the end of the input ring, $\tilde{Y}_n$.

propagation of the wave in the thin region of the ring of thickness $h_{r,n}$. As in the analytical model, losses may be included in the system using a complex speed of sound, and, therefore, also a complex wavenumber.

The effect of the compressibility of the cavity can be approximately modelled by a lumped admittance [54]

$$Y_{c,n} = \mathrm{i}\frac{k}{z_0}V_n, \tag{3.49}$$

where V_n is the volume of the cavity. The volume of the cavity can either be regarded as the difference of two cylinders of radii r_0 and r_n, shown as a lined region of dark grey lines in Figure 3.2, or as the difference of a cylinder of radius r_0 and a truncated cone of end radii r_n and r_{n+1}, which covers the whole lined region in Figure 3.2. In the former case, the volume of the cavity is given by

$$V_{n,cyl} = \pi h_{c,n}\left(r_0^2 - r_n^2\right), \tag{3.50}$$

whereas, in the latter case, the volume is given by

$$V_{n,cone} = \pi h_{c,n} \left[r_0^2 - \frac{1}{3} \left(r_n^2 + r_{n+1}^2 + r_n r_{n+1} \right) \right]. \tag{3.51}$$

It should be noted that modelling the compliance of the cavity as a lumped-parameter element assumes that the depth of the cavity is much smaller than the wavelength or, equivalently, that $k(r_0 - r_n) \ll 1$, which is ensured if only plane-wave propagation is assumed in the duct of radius r_0.

The output admittance of the element, Y_{n+1} in Figure 3.2, is in parallel with the cavity admittance, so that their combination is written as

$$\tilde{Y}_{c,n} = Y_{c,n} + Y_{n+1}, \tag{3.52}$$

where $Y_{c,n}$ is calculated with Equation (3.49) using either of Equations (3.50) and (3.51), leading to two versions depending on the assumed volume, $Y_{c,n,cyl}$ and $Y_{c,n,cone}$, respectively, and to two versions of combined admittances, $\tilde{Y}_{c,n,cyl}$ and $\tilde{Y}_{c,n,cone}$.

The propagation region of length $h_{c,n}$ in the core of the waveguide between two consecutive rings can be considered either as a cylinder of radius r_n or as a truncated cone of end radii r_n and r_{n+1}. In Figure 3.2, these regions are delimited by the dark and light grey dashed lines connecting the two rings, respectively. In the former case, the admittance $\tilde{Y}_n$ in Figure 3.2 can be calculated from the admittance at the other end of the element, $\tilde{Y}_{c,n}$ in Figure 3.2, using the Transfer Function method to account for the effect of propagation through a cylindrical region [54], as

$$\tilde{Y}_{n,cyl} = \frac{S_n}{z_0} \frac{\mathrm{i} S_n \sin(k h_{c,n}) + \tilde{Y}_{c,n} z_0 \cos(k h_{c,n})}{S_n \cos(k h_{c,n}) + \mathrm{i} \tilde{Y}_{c,n} z_0 \sin(k h_{c,n})}, \tag{3.53}$$

where $S_n = \pi r_n^2$ is the cross-sectional area of the region of propagation. In the latter case, the corresponding admittance for the conical region is given by [55]

$$\tilde{Y}_{n,cone} = \frac{S_n}{z_0} \frac{S_{n+1} \sin(k h_{c,n} + \theta_{n,1} - \theta_{n,2}) - \mathrm{i} \tilde{Y}_{c,n} z_0 \sin(k h_{c,n} + \theta_{n,1}) \sin\theta_{n,2}}{\mathrm{i} S_{n+1} \sin(k h_{c,n} - \theta_{n,2}) \sin\theta_{n,1} + \tilde{Y}_{c,n} z_0 \sin(k h_{c,n}) \sin\theta_{n,1} \sin\theta_{n,2}}, \tag{3.54}$$

where $\theta_{n,1} = \tan^{-1}(k h_{c,n} r_n / d_n)$, $\theta_{n,2} = \tan^{-1}(k h_{c,n} r_{n+1} / d_n)$ and $d_n = r_{n+1} - r_n$. In both of Equations (3.53) and (3.54), $\tilde{Y}_{c,n}$ can be either $\tilde{Y}_{c,n,cyl}$ or $\tilde{Y}_{c,n,cone}$, depending on the assumed volume for the lateral cavity.

The third effect that needs to be accounted for in the element of the waveguide shown in Figure 3.2 is the propagation through the short cylindrical region of the ring of thickness $h_{r,n}$. The corresponding Transfer Function is similar to Equation (3.53),

$$Y_n = \frac{S_n}{z_0} \frac{\mathrm{i} S_n \sin(k h_{r,n}) + \tilde{Y}_n z_0 \cos(k h_{r,n})}{S_n \cos(k h_{r,n}) + \mathrm{i} \tilde{Y}_n z_0 \sin(k h_{r,n})}, \tag{3.55}$$

where $\tilde{Y}_n$ can be either $\tilde{Y}_{n,cyl}$ or $\tilde{Y}_{n,cone}$. The admittance at the input of the element can therefore be calculated from the admittance at the input of the next element using Equations (3.49) to (3.55). It can be seen from the above that there are four cases for the calculation of the input admittance of the waveguide element, depending on whether the cylindrical or conical shapes are assumed for the cavity and for the propagation region between the two rings. The differences in the results from the four cases will be discussed in Section 3.4.2.

To calculate the input admittance with the Transfer Function method, the boundary condition at the end of the waveguide needs to be known. This boundary condition may be expressed in the form of an admittance, Y_{end} in Figure 3.1. Starting from this known admittance, the admittance at the input of the last ring can be calculated, from which the admittance at the input of the penultimate ring can be calculated. In this iterative manner, the input admittance of the waveguide, Y_{in}, can be found. The reflection coefficient can then be calculated as

$$R = \frac{Y_0 - Y_{in}}{Y_0 + Y_{in}}, \tag{3.56}$$

where Y_0 is the characteristic admittance of the cylindrical tube, given by $Y_0 = S_0/z_0$, where S_0 is the cross-sectional area of the tube. Figure 3.3 shows the basic quantities involved in the procedure within the waveguide.

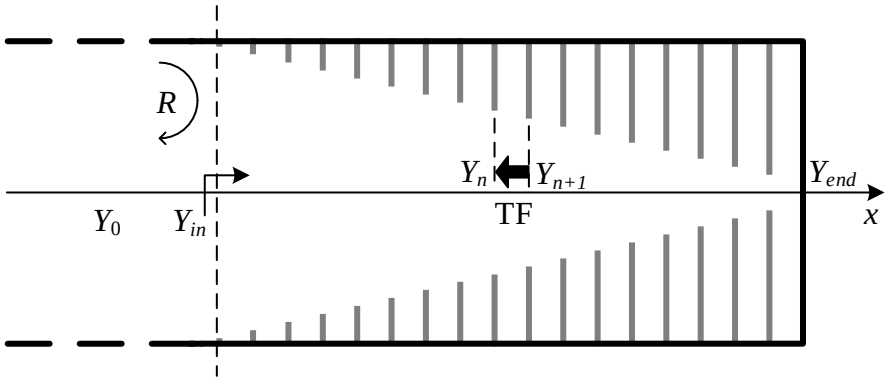

Figure 3.3. Schematic of a longitudinal cross section of the waveguide. The admittance at the termination, Y_{end}, the admittances at the inputs of two arbitrary consecutive rings, Y_n and Y_{n+1}, the input admittance of the waveguide, Y_{in}, the characteristic admittance of the cylindrical tube, Y_0, and the reflection coefficient, R, are shown. The thick arrow represents the calculation of Y_n from Y_{n+1} using Transfer Functions (TF).

The Transfer Function method relies on a number of physical assumptions. First, plane-wave propagation is assumed, as was the case in the analytical model of Section 3.2. This means that, for a given waveguide, the method is only applicable up to the cut-off frequency of the first higher-order transverse mode. Furthermore, specific three-dimensional shapes are assumed to approximate both the inter-ring cavities, which determine the radial lumped admittances, and the regions of wave propagation, involving either cylinders or differences of cylinders and

cones, as mentioned earlier. Losses are accounted for by a uniform complex speed of sound, thus neglecting their dependence on both the geometry of the system and on frequency. Finally, the method does not consider any end correction for the acoustic radiation from a ring into its adjacent cavity. All of these assumptions will limit the accuracy of the model, but it still provides a useful prediction of the true behaviour.

3.3.2 Transmission Line model

The model presented above may be further simplified to a form similar to a Transmission Line using lumped acoustic parameters for the inertance and compliance of each region between two consecutive rings, by assuming that the dimensions of each element of the waveguide are much smaller than the wavelength. It should be noted that the term 'Transmission Line' is used here in a looser sense, since in the formal theory, the Transmission Line is modelled as an array of series and shunt impedances, or admittances, per unit length [56], whereas in the current model, lumped series and shunt admittances are used to represent lumped acoustic properties of the system corresponding to a certain length of the waveguide. Nevertheless, the use of the term can be justified by the assumed small acoustic length of the waveguide elements. A circuit representation of the n-th element within the waveguide using lumped parameters is shown in Figure 3.4. The assumptions for the dimensions of each element are expressed as $h_n \ll \lambda \Leftrightarrow kh_n \ll 1$ and $r_0 \ll \lambda \Leftrightarrow kr_0 \ll 1$. These assumptions imply that the Transmission Line model is accurate only at relatively low frequencies.

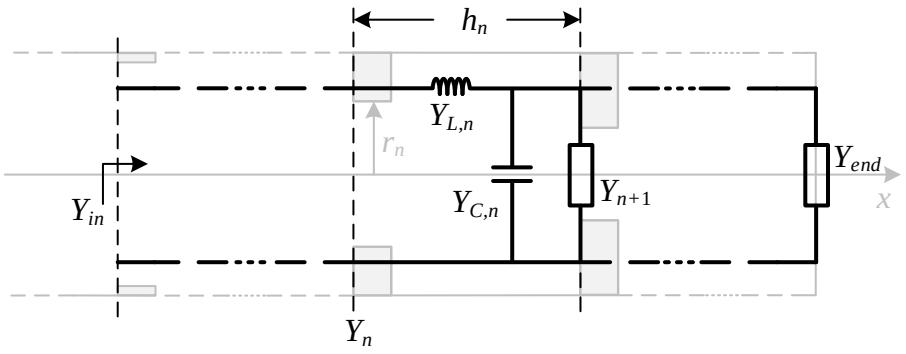

Figure 3.4. Circuit representation of an element of the waveguide using acoustic admittances, drawn over a longitudinal cross section of the waveguide. The input and end of the system are also shown along with the respective admittances, Y_{in} and Y_{end}. Y_n is the admittance at the input of the n-th element, and $Y_{L,n}$ and $Y_{C,n}$ are the admittance due to the inertia of the fluid fluctuating in the longitudinal direction and the admittance due to the compressibility of the fluid, respectively, in the region of length h_n between the input boundaries of two consecutive rings.

The effect of the compressibility of the volume of air in the whole region of length h_n, including both the cavity and the core, is expressed as the admittance $Y_{C,n}$, which is parallel to the admittance of the next element, Y_{n+1}, while the effect of the inertia of the fluid fluctuating

longitudinally in the core of the waveguide is expressed as the admittance $Y_{L,n}$, which is in series with the parallel combination of $Y_{C,n}$ and Y_{n+1}. The shunt admittance of an element between two rings is given by

$$Y_{C,n} = \frac{\mathrm{i}k}{z_0}\left(h_{c,n}S_0 + h_{r,n}S_n\right), \tag{3.57}$$

where $S_0 = \pi r_0^2$ is the cross-sectional area of the tube and $S_n = \pi r_n^2$ is the cross-sectional area of the opening of the n-th ring. In Equation (3.57), two regions are included for the volume of the compliance: the main region of length $h_{c,n}$ and radius r_0 and a small region of length $h_{r,n}$ and radius r_n at the input of the element, which combined give the full volume of air in an element of the waveguide, as can be seen in Figure 3.2.

The region for the series admittance due to the inertance of the fluid may be considered in two ways: either as a cylinder of length h_n and radius r_n or as a combination of a short cylinder of length $h_{r,n}$ and radius r_n and a truncated cone of length $h_{c,n}$ and end radii r_n and r_{n+1}. In the former case, the inertive admittance is given by

$$Y_{L,n,cyl} = \frac{S_n}{\mathrm{i}z_0 k h_n}, \tag{3.58}$$

whereas, in the latter case, the series combination of the inertances of the two regions gives

$$Y_{L,n,cone} = \frac{\pi r_n^2 r_{n+1}}{\mathrm{i}z_0 k(r_n h_{c,n} + r_{n+1}h_{r,n})}. \tag{3.59}$$

From circuit theory, the admittance of the n-th element can be written as

$$Y_n = \frac{Y_{C,n} + Y_{n+1}}{Y_{L,n} + Y_{C,n} + Y_{n+1}} Y_{L,n}. \tag{3.60}$$

For a given end admittance, Y_{end}, the input admittance of the waveguide can be calculated with Equation (3.60) following a similar iterative procedure as in the previous section, and, from this, the reflection coefficient can be found using Equation (3.56). It can be shown that Equation (3.60) in combination with either of Equations (3.58) or (3.59) is equivalent to Equation (3.55) combined with the corresponding one of Equations (3.53) and (3.54), if the leading-order approximations for the sines and cosines are applied, and if second-order terms for kh_i, where the index i can be either n, c,n or r,n, are neglected.

3.4 Results from different simulation methods

The geometrical properties of the non-uniform waveguides used to compare the results of the different models are given in Table 3.1. The ring thickness, $h_{r,n}$, and the length of the cavity region, $h_{c,n}$, are considered to be constant, so that $h_{r,n} = h_r$, $h_{c,n} = h_c$ and $h_n = h$ for all n. For

a linear variation of the inner radius of the rings, the inner radius is given by $r_n = r_0(1-x_n/l_0)$, where x_n is the distance of the n-th ring from the input of the non-uniform waveuide, as shown in Figures 3.1 and 3.2. In the quadratic case, the inner radius varies as $r_n = r_0(1-x_n/l_0)^2$. For the continuous analytical model, the radius is given by $r(x) = r_0(1-x/l_0)$ and $r(x) = r_0(1-x/l_0)^2$ for the linear and the quadratic waveguide, respectively.

Geometrical property	Value	Geometrical property	Value
Tube radius (r_0)	0.23 m	Ideal length - linear (l_0)	0.5 m
Actual length (l_1)	0.47 m	Truncation length - linear (l_{tr})	0.03 m
Truncation radius ($r(l_1)$)	0.0138 m	Ideal length - quadratic (l_0)	0.6225 m
Ring thickness (h_r)	0.001 m	Truncation length - quadratic (l_{tr})	0.1525 m

Table 3.1. Assumed geometrical properties of the non-uniform waveguide model for comparing the different modelling methods.

For an insightful comparison between the linear and quadratic waveguides, the two geometries are considered with the same actual length, l_1, and the same truncation radius, $r(l_1)$. These settings require different ideal lengths and truncation lengths for the two geometries, as shown in Table 3.1. In all following results, a rigid-wall termination is considered, which is equivalent to a zero admittance at the end, that is, $y_{end} = 0$ for the analytical model and $Y_{end} = 0$ for the Transfer Function method. Most simulations in this section are for a waveguide with 40 equally spaced rings. Waveguides with 10 and 400 rings are also considered later, to illustrate some aspects of the model.

The frequency range in which only the fundamental mode propagates in the waveguide is defined by the cut-off frequency of the first higher-order mode of the main duct, which, for a cylindrical tube, is given by $f_c = 0.293c/r_0$ [57]; this should not be confused with the cut-off frequency due to the geometrical variation of the linear waveguide, $f_{c,lin}$, mentioned in Section 3.2.1. For a radius of 0.23 m, the cut-off frequency of the first higher-order mode is about 437 Hz, thus imposing an upper limit for the applicability of both the analytical and the Transfer Function method. The values for air density and speed of sound used are $\rho = 1.2$ kg·m^{-3} and $c_0 = 343$ m·s^{-1}, respectively. A loss parameter with value $\mu = 0.05$ has been used throughout this analysis, since it is found that this best matches some experimental results discussed later.

3.4.1 Analytical results for the effective wavenumber, the propagation velocities and the effective length

First, some results are given for the effective wavenumber, the phase and group velocities and the effective length, based on the analytical model, using the formulas presented in Sections 3.2.1 and 3.2.2, where the ring inner radius and the admittance of the cavities are approximated by a continuous waveguide radius and a continuous wall admittance. Therefore, the number of rings is not accounted for in these results.

The phase and group velocities, normalised with respect to the speed of sound in air, are plotted against position in Figures 3.5a and 3.5b, for a linear and a quadratic waveguide, respectively, for three different frequencies, calculated with Equations (3.20), (3.21),(3.36) and (3.37) for the respective waveguides. It should be noted that both velocities are calculated without including losses for convenience of analytical manipulation, as is explained in Section 3.2.1. It can be seen that both the phase and group velocities for both waveguides start from a value which is close to the speed of sound in free space at the input of the waveguide and then gradually decrease to a very small value at the end. Therefore, incident waves slow down to a very small propagation velocity as they travel along the waveguide. For an ideal waveguide, that is, without truncation, both velocities would vanish at the end.

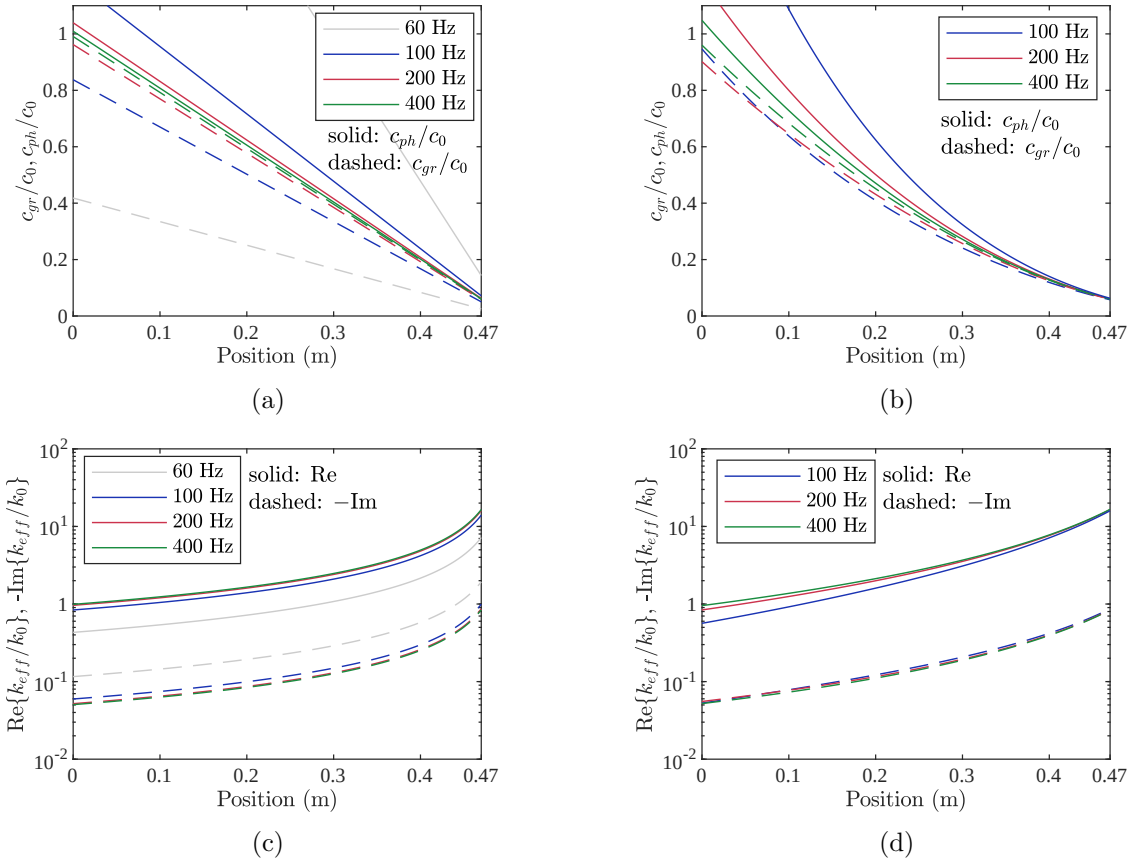

Figure 3.5. Normalised phase and group velocity against position, x in Figure 3.1, for three different frequencies, for (a) a linear and (b) a quadratic waveguide; the solid lines represent phase velocities and the dashed lines represent group velocities. Normalised real and opposite of the imaginary part of the wavenumber against position, plotted on a logarithmic scale, for three different frequencies, for (c) a linear and (d) a quadratic waveguide; the solid lines represent real parts of the wavenumber and the dashed lines represent opposite imaginary parts of the wavenumber.

It can be observed in Figures 3.5a and 3.5b that both the phase and group velocity at the input to the absorber, $x = 0$, are different from the speed of sound in free space. This can be attributed to the discontinuity that the non-uniform part of the waveguide imposes at its input. The effect of the discontinuity is less prominent as frequency increases, as the wavelength becomes smaller and the wave is more efficient in 'following' the discontinuity.

Therefore, the propagation velocities tend to the speed of sound in free space as frequency increases, in accordance with Equations (3.22) and (3.38).

The real and imaginary parts of the wavenumber for the linear and quadratic waveguide are plotted in Figures 3.5c and 3.5d, respectively, for three different frequencies. It should be noted that losses are now included for the calculation of the wavenumber. The imaginary part of the wavenumber is negative, and, therefore, its opposite is plotted on the logarithmic scale. A greater negative imaginary wavenumber corresponds to greater losses in the system. The increasing real part along the waveguide complies with the decreasing propagation velocities, and the increase of the negative imaginary part implies that losses become greater towards the end of the waveguide. Combining the analytical results for the propagation velocities and the wavenumber provides a description of the qualitative behaviour of the system, where the waves slow down as they propagate along the waveguide and the attenuation increases; waves are thus mainly absorbed in the vicinity of the termination, where the propagation speed is very small and the attenuation is very large.

A plot of the phase and group velocities at the input boundary as a function of frequency is shown in Figure 3.6a. The velocities all tend to the speed of sound in free space with increasing frequency, as noted above. For the linear waveguide, the low cut-off frequency described in Section 3.2.1 can be seen at about 55 Hz, where the phase velocity becomes infinite and the group velocity vanishes. For the quadratic waveguide, both the phase and the group velocity tend to infinity towards the low frequency limit.

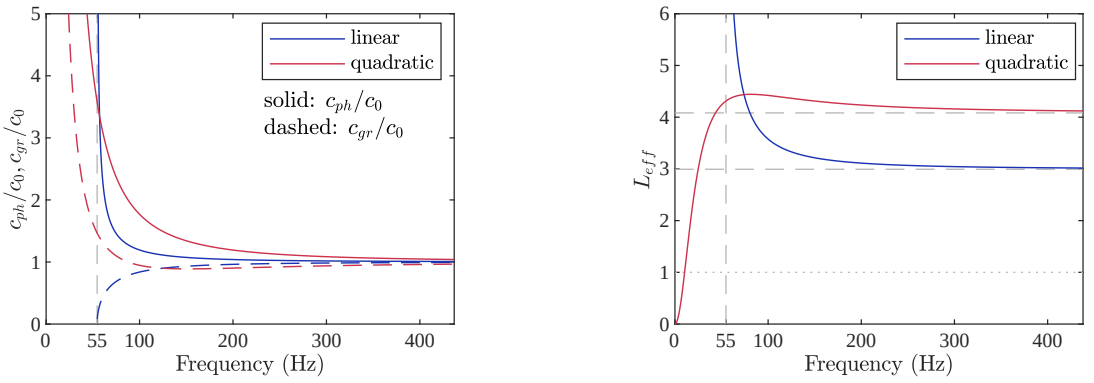

Figure 3.6. (a) Normalised phase and group velocity at the input boundary of the waveguide against frequency, for a linear and a quadratic waveguide. (b) Normalised effective length plotted against frequency. The dotted horizontal line at $L_{eff} = 1$ denotes the actual length of the waveguide, and the two dashed horizontal lines denote the limit values of the normalised effective length at high frequencies for the two different waveguides. The cut-off frequency for the linear waveguide is denoted by a vertical line in both graphs.

The normalised effective lengths of the linear and quadratic waveguides with the specifications of Table 3.1 are plotted in Figure 3.6b as a function of frequency, calculated with Equations (3.23) and (3.39). The normalised effective length of the quadratic waveguide is larger than that of the linear waveguide over most of the frequency range, which implies that

the resonances in the quadratic waveguide, and, therefore, the dips in the reflection coefficient, start from a lower frequency and are more densely spaced in the spectrum compared to the linear waveguide, as will be seen in Section 3.4.2.

The fact that the effective length for the linear waveguide tends to infinity as frequency approaches the cut-off frequency is due to the inverse trend of the group velocity, as observed in Figure 3.6a. However, the effective length close to cut-off has limited meaning, since the absolute value of the imaginary part of the wavenumber becomes large throughout the waveguide and waves are greatly attenuated, as can be seen in Figure 3.5c for a frequency of 60 Hz. The mismatch between the propagation velocities and the speed of sound in air at the input boundary of the waveguide, as illustrated in Figure 3.5a, will cause the waves incident from the uniform part of the duct to be strongly reflected below the cut-off frequency of the linear waveguide.

3.4.2 Simulations of the reflection coefficient

Analytical results for the modulus of the reflection coefficient of both a linear and a quadratic waveguide with the specifications of Table 3.1 are shown in Figure 3.7 calculated using Equations (3.33) and (3.48). The modulus of the reflection coefficient of a quarter-wave resonator, that is, a rigidly terminated uniform tube, of the same length, terminating a uniform tube of a cross-sectional area five times larger than that of the quarter-wave resonator is also plotted. This difference in cross-sectional area is included to provide a discontinuity between the input waveguide and the quarter-wave resonator termination, so that a prominent dip appear in the reflection coefficient. A phenomenological complex speed of sound is also used for the quarter-wave resonator with $\mu = 0.05$, for ease of comparison with the non-uniform waveguides with rings.

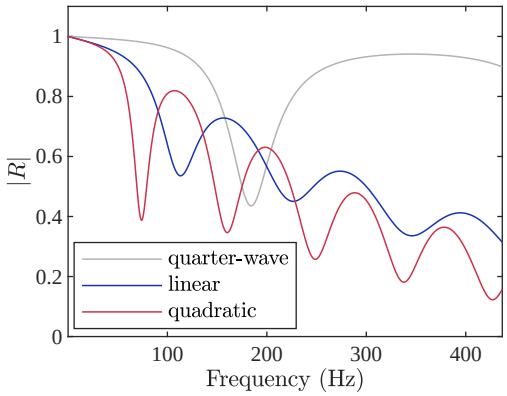

Figure 3.7. Modulus of the reflection coefficient of a linear and a quadratic waveguide calculated with the analytical method, and modulus of the reflection coefficient of a quarter-wave resonator of the same length and cross-sectional area, terminating a uniform tube of cross-sectional area five times larger than that of the quarter-wave resonator.

Only the first dip of the quarter-wave resonator is visible in Figure 3.7, which occurs at a frequency corresponding to a quarter of the wavelength, which, for a tube of length $l_1 = 0.47$ m,

occurs at 184 Hz. It can be seen that the first dip of the quadratic waveguide appears at the lowest frequency, followed by the first dip of the linear waveguide, which, in turn, occurs at a lower frequency than the first dip of the quarter-wave resonator. Accordingly, the dips are more densely spaced in the spectrum for the quadratic waveguide than for the linear one, the dips of the latter being more densely spaced than those for the quarter-wave resonator. These results were implied by the relative values of the normalised effective length, plotted in Figure 3.6b, where the normalised effective length of the quarter-wave resonator is 1 but those of the linear and quadratic absorbers are about 3 or 4 at higher frequencies.

It can also be seen in Figure 3.7 that the reflection coefficient for the quadratic waveguide is generally lower than that of the linear one. This may be attributed to the fact that the propagation velocities in the quadratic case decrease according to a power-law, as can be seen from Equations (3.36) and (3.37), whereas the respective velocities in the linear case decrease linearly along the waveguide, as can be seen from Equations (3.20) and (3.21). Therefore, the propagation velocities, which all start from a value close to the speed of sound in free space at the input boundary for most of the considered spectrum, become smaller earlier on along the quadratic waveguide, as can be seen in Figure 3.5, which leads to comparatively higher absorption, and, accordingly, to lower reflection.

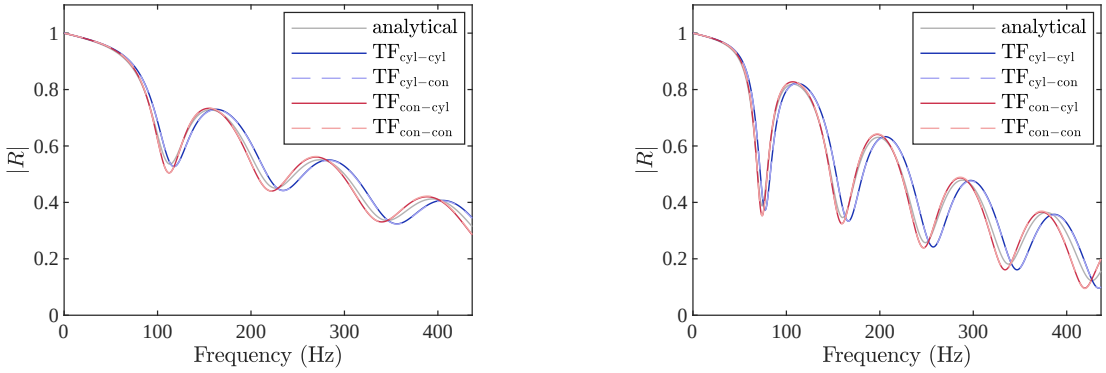

Figure 3.8. Modulus of the reflection coefficient of a waveguide with 40 equally spaced rings and the geometrical properties given in Table 3.1, calculated with the analytical model and with the Transfer Function method, for (a) linear and (b) quadratic inner-radius variation. Results with all the different configurations for the geometrical shape of the core and the lateral cavity of the waveguide are shown, where 'cyl' stands for cylinder and 'con' stands for cone in the subscripts in the legend; the first subscript corresponds to the shape of the core and the second to the shape of the lateral cavity. Configurations with the same first subscript, that is, with the same core geometry, give practically indistinguishable results.

Figures 3.8a and 3.8b show the modulus of the reflection coefficient for linear and for quadratic inner-radius variation, respectively, using the analytical method and the Transfer Function method for a waveguide with 40 equally spaced rings. Results with the Transfer Function method are produced with the four different configurations for the geometrical shape of the core of the waveguide and of the lateral cavities presented in Section 3.3. It can be seen that the choice of shape for the lateral cavity makes practically no difference in the frequency range

considered, as the dashed lines coincide with their corresponding continuous lines. Therefore, in the Transfer Function results presented henceforth, only the cases where the core and the cavity of each element of the waveguide are both considered to be either cylindrical, denoted by a subscript 'cyl', or conical, denoted by a subscript 'con', are shown.

It can also be seen in Figures 3.8a and 3.8b that the analytical and Transfer Function results with conical-core geometry match at lower frequencies, but they deviate slightly as frequency increases. Overall, however, the matching between the different methods is good for the geometrical properties given in Table 3.1, with the conical-core approach giving slightly better matching with the analytically calculated reflection coefficient over most of the considered spectrum.

The modulus of the reflection coefficient with 10 and with 400 rings is plotted in Figures 3.9a and Figure 3.9b for a linear and a quadratic waveguide, respectively, calculated analytically and using the Transfer Function method. The ring thickness is set to be $h_r = 1$ µm for the case of 400 rings, so that it remains small compared to the length of each element, which for a waveguide of length 0.47 m is $h = 0.0012$ m. These results demonstrate the limiting behaviour of the Transfer Function method. It can be seen that both for the linear and the quadratic waveguide, the analytical results coincide with the Transfer Function results with 400 rings. This is expected, since for a very large number of rings with very small thickness, the two geometrical approaches match, and they both approach the continuous geometry of the analytical model.

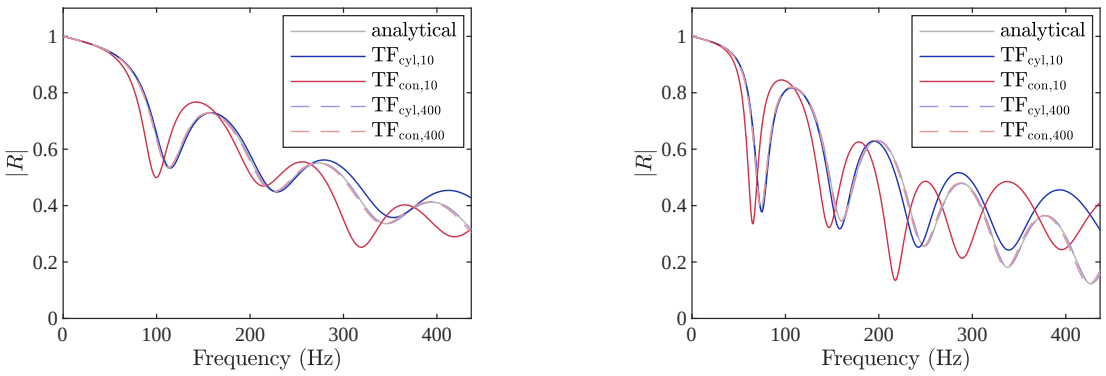

Figure 3.9. Modulus of the reflection coefficient of a waveguide with 10 and 400 rings and the geometrical properties given in Table 3.1, calculated with the analytical model and with the Transfer Function method, for (a) linear and (b) quadratic inner-ring radius variation. For the waveguide with 10 rings, a ring thickness of $h_r = 1$ mm is used, as in the case of 40 rings, whereas in the case of 400 rings, a ring thickness of $h_r = 1$ µm is used.

Perhaps unexpectedly, however, in the case of only 10 rings, the Transfer Function cylindrical approach results match well with the analytical ones at low frequencies. The conical-core results for both the linear and the quadratic waveguide with 10 rings are significantly different from the analytical ones, even though in the case of 40 rings, the conical approach gave better matching than the cylindrical one. This discrepancy could be due to the basic assumptions behind the

conical Transfer Function of Equation (3.54), which is based on the solution of the Helmholtz equation for a spherical wave in a conical horn [54], thus assuming that the pressure is uniform on a spherical surface. This assumption might not be applicable in the waveguide studied here, especially when the element size is large, as in the case of 10 rings.

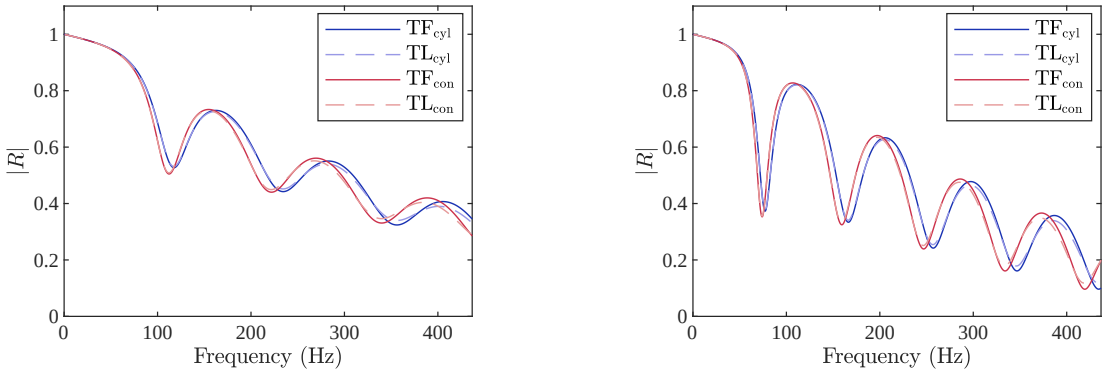

Figure 3.10. Modulus of the reflection coefficient of a waveguide with 40 rings and the geometrical properties given in Table 3.1, calculated with the Transfer Function, TF, method and with the Transmission Line, TL, model, both with the cylindrical- and the conical-core geometrical approach, for (a) linear and (b) quadratic inner-radius variation.

Figures 3.10a and 3.10b show the results from the Transfer Function method and the Transmission Line model for a linear and a quadratic waveguide with 40 rings, respectively. It can be seen that results from the two methods for both the cylindrical- and conical-core assumptions match well, both for the linear and for the quadratic waveguide, with only a small deviation at higher frequencies. The accuracy of the Transmission Line model lies on the assumption that the length of an element, which corresponds to the distance between consecutive rings, is much smaller than the wavelength. Although this assumption is reasonable for the arrangement with 40 rings, it will not be so if fewer rings are used.

3.5 Comparison of results from simulations with ones from experiments

The reflection coefficient of a non-uniform acoustic waveguide with fitted rings of varying inner radius was measured experimentally by Azbaid El Ouahabi et al. [3], using the two-microphone Transfer Function method [58]. The linear model used has 18 rings while the quadratic one has 15 rings. For the latter, the original paper mentions 14 rings but 15 rings were actually used, as can be deduced from the geometrical guidelines in the paper for calculating the inter-ring distances and was also confirmed by one of the authors [59]. In [3], the non-uniform waveguides terminate a uniform tube of slightly smaller radius, to reduce the reflection at the input described above, which is also implemented in the modelling.

A schematic representation of the linear and quadratic waveguides is shown in Figures 3.11a

(a) (b)

Figure 3.11. Schematic of the waveguide with fitted rigid rings used in the experimental implementations in [3], with the geometrical properties given in Table 3.2, for (a) linear and (b) quadratic inner radius variation. The inner radius of the rightmost ring in (b) is very small but non-zero.

and 3.11b, respectively, and the main geometrical properties of the non-uniform waveguides used are given in Table 3.2, taken from [3]. The distances between consecutive rings are variable in this arrangement. Among the experimental setups presented in [3], the case with no added damping material is considered here. The frequency band where the experimental results are accurate is approximately between 114 and 884 Hz, as explained in [3]; therefore, a frequency band with similar limits is considered in the simulations. The upper frequency limit is defined by the cut-off frequency of the first higher-order mode. It should be noted that, for this system, it is not possible to acquire solutions for the reflection coefficient with the analytical model presented in Section 3.2, since the equivalent continuous radius vanishes at the end of the waveguide, which would lead to infinite pressure there for the analytical model.

Geometrical property	Value	Geometrical property	Value	
			Linear	Quadratic
Radius of tube with rings (r_0)	115 mm	Number of rings (N)	18	15
Ring thickness (h_r)	2 mm	Position of first ring (x_1)	6 mm	
Length of tube with rings (l)	255 mm	Distance between n-th and $(n+1)$-th ring ($h_{c,n}$)	$(21-n)$ mm, $1 \leq n \leq N$	
Radius of uniform tube (r_u)	112.5 mm	Position of n-th ring (x_n)	$x_1 + \sum_{m=1}^{n-1}(h_r + h_{c,m})$, $2 \leq n \leq N$	
		Distance between last ring and end	9 mm	30 mm
		Ring inner radius (r_n)	$r_0(1 - x_n/l)$	$r_0(1 - x_n/l)^2$

Table 3.2. Geometrical properties of the linear and quadratic experimental arrangements, based on [3].

A comparison of the Transmission Line approximation with the Transfer Function method is given first, with the modulus of the reflection coefficient plotted for both the cylindrical and conical approaches in Figures 3.12a and 3.12b for the linear and quadratic waveguides. It can be seen that the Transmission Line approximation deviates significantly from the Transfer Function approach above about 400 Hz. This may be attributed to two reasons. First, the distances between consecutive rings is larger for the waveguides used here compared to the waveguide in Section 3.4, leading to a relatively smaller wavelength compared to the element length for a given frequency. Second, the difference in the tube radius gives different higher

limits for uni-modal propagation, extending the working spectrum of the waveguides used in this section to higher frequencies, where the wavelength becomes even smaller, thus further deteriorating the accuracy of the Transmission Line approximation. It is, therefore, concluded that for the waveguides with the properties of Table 3.2, the Transmission Line approximation should not be used.

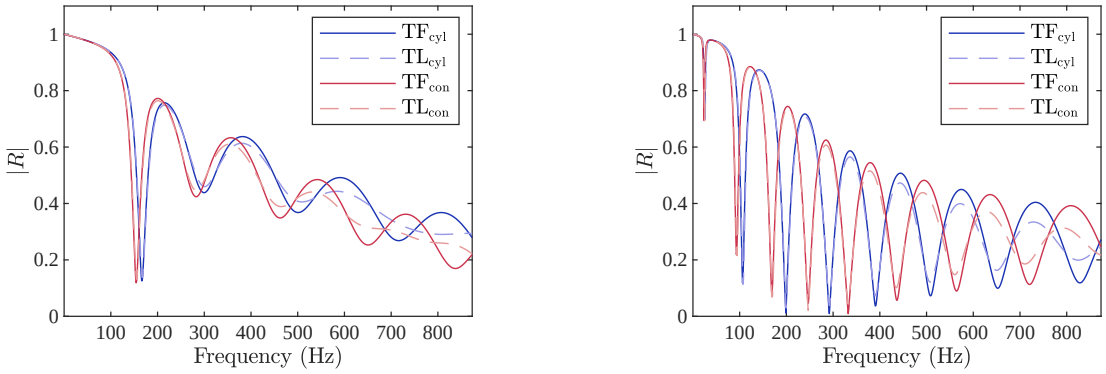

Figure 3.12. Modulus of the reflection coefficient of the model used in [3], for (a) a linear and (b) a quadratic non-uniform termination. For the Transfer Function results, a loss parameter with value $\mu = 0.05$ is used.

The experimental results for the modulus of the reflection coefficient, taken from [3], are shown in Figures 3.13a and 3.13b for the linear and quadratic waveguide, along with the predicted results using the Transfer Function method. The results with the conical assumption appear to be the most accurate representation of the experimental results, and so simulation results only with the conical approach are shown. For the Transfer Function results, a value of 0.05 was chosen for the loss parameter, μ, to approximate the experimental results in the middle spectral region, which is also the value used in the simulations of Section 3.4. Some peaks in the experimental results for the modulus of the reflection coefficient appear to be suppressed, possibly by resonances of the measurement setup that may not be related to the non-uniform termination, as for example between 700 and 800 Hz in Figure 3.13a, or between 250 and 350 Hz in Figure 3.13b.

Reasonable matching between the experimental results and the predictions of the Transfer Function method can be observed for the linear waveguide in the middle spectral region, between about 300 and 600 Hz, as can be seen in Figure 3.13a. If higher values are used for μ, the conical Transfer Function results approach the experimental ones even better at higher frequencies, but they deviate from them in the middle of the spectrum. Even so, the Transfer Function method with the conical approach appears to give a good prediction for the frequencies where the two main dips of the reflection coefficient occur in the experimental results at high frequencies, around 670 Hz and 850 Hz, respectively. At lower frequencies, the Transfer Function predictions do not match with the experimental results. Specifically, a prominent dip in the reflection coefficient is predicted at around 155 Hz which is not seen in the experimental results. For the

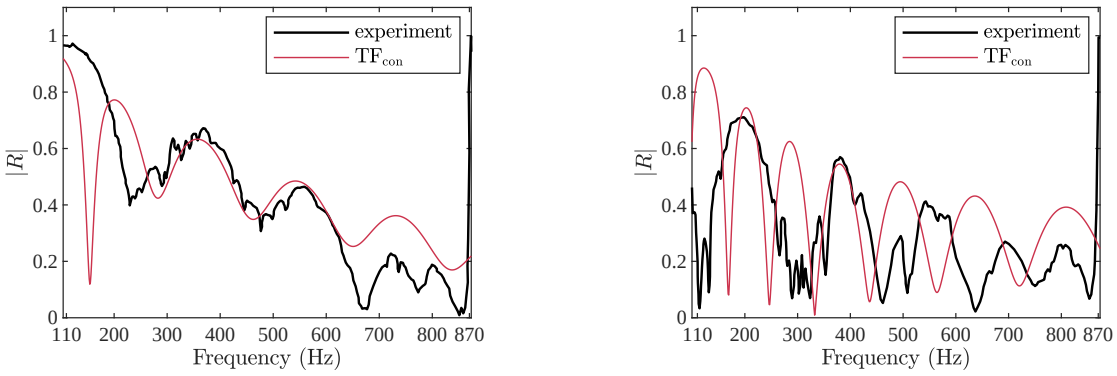

Figure 3.13. Modulus of the reflection coefficient of the model used in [3], for (a) a linear and (b) a quadratic non-uniform termination, with the experimental results taken from [3]. For the Transfer Function results, a loss parameter with value $\mu = 0.05$ is used.

quadratic waveguide, results for which are shown in Figure 3.13b, only the general level of the reflection coefficient, around which it fluctuates with frequency, is predicted by the Transfer Function method, whereas the details of the fluctuating reflection coefficient are not predicted over any extended part of the spectrum.

The absorption due to viscothermal losses depends on frequency, with greater losses occurring at higher frequencies, whereas the loss parameter μ is assumed here to be constant. A frequency-dependent loss parameter would thus be expected to improve the model predictions, as it would give lower reflection at higher frequencies.

3.6 Summary and conclusions

An acoustic absorber consisting of a tube termination with fitted rigid rings of tapering inner radius has been studied using different methods. Both linear and quadratic ring inner-radius variation was considered. The main characteristics of the system were analysed using a continuous analytical model. The phase and group velocities for an incident wave travelling through the system decrease to very small values towards the end, where attenuation rapidly increases. Therefore, incident waves slow down and are significantly absorbed near the end of the system.

A Transfer Function method was presented, which is a simplification of the full Transfer Matrix method if only the reflection coefficient is sought. A cylindrical and a conical modelling approach were used for the main core and the inter-ring cavities. It was shown that the Transfer Function method matches the analytical results for a sufficiently large number of rings. A Transmission Line model was also implemented, which forms a low-frequency approximation of the Transfer Function method, and its limitations were illustrated.

Results for the reflection coefficient using the Transfer Function method were compared with ones from experiments taken from [3]. For the linear waveguide with the geometry used

in [3], it was observed that the Transfer Function method using the conical approach provides reasonably good matching with the experimental results over most of the spectrum. For the quadratic waveguide, however, results from the Transfer Function method only predict the general level of reflection, but fail to predict the details of the fluctuations of the reflection coefficient with frequency.

This comparative analysis has illustrated that more accurate modelling is required to simulate such a system. Specifically, the losses occurring at the lateral boundaries of the cavities need to be explicitly accounted for, as well as the radiation from a ring to its adjacent cavity. A detailed form of the Transfer Matrix method used in [51], where these effects are accounted for, is expected to give better results, although this was not implemented here. The Finite Element method would also be expected to provide more accurate predictions, and, therefore, Finite Element models were implemented for both the linear and quadratic waveguides, as presented in Appendix K. However, the results from these models were very different from the experimental ones, most likely due to some unidentified error in the modelling. Finally, it should be pointed out that the experimental arrangement in [3], even though it provides some absorption, is still a poor approximation to an ideal anechoic termination.

Chapter 4

The cochlea as a non-uniform waveguide

4.1 Introduction

The auditory system is responsible for transforming acoustic signals into perceived sound. Two remarkable features of human hearing are the very large dynamic range of perceivable, non-damaging sound levels, which is about 130 dB, and the frequency selectivity, with a wide audible spectrum ranging over about ten octaves, and a perceivable resolution of about 0.3% of an octave [14]. A central role in the hearing processes is played by the cochlea, a complex organ of the inner ear, where mechanical vibrations are transduced to neural signals. It is widely accepted that the cochlea accomplishes these tasks through the specific characteristics of dispersive waves that travel along its length [13], as observed experimentally by von Békésy [60]. These waves arise from the interaction of the fluid in the cochlea with a flexible membrane, the basilar membrane, whose stiffness varies along the length of the cochlea, producing a coupled response [13]. Therefore, the cochlea forms a non-uniform waveguide.

The waves in the cochlea slow down and build up in magnitude as they travel along its length, up to a certain position where they peak, beyond which they are greatly attenuated [13]. This characteristic position is different for different frequency components, leading to a tonotopic mapping, which consists in different frequencies being localised at different positions along the length of the cochlea [13]. Thus the sensory cells, which appear throughout the cochlear length and are linked to the auditory nerve, are excited at different positions by different frequencies [13].

It is interesting to note that apart from tonotopic mapping, the cochlea also has the property of acting as a 'black hole' as do the systems presented in Chapters 2 and 3. This is demonstrated by measurements that have been made of the acoustic input impedance of the cochlea, which is remarkably frequency-independent and almost real [61], indicating that a wave that begins to propagate in the cochlea is never reflected.

It is believed that a nonlinear active mechanism exists inside the cochlea which enhances its mechanical response at lower input levels, thus extending its dynamic range. The term 'cochlear amplifier' is often used for this active mechanism [62]. Micromechanical models of the cochlea have been implemented, incorporating active elements to account for the 'cochlear amplifier', as for example in [4]. A presentation of the modelling of the active cochlea using a nonlinear two-degree-of-freedom micromechanical model is given in Appendix B. This work was undertaken early in the PhD programme and although it resulted in a conference presentation [63], it was not pursued further and so does not fit in with the main narrative in this chapter.

Models of varying complexity and employing different mathematical formulations have been used for modelling the mechanics of the cochlea. One-dimensional models have been widely used, which are simple but still capture a large part of the functioning of the cochlea, both qualitatively and quantitatively. In such models, a wave equation is derived for the cochlear wave, the solution of which provides the pressure distribution and the basilar membrane vibration along its length. The wave equation is only solvable for a limited number of simple mathematical expressions for the micromechanical properties of the cochlea [64], so that, usually, approximate mathematical methods need to be used.

A method for obtaining approximate analytical solutions of different orders of approximation to differential equations is the WKB method [28, 27], which has been widely used in cochlear mechanics for solving the wave equation. The applicability of the WKB method formally depends on the satisfaction of certain validity conditions, the most common of which expresses the requirement that the wavenumber vary slowly along the cochlea within a wavelength [65]. The WKB method was used in [65] for solving a one-dimensional wave equation with single-degree-of-freedom micromechanics; it has also been used in two-dimensional and three-dimensional models, for example in [66] and [67], respectively.

Approximate discrete models for the continuous cochlea have also been extensively used, such as Transmission Line models [68, 69]. A mathematically equivalent method uses Finite Difference approximations for the derivatives in the wave equation and the boundary conditions [66, 70]. An extension of the Transmission Line model is the elemental model presented in [71], which accounts for more complicated effects in the cochlea. Finite Element models have also been used, as for example in [72, 73], as well as the Wave Finite Element method in [73].

For one-dimensional models, the Transmission Line approach and the Finite Difference method provide solutions for the cochlear response without being restricted by any validity condition, in contrast to the WKB method. They are, however, computationally more demanding than the WKB method, as a fine spatial mesh is required to capture the details of the model response, and matrix inversion is required for the calculation of the coupled response. The WKB method is computationally less intensive and provides analytical solutions

whose physical interpretation is usually clearer. The exceptional characteristics of the cochlea have led to its classification as a smart structure [14], which has inspired manufactured systems with similar physics, as presented for example in [74, 2, 75].

Insight into the functioning of the cochlea can be gained by analysing its response when varying a set of non-dimensional parameters. Such a parametric analysis can both extend the understanding of the cochlea and also facilitate incorporating the features of the cochlear functioning into artificial designed systems.

In this chapter, a one-dimensional model of the cochlea is considered. A general presentation of the structure and functioning of the cochlea is given in Section 4.2, including a derivation of the one-dimensional wave equation. An analysis of the general behaviour of the cochlea is then carried out based on the spatial and spectral variation of the real and imaginary parts of the wavenumber and the phase and group velocities. The formulation of the solution to the wave equation using the WKB method and the Finite Difference method is given in Section 4.3, providing the coupled response of the cochlea in terms of pressure and basilar membrane velocity.

An analysis of the dependence of the coupled response on the variation of a set of non-dimensional parameters is then presented in Section 4.5. In particular, the separate influence of the local resonance quality factor, the mass ratio and the phase-shift parameter are considered. The sensitivity of the Finite Difference model to the resolution of the spatial discretisation is also assessed. Conclusions are summarised in Section 4.6.

4.2 General structure and functioning of the cochlea

A schematic of the organs involved in the mechanical processes involved in hearing is shown in Figure 4.1. External acoustic pressure waves reach the eardrum, or tympanic membrane, where they are transformed into mechanical vibrations, which are transmitted to the fluid-filled cochlea through the three ossicles of the middle ear, namely, the incus, the maleus and the stapes. The latter is attached to the oval window of the cochlea, thus forcing the cochlear fluid into motion.

The cochlea is a snail-shaped organ in the inner ear, which is responsible for transducing mechanical vibrations induced by external sounds to neural signals that travel to the brain. A simpified drawing of a cross section of the cochlea at a given position along its length is shown in Figure 4.1b. The main features of the cochlea are outlined, including the two main fluid-filled chambers, namely, scala vestibuli and scala tympani, and the basilar membrane, which is part of the organ of Corti. The organ of Corti is a complex structure, drawn in a simplified way in Figure 4.1b, which includes the cells which are responsible for the tranduction of mechanical vibrations to neural signals [13]. At low sound pressure levels, the dynamics within the organ of Corti are complicated and give rise to a 'cochlear amplifier' which enhances the response of the cochlea. At high sound pressure levels, however, the 'cochlear amplifier' is saturated and

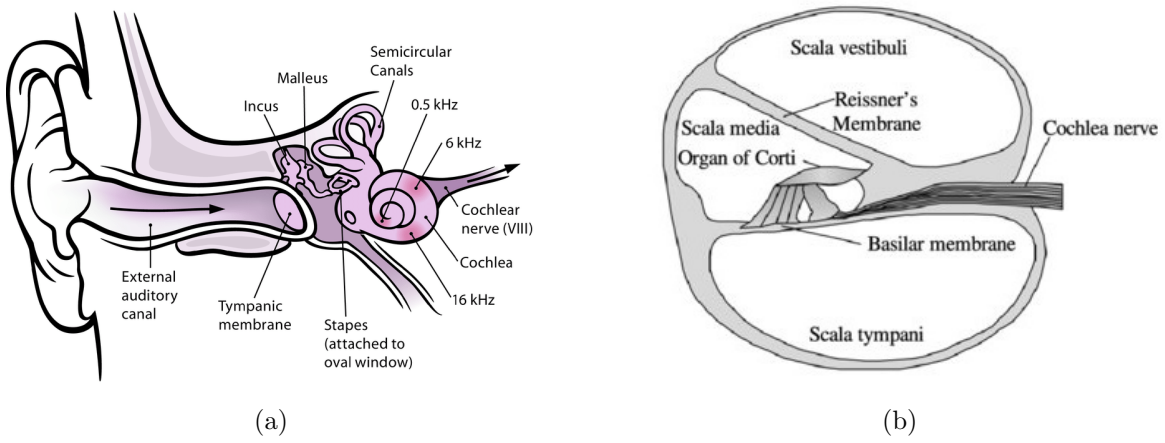

(a) (b)

Figure 4.1. (a) Overview schematic of the organs of the auditory system, illustrating the external structure of the cochlea. Image taken from Figure 1a in [76], published in an open access journal under the terms of the Creative Commons Attribution License. (b) Simplified drawing of a cross section of the cochlea, reproduced from Figure 1b in [77] with permission.

plays little part in the organ of Corti dynamics. All the parts of the organ of Corti then move together as a single mass. It is this 'passive' organ of Corti dynamics which will be mainly considered in this chapter, in order to keep the analysis analytically tractable.

A widely used three-dimensional 'box model' of the cochlea, where the coiling and longitudinal tapering are neglected, is shown in Figure 4.2a, and an even simpler one-dimensional waveguide model, which is a simplification of this, is shown in Figure 4.2b. Despite its simplicity, however, the one-dimensional version of the 'box model' displays many of the important dynamic characteristics of the cochlea. The simplifying assumptions of the uniform 'box model' are given in [78]. Reissner's membrane, scala media and the organ of Corti are omitted, and instead only the basilar membrane is shown, as representative of the mechanical properties of the structures between the two main fluid chambers, the scala vestibuli and the scala tympani [13]. The region where the oval and round windows are located is called the base, which is also used as the origin of the spatial coordinate system, and the region at the other end is called the apex, where there is an opening between the two chambers, called the helicotrema.

The system is driven by the vibration of the stapes, represented by the stapes velocity, u_{st} in Figure 4.2b, via the vibration of the oval window, which drives the fluid in the chambers into motion; the fluid in the chambers has elastic and inertial properties that are practically those of water. For the dimensions and working frequency range of the cochlea, the fluid in the chambers can be considered as incompressible [13]. Therefore, an inward movement of the fluid adjacent to the oval window at the basal end of the scala vestibuli causes an outward movement of the fluid at the round window, which is sufficiently flexible to effectively provide a pressure release boundary condition.

The excitation of the cochlear fluid by the stapes results in an average pressure, which is practically uniform along the length of the cochlea and has negligible effect in the dynamics

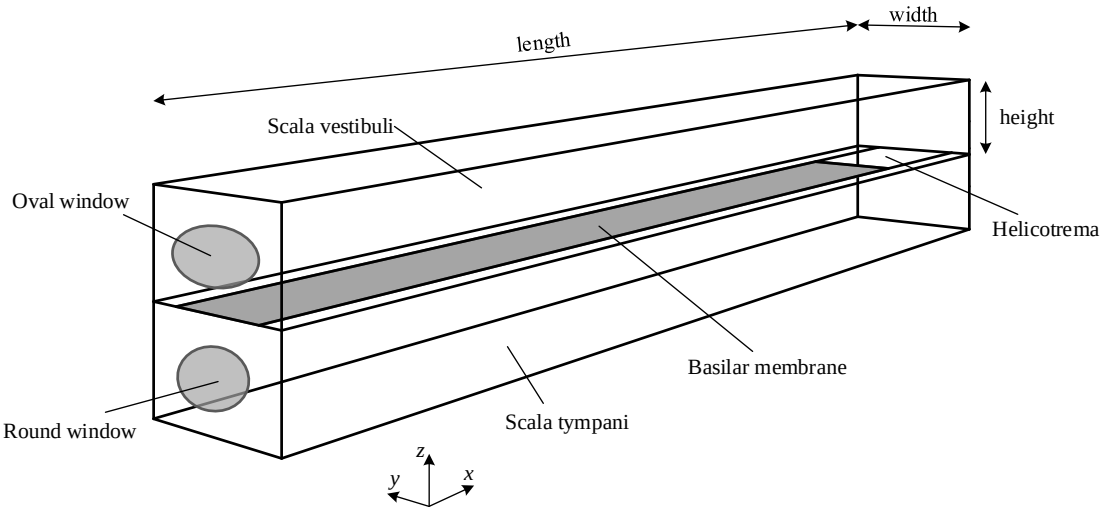

(a)

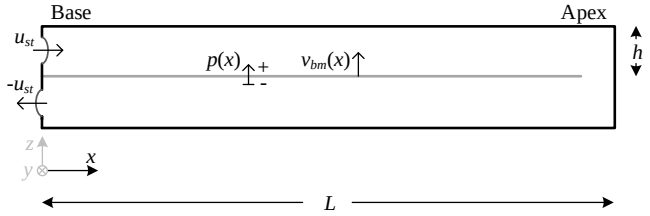

(b)

Figure 4.2. (a) Schematic of a three-dimensional 'box model' of the cochlea, drawn after Figure 1 in [4]. The two main cochlear chambers, scala vestibuli and scala tympani, are shown with the basilar membrane between them, along with the oval and round windows at the base and the helicotrema at the apex. The chamber dimensions along the directions of the coordinate system are also drawn. (b) Simple schematic of a one-dimensional 'box model' of the cochlea. The main variables are shown, namely, the pressure difference between the two chambers, p, and the transverse velocity of the basilar membrane, v_{bm}, which both vary with the longitudinal position, x, and the stapes velocity, u_{st}, which forms the input of the system, and the opposite velocity at the round window. The length of the cochlea, L, and the effective chamber height, h, are also shown, the latter defined by Equation (4.3).

of the system, and in a pressure difference between the two chambers and across the basilar membrane at any given position along the length of the cochlea [13]. This pressure difference exerts a transverse force locally on the basilar membrane, which drives it into motion. On the other hand, a transverse motion of the basilar membrane results locally in a pressure difference between the chambers. A travelling wave is generated by the interaction between the inertia of the fluid in the chambers and the stiffness of the basilar membrane [13]. The pressure difference, p, and the basilar membrane velocity, v_{bm}, are illustrated in the schematic of Figure 4.2b.

4.2.1 The one-dimensional wave equation

In the formulation of the one-dimensional wave equation, it is assumed that the pressure is uniform across each chamber, in the plane perpendicular to the basilar membrane. This assumption is practically applicable as long as the local wavelength of the travelling wave is

larger than the cross-sectional dimensions of the chambers, which holds for the case of a passive cochlea [71]. It is also assumed that no longitudinal coupling along the basilar membrane occurs, that is, its stiffness along the longitudinal direction is negligible, as the experiments by von Békékesy [60] showed no longitudinal tension in the basilar membrane [13]. Therefore, the basilar membrane is assumed to be locally reacting, so that the only mechanism for longitudinal coupling is through the surrounding fluid [13]. The wave equation can be derived either by applying the principles of continuity and momentum conservation for the cochlear fluid [13], or, equivalently, by applying Kirchoff's laws to an equivalent Transmission Line model [65].

Assuming time-harmonic dependence for all the time-varying physical quantities, proportional to $\mathrm{e}^{\mathrm{i}\omega t}$, where ω is the angular frequency, the fluid dynamics in each chamber are governed by equations describing the conservation of fluid mass and the conservation of fluid momentum,

$$u'(x) = \frac{v_{bm}(x)}{h} \tag{4.1}$$

and

$$p'(x) = -2\mathrm{i}\omega\rho u(x), \tag{4.2}$$

where $u(x)$ is the longitudinal fluid velocity, $v_{bm}(x)$ is the transverse velocity of the basilar membrane, $p(x)$ is the pressure difference, which are all complex quantities at angular frequency ω, the prime denotes the spatial derivative, ρ is the fluid density and h is the effective height of the fluid chamber. When the one-dimensional formulation is derived as a special case of the more general three-dimensional formulation, the effective height can be shown to be [71]

$$h = \frac{\pi S}{8w}, \tag{4.3}$$

where S is the cross-sectional area of each fluid chamber and w is the width of the basilar membrane, both of which are assumed here to be independent of x.

Equations (4.1) and (4.2) can be combined to give

$$p''(x) + \frac{2\mathrm{i}\omega\rho}{h} v_{bm}(x) = 0. \tag{4.4}$$

The basilar membrane velocity, $v_{bm}(x)$, depends on the pressure difference due to the locally reacting basilar membrane dynamics, so that

$$v_{bm}(x) = -Y_{bm}(x)p(x), \tag{4.5}$$

where Y_{bm} is the admittance, or mobility, of the basilar membrane at position x and the minus sign is a result of the sign conventions used for $v_{bm}(x)$ and $p(x)$, as shown in Figure 4.2b.

Substituting Equation (4.5) into Equation (4.4) results in the wave equation

$$p''(x) + k(x)^2 p(x) = 0, \tag{4.6}$$

where $k(x)$ is the wavenumber, given by

$$k(x) = \sqrt{-\frac{2\mathrm{i}\omega\rho Y_{bm}(x)}{h}}. \tag{4.7}$$

It should be noted that the pressure difference, the wavenumber, the basilar membrane velocity and the basilar membrane admittance all depend both on position and frequency; however, the corresponding notation is generally omitted in the subsequent analysis for convenience. Throughout this chapter, the pressure difference will generally be called the pressure, also for convenience.

4.2.2 Single-degree-of-freedom micromechanical model

For the wavenumber to be fully defined, a mathematical expression for the basilar membrane admittance, Y_{bm}, needs to be formulated. This can be done by looking into the details of the mechanical properties and relations of the structures between the two chambers; these properties and relations are often collectively called the micromechanics of the cochlea. In the simplest case, the passive micromechanics can be approximated by a single-degree-of-freedom mass-spring-damper mechanical system for a longitudinal element of the basilar membrane, as is done for example in [65]. More complicated micromechanical models for the active cochlea have also been used, such as a two-degree-of-freedom system [79, 4], but these will not be considered here.

The mechanical admittance of a mass-spring-damper system, as defined in Equation (4.5), can be written as [71]

$$Y_{bm} = \frac{\mathrm{i}\omega}{s + \mathrm{i}\omega r - \omega^2 m}, \tag{4.8}$$

where s and r are the stiffness and the resistance of the basilar membrane per unit area, respectively, and are functions of position, although the notation is omitted, and m is the combination of the mass per unit area of the structures between the two chambers and the mass per unit area of the adjacent fluid load that moves along with it [80]; this mass will be called the basilar membrane mass in the following analysis for convenience. The basilar membrane mass varies little along the cochlea and can therefore be reasonably modelled as being constant, $m = m_0$ [13]. Due to the variation of the stiffness, the natural frequency of the locally reacting basilar membrane also varies along the cochlea.

Following experimental measurements, the natural angular frequency of the basilar

membrane, ω_n, can be approximated as varying exponentially with position, expressed as [13]

$$\omega_n = \omega_b \mathrm{e}^{-x/l}, \tag{4.9}$$

where ω_b is the natural angular frequency at the base and l is the characteristic length of exponential decrease; the natural frequency is defined by $f_n = \omega_n/2\pi$. With a constant mass, m_0, the stiffness per unit area of the basilar membrane thus must vary as

$$s = \omega_b^2 m_0 \mathrm{e}^{-2x/l}, \tag{4.10}$$

since $\omega_n = \sqrt{s/m}$ [16]. The resistance per unit area is expressed as [71]

$$r = \frac{\omega_b m_0}{Q_0} \mathrm{e}^{-x/l}, \tag{4.11}$$

where Q_0 is the local resonance quality factor, given by [42]

$$Q_0 = \frac{\omega_n m_0}{r}. \tag{4.12}$$

The quality factor, Q_0, is assumed to be constant throughout the cochlea, which is equivalent to a constant damping factor [13]. The position which corresponds to a specific natural frequency can be derived from Equation (4.9) to be

$$x_n = l \ln \frac{\omega_b}{\omega_n}. \tag{4.13}$$

By substituting Equations (4.10) and (4.11) into Equation (4.8), also using $m = m_0$, the basilar membrane admittance is written as

$$Y_{bm} = \frac{\mathrm{i}}{\omega m_0} \frac{1}{\left(\frac{\omega_n}{\omega}\right)^2 + \mathrm{i}\frac{\omega_n}{\omega Q_0} - 1}, \tag{4.14}$$

and the wavenumber of Equation (4.7) is written as

$$k = \frac{1}{d} \frac{1}{\left[\left(\frac{\omega_n}{\omega}\right)^2 + \mathrm{i}\frac{\omega_n}{\omega Q_0} - 1\right]^{1/2}}, \tag{4.15}$$

where

$$d = \sqrt{\frac{h m_0}{2\rho}} \tag{4.16}$$

is the decay length, whose physical meaning is explained below. The wavelength is defined by

$$\lambda = \frac{2\pi}{\mathrm{Re}\{k\}}, \tag{4.17}$$

the phase velocity by

$$c_{ph} = \frac{\omega}{\mathrm{Re}\{k\}} \tag{4.18}$$

and the group velocity by

$$c_{gr} = \frac{\mathrm{d}\omega}{\mathrm{d}(\mathrm{Re}\{k\})}. \tag{4.19}$$

4.2.3 Simulations for the wavenumber, the propagation velocities and the effective length

By substituting Equation (4.9) into Equation (4.15), the wavenumber can be written as

$$k = \frac{1}{d}\frac{1}{\left[\mathrm{e}^{-2\left(\frac{x}{l}+\ln\frac{\omega}{\omega_b}\right)} + \frac{\mathrm{i}}{Q_0}\mathrm{e}^{-\left(\frac{x}{l}+\ln\frac{\omega}{\omega_b}\right)} - 1\right]^{1/2}}. \tag{4.20}$$

It can be seen that the wavenumber has the same dependence on position normalised by the characteristic length, as it has with logarithmic frequency normalised by the basal natural frequency, a property which is called 'scaling symmetry' [81]. Either at high frequencies with a fixed position or at apical positions, that is, at a large distance from the stapes, for a fixed frequency, the wavenumber asymptotes to

$$k \to -\frac{\mathrm{i}}{d}. \tag{4.21}$$

In this region, the wave is thus evanescent. Equation (4.21) justifies the role of d as a decay length. It can also be deduced from Equation (4.15) that, at low frequencies, for a given position not too far from the base, the wavenumber becomes

$$k \approx \frac{\omega}{\omega_n d} = k_b, \tag{4.22}$$

and, by also using Equations (4.18) and (4.19), it can be deduced that at low frequencies the phase and group velocities become

$$c_{ph} \approx c_{gr} \approx \omega_n d = c_b. \tag{4.23}$$

Using Equation (4.9) for ω_n, the spatial dependence of these limiting quantities can be written as

$$k_b = \frac{\omega}{\omega_b d}\mathrm{e}^{x/l} \tag{4.24}$$

and

$$c_b = d\omega_b \mathrm{e}^{-x/l}. \tag{4.25}$$

Table 4.1 presents the values of the parameters used for the model of the passive human cochlea. The value of 2 for the local resonance quality factor, Q_0, is chosen for the passive

cochlear model, which is close to the value used in [71]. The value for the characteristic length is taken from [71], and it gives a good approximation for the mapping of natural frequencies along the cochlear length, starting from a natural frequency of $f_b = 20$ kHz at the base, and giving a natural frequency of 135 Hz at the apex. The latter is higher than the lowest audible frequency for healthy humans, which is close to 20 Hz. However, due to the differences in the response of the cochlea close to the apex compared to close to the base, as observed for example in [82], the accuracy of the model at the lower frequency end is expected to deteriorate, and the difference in the natural frequency at the apex should not compromise the general facility of the model, which is used nearer the base.

Model parameter	Value	Model parameter	Value
Cochlear length (L)	35 mm	Fluid density (ρ)	1000 kg·m^{-3}
Effective chamber height (h)	4 mm [71]	Mass per unit area (m_0)	0.3 kg·m^{-2} [80]
Characteristic length (l)	7 mm [71]	Base natural ang. freq. (ω_b)	$2\pi \cdot 2 \cdot 10^4$ rad·s^{-1}
Decay length (d)	0.77 mm	Quality factor (Q_0)	2

Table 4.1. Nominal parameters for the passive human cochlea.

The real and imaginary parts of the wavenumber, and the wavelength, are plotted as a function of position along the cochlea in Figure 4.3a, for an excitation frequency of 1.65 kHz; the phase and group velocities are plotted for the same configurations in Figure 4.3c. It can be seen that the real part of the wavenumber builds up as the wave propagates along the cochlea, according to Equation (4.24) for positions near the base, until it reaches a maximum, which also corresponds to the minimum wavelength and minimum phase velocity, at a position denoted by a dotted vertical line. Both the phase and group velocities decrease approximately exponentially at the basal region, as implied by Equation (4.25).

The imaginary part of the wavenumber plotted in Figure 4.3a starts from approximately zero at the base and starts to increase, in absolute terms, at a position slightly basal to the position of minimum wavelength, at which point it has reached a large negative value; beyond this point, the imaginary wavenumber retains large negative values. Therefore, the cochlear wave slows down as it propagates through the cochlea until it reaches a point of minimum velocity, beyond which it is greatly attenuated. At the position of minimum wavelength, the group velocity changes from $+\infty$ to $-\infty$, and then retains negative values, which results from strong dispersion, so that the group velocity ceases to represent energy propagation beyond this point [83].

The real and imaginary parts of the wavenumber, as well as the wavelength, are plotted as a function of logarithmic frequency in Figure 4.3b, for a distance of 17.5 mm along the cochlea from the stapes, and the phase and group velocities are plotted in Figure 4.3d for the same configurations. The plots for the real and imaginary parts of the wavenumber, and for the wavelength, are identical to those against the linear cochlear length shown in Figure 4.3a,

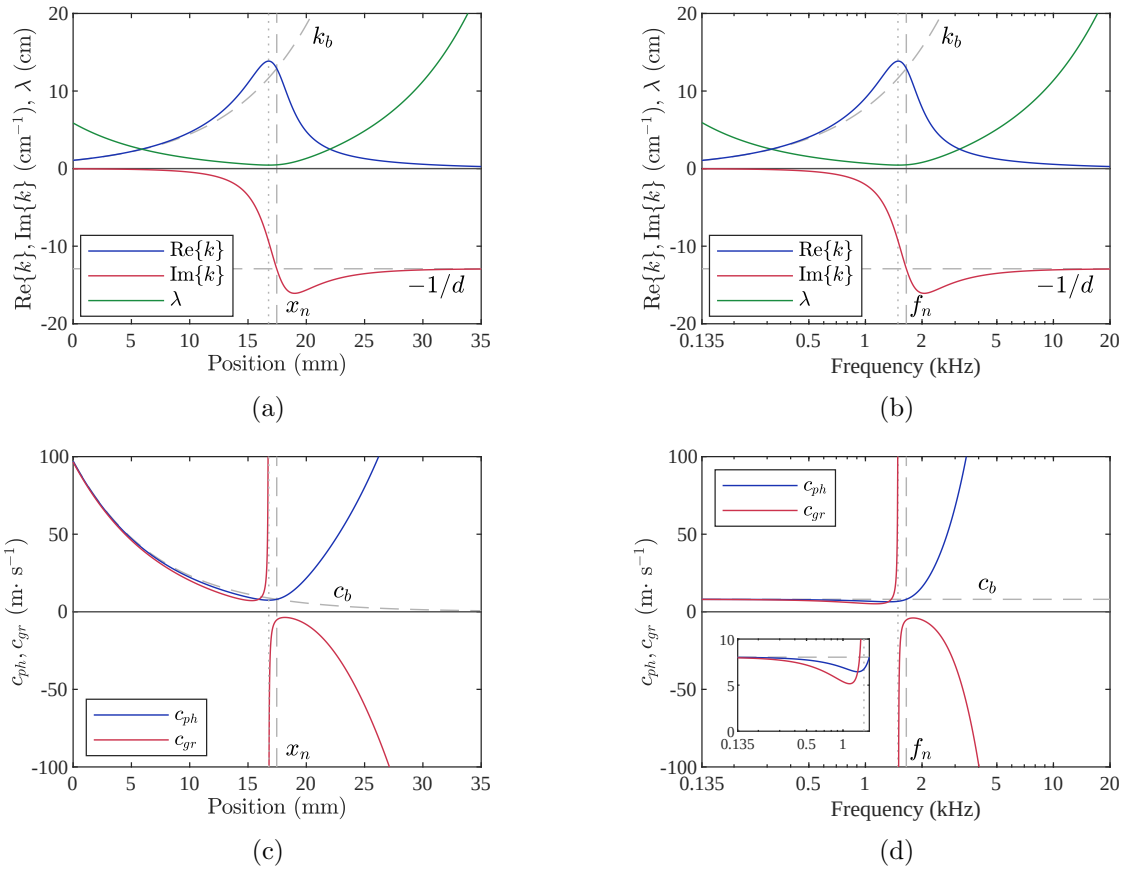

Figure 4.3. Real and imaginary parts of the wavenumber, along with the wavelength, (a) for an excitation frequency of 1.65 kHz, plotted against position and (b) at position 17.5 mm, plotted against frequency. Phase and group velocity (c) for an excitation frequency of 1.65 kHz, plotted against position, and (d) at position 17.5 mm, plotted against frequency, including a detail at low frequencies. In (a) and (c), the dashed vertical line corresponds to the position with natural frequency 1.65 kHz. In (b) and (d), the dashed vertical line corresponds to the natural frequency at 17.5 mm. In all plots, the dotted vertical line corresponds to the position of discontinuity of the group velocity, which coincides with the position of minimum wavelength and maximum real part of the wavenumber. The dashed curves and the dashed horizontal lines denote asymptotic behaviours. The specific excitation frequency has been chosen for illustrational purposes, so that it occurs at the middle of the logarithmic spectrum used, and so that the position with that natural frequency also occurs at the middle of the linearly plotted cochlear length.

due to the scaling symmetry suggested by Equation (4.20) and the specific choice of excitation frequency and observation position, so that the natural frequency, f_n, and its corresponding position, x_n, appear at the same location in their corresponding axes. Therefore, corresponding conclusions can be drawn for the variation of the real and imaginary parts of the wavenumber and for the variation of the wavelength with increasing frequency, as was done for increasing distance from the stapes.

The phase and group velocities plotted against frequency in Figure 4.3d follow different variational patterns compared to those against position of Figure 4.3c, due to the dependence of the phase and group velocities on frequency with respect to the wavenumber, as can be seen in Equations (4.18) and (4.19). It can be seen more clearly in the small enclaved plot in Figure 4.3d that at low frequencies, both velocities tend to a specific value, $c_b = \omega_n d$, according to Equation (4.23). As frequency increases, the velocities decrease, until they reach a frequency

where the phase velocity reaches a minimum and the group velocity shifts from $+\infty$ to $-\infty$. At higher frequencies, the phase velocity obtains very high values and the group velocity is negative, due to intense dispersion. From Figures 4.3b and 4.3d, it can be concluded that at a given position along the cochlea, frequencies up to a frequency slightly lower than the natural frequency for this position can propagate, whereas higher frequencies are attenuated.

The position where the wavelength becomes minimum is the position where the real part of the wavenumber peaks, as implied by Equation (4.17). It can be seen in Figure 4.3a that this position, denoted by a dotted vertical line, is very close to x_n, denoted by a dashed vertical line. Therefore, the minimum wavelength can be approximated by

$$\lambda_{min} \approx \frac{2\pi}{\mathrm{Re}\{k(x_n, \omega_n)\}}. \tag{4.26}$$

At x_n, where the excitation frequency corresponds to the natural frequency, the wavenumber of Equation (4.20) takes the value

$$k(x_n, \omega_n) = \frac{1}{d}\sqrt{\frac{Q_0}{2}}(1 - \mathrm{i}), \tag{4.27}$$

so that the minimum wavelength becomes

$$\lambda_{min} \approx 2\pi d\sqrt{\frac{2}{Q_0}}. \tag{4.28}$$

An effective length can be defined by equating the travel time of a narrowband pulse at a given frequency from the base to the position of minimum, positive, group velocity with the travel time of a narrowband pulse at the same frequency along a uniform model whose basilar membrane stiffness is constant and equal to the basilar membrane stiffness at the base of the original model. The effective length is defined as the length of the equivalent uniform model. The travel time of a narrowband pulse from the base to the position of minimum group velocity is given by

$$t_c = \int_0^{x_m} \frac{\mathrm{d}x}{c_{gr}} \tag{4.29}$$

where x_m is the position of minimum group velocity, which varies with frequency. The travel time along the equivalent uniform model is given by

$$t_u = \frac{l_{eff}}{c_{gr,u}}, \tag{4.30}$$

where l_{eff} is the effective length and $c_{gr,u}$ is the group velocity in the uniform model, which is equal to the group velocity at the base in the model here. Equating the two travel times given

by Equations (4.29) and (4.30) gives the effective length as

$$l_{eff} = c_{gr,u} \int_0^{x_m} \frac{\mathrm{d}x}{c_{gr}}. \tag{4.31}$$

A normalised effective length can also be defined with respect to the position of minimum group velocity as

$$L_{eff} = \frac{l_{eff}}{x_m}. \tag{4.32}$$

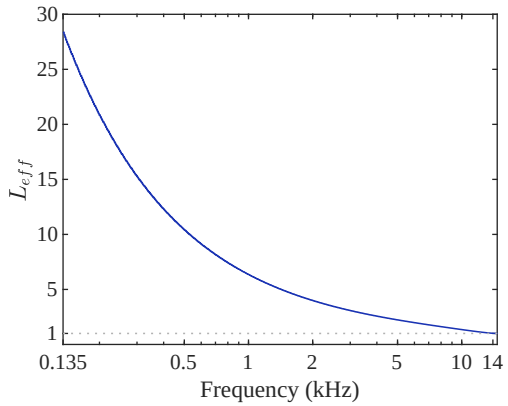

Figure 4.4. Normalised effective length of the cochlear model, plotted against frequency. The dotted horizontal line corresponds to a value of 1.

A plot of the normalised effective length against frequency is shown in Figure 4.4. The uppermost part of the working frequency range is not shown, since the minimum of the group velocity is not well defined there. It can be seen that the normalised effective length is larger than one over the plotted frequency range. This means that the non-uniform properties of the cochlea manifest an effectively longer waveguide compared to a uniform waveguide of length x_m, since in the cochlea the wave slows down as it propagates from the base to the position of minimum group velocity and therefore it takes longer for a wave to travel along this distance. It can also be observed in Figure 4.4 that the effective length is larger at lower frequencies and gradually decreases with increasing frequency. This can be linked to the larger phase shift in the coupled response at lower frequencies, as will be seen below.

4.3 Methods for solving the wave equation

The pressure along the cochlea can be calculated by solving Equation (4.6). The basilar membrane velocity can then be obtained using Equation (4.5). In this section, two methods for solving the wave equation are presented, an analytical and a numerical one, namely, the WKB method and the Finite Difference method.

4.3.1 The WKB method

Equation (4.6) can be identified as a form of the one-dimensional Schrödinger equation, as discussed in the Appendix Section C.2.1. For a constant wavenumber, Equation (4.6) would reduce to the Helmholtz equation. The Schrödinger equation has only been solved for a limited number of forms of the potential energy function [84], which corresponds to a limited number of forms for the wavenumber in Equation (4.6).

The WKB method, which was presented in Chapter 2 and described further in Appendix C, is an asymptotic method that can provide approximate analytical solutions of different orders of approximation to a differential equation of the form of Equation (4.6). The WKB validity condition, given in Equation (2.1), is re-written here,

$$\left|\frac{k'}{k^2}\right| \ll 1, \tag{4.33}$$

which requires that the wavenumber vary little along a distance of the order of the local wavelength. Plots of the left-hand side of Equation (4.33) against position for five different frequencies and against frequency for five different positions are shown in Figures 4.5a and 4.5b, respectively. It can be seen that the validity of the WKB method deteriorates at lower frequencies and at basal positions. Due to the mapping of low frequencies to apical positions and of high frequencies to basal positions, the WKB approximation for the cochlea can be considered valid for positions that are not very close to either end of the cochlear length, and for frequencies that are not very close to either end of the working spectrum, as was also mentioned in [65].

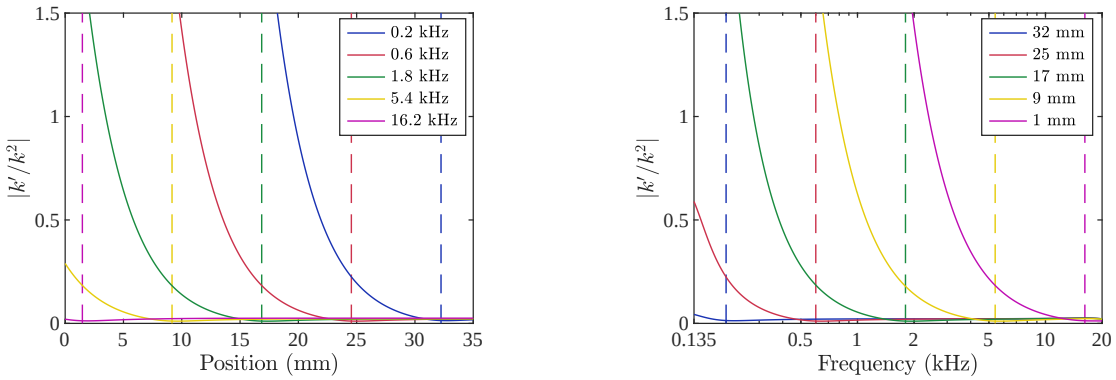

(a) (b)

Figure 4.5. WKB validity term (a) plotted against position for five different frequencies, and (b) plotted against frequency for five different positions. The vertical dashed lines correspond to the natural frequencies in (b) and to the corresponding positions in (a) for the plot lines of the same colour.

It should be clarified that the validity condition of Equation (4.33) does not provide a well-defined quantitative criterion for the accuracy of the WKB method and should not be interpreted as a comparison with the value 1, as was done in [65]. Instead, this validity condition implies that for the first-order WKB approximation to be an asymptotic solution

of the differential equation, the left-hand side of Equation (4.33) should be negligible compared to a number of the order of magnitude of one [27]; it is therefore a strict mathematical requirement in terms of the asymptotic behaviour of the WKB approximation. However, it has been shown that the WKB method may still provide good approximations when the validity condition of Equation (4.33) is not satisfied [27], or even when the properties of the system vary discontinuously [85]. A more detailed presentation of the different WKB validity conditions is given in Appendix C.

The first-order WKB solution of Equation (4.6), often simply called the WKB solution, is [65]

$$p = Ak^{-1/2}\mathrm{e}^{-\mathrm{i}\int_0^x k(\tilde{x},\omega)\mathrm{d}\tilde{x}}, \tag{4.34}$$

where A is a complex constant with respect to the spatial coordinate, which varies with frequency, $\tilde{x}$ is an auxiliary integration variable for the spatial coordinate, and the lower limit of integration in this case corresponds to the base of the cochlea; a derivation of the first-order WKB solution to Equation (4.6) is presented in the Appendix Section C.2.1. The pressure in Equation (4.34) corresponds to a positive-x travelling wave. In general, a negative-x travelling wave, which has an opposite sign in the exponent of the natural exponential, is also a solution to Equation (4.6), but it is usually omitted in cochlear mechanics, since no significant reflection occurs within the healthy cochlea [13]. It should be noted, however, that even if the backward travelling wave solution were included, the WKB method would still not account for reflections along the length of the cochlea; it would only include reflections from the helicotrema, which are not considered here. An expression for the WKB approximation to the coupled basilar membrane velocity can be derived by combining Equations (4.7), (4.5) and (4.34), yielding

$$v_{bm} = Bk^{3/2}\mathrm{e}^{-\mathrm{i}\int_0^x k(\tilde{x},\omega)\mathrm{d}\tilde{x}}, \tag{4.35}$$

where the complex amplitude is related to that of the pressure by $B = hA/2\mathrm{i}\omega\rho$.

Two boundary conditions apply to the system, one at the basal end and one at the apical end. At the base, the gradient of the pressure in the upper chamber, that is, in scala vestibuli, is equal to the stapes velocity, through momentum conservation, so that the pressure difference is related to the stapes velocity by [71]

$$p'(0) = -2\mathrm{i}\omega\rho u_{st}. \tag{4.36}$$

The helicotrema is usually taken to be a pressure release boundary, so that the pressure difference vanishes there [71], which is expressed as

$$p(L) = 0, \tag{4.37}$$

where L is the length of the cochlea. The boundary condition of Equation (4.37) is not required if only positive-x travelling waves are assumed. In the results presented in this analysis, the pressure is normalised with respect to the pressure at the base and the basilar membrane velocity is normalised with respect to the stapes velocity, u_{st}, so that an arbitrary value for u_{st} can be used as the input of the system.

The integral in the exponent of Equations (4.34) and (4.35) is in general not solvable analytically for any arbitrary form of the wavenumber. For the case of a single-degree-of-freedom micromechanical model, where the wavenumber is given by Equation (4.15), an analytical solution to this integral can be found. The WKB approximation for such a model was analytically derived in [65]. Some inconsistencies were identified in this solution and a corrected solution was derived by Marrocchio [86]. The solution by Marrocchio is expressed in terms of the ratio of the basilar membrane displacement to the stapes displacement. This is equivalent to the normalised basilar membrane velocity, defined as

$$V_{bm} = \frac{v_{bm}}{u_{st}}, \tag{4.38}$$

since in the frequency domain, both the basilar membrane and the stapes displacement and velocity are related simply by a factor $\mathrm{i}\omega$. After applying some simplifying approximations, the normalised basilar membrane velocity is written as [86]

$$V_{bm} = -\frac{16N_c}{\mu^{1/2}} \frac{\omega^2 \mathrm{e}^{-4\mathrm{i}N_c\left[\arcsin\left(\frac{\omega}{\omega_n}-\frac{\mathrm{i}}{2Q_0}\right)-\arcsin\left(\frac{\omega}{\omega_b}-\frac{\mathrm{i}}{2Q_0}\right)\right]}}{\omega_b^{1/2}\left[\omega_n^2-\left(\omega-\mathrm{i}\frac{\omega_n}{2Q_0}\right)^2\right]^{3/4}\left(2+16\mathrm{i}N_c\frac{\omega}{\omega_b}\right)}, \tag{4.39}$$

where μ is the mass ratio, defined as the ratio of the mass per unit area of the basilar membrane to the mass per unit area of the fluid in the chambers, which is expressed mathematically as

$$\mu = \frac{m_0}{2\rho h}, \tag{4.40}$$

and

$$N_c = \frac{l}{4d} \tag{4.41}$$

is a non-dimensional parameter introduced in [65], where l is the characteristic length of the natural frequency distribution in Equation (4.9) and d is the decay length defined by Equation (4.16). Combining Equations (4.16) and (4.40), the decay length can also be expressed as

$$d = h\sqrt{\mu}. \tag{4.42}$$

A normalised pressure difference can be defined with respect to the pressure difference at the base of the cochlea as

$$P = \frac{p}{p_0}, \tag{4.43}$$

where $p_0 = p(0)$ is the pressure at the the base, which from Equations (4.5) and (4.38) can be written as

$$p_0 = -\frac{u_{st} V_{bm}(0)}{Y_{bm}(0)}, \tag{4.44}$$

where $V_{bm}(0)$ and $Y_{bm}(0)$ are the normalised basilar membrane velocity and the basilar membrane admittance both evaluated at the stapes. Combining Equations (4.5), (4.38), (4.43) and (4.44), the normalised pressure can be written with respect to the normalised basilar membrane velocity as

$$P = \frac{Y_{bm}(0) V_{bm}}{V_{bm}(0) Y_{bm}}, \tag{4.45}$$

By substituting the normalised basilar membrane velocity from Equation (4.39) into Equation (4.45), the normalised pressure is written as

$$P = \frac{8\mathrm{i}\rho l Y_{bm}(0)}{V_{bm}(0)} \frac{\omega \left(\omega_n^2 + \frac{\omega\omega_n}{Q_0} - \omega^2\right) \mathrm{e}^{-4\mathrm{i}N_c \left[\arcsin\left(\frac{\omega}{\omega_n} - \frac{\mathrm{i}}{2Q_0}\right) - \arcsin\left(\frac{\omega}{\omega_b} - \frac{\mathrm{i}}{2Q_0}\right)\right]}}{\omega_b^{1/2} \left[\omega_n^2 - \left(\omega - \mathrm{i}\frac{\omega_n}{2Q_0}\right)^2\right]^{3/4} \left(2 + 16\mathrm{i}N_c \frac{\omega}{\omega_b}\right)}. \tag{4.46}$$

4.3.2 The Finite Difference method

Equation (4.6) can be solved numerically by approximating the derivatives in Equations (4.6) and (4.36) by their Finite Difference equivalent forms, as is presented for example in [71], which is equivalent to a Transmission Line model. The cochlea is spatially discretised by dividing its length into $N-1$ equally spaced elementary segments, thus defining a spatial vector of length N as $\mathbf{x} = [x_1, x_2, \ldots x_N]^{\mathrm{T}}$, where $x_1 = 0$ and $x_N = L$. All quantities that vary with position are evaluated at the discrete set of positions defined by the elements of the spatial vector.

The Finite Difference form of Equation (4.6) is

$$\frac{p_{n-1} - 2p_n + p_{n+1}}{\Delta} + \Delta k_n^2 p_n = 0, \tag{4.47}$$

where $\Delta = L/(N-1)$ is the element length and k_n is the wavenumber at the n-th element, calculated with Equation (4.7) for $x = x_n$. Equation (4.47) holds for $2 \leq n \leq N-1$. The boundary condition at the stapes, expressed by Equation (4.36), is written in Finite Difference form as

$$\frac{p_2 - p_1}{\Delta} = -2\mathrm{i}\omega\rho u_{st}. \tag{4.48}$$

Equations (4.47) and (4.48), along with the boundary condition at the helicotrema, expressed

as $p_N = 0$, can be written in matrix form as

$$\begin{bmatrix} -\frac{1}{\Delta} & \frac{1}{\Delta} & 0 & \dots & & & 0 \\ \frac{1}{\Delta} & -2\left(\frac{1}{\Delta}+\Delta k_2^2\right) & \frac{1}{\Delta} & 0 & \dots & & 0 \\ 0 & \frac{1}{\Delta} & -2\left(\frac{1}{\Delta}+\Delta k_3^2\right) & \frac{1}{\Delta} & 0 & \dots & 0 \\ \vdots & & & \ddots & & & \\ 0 & \dots & & & \frac{1}{\Delta} & -2\left(\frac{1}{\Delta}+\Delta k_{N-1}^2\right) & \frac{1}{\Delta} \\ 0 & \dots & & & & 0 & \frac{1}{\Delta} \end{bmatrix} \begin{bmatrix} p_1 \\ p_2 \\ \\ \vdots \\ \\ p_N \end{bmatrix} = \begin{bmatrix} -2\mathrm{i}\omega\rho u_{st} \\ 0 \\ \\ \vdots \\ \\ 0 \end{bmatrix}, \tag{4.49}$$

which, in compact form, can be written as

$$\mathbf{M}\mathbf{p} = \mathbf{u}_{st}. \tag{4.50}$$

The coupled pressure distribution for a given frequency and stapes excitation is then obtained by left multiplying both sides of Equation (4.50) with the inverse of the system matrix $\mathbf{M}$. The n-th element of the basilar membrane velocity vector can be calculated from the respective pressure element, since, using Equation (4.5), $v_{bm,n} = -Y_{bm,n}p_n$. The vector of normalised basilar membrane velocities can then be calculated with Equation (4.38).

It should be noted that the Finite Difference method requires matrix inversion, which can often be computationally demanding, although for the simple one-dimensional model used here, this does not impose serious limitations due to its tridiagonal form. Nevertheless, the analytical solution provided by the WKB method is computationally much faster.

4.4 Results from simulations of the coupled response

Results for the normalised pressure calculated both with the Finite Difference method, with $N = 500$ elements, and with the WKB method are shown in Figure 4.6. In Figures 4.6a and 4.6c, the modulus and phase of the normalised pressure are plotted against position for three different frequencies, and in Figures 4.6b and 4.6d, the respective quantities are plotted against frequency at three different positions. It can be seen that the pressure modulus predicted by the model for the passive cochlea decreases monotonically both with position and frequency, at a slow rate at first, until it reaches a specific position or frequency, respectively, beyond which it decreases rapidly.

The position and the frequency beyond which the pressure starts to decrease rapidly in Figures 4.6a and 4.6b are smaller than the position x_n, which corresponds to natural frequency f_n, and the natural frequency, f_n, as can be seen by comparison with the vertical dashed lines

in the figures, and also smaller than the corresponding position and frequency of maximum real part of the wavenumber, denoted by dotted vertical lines. This complies with the position and frequency of peak basilar membrane velocity response, which also occurs before the position or frequency of maximum real wavenumber, as will be seen below. The phase shift in Figures 4.6c and 4.6d accumulates up to a point beyond the position x_n, or the corresponding natural frequency, f_n, beyond which it stabilises, or even increases in the frequency response, although the pressure is already very small by this point and the phase calculation becomes unreliable.

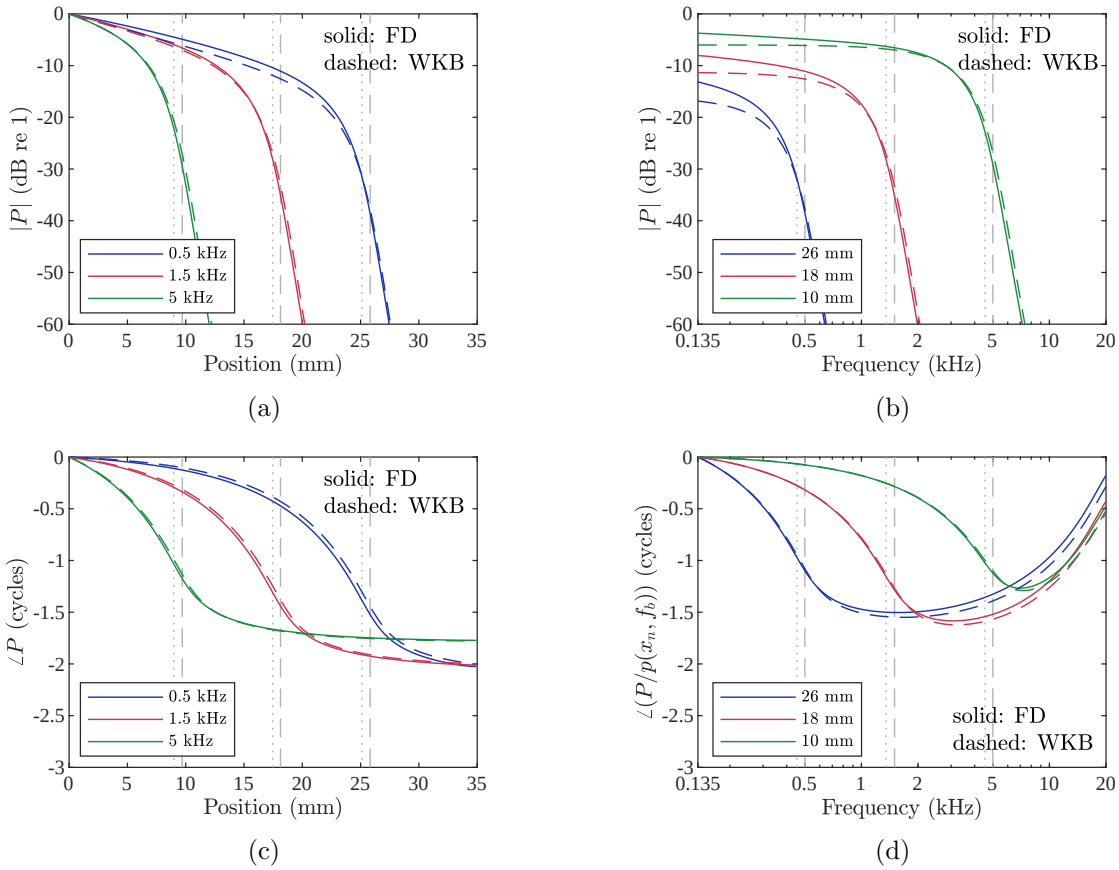

Figure 4.6. Normalised pressure (a) modulus and (c) phase plotted against position for three different frequencies. Normalised pressure (b) modulus and (d) phase plotted against frequency at three different positions. The solid-line plots are produced with the Finite Difference method and the dashed-line plots with the WKB method. The phase in (d) is also normalised with respect to the phase of the pressure at the basal natural frequency, f_b. The dotted vertical lines correspond to the positions of maximum real part of the wavenumber, as in Figure 4.3. In (a) and (c), the dashed vertical lines correspond to the positions whose natural frequency is the excitation frequency, and in (b) and (d), they correspond to the natural frequencies at the specified positions, as in Figure 4.3.

Modulus and phase plots against position and frequency are given in Figure 4.7 for the normalised basilar membrane velocity for the same parameters as used in Figure 4.6, calculated both with the Finite Difference method and with the WKB method. It can be seen in Figure 4.7a that the modulus of the basilar membrane velocity increases with position and peaks at a position basal to that of maximum real part of the wavenumber, which is denoted by the dotted vertical line. Equivalently, when plotted against frequency, the modulus of the basilar membrane velocity can be seen to increase and peak at a frequency lower than the frequency

of maximum real part of the wavenumber, also denoted by a dotted vertical line. Beyond these positions and frequencies, respectively, the modulus of the basilar membrane velocity rapidly decreases.

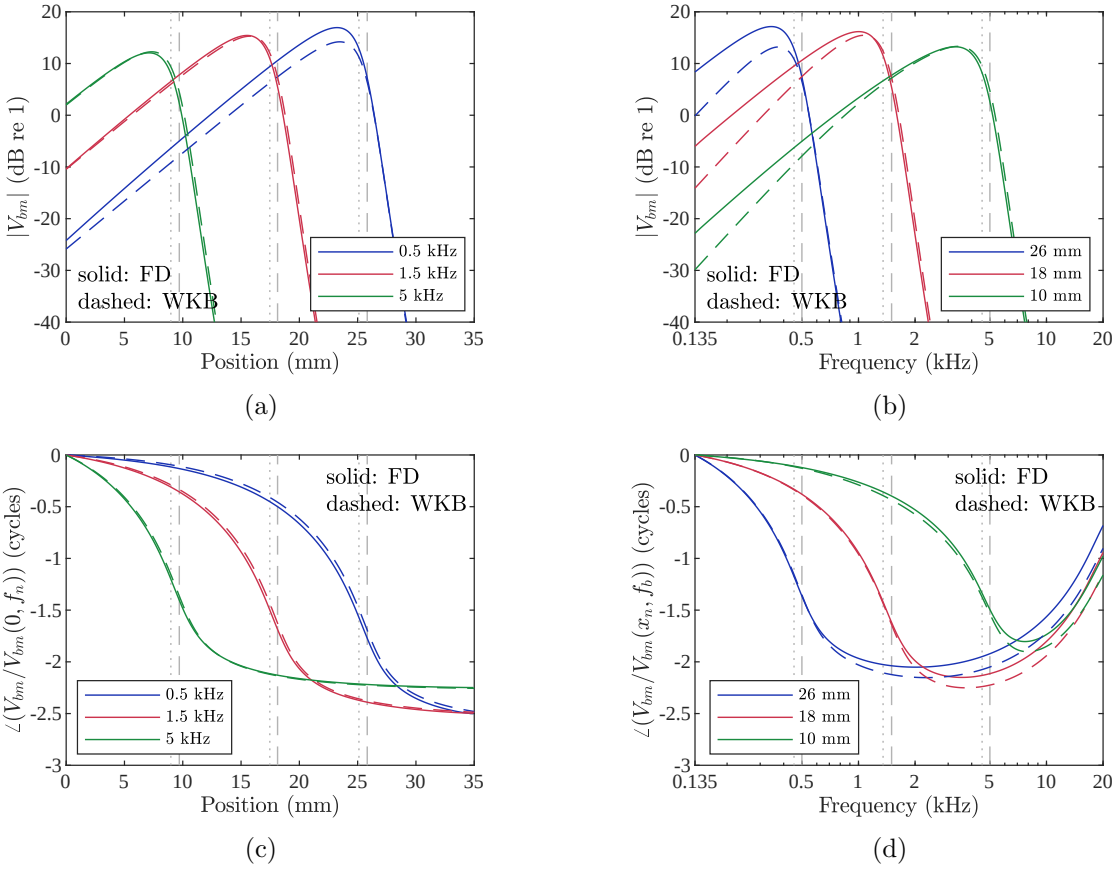

Figure 4.7. Normalised basilar membrane velocity (a) modulus and (c) phase plotted against position for three different frequencies. Normalised basilar membrane velocity (b) modulus and (d) phase plotted against frequency at three different positions. The solid-line plots are produced with the Finite Difference method and the dashed-line plots with the WKB method. The phase in (c) is also normalised with respect to the phase of the basilar membrane velocity at the base, and in (d) it is also normalised with respect to the phase at the basal natural frequency, f_b. The vertical lines are explained in the caption of Figure 4.6.

The fact that the coupled response peaks at a position basal to that of maximum wavenumber is due to the fact that the imaginary part of the wavenumber is rapidly growing in absolute terms at this region, as can be seen in Figure 4.3a, thus causing more attenuation at the position of minimum phase velocity than at positions basal to it. A corresponding conclusion can be drawn for the frequency response. The phase variation of the basilar membrane velocity is similar to that of the pressure, as can be seen by comparing Figure 4.6b with Figure 4.7b and Figure 4.6d with Figure 4.7d, although the phase accumulation is greater for the basilar membrane velocity.

The main characteristics of the cochlear coupled response are highlighted by the plots in Figure 4.7. For a given excitation frequency, the basilar membrane velocity peaks at a specific position, with low frequencies peaking at apical positions and high frequencies peaking at basal positions. Accordingly, at a given position, the basilar membrane velocity peaks at a specific

frequency. The sensory cells which induce the neural signals in the auditory nerve are included in the organ of Corti, which vibrates along with the basilar membrane, and are therefore excited at the peak position for a given frequency or at the peak frequency for a given position [13]. Thus the cochlea functions as a spatial spectrum analyser. The mapping of frequency and position does not exactly coincide with the mapping of natural frequencies along the cochlea, defined by Equation (4.9), since the peaks do not occur at the vertical dashed lines in the plots of Figure 4.7, although they occur close to them.

It can be observed in the phase plots in Figures 4.6c and 4.7c that the overall phase shift up to position x_n, both for the pressure and for the basilar membrane velocity, is larger at lower excitation frequencies. This can be linked to the fact that the effective length is accordingly larger at lower frequencies, as seen in Figure 4.4, which may allow for larger phase accumulation.

The spatial variation of the coupled basilar membrane response is plotted in Figure 4.8, calculated as $\mathrm{Re}\{V_{bm}\mathrm{e}^{\mathrm{i}\omega t}\}$, at different instances within a period for an excitation frequency of 1.5 kHz, where V_{bm} is calculated using the WKB method. The envelope of the fluctuating velocities corresponds to the modulus of the coupled response for this frequency plotted in Figure 4.7a. The linear vertical scale of Figure 4.8 illustrates the rapid decay of the response beyond the peak position.

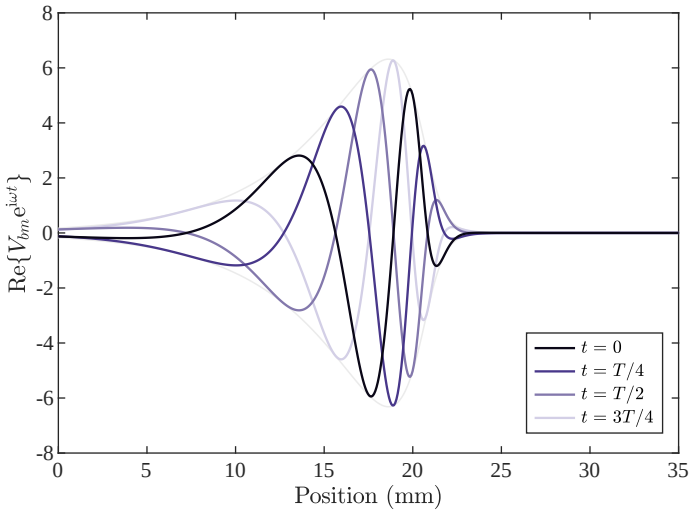

Figure 4.8. Normalised coupled basilar membrane response at different time instances within a period, calculated with the WKB method. The envelope is also shown, whose positive part corresponds to the modulus of the coupled response.

The 3-dB quality factor for the frequency response of the coupled cochlear model can be calculated from Figure 4.7b by [42]

$$Q_c = \frac{f_{ch}}{f_h - f_l}, \tag{4.51}$$

where f_{ch} is the frequency where the peak occurs, called the characteristic frequency, and f_l and f_h are the low and high frequencies, respectively, where the response drops by a factor of $1/\sqrt{2}$, that is, 3 dB, compared to the peak, which also correspond to the frequencies where the power

drops by half. It should be mentioned that the characteristic frequency is formally defined with respect to the sensitivity of the nerve fibres at different positions along the cochlea [13], and that other quality factors are also used in the cochlear literature, such as the 10-dB quality factor, where the response has fallen by 10 dB. Using the Finite Difference results, the 3-dB quality factors are found to be 1.4, 1.5 and 1.6 at positions 10, 18 and 26 mm away from the stapes, respectively. These values are different from the local resonance quality factor, Q_0, which is equal to 2 throughout the cochlea; they are also different from each other. Therefore, Q_0 does not correspond to the quality factor of the coupled response.

Comparing the WKB results, plotted in dashed lines in Figures 4.6 and 4.7, with the corresponding Finite Difference results, plotted in solid lines, it can be seen that the WKB method provides results that are similar to those with the Finite Difference method. The matching deteriorates at lower frequencies, which is expected since the WKB method is generally less valid at lower frequencies, as explained in Section 4.3.1. The Finite Difference approximation is reasonably well satisfied in these simulations since if N is increased to 1000, negligible differences are observed. In the context of this analysis, where the cochlea is approximated by a one-dimensional 'box model' with single-degree-of-freedom micromechanics, the accuracy of the WKB method can be regarded as sufficient to predict the general characteristics of the cochlear response, and can provide greater insight than the Finite Difference method.

It is apparent from the plots presented in this section that a correspondence between linear position and logarithmic frequency exists in the cochlea, as was also illustrated in Section 4.2.3. It can also be observed that the general characteristics of the response are similar, regardless of the excitation frequency when plotted against position, or regardless of the specific position when plotted against frequency. Therefore, the physical quantities in the cochlear model can also be plotted against normalised variables [81].

The natural frequency can be used to normalise the frequency, defined as

$$F_n = \frac{f}{f_n}, \tag{4.52}$$

and the respective normalised position can be defined as

$$X_n = \frac{x}{x_n}. \tag{4.53}$$

In some cases, it is helpful to normalise frequency with respect to the characteristic frequency, that is, the frequency at which the peak of the response occurs, which leads to the normalised frequency and position defined as

$$F_{ch} = \frac{f}{f_{ch}} \tag{4.54}$$

and

$$X_{ch} = \frac{x}{x_{ch}}, \tag{4.55}$$

respectively, where x_{ch} is the peak, or characteristic, position.

4.5 Parametric analysis with non-dimensional parameters

Insight into the behaviour of the cochlea can be gained by examining the variation of the coupled response of the cochlear model for different parameters. Non-dimensional parameters are particularly useful, as they do not depend on the specific model dimensions, and can therefore convey information of a more general nature. Especially relevant for this thesis is that non-dimensional parameters can facilitate the design of systems with response characteristics similar to those of the cochlea but with different dimensions and even lying within different physical contexts, as presented for an acoustic system in Chapter 5. In the figures presented in this section, quantities are plotted against normalised position and normalised frequency.

4.5.1 Dependence of the coupled response on the variation of F_{ch}

The frequency normalised with respect to the characteristic frequency, F_{ch}, defined in Equation (4.54), can be considered as an initial non-dimensional parameter. The dependence of the coupled cochlear model to this normalised frequency can be examined by letting the frequency, f, vary continuously, while choosing specific values for the characteristic frequency. A detail of the modulus of the basilar membrane velocity, normalised with respect to the stapes velocity, in the vicinity of the peak is plotted against normalised frequency in Figure 4.9a, for different positions along the cochlea, which correspond to different characteristic frequencies. The results for these plots are calculated with the Finite Difference method, to illustrate some features that are not captured accurately by the WKB approximation, as discussed below. It can be seen that the peak of the response drops as the position shifts from apical to basal. This may be linked to the fact that at greater distances from the base, the wave has more length over which to build up, although this effect saturates beyond some position, as can be seen for the two furthest points plotted. The same plots are shown in Figure 4.9b, but shifted upwards so that they coincide at the peak. It can be seen that the width of the resonance-like coupled response varies slightly with position, as was illustrated by the different coupled quality factors calculated in Section 4.4.

4.5.2 Dependence of the coupled response on the variation of Q_0

A nominal value of 2 has been used for the local resonance quality factor of the passive micromechanics. Although the functioning of the active cochlea involves more complicated dynamics within the organ of Corti than are represented by the single-degree-of-freedom model assumed here, it is still of interest to investigate the response of this simplified model with less damping. In [65], for example, a loss factor of 0.02 is used, which gives a value of $Q_0 = 50$.

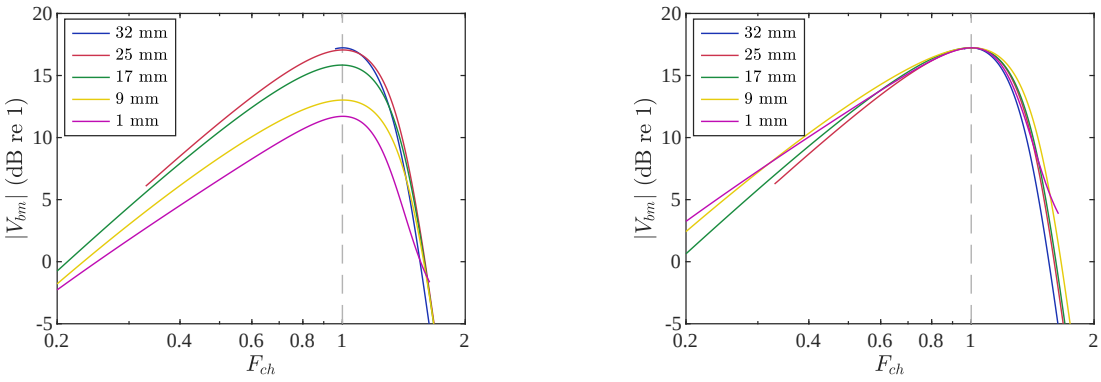

Figure 4.9. (a) Detail of the modulus of the normalised basilar membrane velocity plotted against normalised frequency, F_{ch}, at five different positions along the cochlea, calculated with the Finite Difference method. The corresponding natural frequencies at these positions are 0.2, 0.6, 1.8, 5.4 and 16.2 kHz, and the respective characteristic frequencies are 0.14, 0.41, 1.21, 3.5 and 12.2 kHz. The dashed vertical line denotes the normalised frequency $F_{ch} = 1$. The visible truncations of some of the lines is due to the normalisation of the frequency. (b) The same plots as in (a), shifted in magnitude to coincide at the peak.

The modulus of the coupled basilar membrane velocity response is plotted in Figure 4.10a against normalised position for a natural frequency of $f_n = 1.5$ kHz, which corresponds to a position 18 mm from the base, close to the middle of the cochlear length, for different values of Q_0, which are chosen to increase exponentially. The lowest value, 1, is smaller than the nominal value for passive functioning, and the highest value is chosen to be 100, which is larger than values typically used in the literature [65, 13]. It can be seen in Figure 4.10a that, as expected, the response peak becomes sharper with increasing Q_0 and it occurs at a position slightly closer to x_n, that is, the position whose natural frequency is f_n. It can also be seen that the response decay after the peak is steeper for increasing Q_0.

The modulus of the coupled response is also plotted against normalised frequency in Figure 4.10b, for a natural frequency of 1.5 kHz. The modulus variation is similar to that against normalised position, plotted in Figure 4.10a. For higher values of Q_0, the frequency response peak becomes sharper and occurs at a frequency closer to the natural frequency, and the decay beyond the natural frequency is also steeper.

In the phase plots against normalised frequency in Figure 4.10d, it can be seen that the phase shift near the natural frequency is steeper for larger values of Q_0, approximating that of a lightly damped true resonance. The phase shift predicted by the non-dimensional parameter N_c in Equation (4.41) is shown as a dotted horizontal line, where, according to [65], N_c approximately corresponds to the number of cycles of phase shift from low frequencies, much below the peak, to high frequencies, beyond the peak. It can be seen in Figure 4.10d that for a natural frequency of 1.5 kHz, which lies approximately in the middle of the logarithmic working spectrum, and for high values of Q_0, the phase shift around $F_n = 1$ is about N_c. Therefore, for a cochlear model with little damping and at the middle spectral region, it appears that the value of N_c does approximately correspond to the number of cycles of phase shift from the

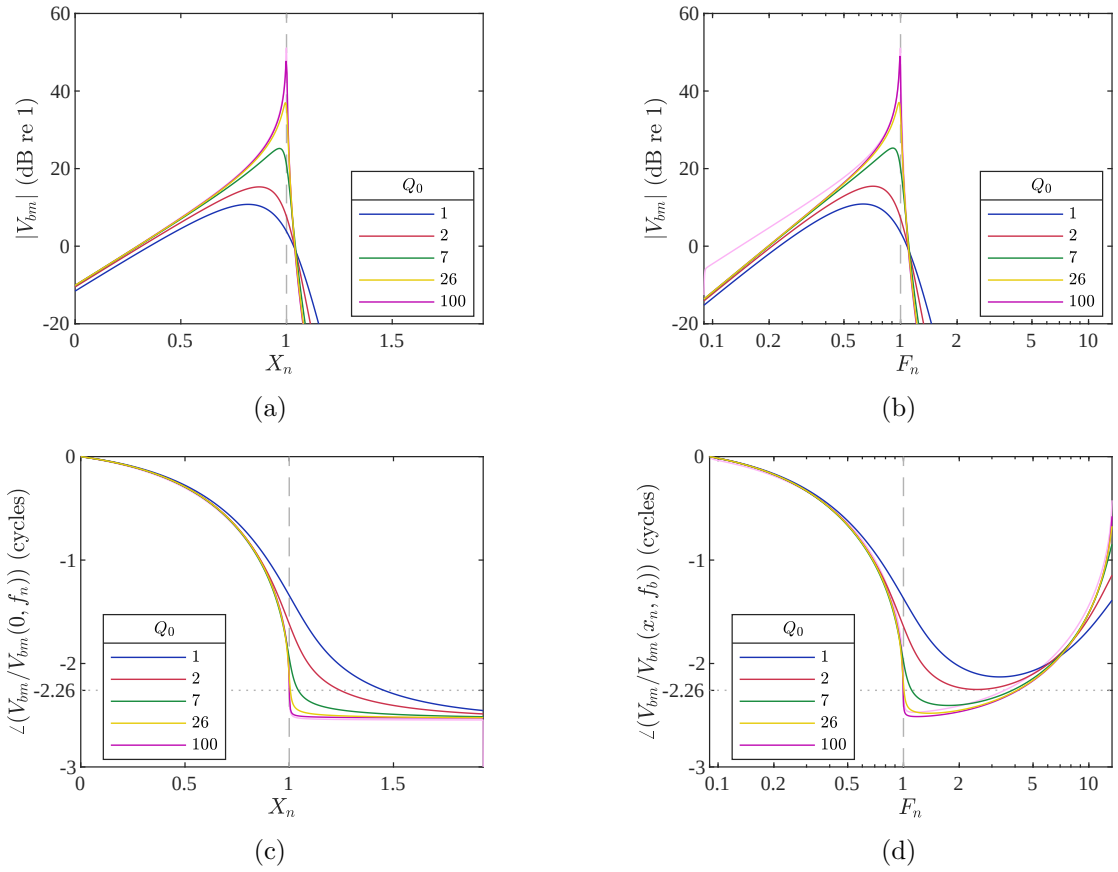

Figure 4.10. (a) Modulus and (c) phase of the normalised basilar membrane velocity plotted against normalised position with natural frequency 1.5 kHz, which occurs at $x_n = 18$ mm, for different values of Q_0. (b) Modulus and (d) phase of the normalised basilar membrane velocity plotted against normalised frequency at position $x = 18$ mm, which has natural frequency 1.5 kHz, for different values of Q_0. The chosen values of Q_0 increase approximately exponentially from a value of 1, below the nominal value of 2 for the passive cochlea, up to 100, which is taken to represent a fully active cochlea. Results are calculated with the WKB method. The Finite Difference coupled response for $Q_0 = 100$ is also plotted in pink, although this is only distinguishable from the corresponding WKB results in (b) at lower frequencies. The vertical dashed line in (a) and (c) corresponds to $X_n = 1$ and in (b) and (d) to $F_n = 1$. The dotted horizontal line in (c) and (d) denotes the opposite of the nominal value of $N_c = 2.26$.

lowest working frequency to the natural frequency. For $Q_0 = 2$, that is, for the passive case, a phase shift of $-N_c$ cycles occurs at around $2.5f_n$, however.

It was demonstrated in Section 4.4 that the quality factor Q_0, which characterises the local resonance of the basilar membrane, is different from the quality factor of the coupled response, Q_c, defined in Equation (4.51). The quality factors for the coupled response corresponding to the values of Q_0 used in Figure 4.10, starting from 1 and going up to 100, are 1.4, 1.7, 3.7, 15.4 and 53.3, respectively. It is also clear that for large values of Q_0 the coupled resonances are far from symmetrical about the natural frequency.

It was suggested in [65] that the cochlea accomplishes a compromise between low enough damping, or, equivalently, high enough Q_0, to produce a rapidly rising response up to the peak, so that it has the desired frequency selectivity, and high enough damping, or low enouh Q_0, to avoid reflections from the peak region. It can be observed, however, that the coupled response calculated with the Finite Difference method for $Q_0 = 100$, plotted in pink in Figure 4.10, is

smooth and without ripples, indicating that even for little damping, no reflections occur. The Finite Difference method was used for this result, since the WKB method does not account for reflections, as was mentioned in Section 4.3.1. This is consistent with the result in [64] that, even for very little damping, no reflections occur from the peak region, where the wave is practically localised and absorbed, similarly to the tapered elastic wedge studied in Chapter 2. Even the term 'hole' was used in [64] for the position where energy is localised and dissipated, which is reminiscent of the term 'Acoustic Black Hole', which was applied later to absorbing tapered wedges.

4.5.3 Dependence of the coupled response on the variation of μ and N_c

The mass ratio, μ, and the phase-shift parameter, N_c, defined in Equations (4.40) and (4.41), are related to each other by

$$N_c = \frac{l}{4h\mu^{1/2}}. \tag{4.56}$$

Their nominal values for the parameter values of Table 4.1 are $\mu = 0.0375$ and $N_c = 2.26$. The modulus and phase of the coupled response is plotted against normalised frequency for different values of μ and hence N_c in Figures 4.11b and 4.11d, respectively. The mass ratio, defined by Equation (4.40), is varied by varying m_0, whereas ρ and h are kept with their nominal values given in Table 4.1; the rest of the model parameters are also the nominal ones given in Table 4.1. The corresponding values of N_c are calculated with Equation (4.56). It can be seen that as the mass ratio increases, the decrease of the modulus of the coupled response becomes more gradual and, for a given value of μ, which in this case is 25 times larger than the nominal value, the coupled response becomes almost symmetrical with respect to logarithmic frequency, thus resembling a true resonance. Beyond this value of μ, the coupled response becomes asymmetric in the opposite way compared to the response with nominal μ, increasing rapidly up to a peak and then decreasing more gradually. It can also be seen that the peak frequency coincides with the natural frequency when the response is symmetric, and for higher values of μ, the peak shifts beyond the natural frequency.

Plots of the basilar membrane coupled response against normalised position are shown in Figures 4.11a and 4.11c in terms of modulus and phase, respectively. The modulus response is similar to that with respect to normalised frequency shown in Figure 4.11b. The effect of the response becoming symmetric for a large mass ratio with respect to position was also observed in [87].

In the phase plots of Figure 4.11c, it can be seen that increasing the mass ratio, μ, and, accordingly, decreasing the phase parameter, N_c, leads to less phase shift along the cochlear length. It can also be observed that the correspondence between N_c, plotted as dotted horizontal lines, and the number of cycles also depends on the values of μ.

The symmetric response, which in this case occurs for $\mu = 25\mu_{nom}$ and hence $N_c =$

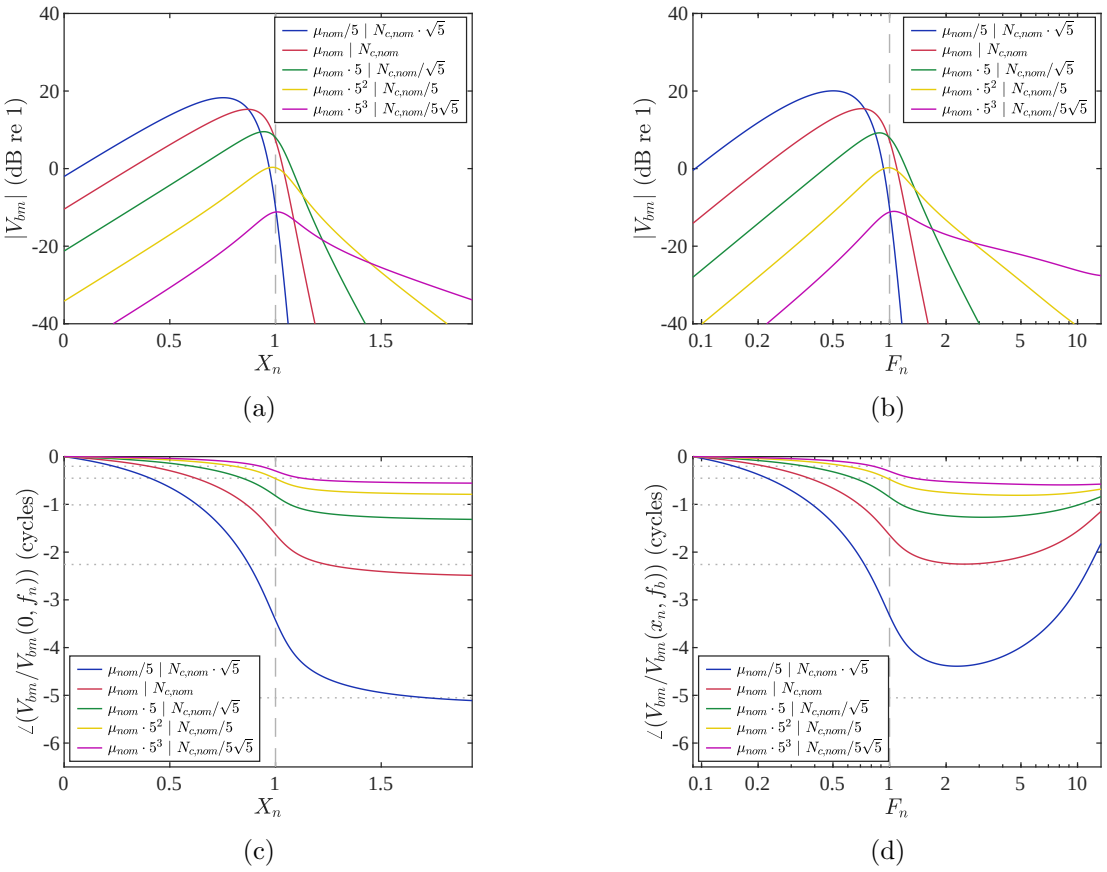

Figure 4.11. (a) Modulus and (c) phase of the normalised basilar membrane velocity plotted against normalised position with natural frequency 1.5 kHz, which occurs at $x_n = 18$ mm, for different values of μ and hence N_c. (b) Modulus and (d) phase of the normalised basilar membrane velocity plotted against normalised frequency at position $x = 18$ mm, which has natural frequency 1.5 kHz, for different values of μ and N_c. Results are calculated with the WKB method. The chosen values of μ and N_c increase and decrease exponentially, respectively. The vertical dashed line in (a) and (c) corresponds to $X_n = 1$ and in (b) and (d) to $F_n = 1$. The horizontal lines in (c) and (d) denote the opposite of the phase-shift parameter, N_c. The subscript *nom* in μ and N_c means nominal.

$0.2N_{c,nom}$, where the subscript *nom* denotes the nominal value, corresponds to the high mass ratio scenario in [87]. As described in [87], the high mass ratio results in little coupling between the fluid in the chambers and the basilar membrane, which causes the pressure to be almost uniform throught the cochlea, so that the basilar membrane vibration corresponds to a driven single-degree-of-freedom system. The small phase shift along the cochlea is also observed here in Figure 4.11c. Values for the mass per unit area of the basilar membrane, m_0, that lead to high mass ratios, however, are not reasonable given the cochlear physiology, while values for m_0 close to the nominal value used here are physiologically justified [87], so that normal cochlear functioning does involve a wave of the form described in Section 4.4.

4.5.4 Dependence of the coupled response on the variation of the length of the cochlea

A question arises in cochlear mechanics regarding the relation of the length of the cochlea and its frequency range and frequency resolution. If the cochlear length, L, is varied in a way that

the frequency range remains intact, that is, the basal and apical natural frequencies retain the values 20 kHz and 135 Hz, respectively, for the human cochlear model used here, then the characteristic length, l, has to be adjusted according to Equation (4.9), given that $f_n = \omega_n/2\pi$ and $f_b = \omega_b/2\pi$, as

$$l = \frac{L}{\ln \frac{f_b}{f_a}}, \tag{4.57}$$

where $f_a = f_n(L)$ is the apical natural frequency. Therefore, the phase-shift parameter, N_c, also changes, proportionally to l according to Equation (4.56), while μ remains unchanged, provided that m_0, ρ and h are not changed.

Figure 4.12a shows the variation of the natural frequency plotted on a logarithmic scale against position for the nominal cochlear length and for shorter lengths, and the corresponding variation of the absolute value of the spatial derivative of the natural frequency, $|f_n'| = |\mathrm{d}f_n/\mathrm{d}x|$, is shown in Figure 4.12b. It can be seen that at a given proportional position, for example at position $0.6L$ denoted by different dotted lines for the different lengths in Figure 4.12b, the absolute slope increases for smaller cochlear length. Equivalently, for a given natural frequency, the absolute slope is larger for smaller cochlear lengths, as can be seen in Figure 4.12a. Accordingly, the absolute spatial rate of change of the stiffness and the resistance of the basilar membrane, given by Equations (4.10) and (4.11), respectively, will become larger for a given natural frequency, or for a given proportional position.

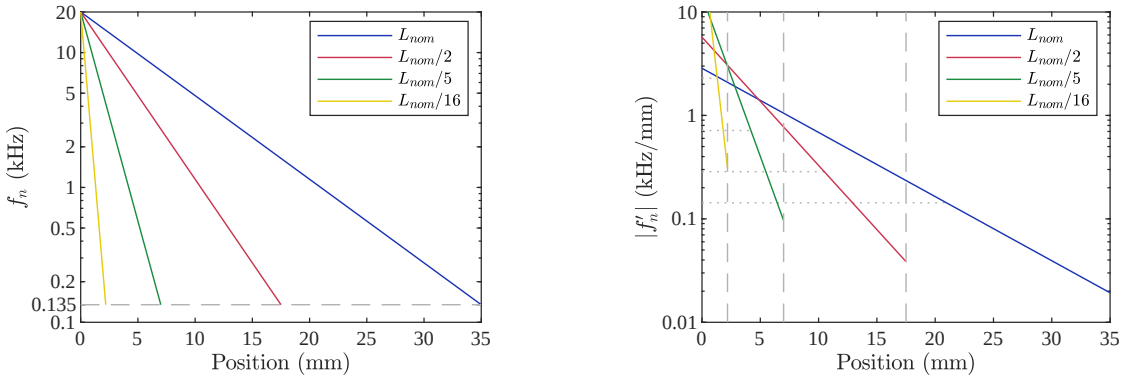

Figure 4.12. Variation of (a) the natural frequency and (b) the absolute value of the slope of the natural frequency with respect to position, plotted on a logarithmic scale against position, for different lengths of the cochlea, with the characteristic length adjusted so that the highest and lowest natural frequencies remain intact. The dashed vertical line in (a) corresponds to the lowest natural frequency, f_a. In (b), the dashed vertical lines correspond to cochlear lengths and the dotted horizontal lines correspond to natural frequency slopes at length $0.6L$ for each plot line. The subscript *nom* in L means nominal.

The effect of the change in the rate of change of the stiffness and the resistance of the basilar membrane induced by the change in the cochlear length is illustrated by the corresponding change of the coupled response. The modulus and phase of the coupled response are plotted against normalised position in Figures 4.13a and 4.13c and against normalised frequency in Figures 4.13b and 4.13d, for different cochlear lengths, where the corresponding characteristic

lengths are also adjusted by Equation (4.57) to keep the basal and apical natural frequencies unchanged, with a resultant change in N_c according to Equation (4.41). It can be observed that the variation of the response is similar to that when the mass ratio is varied, with the rest of the model parameters having their nominal values given in Table 4.1, as shown in Figure 4.11, since in both cases the variation in the physical parameter directly affects N_c.

In Figures 4.11a, 4.11b, 4.13a, and 4.13b, it can be seen that the response is symmetric when $N_c = N_{c,nom}/5$ and $L = L_{nom}/5$, respectively, since the value $L = L_{nom}/5$ corresponds to $N_c = N_{c,nom}/5$ when the other parameters are kept unchanged, as can be seen from Equations (4.56) and (4.57). Therefore, it is the variation of N_c that causes the response to change from asymmetric to symmetric to inverse asymmetric, and not the variation of the mass ratio, μ, independently of N_c and l.

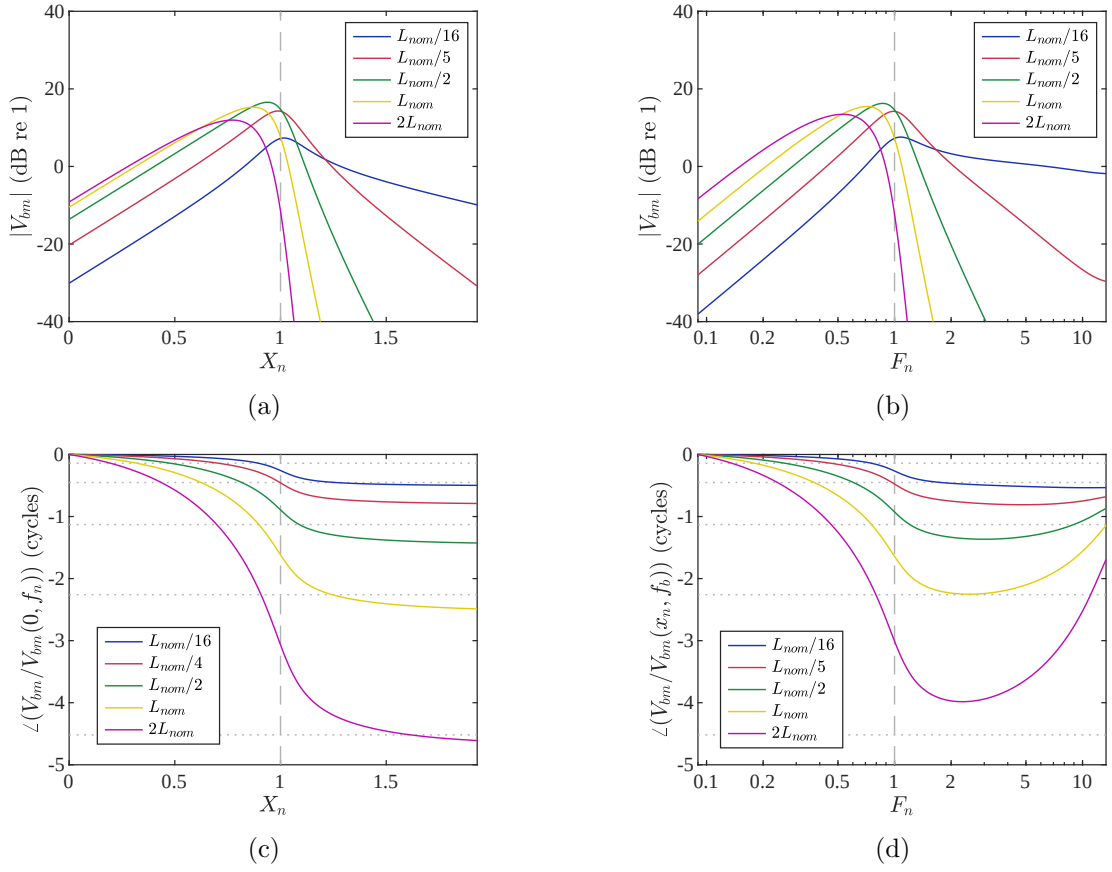

Figure 4.13. (a) Modulus and (c) phase of the normalised basilar membrane velocity plotted against normalised position with natural frequency 1.5 kHz, which occurs at $x_n = 18$ mm, for different values of L, with l adjusted to keep the basal and apical natural frequencies unchanged. (b) Modulus and (d) phase of the normalised basilar membrane velocity plotted against normalised frequency with natural frequency 1.5 kHz at position $x = 18$ mm, for different values of L, with l adjusted to keep the basal and apical natural frequencies unchanged. The results are calculated with the WKB method. The vertical dashed line in (a) and (c) corresponds to $X_n = 1$ and in (b) and (d) to $F_n = 1$. The horizontal lines in (b) denote the opposite of the phase-shift parameter, N_c. The subscript *nom* in L means nominal.

Varying the chamber effective height, h, can also cause similar variation for the coupled response, although this affects both the value of N_c and μ, as can be seen from Equations (4.56) and (4.40). From the plots in Figure 4.11 it can be concluded that the value of N_c should not

be much less that the nominal value of 2.26 for the coupled response to have the asymmetric response of the actual cochlea. Taking the plot with $N_{c,nom}/\sqrt{5}$ as a low limit, the value of N_c should not be less than 1. This gives a corresponding upper limit of approximately 0.2 for the mass ratio, if l and h have the nominal values of Table 4.1.

The fact that the mass ratio does not by itself change the form of the coupled response is illustrated in Figures 4.14a and 4.14b, where the modulus of the basilar membrane velocity is plotted against normalised position and normalised frequency, respectively. For these plots, the mass ratio is varied and the characteristic length is also varied accordingly by

$$l = 4hN_c\sqrt{\mu}, \tag{4.58}$$

in order to maintain a constant value of N_c according to Equation (4.56). The cochlear length is also adjusted using Equation (4.57) to keep the basal and apical natural frequencies intact. The form of the coupled response plotted in Figures 4.14a and 4.14b also does not change, although there is a change in amplitude. This result is also apparent from the form of the WKB solution of Equation (4.39), where the mass ratio only affects the constant amplitude of the basilar membrane velocity, as is also observed in Figures 4.14a and 4.14b. The phase variation, plotted in Figures 4.14c and 4.14d, is the same for all the corresponding combinations of values for μ and l, and also L, and it coincides with the phase variation for the nominal values shown in Figures 4.11c and 4.11d. Therefore, neither the variation of the mass ratio nor of the cochlear length affect the form of the response, if the phase-shift parameter remains unchanged.

One point that needs to be made when assuming a smaller cochlear length is that below some length, the dimensions of the discrete microstructures in the organ of Corti, for example the dimensions of the sensory cells that transduce the vibrations to neural signals, may become significant. In the models used here, the properties of the cochlea are assumed to vary continuously along its length or, for the Finite Difference method, it is assumed that the longitudinal discretisation is fine enough to approximate a continuous variation. If the cochlea is significantly shortened while the working frequency range is retained, then the same number of sensory cells will need to fit in a much smaller length to keep the same frequency resolution. This can be pictured with the help of Figure 4.12a, if it is assumed that the y-axis of natural frequencies is discretised to a number of frequencies, and that the x-axis of cochlear length is accordingly discretised to the same number of corresponding positions. If the discretisation of natural frequencies is kept unchanged, while the length is decreased for example from L_{nom} to $L_{nom}/16$, then the discrete number of positions that correspond to the nominal length will have to fit in the much smaller length, which may not be possible given the length of the discrete structures in the organ of Corti.

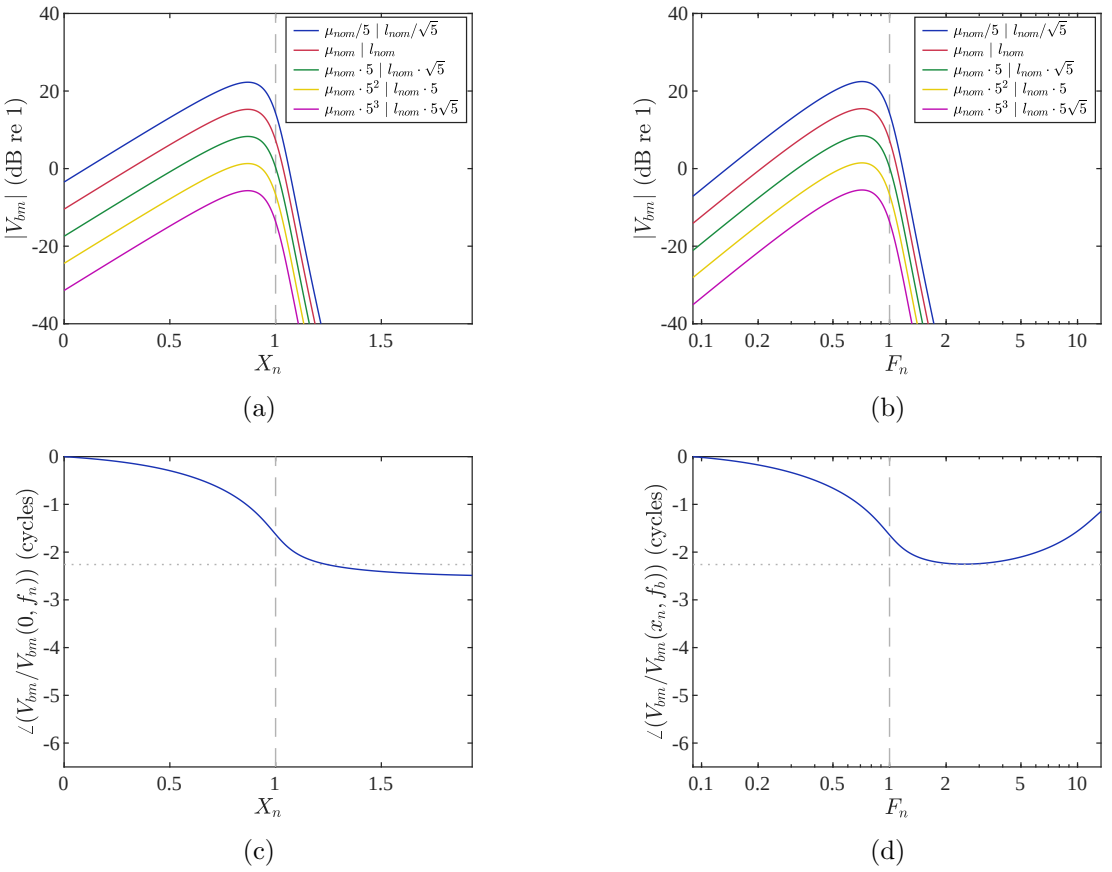

Figure 4.14. (a) Modulus and (b) phase of the normalised basilar membrane velocity for different values of μ, with l and L adjusted to keep N_c and the basal and apical natural frequencies unchanged, plotted against normalised position with natural frequency 1.5 kHz. (b) Modulus and (d) phase of the normalised basilar membrane velocity for different values of μ, with l and L adjusted to keep N_c and the basal and apical natural frequencies unchanged, plotted against normalised frequency with natural frequency 1.5 kHz. The phase variation, either with respect to normalised position or with respect to normalised frequency, is the same for the different values of μ and l. Results are calculated with the WKB method.

4.5.5 Dependence of the Finite Difference model on the discretisation

It is useful to know how fine the discretisation of the cochlear length has to be to ensure accurate results, when implementing the Finite Difference model presented in Section 4.3.2. Apart from providing a lower limit on the number of elements, which leads to less calculation time, the required resolution of discretisation can also be utilised to design discrete systems having a similar response, as is done in Chapter 5. A lower limit often used in Finite Element modelling requires at least six elements per minimum wavelength, although this also depends on the order of polynomial interpolation [40]. In the Finite Difference model used here, where the element length is constant, that is, it does not vary along the cochlea, the element length has to be compared with the minimum local wavelength. Since the quality factor, Q_0, is assumed to be constant throughout the cochlea, the minimum wavelength, which is approximately given by Equation (4.28), is also constant. A non-dimensional parameter can thus be defined as

$$\Lambda = \frac{\lambda_{min}}{\Delta}, \tag{4.59}$$

where Δ is the element length of the Finite Difference model.

The modulus and phase of the coupled basilar membrane velocity response are plotted in Figures (4.15)a and (4.15)c, respectively, using the Finite Difference method, for different values of Λ, with $Q_0 = 2$ and corresponding minimum wavelength $\lambda_{min} = 4.9$ mm. The value of $\Lambda = 70$ corresponds to $N - 1 = 499$ elements, which are sufficient even for the value $Q_0 = 100$ used in Section 4.5.2, for which the minimum wavelength is $\lambda_{min} = 0.69$ mm and the resulting discretisation ratio is $\Lambda = 10$, which corresponds to ten elements per minimum wavelength. It can be seen that six elements per minimum wavelength provide good matching with the reference solution, slightly deviating from it beyond the peak. Five elements per minimum wavelength still provide good matching, while using three elements per minimum wavelength produces significant deviation, with fluctuations in the frequency response. Using even fewer elements deteriorates the solution further, although these results are not plotted here.

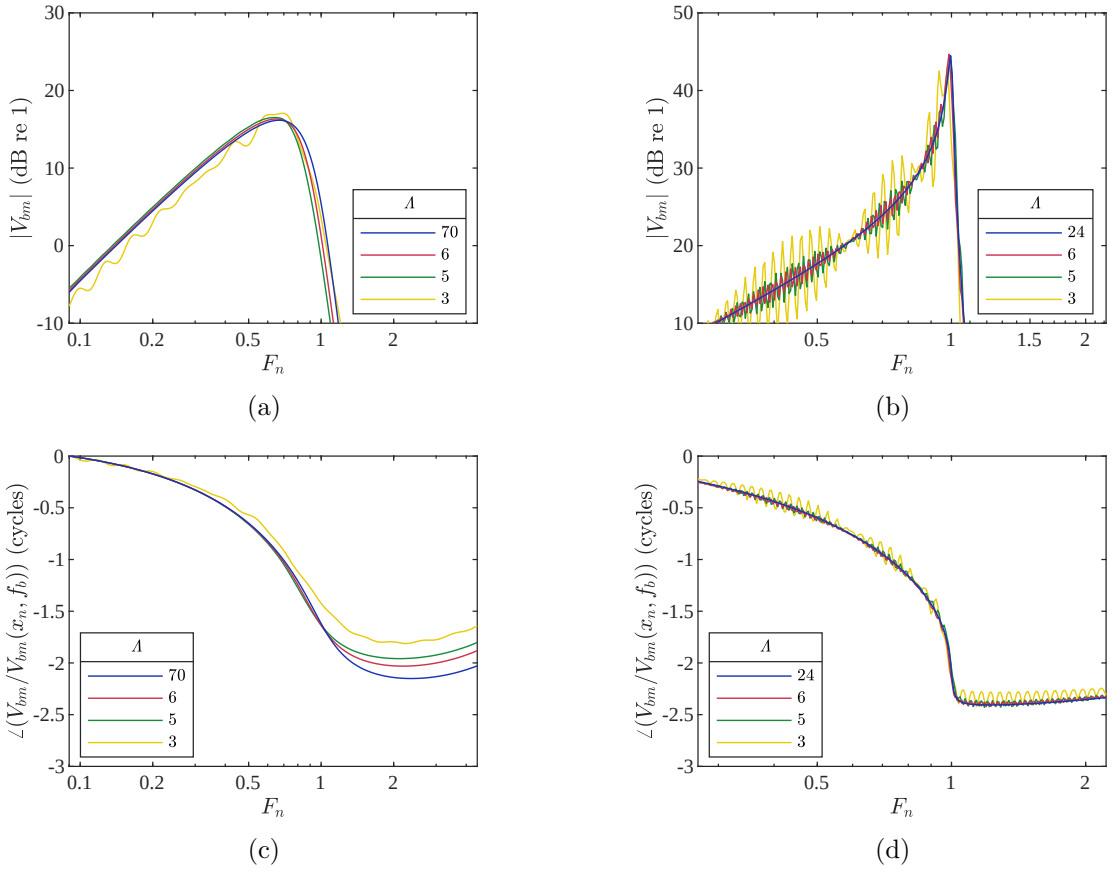

Figure 4.15. (a) Modulus and (c) phase of the normalised basilar membrane velocity plotted against normalised frequency with natural frequency 1.5 kHz, calculated with the Finite Difference method, for different values of Λ, with the nominal parameter values of Table 4.1. The reference value of $\Lambda = 70$ corresponds to 499 elements, that is, to $N = 500$ for the Finite Difference model, while $\Lambda = 6$, $\Lambda = 5$ and $\Lambda = 3$ correspond to 42, 34 and 20 elements, respectively. (b) Modulus and (d) phase of the normalised basilar membrane velocity plotted against normalised frequency with natural frequency 1.5 kHz, calculated with the Finite Difference method, for different values of Λ, with $Q_0 = 50$. The reference value $\Lambda = 24$ corresponds to 861 elements, while $\Lambda = 6$, $\Lambda = 5$ and $\Lambda = 3$ correspond to 214, 178 and 106 elements, respectively. The difference in scaling in both axes in the different plots is used to allow for more detail.

A corresponding set of plots with a high value for the resonance quality factor $Q_0 = 50$ is

given in Figures 4.15b and 4.15d. It can be seen that when six or less elements per minimum wavelength are used, some fluctuations now occur in the response, although in the phase response modulus, results appear to be respectively better than for $Q_0 = 2$ with the same values of Λ. It should be noted, however, that the minimum wavelength for all the plots in Figure 4.15 is calculated with the approximate form of Equation (4.28), which gives an overestimation of about 7% for $Q_0 = 2$ and about 12% for $Q_0 = 50$. The same quantities as in Figures 4.15b and 4.15d are plotted in Figures 4.16b and 4.16d, respectively, but with the minimum wavelength calculated by

$$\lambda_{min,ex} = \frac{2\pi}{\min\{\mathrm{Re}\{k\}\}}, \tag{4.60}$$

where the wavenumber is given by Equation (4.15), min{} denotes the minimum value of its argument and the subscript *ex* stands for exact, giving the discretisation ratio $\Lambda_{ex} = \lambda_{min,ex}/\Delta$. It can be seen that the results are slightly improved by using the exact minimum wavelength, although fluctuations are still present even for the case of $\Lambda_{ex} = 6$. In general, by comparing the coupled response with varying Λ for $Q_0 = 2$ and $Q_0 = 50$, it can be concluded that the dependence of the coupled response on Λ is slightly different for different values of Q_0, but that a value of Λ larger than 6 is still a good rule of thumb.

The modulus and phase of the coupled response with $Q_0 = 50$ for different values of Λ_{ex} are also plotted against normalised position in Figures 4.16a and 4.16c. It can be seen that when a small number of elements is used, fluctuations occur in the coupled response, which are indicative of reflections. These reflections occur due to the discontinuities between consecutive elements, as the difference of the properties of the basilar membrane between consecutive elements becomes larger with decreasing number of elements. Therefore, even though reflections do not occur at the peak of the continuous system, even for very high values of Q_0, that is, for very little damping, as shown in [64], a sufficient number of elements needs to be used for the spatial discretisation to prevent distributed reflections. Overall, however, and in view of the simplifying assumptions of the model, it can be concluded that six elements per minimum wavelength provide a reasonable approximation.

4.6 Summary and conclusions

The cochlea of the inner ear has been described in view of its functioning as a non-uniform waveguide. A simple one-dimensional 'box model' was used, which leads to the one-dimensional wave equation for the coupled cochlea, and the basilar membrane admittance is modelled with single-degree-of-freedom micromechanics. From the basilar membrane admittance, the wavenumber is obtained, from which the wavelength of the cochlear wave and the phase and group velocities are calculated. An analysis of these quantities was carried out, which

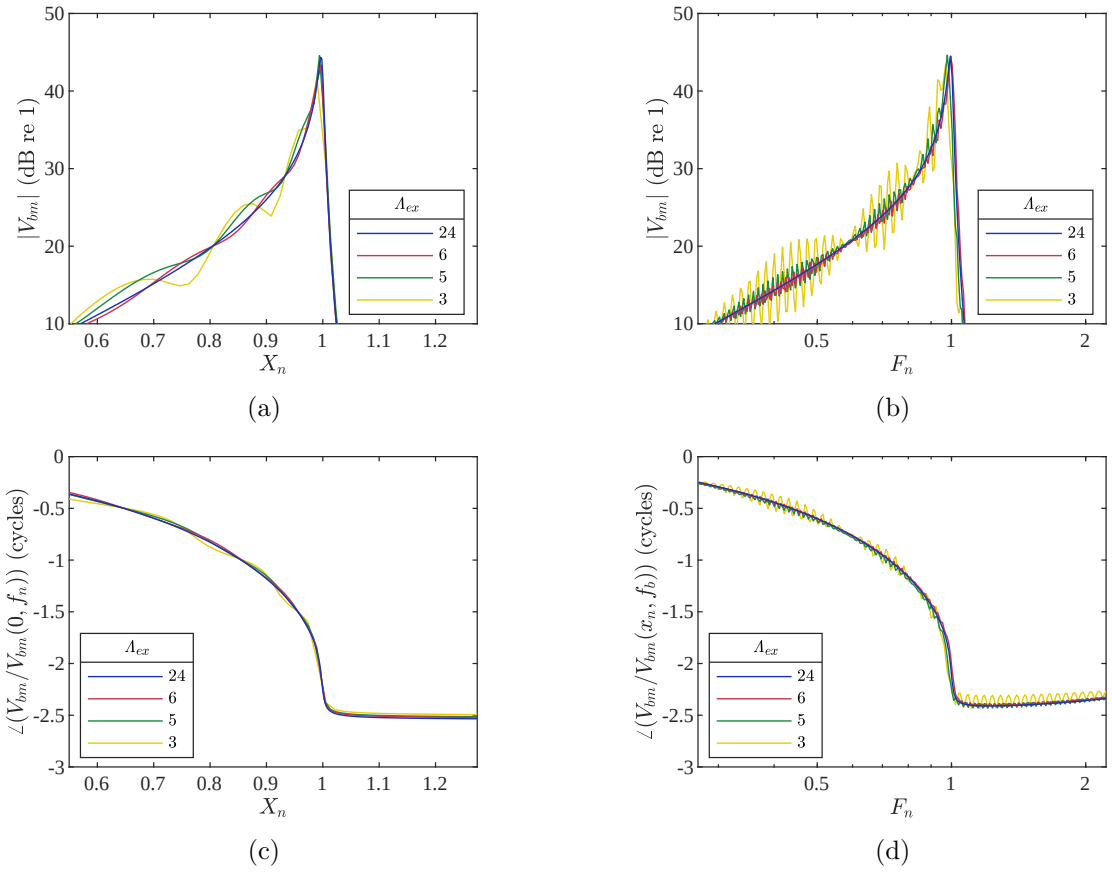

Figure 4.16. (a) Modulus and (c) phase of the normalised basilar membrane velocity plotted against normalised position with natural frequency 1.5 kHz, which occurs at $x = 18$ mm, for different values of Λ_{ex}, with $Q_0 = 50$. (b) Modulus and (d) phase of the normalised basilar membrane velocity plotted against normalised frequency at position $x = 18$ mm, which has natural frequency 1.5 kHz, for different values of Λ_{ex}, with $Q_0 = 50$. Results are calculated with the Finite Difference method.

highlighted the basic functioning of the cochlea and the symmetry between position and frequency, with the cochlear wave slowing down up to a specific position, which depends on frequency, beyond which it decays rapidly. Accordingly, at a given position, the wave slows down with increasing frequency up to a specific position-dependent frequency, beyond which it decays rapidly. The effective length was also introduced, which illustrates that the cochlea functions as an effectively longer equivalent uniform waveguide, due to the slowing down of the cochlear waves.

Two methods for obtaining the coupled response of the cochlea by solving the wave equation were presented, namely, the WKB method, which provides approximate analytical solutions, and the Finite Difference method. The WKB method gives fairly accurate results at frequencies not too close to the basal and apical natural frequencies and at positions not too near the base and the apex, as has previously been shown in the literature.

The main contribution of this chapter is a parametric analysis of the coupled cochlea conducted with respect to a set of non-dimensional parameters. It was shown that even with very little damping, no reflections occur. The correspondence of the phase-shift parameter, N_c, with the actual phase shift was shown to depend on the value of the local resonance quality

factor, Q_0. It was also shown that N_c, rather than just the mass ratio, defines the nature of the coupled response. High values of N_c produce a response with a steep cut-off and significant phase shift, as is actually observed in the cochlea. As N_c decreases, the cut-off becomes less steep, until, for a certain value of N_c, it reaches a point where it is symmetric with logarithmic frequency, thus resembling an uncoupled resonance. For even smaller values of N_c, the decay beyond the peak becomes even more gradual, and the coupled response becomes asymmetric in an inverse way compared to the typical cochlear coupled response. Varying the cochlear length while keeping the same working frequency range has a similar effect on the coupled response, whereas the variation of the mass ratio only affects the amplitude of the coupled response, if the characteristic length is adjusted to keep N_c unaltered.

The accuracy of the Finite Difference model with respect to the resolution of spatial discretisation was assessed by varying the ratio of the minimum wavelength over the element length. It was shown that the accuracy of the coupled response for the same discretisation ratio depends on the quality factor, Q_0. Poor spatial resolution with respect to the minimum wavelength was shown to lead to reflections in the predicted coupled response. In general, six elements per minimum wavelength were found to provide sufficient accuracy for the purposes of the cochlear model used.

Chapter 5

Acoustic 'rainbow' sensors

5.1 Introduction

Acoustic 'rainbow' sensors consist of arrays of units of sub-wavelength dimensions, whose properties vary with position, and, through strong wave dispersion, can enhance and spatially separate different frequency components of incident acoustic waves [2]. The sub-wavelength dimensions of the unit elements of acoustic 'rainbow' sensors and their strongly dispersive behaviour, which is not encountered in natural materials, classify them in the realm of acoustic metamaterials [88].

A one-dimensional 'rainbow' sensor consisting of narrow grooves of varying depth perforated in a rigid substrate was presented in [15]. It was demonstrated both by simulations and experimentally that incident waves slow down and get amplified as they propagate along the system, until they reach a position, which is different for different frequency components, where they are trapped; beyond this position, waves are greatly attenuated. It was shown, however, both in simulations, where losses were not accounted for, and in experiments, that the spatial envelope of the response did not vary smoothly but was uneven.

In [89], an acoustic 'rainbow' sensor with grooves of different geometry was numerically simulated and experimentally tested. The enhanced frequency response was demonstrated, where it was also shown that fluctuations of the pressure envelope occur along the spectrum. A quasi-two-dimensional system, similar to that in [15] but consisting of perforations of square cross-section over a rigid two-dimensional substrate, whose depth varies only along one dimension, was presented in [90]. Viscous and thermal losses were included in the simulations, which predicted a relatively smooth frequency response in terms of the acoustic pressure, with only shallow fluctuations with frequency.

A design consisting of a main duct of constant cross section loaded with an array of side branches consisting of Helmholtz Resonators of varying cavity volume was proposed by Zhao and Zhou [2] and is depicted in Figure 5.1a. The coiling of the system was loosely based on the form of the cochlea. Simulations predicted the 'rainbow' trapping effect, although with fluctuations

in the pressure modulus both in the spatial and spectral domain, since no losses were accounted for. A similar design of acoustic absorber, using a small number of Helmholtz Resonators, was also presented by Jimenez et al. [1], where the dimensions of both the resonators and the main duct vary with position, as shown in Figure 5.1b. The geometrical parameters of the system were numerically optimised in order to maximise the absorption over a given frequency band. Very good absorption performance was demonstrated experimentally and the enhancing and, as a side-effect, trapping of different frequency components at different resonators was predicted.

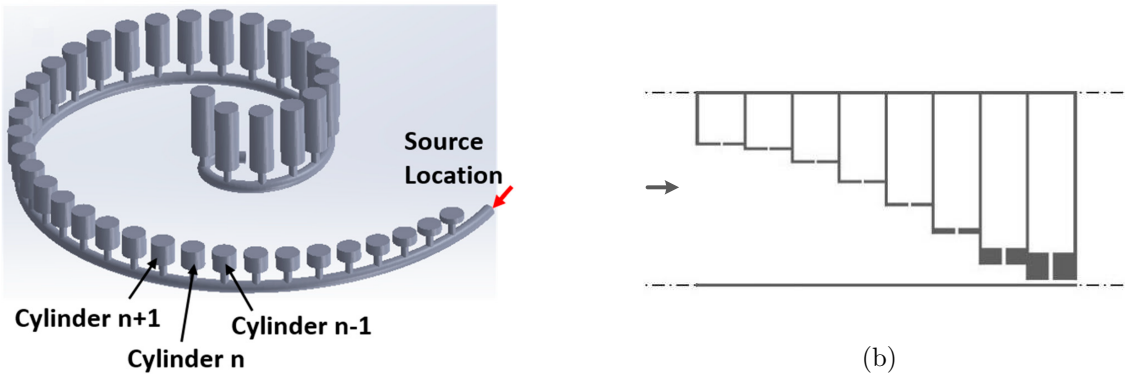

Figure 5.1. Schematics of examples of acoustic 'rainbow' sensors using Helmholtz Resonators: (a) Uniform duct with side branches of Helmholtz Resonators; the arrow shows the direction of incidence. The image is taken from Figure 1d in [2]. (b) Duct of varying height with side branches of Helmholtz Resonators; the arrow shows the direction of incidence. The image is taken from Figure 1d in [1], with the labels removed and the arrow added. Both articles [2] and [1] are published in open access under a Creative Commons Attribution 4.0 International License, https://creativecommons.org/licenses/by/4.0/.

In this chapter, a design of an acoustic 'rainbow' sensor consisting of a main duct of constant cross section with an array of side branches of Helmholtz Resonators of varying geometry is presented, based on the response characteristics of the human cochlea. A main aim of the new design is to reproduce the smooth spatial and spectral response of the cochlea over a certain bandwidth. A basic analysis of a Helmholtz Resonator is first given in Section 5.2, using a lumped-parameter approximation. An analysis of a duct with an infinite array of identical Helmholtz Resonators is carried out in Section 5.3, based on a Transmission Line approximation. The formulation of a Transfer Function method for simulating a system consisting of a main duct with a number of Helmholtz-Resonator side branches is then presented in Section 5.4. In Section 5.5, the response is then computed for the two models from the literature depicted in Figure 5.1, where it is shown that the model by Jimenez et al. acts as an acoustic 'rainbow' sensor, whereas the model by Zhao and Zhou is shown to have limited potential use as a 'rainbow' sensor due to its uneven response.

A novel design of a cochlea-inspired acoustic 'rainbow' sensor is then presented in Section 5.6. Results from simulations are presented and discussed in Section 5.7, where the performance of the system as an acoustic 'rainbow' sensor is demonstrated. Conclusions are summarised in Section 5.8.

5.2 Basic analysis of a Helmholtz Resonator

A Helmholtz Resonator is depicted in Figure 5.2a, consisting of a neck of radius a and length l_a, and a cavity of volume V_H, which are all assumed to be small compared with the acoustic wavelength, so that a lumped-parameter model can be used. The main inertive element of the resonator is the neck and the main compliant element is the cavity, a balance between which results in resonance [48]. The acoustic resistance in this initial analysis is considered to be only due to viscous and thermal losses occurring at the neck boundary. An effective neck length, denoted by l_H, is used both for the inertance and the resistance of the neck, which is larger than the actual neck length, l_a, since it includes end corrections due to radiation at both sides of the neck.

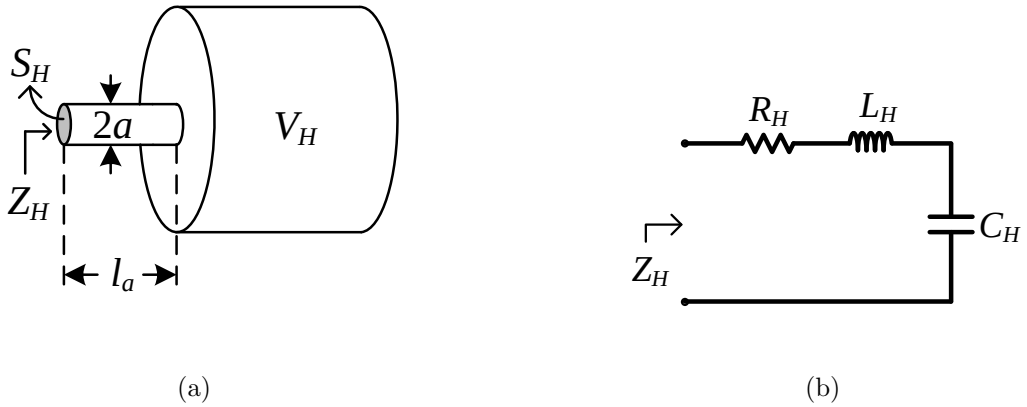

Figure 5.2. (a) Schematic of a Helmholtz Resonator. The neck radius, a, length, l_a, and cross-sectional area, S_H, are shown, along with the cavity volume, V_H. The input impedance, Z_H, of the resonator is also shown. (b) Equivalent circuit will lumped parameters, showing the acoustic resistance, R_H, and inertance, L_H, of the neck, and the compliance, C_H, of the cavity.

Assuming wave propagation in the neck, the input impedance looking into the resonator, as depicted in Figure 5.2a, is given by [54]

$$Z_H = Z_{0,n}\frac{Z_C + \mathrm{i}Z_{0,n}\tan k_H l_H}{Z_{0,n} + \mathrm{i}Z_C \tan k_H l_H}, \tag{5.1}$$

where i is the imaginary unit and $Z_{0,n} = \rho c_0/S_H$ is the characteristic impedance for wave propagation in the neck, where ρ is the density of air and c_0 is the speed of sound in air, k_H is a complex wavenumber accounting for both propagation and attenuation in the neck, and Z_C is the impedance of the cavity, given by

$$Z_C = \frac{1}{\mathrm{i}\omega C_H}, \tag{5.2}$$

where $C_H = V_H/\rho c_0^2$ is the compliance of the cavity and ω is the angular frequency. If the neck length is assumed to be much smaller than the wavelength, and provided that the imaginary part of the wavenumber is much smaller than its real part, it follows that $|k_H l_H| \ll 1$. If it is

also assumed that the volume of the cavity is large compared to the volume of the neck, so that $|Z_C|k_H l_H \ll Z_{0,n}$, Equation (5.1) takes the approximate form

$$Z_H = \mathrm{i} Z_{0,n} k_H l_H + Z_C. \tag{5.3}$$

The viscous boundary layer thickness for sound propagation in the neck is given by [42]

$$\delta = \sqrt{\frac{2\eta}{\omega\rho}}, \tag{5.4}$$

where η is the dynamic viscosity. Assuming that the neck radius is much greater than the viscous boundary layer thickness, $a \gg \delta$, the wavenumber for sound propagation in the neck can be written as [42]

$$k_H = k_0 - \mathrm{i}\alpha, \tag{5.5}$$

where $k_0 = \omega/c_0$ is the lossless wavenumber and α is the loss coefficient, which represents the exponential decay spatial rate, given by [42]

$$\alpha = \frac{k_0 \delta}{2a}\left(1 + \frac{\gamma - 1}{\sqrt{\mathrm{Pr}}}\right), \tag{5.6}$$

where γ is the ratio of specific heats and Pr is the Prandtl number. In Equation (5.6), the first term in parentheses multiplied by the common term corresponds to viscous losses, and the second term multiplied by the common term corresponds to thermal losses. For typical parameter values for air at room temperature ($\rho = 1.2$ kg·m^{-3}, $c_0 = 343$ m·s^{-1}, $\eta = 1.8 \cdot 10^{-5}$ Pa·s, $\gamma = 1.4$, Pr $= 0.71$ [1]), the loss coefficient can be written approximately as

$$\alpha \approx 3 \cdot 10^{-5} \frac{\sqrt{f/\mathrm{Hz}}}{a}, \tag{5.7}$$

where f is in Hz, so that if a is in meters then α is in Np/m.

Substituting Equation (5.5) into Equation (5.3), the impedance of the Helmholtz Resonator takes the form

$$Z_H = \mathrm{i}\frac{\rho c_0 l_H}{S_H}(k_0 - \mathrm{i}\alpha) + Z_C = R_H + \mathrm{i}\omega L_H + \frac{1}{\mathrm{i}\omega C_H}, \tag{5.8}$$

where

$$R_H = \frac{\alpha \rho c_0 l_H}{S_H} = Z_{0,n}\alpha l_H,\ L_H = \frac{\rho l_H}{S_H},\ C_H = \frac{V_H}{\rho c_0^2} \tag{5.9}$$

are the acoustic resistance and inertance of the neck, and the compliance of the cavity, respectively. Equation (5.8) is equivalent to a lumped-parameter representation of the Helmholtz Resonator, an equivalent circuit of which is depicted in Figure 5.2b.

The resonance angular frequency of the Helmholtz Resonator, when $\mathrm{i}\omega L_H$ is equal to

$-\mathrm{i}(\omega C_H)^{-1}$, is given by [48]

$$\omega_0 = c_0\sqrt{\frac{S_H}{l_H V_H}}, \tag{5.10}$$

and the quality factor of the Helmholtz Resonator is given by [91]

$$Q = \frac{\omega_0 L_H}{R_H(\omega_0)}, \tag{5.11}$$

where the acoustic resistance is evaluated at the resonance frequency. Using Equations (5.7) and (5.9), the quality factor takes the approximate form

$$Q \approx 600(a/\mathrm{m})\sqrt{f_0/\mathrm{Hz}}, \tag{5.12}$$

where $f_0 = \omega_0/2\pi$ is the resonance frequency in Hz, and a is in meters.

The effective length of the neck is equal to the sum of its physical length and end corrections at both ends. For the inertance, these end corrections account for the mass of air outside the neck that gets accelerated by the air within it [42], whereas for the resistance, the end corrections account for the additional loss as the air flows around the two ends of the neck [48]. For the sake of this initial design study, it is assumed that the end correction for the resistance is equal to that for the inertance.

The well-known results for the end correction are that it is approximately $0.6a$ for an unflanged end and $0.85a$ for a flanged end, although more complicated formulas have also been proposed for a baffle of finite size [92]. In the designs considered here, the baffle is large relative to the size of the neck so, again for the sake of simplicity in this initial design, the total end correction length, accounting for both ends of the neck, is assumed to be [48]

$$l_{cor} = 2 \cdot 0.85a = 1.7a. \tag{5.13}$$

The effective neck length is thus related to the actual neck length by $l_H = l_a + l_{cor}$.

5.3 Behaviour of an array of identical Helmholtz Resonators

A system consisting of a main duct with an array of identical Helmholtz-Resonator side branches is considered, as depicted in Figure 5.3a. A similar system has been studied in [92]. Each element of the system comprises a segment of the main duct of length l_D and a Helmholtz Resonator at its end. Each Helmholtz Resonator consists of a neck of length l_a and cross-sectional area S_H and a cavity of volume V_H. Viscous and thermal losses are only considered in the neck. Such a system produces a 'slow wave', that is, a wave whose propagation speed is smaller than that of a plane wave in a uniform tube, up to a frequency where the propagation speed becomes very small [92]. Above this frequency, there is a stop band, where the wavenumber is mainly

imaginary. Beyond the stop band, there is another pass band, in which waves propagate with a speed that approaches the speed of plane-wave propagation as frequency increases. The aim of this section is to provide a simple model of the wave propagation in this system that can be used for design purposes below.

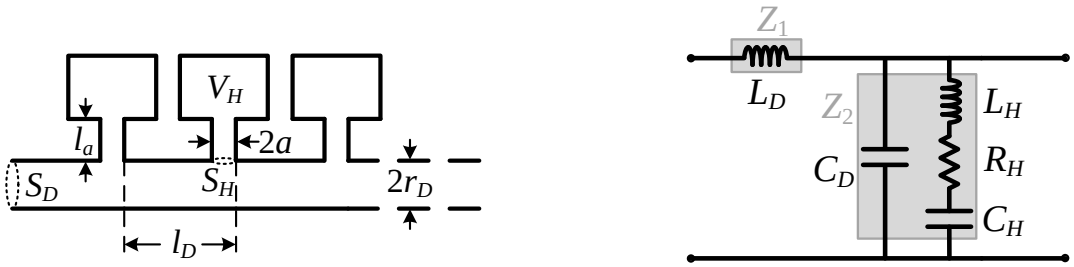

(a) (b)

Figure 5.3. (a) Schematic of a longitudinal cross section of a waveguide consisting of a main duct and an array of side branches of identical Helmholtz Resonators. One element of the waveguide is defined by the vertical dashed lines. The radius of the duct, r_D, the cross-sectional area of the duct, S_D, and the length of each element, l_D, are shown, along with a Helmholtz Resonator whose neck has radius a, cross-sectional area S_H, and length l_a, and whose cavity volume is V_H. (b) Equivalent circuit representation of an element of the waveguide. L_D and C_D are the inertance and compliance of the duct segment, respectively, and L_H, R_H and C_H are the inertance, acoustic resistance and compliance of the Helmholtz Resonator, respectively. Z_1 is the series impedance, due to the inertance of the duct segment, and Z_2 is the shunt impedance, due to the duct compliance and the impedance of the Helmholtz Resonator.

5.3.1 Transmission Line model

Assuming that the dimensions of the components of an element are much smaller than the wavelength, an equivalent circuit with lumped parameters can be used [93], as shown in Figure 5.3b. This assumption also ensures that only the fundamental mode is supported in the considered spectrum. Since the elements of the waveguide are identical and their length is much smaller than the wavelength, the system can be analysed using Transmission Line theory, as presented for example in [56]. Similarly to the Transmission Line model for the acoustic waveguide with fitted rings presented in Section 3.3.2, the lumped parameters here represent lumped acoustic properties of the system corresponding to an element of a certain length, whereas in the formal theory, the Transmission Line is represented by interchanging series and shunt elements per unit length. However, the assumed small acoustic length of the different parts of the waveguide can justify the looser use of the term 'Transmission Line'.

The series impedance of each element in this case is only due to the inertance of the duct segment and is denoted by Z_1, whereas the shunt impedance, denoted by Z_2, in this case consists of the parallel combination of the compliance of the duct and the impedance of the Helmholtz Resonator, as shown in Figure 5.3b. It should be noted that in the system considered here, the element lumped parameters correspond to those of a finite length of duct, whereas in

classical Transmission Line theory, the lumped parameters of each infinitesimal segment of the waveguide represent inertances, compliances and resistances per unit length of the Transmission Line. Therefore, in the considered system, the ratio of each lumped parameter to the element length, l_D, corresponds to the respective parameter per unit length used in Transmission Line theory.

The inertance and compliance of the duct and the inertance, resistance and compliance of the Helmholtz Resonator are given, respectively, by

$$L_D = \frac{\rho l_D}{S_D},\ C_D = \frac{S_D l_D}{\rho c_0^2},\ L_H = \frac{\rho l_H}{S_H},\ R_H = \frac{\alpha \rho c_0 l_H}{S_H},\ C_H = \frac{V_H}{\rho c_0^2}, \tag{5.14}$$

where $l_H = l_a + l_{cor}$ is the effective length of the neck, where l_{cor} is the end correction, and the loss coefficient, α, is given by Equation (5.7). It should be noted that the acoustic resistance R_H depends on frequency due to the form of the loss coefficient α in Equation (5.7).

The element impedances are expressed with respect to the lumped parameters as [48]

$$Z_1 \equiv Z_{L_D} = \mathrm{i}\omega L_D \tag{5.15}$$

and

$$Z_2 = \frac{Z_{C_D} Z_H}{Z_{C_D} + Z_H}, \tag{5.16}$$

where

$$Z_{C_D} = \frac{1}{\mathrm{i}\omega C_D} \tag{5.17}$$

and

$$Z_H = Z_{L_H} + R_H + Z_{C_H}, \tag{5.18}$$

where

$$Z_{L_H} = \mathrm{i}\omega L_H,\ Z_{C_H} = \frac{1}{\mathrm{i}\omega C_H}. \tag{5.19}$$

From Transmission Line theory [56], the characteristic impedance and the wavenumber of the Transmission Line are given, respectively, by

$$Z_c = \sqrt{Z_1 Z_2} \tag{5.20}$$

and

$$k = \frac{1}{\mathrm{i} l_D}\sqrt{\frac{Z_1}{Z_2}}, \tag{5.21}$$

where Equation (5.21) has been derived taking into account that $\mathrm{i}kl_D$ corresponds to the propagation constant of the Transmission Line. The wavenumber in Equation (5.21) corresponds to a wave travelling along the system as if it were a uniform Transmission Line, so that the Helmholtz-Resonator side branches have been incorporated into the characteristic

impedance and the wavenumber as intrinsic properties of the line. In other words, with the assumption that the dimensions of an element are much smaller than the wavelength, the duct with the array of Helmholtz Resonators is transformed into a uniform acoustic waveguide, whose properties are smeared out so that the properties of the waveguide do not change with position. By manipulation of Equations (5.20) and (5.21) and also using the definitions for L_D and C_D given in Equations (5.14), it follows that

$$kZ_c = k_0 Z_0 = \frac{\omega\rho}{S_D}, \tag{5.22}$$

where $k_0 = \omega/c_0$ is the wavenumber in free space and $Z_0 = \rho c_0/S_D$ is the characteristic impedance of the main duct.

The resonance angular frequency of each Helmholtz Resonator is given by Equation (5.10), which in this section will be denoted by ω_1 for notational convenience. A cut-on angular frequency is also introduced, whose role will be made clear later on, defined by

$$\omega_2 = \omega_1 \left[1 + \frac{C_H}{C_D}\right]^{1/2}. \tag{5.23}$$

Two frequency-dependent quality factors are also defined as

$$Q_1 = \omega_1 \frac{L_H}{R_H(\omega)} \tag{5.24}$$

and

$$Q_2 = \frac{\omega_2}{\omega_1} Q_1(\omega). \tag{5.25}$$

By substituting Equations (5.15) and (5.16) into Equation (5.21), and also using Equation (5.10) and Equations (5.23) to (5.25), the wavenumber takes the relatively simple form

$$k = k_0 \left[\frac{\omega_2^2 + \mathrm{i}\frac{\omega\omega_2}{Q_2} - \omega^2}{\omega_1^2 + \mathrm{i}\frac{\omega\omega_1}{Q_1} - \omega^2}\right]^{1/2}. \tag{5.26}$$

Using Equations (5.22) and (5.26), the characteristic impedance of the system can also be written as

$$Z_c = Z_0 \left[\frac{\omega_1^2 + \mathrm{i}\frac{\omega\omega_1}{Q_1} - \omega^2}{\omega_2^2 + \mathrm{i}\frac{\omega\omega_2}{Q_2} - \omega^2}\right]^{1/2}. \tag{5.27}$$

The limiting behaviour of the wavenumber at very low frequencies is given by

$$\omega \ll \omega_1 : k \to k_b = \frac{\omega_2}{\omega_1} k_0, \tag{5.28}$$

where the subscript b has been used in correspondence with the limiting behaviour at the basal end observed in the cochlea. The associated phase and group velocities at very low frequencies

are both equal to

$$c_b = \frac{\omega_1}{\omega_2} c_0, \tag{5.29}$$

where the phase velocity is calculated by $c_{ph} = \omega/\mathrm{Re}\{k\}$ and the group velocity by $c_{gr} = \mathrm{d}\omega/\mathrm{d}(\mathrm{Re}\{k\})$. The limiting behaviour of the wavenumber at very high frequencies is given by

$$\omega \gg \omega_2 : k \to k_0, \tag{5.30}$$

and, accordingly, the phase and group velocities tend to the speed of sound in free space. A wave with the phase velocity given by Equation (5.29) is called the 'slow wave' below. In the middle region of the stop band, where it is assumed that $\omega_1 \ll \omega \ll \omega_2$, the wavenumber takes the form

$$k_s = -\frac{\mathrm{i}}{d}, \tag{5.31}$$

where

$$d = \frac{c_0}{\omega_2} \tag{5.32}$$

is the exponential decay length in the stop band.

An inertance ratio can be defined as

$$\mu \equiv \frac{L_H}{L_D} = \frac{l_H S_D}{l_D S_H}, \tag{5.33}$$

which is the ratio of the inertia of the neck in the Helmholtz Resonator to the inertia of the duct element. If $\omega_2 \gg \omega_1$, or, equivalently, $C_H \gg C_D$, using Equations (5.23) and (5.33), the decay length can be written as

$$d \approx l_D \sqrt{\mu}. \tag{5.34}$$

The limiting behaviours of the characteristic impedance of the system at low and high frequencies are given, respectively, by

$$\omega \ll \omega_1 : Z_c \to Z_b = \frac{\omega_1}{\omega_2} Z_0 \tag{5.35}$$

and

$$\omega \gg \omega_2 : Z_c \to Z_0. \tag{5.36}$$

The wavelength of the wave propagating along the system is given by

$$\lambda = \frac{2\pi}{\mathrm{Re}\{k\}}, \tag{5.37}$$

whereas the wavelength in free space is given by $\lambda_0 = c_0/f = 2\pi/k_0$. Again assuming that the stop band is large, so that $\omega_2 \gg \omega_1$, the wavenumber at the resonance frequency of the

Helmholtz Resonators takes the approximate form

$$k_1 \approx \frac{1}{d}\sqrt{\frac{Q}{2}}(1 - \mathrm{i}). \tag{5.38}$$

The wavelength reaches a minimum at a frequency which is close to the resonance frequency, as will be shown below, which is approximately given by

$$\lambda_{min} \approx \frac{2\pi}{\mathrm{Re}\{k_1\}} = 2\pi d\sqrt{\frac{2}{Q}}. \tag{5.39}$$

5.3.2 Wavenumber and phase and group velocity simulations

The real and imaginary parts of the wavenumber are plotted against frequency in Figure 5.4a, for the example parameter values of $\rho = 1.2$ kg·m^{-3}, $c_0 = 343$ m·s^{-1}, $r_D = 0.02$ m, $l_D = 0.05$ m, $a = 0.0025$ m, $l_a = 0.002$ m, and $V_H = 0.001$ m^{-3}. The quality factor given by Equation (5.24) is thus about 15 and the inertance ratio given by Equation (5.33) is 8. The marked frequencies are $f_1 = \omega_1/2\pi$ and $f_2 = \omega_2/2\pi$, which in this case are about 100 and 400 Hz, respectively. The wavenumber can also be calculated from the eigenvalues of the Transfer Matrix of an element of the system shown in Figure 5.3b, as will be presented in Section 5.4.3. The real and imaginary parts of the wavenumber calculated with the eigenvalues are plotted in Figure 5.4a as dashed lines. There appears to be very little difference between these and the solid lines corresponding to the real and imaginary parts of the wavenumber calculated with the Transmission Line analysis presented in Section 5.3.1, thus justifying the use of the latter for this analysis instead of the more accurate eigenvalue approach.

It can be seen in Figure 5.4a that there are two propagation regions, or pass bands, where the wavenumber is mainly real, the first for $f < f_1$ and the second for $f > f_2$, and a stop band exists between them, that is, for $f_1 < f < f_2$, where the wavenumber is mainly imaginary and therefore waves are evanescent. The wavelength, λ, will be smaller than the wavelength in free space, λ_0, in the first pass band, since the wavenumber is larger than that in free space there. The wavenumber then reaches a minimum value given by Equation (5.39) close to f_1. At higher frequencies in the upper pass band, the wavelength tends to that in free space, as the wavenumber tends to the free-space wavenumber.

The phase velocity and the group velocity are plotted in Figure 5.4b; both are computed numerically, using the real part of the wavenumber of Equation (5.26). It can be seen that at the lower pass band, both velocities start at low frequencies from a value c_b defined in Equation (5.29), which is smaller than c_0, hence the 'slow wave', and they decrease as they approach the resonance frequency of the Helmholtz Resonators, f_1. At a frequency slightly less than f_1, where the real part of the wavenumber reaches its maximum, as can be seen in the detail in Figure 5.4a, the phase velocity reaches a minimum value, whereas the group velocity shifts from almost zero to plus infinity and then to minus infinity.

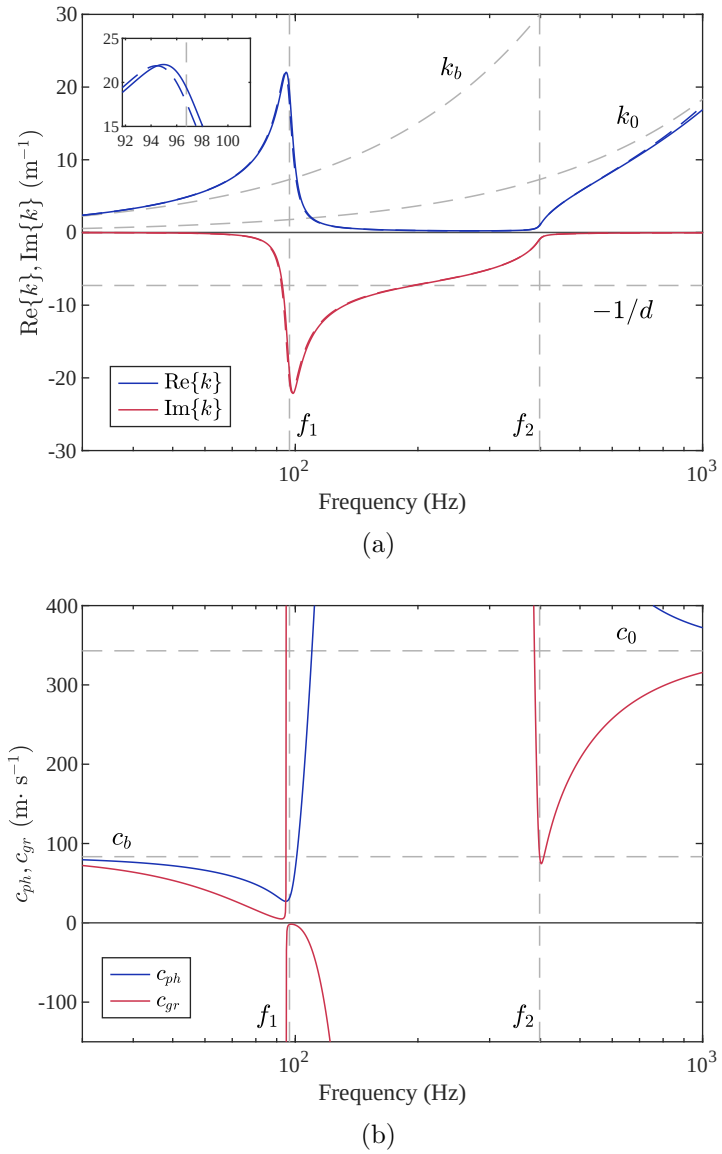

Figure 5.4. (a) Real and imaginary parts of the wavenumber and (b) phase and group velocities, plotted against frequency, for an array of identical Helmholtz Resonators. The marked frequencies are $f_1 = \omega_1/2\pi$ and $f_2 = \omega_2/2\pi$. The dashed coloured lines in (a) correspond to the real and imaginary parts of the wavenumber calculated from the eigenvalues of the Transfer Matrix. The detail in (a) shows that the maximum of the real part of the wavenumber occurs at a frequency slightly lower than the resonance frequency.

In the stop band, the phase velocity increases to very large values, much larger than the speed of sound in air, which corresponds to the wave almost halting, as is explained in [48], although the wave is heavily attenuated in this band. The group velocity transitions from minus infinity to a negative value of very small absolute value right above the mentioned singularity, and then decreases to absolutely very large negative values. It reaches another singularity at a frequency before cut-on, and then decreases to a small value at the cut-on frequency, f_2. In the upper pass band, the phase and group velocities approach the speed of sound in free space with increasing frequency, from higher and from lower values, respectively. The negative group velocity in a great part of the stop band is indicative of strong dispersion. In such a case, where strong dispersion and attenuation are present, the group velocity cannot be regarded as the

speed of energy propagation [83].

5.3.3 System impedances and reflection simulations

The moduli of the various system impedances are plotted in Figure 5.5a, including the characteristic impedance given by Equation (5.27), for the geometrical parameters listed in Section 5.3.2. Approximate equivalent circuits for the three bands and at the cut-off and cut-on frequencies are shown in Figure 5.5b. These circuits are derived from the one shown in Figure 5.3b, by keeping only the dominant lumped circuit elements of the shunt impedance, Z_2, at different frequencies. In the two pass bands, propagation is supported by the balance between the inertive series impedance and the compliant shunt impedance, whereas, in the stop band, the shunt impedance is inertance dominated, so that both the series and shunt impedances are inertive, thus giving rise to a decaying evanescent wave.

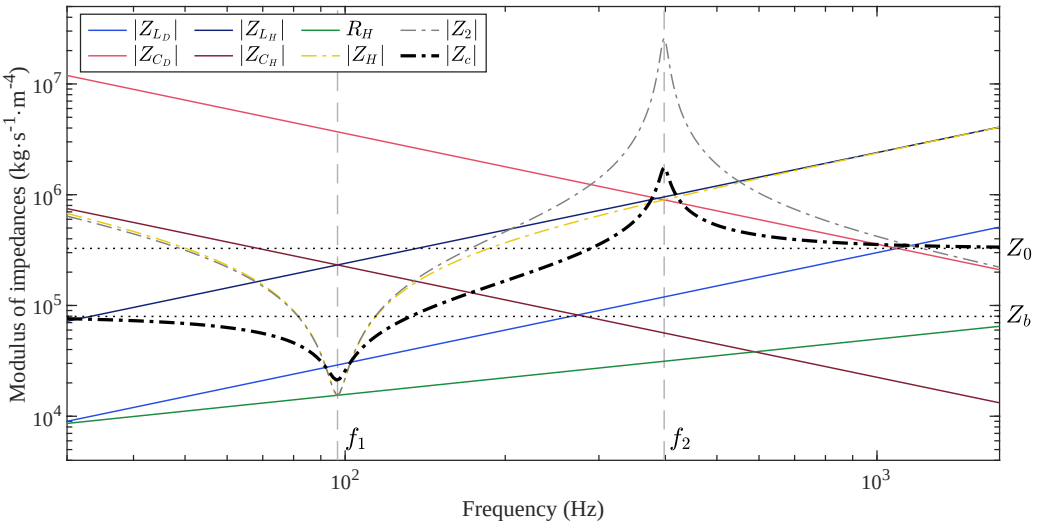

(a)

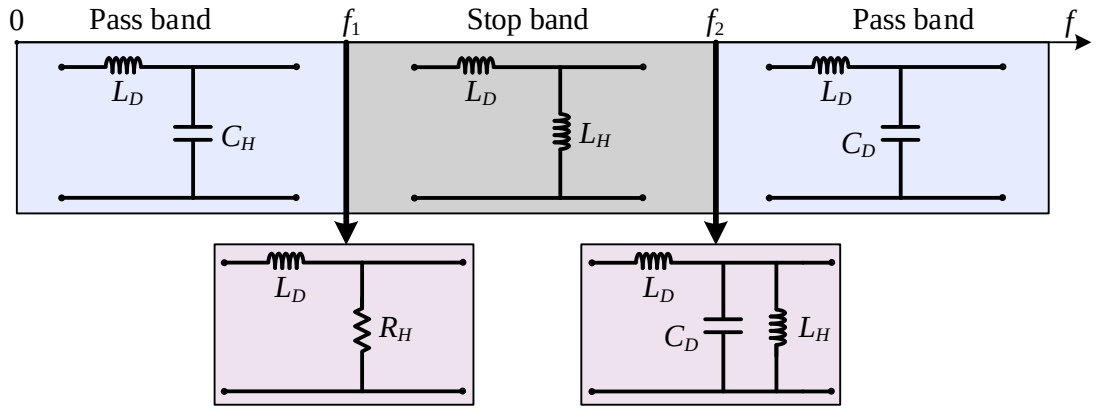

(b)

Figure 5.5. (a) System impedances of an array of identical Helmholtz Resonators plotted against frequency. Z_2 is the shunt impedance, that is, the parallel combination of Z_{C_D} and Z_H. (b) Approximate equivalent circuits of an element of the system at the different frequency bands and at frequencies f_1 and f_2.

At the frequency of resonance of the Helmholtz Resonators, f_1, the impedance of the Helmholtz Resonators becomes purely resistive, while the compliant impedance of the duct, Z_{C_D}, is very large, so that it can be neglected. At the cut-on frequency, f_2, the Helmholtz Resonator is inertance dominated, but the duct compliant impedance is of similar magnitude at this frequency, leading to an anti-resonance for the characteristic impedance. It should also be noted that the characteristic impedance starts from Z_b, given in Equation (5.35), at low frequencies, and tends to Z_0 at high frequencies.

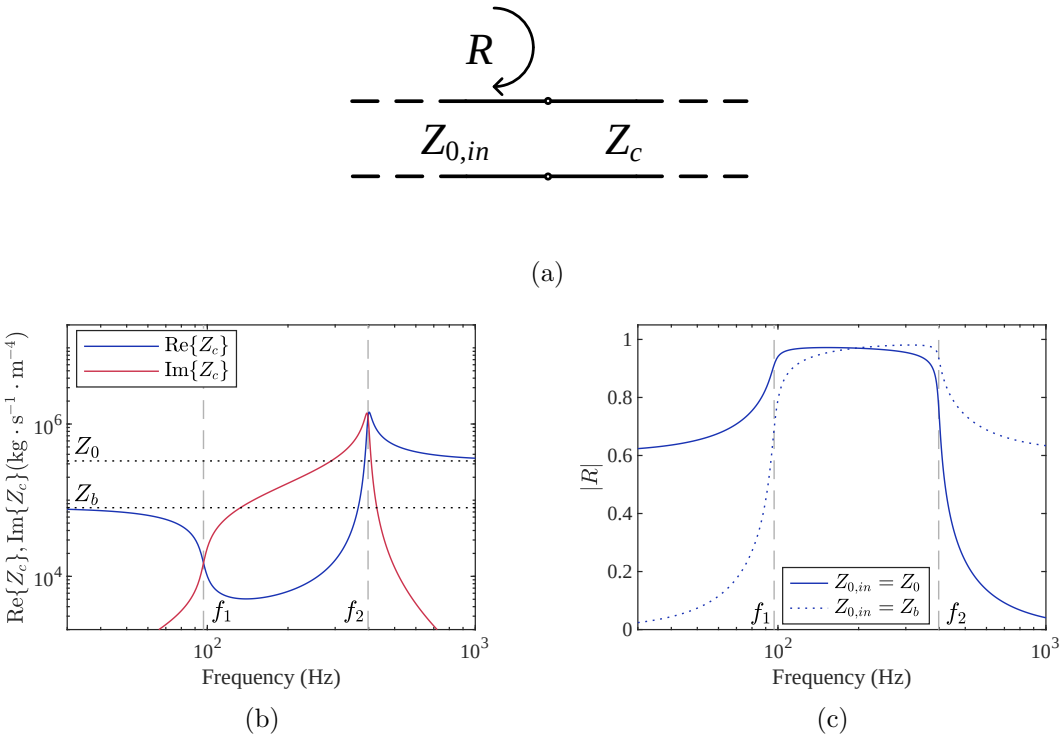

Figure 5.6. (a) Schematic of the tube with the array of Helmholtz Resonators as a Transmission Line with characteristic impedance Z_c connected to a uniform tube of the same dimensions as the main duct, with a characteristic impedance Z_0; the reflection coefficient, R, is also shown. (b) Real and imaginary parts of the characteristic impedance Z_c. (c) Modulus of the reflection coefficient, with the input uniform duct having a characteristic impedance of either Z_0 or Z_b.

If the duct with the Helmholtz Resonators is connected to a semi-infinite uniform tube with characteristic impedance $Z_{0,in}$, as represented by Transmission Lines in Figure 5.6a, the reflection coefficient due to the mismatch of the characteristic impedances can be calculated by [56]

$$R = \frac{Z_c - Z_{0,in}}{Z_c + Z_{0,in}}. \tag{5.40}$$

Two different cases are considered. In the first case, the input duct has the same dimensions as the main duct of the system with Helmholtz resonators, so that $Z_{0,in} = Z_0$. In the second case, the input duct has a cross sectional area of $S_{D,in} = \omega_2 S_D/\omega_1$, so that $Z_{0,in} = Z_b$, where Z_b is the low-frequency limit of the characteristic impedance of Z_c, given in Equation (5.35), so that the system with Helmholtz Resonators forms a matched load at low frequencies.

The real and imaginary parts of the characteristic impedance of the system of the duct with the array of Helmholtz Resonators is shown in Figure 5.6b and the modulus of the reflection coefficient is shown in Figure 5.6c, for the two different characteristic impedances for the input duct. At low frequencies, the characteristic impedance of the array of Helmholtz Resonators is approximately $Z_c \approx Z_b = Z_0\omega_1/\omega_2$, so that in the case where $Z_{0,in} = Z_0$, the reflection coefficient calculated with Equation (5.40) becomes $R \approx (\omega_1 - \omega_2)/(\omega_1 + \omega_2) \approx -0.61$. However, if the input duct with $Z_{0,in} = Z_b$ is used, no reflection occurs at the low frequency limit. In the stop band, the characteristic impedance of the system is mainly reactive, as can be seen in Figure 5.6b, and therefore there is large impedance mismatch with the uniform input line, so that the modulus of the reflection coefficient is close to one for either of the considered input ducts. In the second pass band, the characteristic impedance is again mainly resistive and tends to Z_0 as frequency increases. In the case where $Z_{0,in} = Z_0$, the reflection coefficient tends to zero at higher frequencies, whereas in the case where $Z_{0,in} = Z_b$, the reflection coefficient tends to $R \approx (\omega_2 - \omega_1)/(\omega_1 + \omega_2) \approx 0.61$.

5.3.4 Considerations on the accuracy of the model

The Transmission Line model is applicable under the initial assumption that the various dimensions of an element are much smaller than the free-space wavelength, so that the corresponding acoustic components may be approximated by lumped parameters. The ratios of the example dimensions of an element used in Section 5.3.2 over the free-space wavelength are plotted in Figure 5.7. It can be seen that over the whole of the frequency range considered, the element length, the neck length and the duct radius are much smaller than the free-space wavelength. It can also be concluded that only the fundamental mode can propagate in the main duct, since the first higher-order mode can only propagate for $r_D/\lambda_0 \geq 0.293$ [57]. For the geometrical parameters used, the greatest dimension of the square cuboid cavity, taken to be $w_c = \sqrt{V_H/l_D}$, appears to become quite large at higher frequencies, which implies that the lumped-parameter approximation for the cavity is expected to deteriorate at higher frequencies. However, for the current analysis, which aims at presenting the general characteristics and behaviour of the considered system, the lumped-parameter approximation for the cavity seems adequate.

For a discrete system to approximate a continuous waveguide with accuracy, a minimum number of elements per wavelength along the direction of propagation has to be used; a minimum of six elements per wavelength is often applied, as for example in Finite Element Analysis [40]. In the system of a duct with an array of Helmholtz Resonators, this condition has to be satisfied by the minimum wavelength. Combining Equations (5.39) and (5.34), the ratio of the minimum

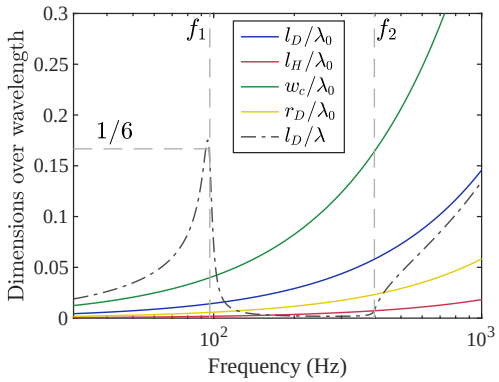

Figure 5.7. Ratios of the dimensions of an element over the wavelength, for an array of identical Helmholtz Resonators. The coloured solid lines correspond to ratios over the wavelength in free space, λ_0, and the dash-dotted grey line corresponds to the ratio of the element length over the system wavelength, that is, the wavelength of the 'slow wave' propagating along the system. The length w_c corresponds to the two dimensions of an assumed square cuboid cavity with length l_D, so that its volume is given by $V_H = l_D w_c^2$.

wavelength to the element length can be written as

$$\frac{\lambda_{min}}{l_D} = 2\pi\sqrt{\frac{2\mu}{Q}}. \tag{5.41}$$

For the condition of at least six elements per wavelength to be satisfied, the ratio of Equation (5.41) can be conveniently set to $\lambda_{min}/l_D \geq 2\pi > 6$, so that the inertance ratio has to be $\mu \geq Q/2$. For the assumed values used above, then $Q = 15$ and $\mu = 8 > Q/2$, so that the resolution condition $\lambda_{min}/l_D > 6$ is satisfied.

The ratio of the element length to the system wavelength, l_D/λ, is also plotted in Figure 5.7 against frequency, where the system wavelength is calculated from Equation (5.37) using Equation (5.26). It can be seen that the ratio of the element length to the minimum wavelength, occurring at f_1, is slightly above 1/6, even though according to the preceding analysis using Equation (5.41), it would be expected to be smaller that 1/6. This discrepancy can be attributed to the use of the mentioned approximations applied in Equations (5.34) and (5.39), and, therefore, in Equation (5.41), and also to the fact that Equation (5.39) calculates the minimum wavelength based on the value of the real part of the wavenumber at the resonance frequency, although it can be seen from the detail in Figure 5.4a that the maximum real wavenumber occurs at a slightly lower frequency than the resonance frequency.

5.4 Transfer Matrix method for calculating the response of a system with a finite number of Helmholtz Resonators of varying dimensions

In this section, the Transfer Matrix method will be used to calculate the response of a system in which the dimensions of the Helmholtz Resonators vary along the length of the duct. In

the most general form of the Transfer Matrix method, it is not necessary to assume that the elements are small compared with the wavelength, thus providing a more general theory than in Section 5.3. A schematic of a system consisting of a main duct with N side branches of Helmholtz Resonators of varying dimensions is shown in Figure 5.8. One element of the system consists of a duct segment and a Helmholtz Resonator. The system is driven by a semi-infinite uniform duct of characteristic impedance Z_0, and is terminated at an impedance Z_{end}. The input end of the system is called the base and the output end is called the apex, by analogy with the cochlea.

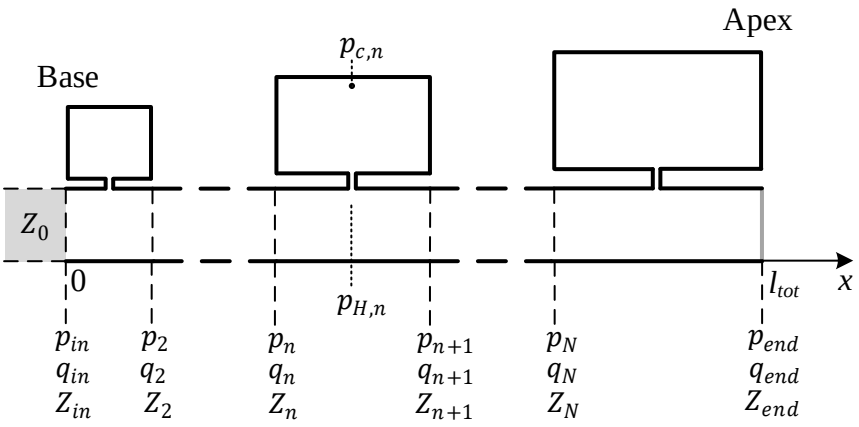

Figure 5.8. Schematic of a longitudinal cross section of a system consisting of a main duct with N side branches of Helmholtz Resonators of varying dimensions. Each element of the system consists of a duct segment and a Helmholtz Resonator. The system is connected to a semi-infinite waveguide of characteristic impedance Z_0, and terminates at an impedance Z_{end}. The pressure in the main duct at the position of the n-th side branch, $p_{H,n}$, and the pressure at the top of the n-th cavity, $p_{c,n}$, are shown. The base and the apex correspond to the input and output ends, respectively.

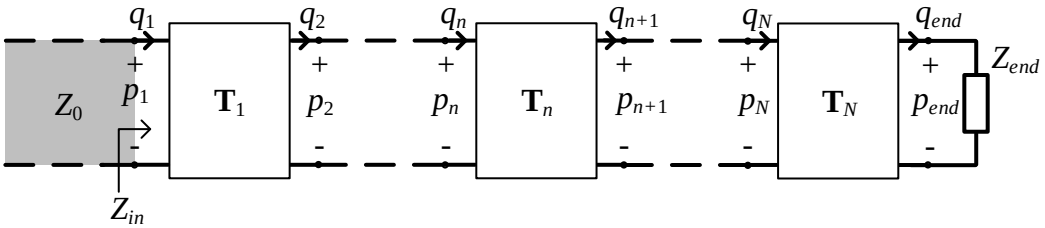

Figure 5.9. Representation of the system of Figure 5.8 where each element is represented by a two-port network. The two-port network of the n-th element has a Transfer Matrix $\mathbf{T}_n$, input variables p_n and q_n and output variables p_{n+1} and q_{n+1}.

The system of Figure 5.8 can be analysed using Transfer Matrices [1]. An equivalent drawing of the system of Figure 5.8 is shown in Figure 5.9, where each element is represented as a two-port network, where the Transfer Matrix of the n-th element is $\mathbf{T}_n$. Therefore, the pressure and volume velocity at the input of an element can be expressed with respect to the

corresponding quantities at its output as [93]

$$\begin{bmatrix} p_n \\ q_n \end{bmatrix} = \begin{bmatrix} T_{11,n} & T_{12,n} \\ T_{21,n} & T_{22,n} \end{bmatrix} \begin{bmatrix} p_{n+1} \\ q_{n+1} \end{bmatrix}, \tag{5.42}$$

which can be written compactly as

$$\mathbf{v}_n = \mathbf{T}_n \mathbf{v}_{n+1}, \tag{5.43}$$

where $\mathbf{v}_n$ is the state vector of the n-th element. The N-th element can be expressed with respect to the state variables at the termination as

$$\mathbf{v}_N = \mathbf{T}_N \mathbf{v}_{end}, \tag{5.44}$$

where $\mathbf{v}_{end} = [p_{end}\ q_{end}]^{\mathrm{T}}$. By iteratively substituting the lower-order vector by its relation with the vector of the next element using Equation (5.43), the first state vector can be expressed with respect to the last one as

$$\mathbf{v}_1 = \mathbf{T} \mathbf{v}_{end}, \tag{5.45}$$

where

$$\mathbf{T} = \mathbf{T}_1 \mathbf{T}_2 \dots \mathbf{T}_{N-1} \mathbf{T}_N \tag{5.46}$$

is the total Transfer Matrix. Equation (5.45) can be written in expanded form as

$$\begin{bmatrix} p_{in} \\ q_{in} \end{bmatrix} = \begin{bmatrix} T_{11} & T_{12} \\ T_{21} & T_{22} \end{bmatrix} \begin{bmatrix} p_{end} \\ q_{end} \end{bmatrix}. \tag{5.47}$$

If two of the quantities p_{in}, q_{in}, p_{end} and q_{end} are known, the other two can be calculated from Equation (5.47), provided that the elements of the total Transfer Matrix are known, or, equivalently, provided that the elements of each of the Transfer Matrices of Equation (5.42) are known. If the input volume velocity, q_{in}, is known, and the termination impedance, Z_{end}, is also known, which is given by

$$Z_{end} = \frac{p_{end}}{q_{end}}, \tag{5.48}$$

the other three state variables, that is, p_{in}, p_{end} and q_{end}, can still be found by solving the system of the three equations formed by Equations (5.47) and (5.48) combined. The input impedance of the system can then be calculated by

$$Z_{in} = \frac{p_{in}}{q_{in}}. \tag{5.49}$$

The pressure and volume velocity at the input of each element can be calculated once p_{end} and q_{end} are found, by iteratively applying Equation (5.42) starting from the last element. The Transfer Matrix method presented here reduces to the Transfer Function method presented in

Chapter 3, if only the impedance, or, equivalently, the admittance, is sought for, whereas the pressure and volume velocity within the waveguide are not required.

5.4.1 Transmission Matrices

The Transfer Matrix relating the state variables at the two sides of the n-th element can be expressed as a product of Transmission Matrices, accounting for wave propagation through the n-th duct segment and for the effect of the Helmholtz Resonator side branch as [93]

$$\mathbf{T}_n = \mathbf{T}_{hd,n}\mathbf{T}_{H,n}\mathbf{T}_{hd,n}, \tag{5.50}$$

where $\mathbf{T}_{hd,n}$ is the Transmission Matrix of half the duct segment of the element and $\mathbf{T}_{H,n}$ is the Transfer Matrix for the Helmholtz Resonator. The Transmission Matrix for half the duct segment of the n-th element is written as [93]

$$\mathbf{T}_{hd,n} = \begin{bmatrix} \cos\frac{k_0 l_{D,n}}{2} & \mathrm{i}Z_0 \sin\frac{k_0 l_{D,n}}{2} \\ \frac{\mathrm{i}}{Z_0}\sin\frac{k_0 l_{D,n}}{2} & \cos\frac{k_0 l_{D,n}}{2} \end{bmatrix}, \tag{5.51}$$

and the Transfer Matrix of the side branch is expressed as [93]

$$\mathbf{T}_{H,n} = \begin{bmatrix} 1 & 0 \\ \frac{1}{Z_{H,n}} & 1 \end{bmatrix}, \tag{5.52}$$

where $Z_{H,n}$ is the impedance of the n-th Helmholtz Resonator.

The Transmission Matrix method can also be used for the calculation of the impedance of the Helmholtz Resonator, $Z_{H,n}$. The Transmission Matrices for the neck, the end corrections and the cavity are given, respectively, by [94]

$$\mathbf{T}_{neck,n} = \begin{bmatrix} \cos k_H l_{a,n} & \mathrm{i}Z_{neck,0}\sin k_H l_{a,n} \\ \frac{\mathrm{i}}{Z_{neck,0}}\sin k_H l_{a,n} & \cos k_H l_{a,n} \end{bmatrix}, \tag{5.53}$$

$$\mathbf{T}_{cor,n} = \begin{bmatrix} 1 & \mathrm{i}Z_{neck,0}\sin k_H l_{cor} \\ 0 & 1 \end{bmatrix} \tag{5.54}$$

and

$$\mathbf{T}_{cav,n} = \begin{bmatrix} \cos k_{c,n} h_H & \mathrm{i}Z_{c,0,n}\sin k_{c,n} h_H \\ \frac{\mathrm{i}}{Z_{c,0,n}}\sin k_{c,n} h_H & \cos k_{c,n} h_H \end{bmatrix}, \tag{5.55}$$

where k_H is the wavenumber of the necks, $l_{a,n}$ is the actual length of the neck of the n-th element, $k_{c,n}$ and $h_{H,n}$ are the wavenumber and the height, respectively, of the cavity of the n-th element, l_{cor} is the total end correction length, $Z_{neck,0}$ is the characteristic impedance of the necks, and $Z_{c,0,n}$ is the characteristic impedance of the n-th cavity. The wavenumber and

characteristic impedance of the neck are the same for all elements due to the necks having the same cross section.

The state vector at the input of the Helmholtz Resonator is related to the state vector at the top of the resonator by [94]

$$\mathbf{v}_{H,n} = \mathbf{T}_{neck,n}\mathbf{T}_{cor,n}\mathbf{T}_{cav,n}\mathbf{v}_{c,n}, \tag{5.56}$$

where $\mathbf{v}_{H,n} = [p_{H,n}\ q_{H,n}]^{\mathrm{T}}$ and $\mathbf{v}_{c,n} = [p_{c,n}\ q_{c,n}]^{\mathrm{T}}$ are the state vectors at the input and at the top of the Helmholtz Resonator, respectively. Considering that the volume velocity at the top of the cavity, $q_{c,n}$, is zero, and that the impedance of the Helmholtz Resonator is given by $Z_{H,n} = p_{H,n}/q_{H,n}$, yields [94]

$$Z_{H,n} = -\mathrm{i}\frac{\cos k_H l_{a,n}\cos k_{c,n}h_{H,n} - \frac{Z_{neck,0}}{Z_{c,0,n}}\sin k_{c,n}h_{H,n}\left(k_H l_{cor}\cos k_H l_{a,n} + \sin k_H l_{a,n}\right)}{\frac{1}{Z_{neck,0}}\sin k_H l_{a,n}\cos k_{c,n}h_{H,n} - \frac{1}{Z_{c,0,n}}\sin k_{c,n}h_{H,n}\left(k_H l_{cor}\sin k_H l_{a,n} - \cos k_H l_{a,n}\right)}. \tag{5.57}$$

The pressure in the main duct at the position of the side branches, that is, half way through the element length, can be calculated by

$$p_{H,n} = \mathbf{T}_{hd,n}(1,1)p_{n+1} + \mathbf{T}_{hd,n}(1,2)q_{n+1}, \tag{5.58}$$

where $\mathbf{T}_{hd,n}(1,1)$ and $\mathbf{T}_{hd,n}(1,2)$ denote the element on the first row and first column and the element on the first row and second column, respectively, of each matrix. The pressure at the top of the cavity can be calculated from Equation (5.56) with $q_{c,n} = 0$, giving

$$p_{c,n} = \frac{p_{H,n}}{\cos k_H l_{a,n}\cos k_{c,n}h_{H,n} - \frac{Z_{neck,0}}{Z_{c,0,n}}\sin k_{c,n}h_{H,n}\left(k_H l_{cor}\cos k_H l_{a,n} + \sin k_H l_{a,n}\right)}. \tag{5.59}$$

A more accurate loss model compared to that presented in Section 5.2 can be used, according to which the complex wavenumbers and characteristic impedances in Equation (5.57) are given, respectively, by [92]

$$k_j = k_0\left[1 + \frac{\beta}{s}\left(1 + \frac{\gamma - 1}{\sqrt{\mathrm{Pr}}}\right)\right] \tag{5.60}$$

and

$$Z_j = Z_0\left[1 + \frac{\beta}{s}\left(1 - \frac{\gamma - 1}{\sqrt{\mathrm{Pr}}}\right)\right], \tag{5.61}$$

where $\beta = (1 - \mathrm{i})/\sqrt{2}$, $s = r/\delta$, where r is the radius of the corresponding tube and δ is the boundary layer thickness, given by Equation (5.4), and the subscript j can be either H or c, n for the wavenumber and either $neck, 0$ or $c, 0, n$ for the characteristic impedance, corresponding to the neck and the cavity, respectively. For necks and cavities, or ducts in general, whose cross

section is not circular, the equivalent hydraulic radius is used for r, defined as [48]

$$r_{hyd} = \frac{2S_{cs}}{P_{cs}}, \tag{5.62}$$

where S_{cs} and P_{cs} are the area and the perimeter of the cross section, respectively. For the special case of a duct of square cross section of side w, it follows that $r_{hyd} = w/2$.

The form of the Helmholtz Resonator impedance of Equation (5.57), using the complex wavenumber and complex characteristic impedance of Equations (5.60) and (5.61), respectively, accounts for losses both at the neck and at the cavity. Losses in the duct can be included by substituting the free-space wavenumber and the characteristic impedance in Equation (5.51) by those given by Equations (5.60) and (5.61) using the hydraulic radius of the duct. It should be noted that Equation (5.57) only accounts for wave propagation in the direction perpendicular to the cross section of the neck, that is, along the height of the cavity. Therefore, it is assumed that the pressure is uniform along the other two directions in the cavity, so that possible pressure fluctuations in these directions are not accounted for.

Instead of Equation (5.13), more accurate formulas for the end corrections of the neck can be used, where the end correction from the neck to the cavity and from the neck to the main duct are calculated, respectively, by [92]

$$l_{cor,c} = 0.82\left[1 - 1.35\frac{a}{r_c} + 0.31\left(\frac{a}{r_c}\right)^3\right]a \tag{5.63}$$

and

$$l_{cor,d} = 0.82\left[1 - 0.235\frac{a}{r_d} - 1.32\left(\frac{a}{r_d}\right)^2 + 1.54\left(\frac{a}{r_d}\right)^3 - 0.86\left(\frac{a}{r_d}\right)^4\right]a, \tag{5.64}$$

where r_c and r_d are the hydraulic radii of the cavity and the duct, respectively, and a is the neck radius.

5.4.2 Lumped-parameter approximation

If the dimensions of the duct are much smaller than the wavelength, which holds at lower frequencies, a lumped-parameter approximation can be applied, leading to the equivalent circuit shown in Figure 5.10. The elements of the n-th Transfer Matrix of Equation (5.42) can then be calculated by solving the circuit shown in Figure 5.10, and are written as

$$\begin{aligned}
T_{11,n} &= \frac{Z_{a,n}}{Z_{b,n}} + \left(1 + \frac{Z_{a,n}}{Z_{b,n}}\right)\left[1 + Z_{a,n}\left(\frac{1}{Z_{b,n}} + \frac{1}{Z_{H,n}}\right)\right] \\
T_{12,n} &= Z_{a,n}\left[2 + Z_{a,n}\left(\frac{1}{Z_{b,n}} + \frac{1}{Z_{H,n}}\right)\right] \\
T_{21,n} &= \frac{2}{Z_{b,n}} + \frac{1}{Z_{H,n}} + \frac{Z_{a,n}}{Z_{b,n}}\left(\frac{1}{Z_{b,n}} + \frac{1}{Z_{H,n}}\right) \\
T_{22,n} &= 1 + Z_{a,n}\left(\frac{1}{Z_{b,n}} + \frac{1}{Z_{H,n}}\right),
\end{aligned} \tag{5.65}$$

where

$$Z_{a,n} = \mathrm{i}\omega\frac{L_{D,n}}{2},\ Z_{b,n} = \frac{1}{\mathrm{i}\omega\frac{C_{D,n}}{2}} \tag{5.66}$$

are the series and shunt impedances due to the inertance and compliance of half the n-th duct segment, respectively, and $Z_{H,n}$ is the n-th Helmholtz Resonator impedance. The pressure in the duct at the input of the Helmholtz Resonator is given by

$$p_{H,n} = p_n - Z_{a,n}q_n. \tag{5.67}$$

Losses in the duct can be included by introducing an acoustic resistance in series with the half-duct inertances $L_D/2$ shown in Figure 5.10, given by

$$\frac{R_D}{2} = \frac{\alpha\rho c_0 l_D}{2S_D}, \tag{5.68}$$

where the loss coefficient is given by Equation (5.7), where the equivalent hydraulic radius for the duct is used.

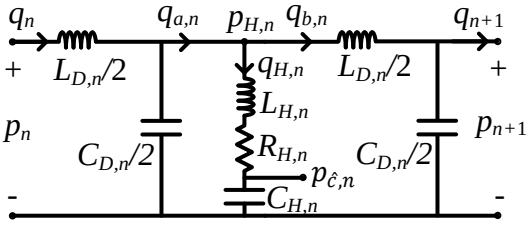

Figure 5.10. Circuit representation of an element of the Transmission Line. The pressures at the input of the element, p_n, at the output of the element, p_{n+1}, at the input of the Helmholtz Resonator, $p_{H,n}$, and at the input of the cavity, $p_{\hat{c},n}$, after the neck of the resonator, are shown. The volume velocity at the input of the element, q_n, and at the output of the element, q_{n+1}, are also shown. The branch of the Helmholtz Resonator is situated between two halves of the duct segment of the element. The volume velocity through the Helmholtz Resonator branch, $q_{H,n}$, and the volume velocities before and after it, $q_{a,n}$ and $q_{b,n}$, respectively, are also shown.

The pressure in the cavity after the neck, that is, at the bottom of the cavity, can be calculated as that of a voltage divider, giving

$$p_{\hat{c},n} = \frac{Z_{C_{H,n}}}{Z_{H,n}}p_{H,n}, \tag{5.69}$$

where $Z_{C_{H,n}}$ is given in Equation (5.19) and $p_{H,n}$ is given by Equation (5.67). In practical terms, however, it is usually easier to measure the pressure by inserting a small microphone at the top of the cavity, where the pressure is also expected to have a maximum, due to the rigid boundary condition there. If phase change across the height of the cavity is taken into account and the rigid boundary condition at the top of the cavity is applied, the pressure at the top of

the n-th cavity can be calculated by

$$p_{c,n} = p_{\hat{c},n} \cos k_{c,n} h_{H,n} - \mathrm{i} Z_{c,0,n} q_{H,n} \sin k_{c,n} h_{H,n}, \tag{5.70}$$

where $k_{c,n}$ and $Z_{c,0,n}$ are the wavenumber and characteristic impedance of the n-th cavity, calculated with Equations (5.60) and (5.61), respectively, and the volume velocity through the Helmholtz Resonator is calculated by $q_{H,n} = q_{a,n} - q_{b,n}$, according to the circuit of Figure 5.10, where the volume velocities at the two sides of the resonator are also calculated from the circuit. For the lumped-parameter approximation, that is, for $k_{c,n} h_{H,n} \ll 1$ Equation (5.70) becomes

$$p_{c,n} = p_{\hat{c},n} - \mathrm{i} Z_{c,0,n} q_{H,n} k_{c,n} h_{H,n}, \tag{5.71}$$

which can be further simplified to

$$p_{c,n} = p_{\hat{c},n} \tag{5.72}$$

if the second term on the right side of Equation (5.71) is assumed to be much smaller than the first one. The approximate Equation (5.72) implies that the pressure inside the cavities is uniform, that is, no pressure change occurs along the height of the cavity. Simulations showed that the pressure at the top of the cavity calculated with Equation (5.72) only slightly diverges from the pressure at the bottom of the cavity, and only at high frequencies.

5.4.3 Wavenumber and effective length

An equivalent wavenumber, k, can be calculated for the system, if it is assumed that the forward-travelling pressure and volume velocity change from the input end of the n-th element to its output, both of which are in the main duct, by a factor of $\psi_n = \exp(-\mathrm{i} k_n \Delta x_n)$, and the respective backward-travelling components by a factor of $\psi_n^{-1} = \exp(\mathrm{i} k_n \Delta x_n)$, where $\Delta x_n = x_{n+1} - x_n$ for the n-th element. This assumption is equivalent to the factors ψ_n and ψ_n^{-1} being the eigenvalues of the n-th Transfer Matrix given in Equation (5.43), as explained in [73].

The wavenumber for the forward-travelling wave at the n-th element can be calculated as

$$k_n = \mathrm{i} \frac{\ln \psi_n}{\Delta x_n}, \tag{5.73}$$

where for each element, the appropriate eigenvalue is used, so that the real part of the wavenumber is positive and the imaginary part is negative, to account for forward propagation and forward attenuation of the wave in the duct, respectively. The calculation of the equivalent wavenumber of Equation (5.73) only uses the values of the pressure and volume velocity at the two ends of the element in the main duct; it does not explicitly use the pressure in the cavities, which, however, is implicitly included in the corresponding Transfer Matrix of Equation (5.43). The phase and group velocities at the n-th element can be calculated from the wavenumber by

$c_{ph,n} = \omega/\mathrm{Re}\{k_n\}$ and $c_{gr,n} = \mathrm{d}\omega/\mathrm{d}(\mathrm{Re}\{k_n\})$, respectively, and the local equivalent wavelength by $\lambda_n = 2\pi/\mathrm{Re}\{k_n\}$.

An effective length for the system, not be confused with the effective length of the necks of the Helmholtz Resonators, can be defined with respect to a system consisting of a main duct with an array of Helmholtz-Resonator side branches whose properties are the same as those of the basal element of the considered system. This effective length is equal to the length of a system with elements identical to the basal element, in which it takes the same time for a wave pulse to travel to its end as it takes for a wave pulse to travel from the input to the position of minimum group velocity in a system with varying Helmholtz Resonators. Therefore, this definition of the effective length is similar to the one given for the cochlea, with the difference that here the system is discretised to a relatively small number of elements, whereas the cochlea was modelled as a continuous system. The effective length is thus given by

$$l_{eff} = c_{gr,1} \sum_{n=1}^{m} \frac{l_{D,n}}{c_{gr,n}}, \tag{5.74}$$

where $c_{gr,1}$ is the group velocity of a system whose elements are identical to the basal element, calculated by $c_{gr,1} = \mathrm{d}\omega/\mathrm{d}k_1$, where k_1 is given by Equation (5.73) for $n = 1$. A normalised effective length can be defined with respect to the length up to the position of minimum group velocity as

$$L_{eff} = \frac{l_{eff}}{l_m}, \tag{5.75}$$

where l_m is the length of the system up to and including the element of minimum group velocity, given by

$$l_m = \sum_{n=1}^{m} l_{D,n}. \tag{5.76}$$

5.4.4 Reflection, transmission and absorption coefficients

The system consisting of a main duct with an array of Helmholtz Resonators is depicted in Figure 5.11, where the pressure and the volume velocity at the input and output boundaries of the system are also shown, along with the reflection, R, transmission, T, and absorption, A, coefficients. The system terminates at a semi-infinite waveguide of characteristic impedance Z_{end}, so that there is no reflected wave beyond the termination at $x = l_{tot}$.

The reflection coefficient of the system can be calculated by the mismatch of the input impedance with the characteristic impedance of the input uniform tube as [48]

$$R = \frac{Z_{in} - Z_0}{Z_{in} + Z_0}, \tag{5.77}$$

where the input impedance, Z_{in}, is given by Equation (5.49). Alternatively, the reflection

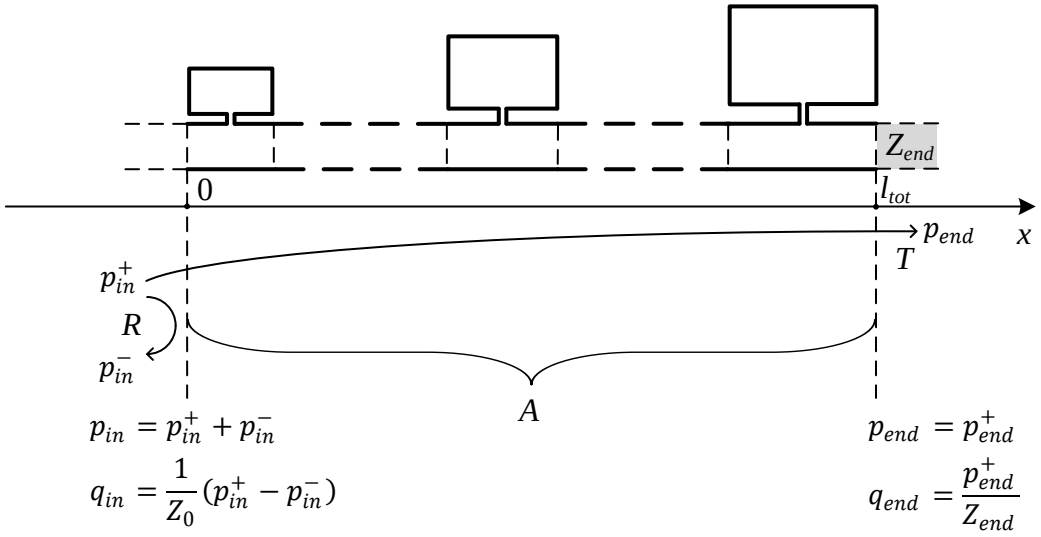

Figure 5.11. Schematic of a waveguide with an array of varying Helmholtz Resonators. The waveguide is terminated by a waveguide of characteristic impedance Z_{end}. The pressure, p_{in}, and volume velocity, q_{in}, at the input, and the respective quantities, p_{end} and q_{end}, at the output of the system are shown, as well as the reflection coefficient, R, transmission coefficient, T, and absorption coefficient, A. The incident and reflected pressure components at the input are also shown separately above and below the reflection coefficient, respectively, and the pressure at the output is also shown next to the transmission coefficient.

coefficient can be calculated using its definition as

$$R = \frac{p_{in}^-}{p_{in}^+}, \tag{5.78}$$

where p_{in}^+ is the incident pressure wave at the input boundary, $x = 0$, and p_{in}^- is the reflected wave at $x = 0$. The total pressure and volume velocity at $x = 0$ are given, respectively, by

$$p_{in} = p_{in}^+ + p_{in}^- \text{ and } q_{in} = \frac{1}{Z_0}\left(p_{in}^+ - p_{in}^-\right). \tag{5.79}$$

By manipulating the two equations of Equation (5.47), also using Equations (5.78) and (5.79), the reflection coefficient can be written as

$$R = \frac{T_{11} + \dfrac{T_{12}}{Z_{end}} - Z_0 T_{21} - \dfrac{Z_0}{Z_{end}} T_{22}}{T_{11} + \dfrac{T_{12}}{Z_{end}} + Z_0 T_{21} + \dfrac{Z_0}{Z_{end}} T_{22}}. \tag{5.80}$$

The transmission coefficient is defined as the ratio of the transmitted wave beyond the end of the waveguide to the incident wave at the input,

$$T = \frac{p_{end}^+}{p_{in}^+}, \tag{5.81}$$

where p_{end}^+ is the transmitted pressure at the output, which coincides with the total pressure

there in the absence of reflections from the semi-infinite termination. The pressure and volume velocity at $x = l_{tot}$ are given by

$$p_{end} = p^+_{end} \text{ and } q_{end} = \frac{1}{Z_{end}} p^+_{end}. \tag{5.82}$$

Combining Equations (5.47), (5.81) and (5.82) yields

$$T = \frac{2}{T_{11} + \frac{T_{12}}{Z_{end}} + Z_0 T_{21} + \frac{Z_0}{Z_{end}} T_{22}}. \tag{5.83}$$

The power absorption coefficient, or, simply, the absorption coefficient, is the ratio of the power absorbed within the waveguide to the incident power, so that it can be calculated by

$$A = 1 - R_p - T_p, \tag{5.84}$$

where R_p and T_p are the power reflection coefficient and the power transmission coefficient, defined as the ratios of the reflected and the transmitted power, respectively, to the incident power, given by [48]

$$R_p = |R|^2 \tag{5.85}$$

and

$$T_p = \frac{Z_0}{Z_{end}} |T|^2. \tag{5.86}$$

The absorption coefficient can thus be written with respect to the amplitude reflection and transmission coefficients, given by Equations (5.80) and (5.83), as

$$A = 1 - |R|^2 - \frac{Z_0}{Z_{end}} |T|^2. \tag{5.87}$$

Two special cases for the termination of the waveguide are considered. First, the system is considered to be terminated by a semi-infinite continuation of the main duct, or, equivalently, by a load matched with the characteristic impedance of the main duct, so that $Z_{end} = Z_0$. The transmission coefficient is then given by

$$T = \frac{2}{T_{11} + \frac{T_{12}}{Z_0} + Z_0 T_{21} + T_{22}}, \tag{5.88}$$

and the reflection coefficient by

$$R = \frac{T_{11} + \frac{T_{12}}{Z_0} - Z_0 T_{21} - T_{22}}{T_{11} + \frac{T_{12}}{Z_0} + Z_0 T_{21} + T_{22}}. \tag{5.89}$$

The absorption coefficient, accordingly, takes the form

$$A = 1 - |R|^2 - |T|^2. \tag{5.90}$$

The second case involves a rigid termination, where $Z_{end} \to \infty$. The amplitude transmission coefficient defined by Equation (5.81) and calculated by Equation (5.83) only gives the amplitude ratio of the transmitted pressure to the incident one. The transmitted volume velocity, however, given by the second of Equations (5.82), is zero in this case, so that no power is transmitted beyond the rigid termination, as can also be seen from Equation (5.86) for $Z_{end} \to \infty$; thus the amplitude transmission coefficient can be neglected. The absorption coefficient of Equation (5.87), which represents the ratio of absorbed power to the incident power, takes the form

$$A = 1 - |R|^2, \tag{5.91}$$

and the reflection coefficient of Equation (5.80) becomes

$$R = \frac{\frac{T_{11}}{T_{21}} - Z_0}{\frac{T_{11}}{T_{21}} + Z_0}. \tag{5.92}$$

For $q_{end} = 0$ due to the rigid termination, it can be deduced from Equation (5.47) that $T_{11}/T_{21} = Z_{in}$, so that Equation (5.92) coincides with Equation (5.77).

5.5 Analysis of previously designed 'rainbow' sensors

The responses of two systems from the literature are discussed in this section, calculated with the Transfer Matrix method. Both systems consist of a main duct with a number of Helmholtz-Resonator side branches of varying geometrical properties. The main difference between the two systems is that in the first one, presented in [1] and shown in Figure 5.1b, the main duct has different geometrical properties for the different elements, while in the second one, presented in [2] and shown in Figure 5.1a, the main duct has constant cross section throughout the system.

5.5.1 Model of Jimenez et al. [1]

The system shown in Figure 5.12a was designed and experimentally tested in [1]. The system comprises a 10x3 array of a unit cell along the direction of its width and height, respectively. The unit cell consists of a main duct of varying height with a series of $N = 9$ side branches of Helmholtz Resonators of varying dimensions, as shown in Figure 5.12b. The dimensions of the geometrical features of the system are optimised by an iterative procedure in order to maximise its absorption, described in [1], with the additional restriction of rounding the dimensions to

precision 0.1 mm, due to the limitations of the additive manufacturing equipment used. It should be noted that the side of the square cross section of the necks is about 1 mm for all the resonators.

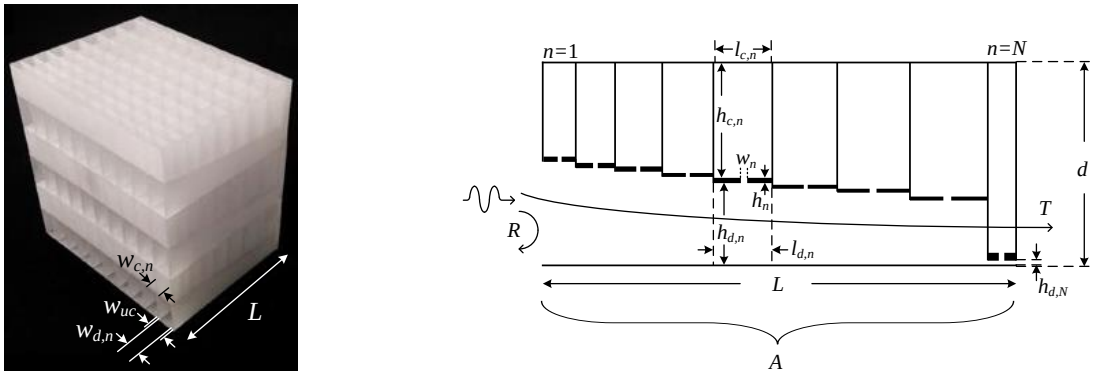

(a) (b)

Figure 5.12. (a) Photograph of the system with Helmholtz Resonators experimentally tested in [1], whose unit cell of length L, consisting of a main duct and nine Helmholtz Resonators, is periodically repeated ten times along the direction of its width and three times along the direction of its height. The width of the main duct of the n-th element, w_d, the width of the n-th resonator cavity, $w_{c,n}$, and the width of the unit cell, w_{uc}, are also shown. The image is taken from Figure 5a in [1]; the widths have been added to the image. (b) Schematic of a cross section along the length, L, of a unit cell of the system shown in (a). The direction of incidence is noted, along with the reflection, transmission and absorption coefficients. The height of the main duct of the n-th element, $h_{d,n}$, and of the last element, $h_{d,N}$, the height of the n-th resonator cavity, $h_{c,n}$, the height of the unit cell, d, the length of the main duct of the n-th element, $l_{d,n}$, the length of the n-th resonator cavity, $l_{c,n}$, the thickness of the n-th neck, h_n, and the width of the square cross section of the n-th neck, w_n, are also shown. The schematic is based on Figures 6 and 1d in [1]. The article [1] is published in open access under a Creative Commons Attribution 4.0 International License, https://creativecommons.org/licenses/by/4.0/.

In [1], the wavenumbers and characteristic impedances for the calculation of the Helmholtz Resonator impedance, given by Equation (5.57), and for the Transmission Matrix of the duct, given by Equation (5.51), are calculated by [1]

$$k_j = \omega\sqrt{\frac{\rho_j}{\kappa_j}} \tag{5.93}$$

and

$$Z_j = \frac{\sqrt{\rho_j \kappa_j}}{b_1 b_2}, \tag{5.94}$$

respectively, where b_1 and b_2 are the two sides of the rectangular cross section, the subscript j can be substituted by appropriate subscripts for the neck, the cavity or the main duct, and the corresponding complex densities and bulk moduli are given by [95]

$$\rho_j = \rho\frac{\eta b_1^2 b_2^2}{4\mathrm{i}\omega}\left[\sum_{l=0}^{\infty}\sum_{m=0}^{\infty}\left[\chi_l^2\psi_m^2\left(\chi_l^2+\psi_m^2+\frac{\mathrm{i}\omega}{\eta}\right)\right]^{-1}\right]^{-1} \tag{5.95}$$

and

$$\kappa_j = \kappa_0\left[\gamma - \frac{4\mathrm{i}\omega\rho\mathrm{Pr}(\gamma-1)}{\eta b_1^2 b_2^2}\sum_{l=0}^{\infty}\sum_{m=0}^{\infty}\left[\chi_l^2\psi_m^2\left(\chi_l^2+\psi_m^2+\frac{\mathrm{i}\omega\rho\mathrm{Pr}}{\eta}\right)\right]^{-1}\right]^{-1}, \tag{5.96}$$

respectively, where $\kappa_0 = \gamma P_{atm}$ is the lossless bulk modulus, where P_{atm} is the atmospheric pressure, and the constants χ and ψ in the infinite sum are given by $(l+0.5)/b_1$ and $(m+0.5)/b_2$, respectively. The values for the different parameters used in [1] are $\rho = 1.213$ kg·m^{-3}, Pr=0.71, $\gamma = 1.4$, $P_{atm} = 101325$ Pa and $\eta = 1.839 \cdot 10^{-5}$ kg·m^{-1}·s^{-1}.

Apart from the end corrections for the neck, calculated with Equations (5.63) and (5.64), additional end corrections for the radiation between waveguide segments are used, calculated by [1]

$$l_{cor,d,n} = 0.82 \left[1 - 1.35 \frac{r_{d,n}}{r_{d,n-1}} + 0.31 \left(\frac{r_{d,n}}{r_{d,n-1}} \right)^3 \right] r_{d,n}. \tag{5.97}$$

The corresponding radiation impedance is given by [1]

$$Z_{rad,n} = \mathrm{i}\omega\rho \frac{l_{cor,d,n}}{\phi_n S_{d,n}}, \tag{5.98}$$

where $\phi_n = r_{d,n-1}/r_{d,n}$, where $r_{d,n}$ is the hydraulic radius of the n-th duct segment, defined by Equation (5.62), and $S_{d,n} = h_{d,n} w_{d,n}$ is the cross-sectional area of the n-th duct segment. For the end correction of the first duct segment, $r_{d,0}$ is the hydraulic radius of the unit cell. For the radiation from the array of unit cells to free space, an end correction due to a periodic array of slits is used [1],

$$l_{cor,d,N+1} = \sigma h_{d,N} \sum_{m=1}^{\infty} \frac{\sin^2(m\pi\sigma)}{(m\pi\sigma)^3}, \tag{5.99}$$

where $\sigma = h_{d,N}/d$. The corresponding radiation impedance is written as [1]

$$Z_{rad,N+1} = \mathrm{i}\omega\rho \frac{l_{cor,d,N}}{\phi_N S_0}, \tag{5.100}$$

where $\phi_N = d/h_{d,N}$ and where $S_0 = w_{uc} d$ is the cross-sectional area of the unit cell.

The n-th Transfer Matrix is written as

$$\mathbf{T}_n = \mathbf{T}_{hd,n} \mathbf{T}_{H,n} \mathbf{T}_{hd,n} \mathbf{T}_{rad,n+1}, \tag{5.101}$$

where

$$\mathbf{T}_{hd,n} = \begin{bmatrix} \cos \frac{k_{d,n} l_{d,n}}{2} & \mathrm{i} Z_{d,n} \sin \frac{k_{d,n} l_{d,n}}{2} \\ \frac{\mathrm{i}}{Z_{d,n}} \sin \frac{k_{d,n} l_{d,n}}{2} & \cos \frac{k_{d,n} l_{d,n}}{2} \end{bmatrix}, \tag{5.102}$$

where $k_{d,n}$ and $Z_{d,n}$ are calculated with Equations (5.93) and (5.94) for the corresponding duct segments,

$$\mathbf{T}_{H,n} = \begin{bmatrix} 1 & 0 \\ \frac{1}{Z_{H,n}} & 1 \end{bmatrix}, \tag{5.103}$$

where $Z_{H,n}$ is calculated with Equation (5.57) with the appropriate wavenumbers, characteristic impedances and correction lengths presented in this section, and the Transmission Matrix due

to radiation is given by [1]

$$\mathbf{T}_{rad,n} = \begin{bmatrix} 1 & Z_{rad,n} \\ 0 & 1 \end{bmatrix}. \tag{5.104}$$

The total Transfer Matrix is given by

$$\mathbf{T} = \mathbf{T}_{rad,1}\mathbf{T}_1\mathbf{T}_2 \dots \mathbf{T}_{N-1}\mathbf{T}_N. \tag{5.105}$$

The reflection, transmission and absorption coefficients are calculated with Equations (5.89), (5.88) and (5.90) where $Z_0 = \rho c_0/S_0$.

The absorption coefficient is plotted in Figure 5.13, calculated with two different loss models, along with the absorption coefficient measured experimentally, the latter taken from [1]. Loss model 1 in the figure corresponds to using the complex wavenumbers and characteristic impedances calculated with Equations (5.93) and (5.94), using the complex density and complex bulk modulus of Equations (5.95) and (5.96), whereas loss model 2 corresponds to using the complex wavenumbers and characteristic impedances calculated with Equations (5.60) and (5.61).

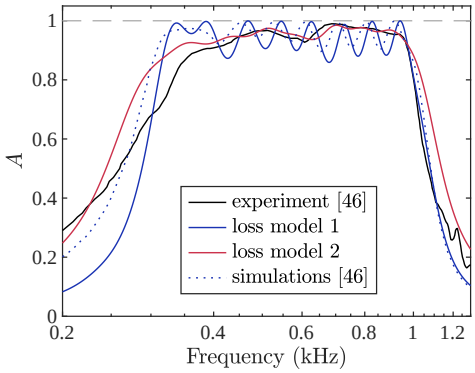

Figure 5.13. Absorption coefficient with two different loss models compared with that experimentally measured in [1]. Loss model 1 corresponds to using the complex density and bulk modulus of Equations (5.95) and (5.96) for the calucaltion of the wavenumber and the characteristic impedance, given by Equations (5.93) and (5.94), while loss model 2 corresponds to calculating the wavenumber and characteristic impedance with Equations (5.60) and (5.61). The experimental results have been taken from Figure 5b in [1]. The dotted line corresponds to the absorption coefficient calculated with loss model 1, taken form Figure 5b in [1], although it does not coincide with the correponding solid line, produced with the analysis presented here. The article [1] is published in open access under a Creative Commons Attribution 4.0 International License, https://creativecommons.org/licenses/by/4.0/.

The absorption coefficient with loss model 1, as implemented in [1], is also plotted as a dotted line in Figure 5.13, taken from Figure 5b in that article. It should be noted that in the formulas of [1] given in this section for the calculation of the losses and for the end corrections, a number of unclear points have been identified, especially regarding the specific dimensions used in different formulas. In the formulas given above, the hydraulic radii have been used in cases where the exact dimensions used are not clarified in [1]. It can be seen that the results taken from [1], plotted as a dotted blue line in Figure 5.13, do not exactly coincide with those produced here, plotted as a solid blue line in the figure, which may be attributed to differences

in the exact dimensions used for the end corrections.

A comparison of the results from simulations with the ones from the experiment plotted in Figure 5.13 illustrates that loss model 1, either as implemented here or in [1], produces considerably greater fluctuations in the frequency band of high absorption. Loss model 2, on the other hand, matches well with the experiment in most of this band. Therefore, in the following analysis of this chapter, loss model 2 is mainly used.

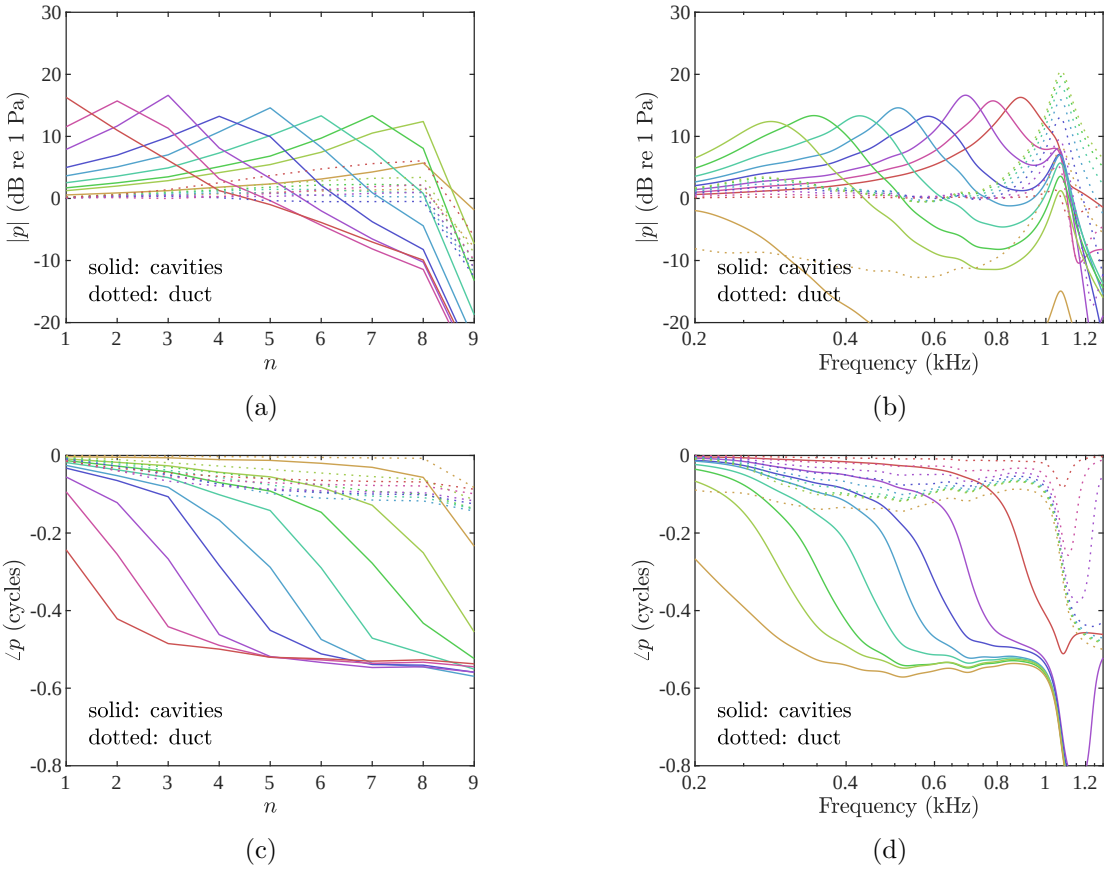

Figure 5.14. (a) Modulus and (c) phase of the pressure at the top of the cavities (solid lines) and in the main duct at the positions of the side branches (dotted lines) plotted against the number of element, n, at the eight frequencies of peak response in the cavities. The solid line that peaks at the first element in (a) corresponds to the highest frequency of peak response in the cavities in (b), and the solid lines that peak at progressively further elements correspond to sequentially lower peak frequencies in the cavities. (b) Modulus and (d) phase of the pressure at the top of the cavities (solid lines) and in the main duct at the positions of the side branches (dotted lines) plotted against frequency, for the nine different elements. The solid line that peaks at the lowest frequency, around 280 Hz, corresponds to the penultimate element, and the solid lines that peak at progressively higher frequencies correspond to sequentially preceding elements. The solid line of consistently low response, below 0 dB, corresponds to the last element.

A set of plots for the modulus and the phase of the pressure in the duct and at the top of the cavities, calculated using the Transfer Matrix method with loss model 2, is given in Figure 5.14, where a constant pressure of 1 Pa at the input boundary is used as an input to the system. The pressure at the top of the cavities is calculated with Equation (5.59) and is plotted with solid lines, and the pressure in the duct at the positions of the side branches is calculated with Equation (5.58) and is plotted with dotted lines. It can be seen in Figure 5.14 that for a given frequency the pressure in the cavities increases along the system, until it reaches a maximum

at a given element, beyond which it decreases. The element of peak pressure depends on the excitation frequency, with higher frequencies peaking at elements close to the input and lower frequencies peaking at elements further along the system. The pressure in the duct slightly increases up to the penultimate element.

A similar behaviour is observed in the frequency responses for the individual resonators plotted in Figure 5.14b. The pressure in the cavities peaks at a different frequency for the different elements, with the elements close to the input having peaks at higher frequencies and the ones further on having peaks at lower frequencies. The pressure in the main duct peaks at a frequency beyond the band of high absorption.

In the phase plots against the element number shown in Figure 5.14c, it can be seen that the phase changes rapidly up to the element slightly further from the element of peak response, beyond which it changes very slightly. Accordingly, in the phase plots against frequency shown in Figure 5.14d, the phase changes rapidly up to a frequency slightly higher than the peak frequency, beyond which it changes very slightly. In general, the phase shift in the cavities is small, of the order of half a cycle. The phase shift in the main duct is very small.

The focusing of different frequency components at different elements and the corresponding smooth frequency response of the different elements produces a tonotopic mapping similar to that observed in the cochlea. Therefore, simulations imply that this system, apart from a broadband absorber, may also be used as an acoustic 'rainbow' sensor, although this aspect of its behaviour was not explored in [1].

5.5.2 Model of Zhao and Zhou [2]

A different system was proposed in [2], consisting of a main duct of constant cross section and an array of Helmholtz-Resonator side branches, as shown in Figure 5.15a, where the coiling of the main duct is not considered to affect the acoustic response of the system. Therefore, this system is similar to the system shown in Figure 5.8. Additionally, in the system of Figure 5.15a, the element length is also constant, unlike the more general case presented in Figure 5.8, where it is allowed to vary. The varying parameter of the elements is the height of the resonators, which increases linearly along the system. The main duct is terminated at a rigid wall. The determined dimensions of the system are given in [2], but it is interesting to note that the radius of the neck was 0.7 mm for all the resonators.

The absorption coefficient and the modulus of the reflection coefficient are plotted against frequency in Figure 5.15b. A band of approximately constant absorption with an absorption coefficient of about 0.95, and accordingly, of constant reflection with a reflection coefficient of modulus around 0.2, can be seen between about 1.2 and 2.5 kHz. Outside these frequencies, the modulus of the reflection coefficient and the absorption coefficient fluctuate with frequency, although they present dips of low reflection and peaks of high absorption, respectively. Above

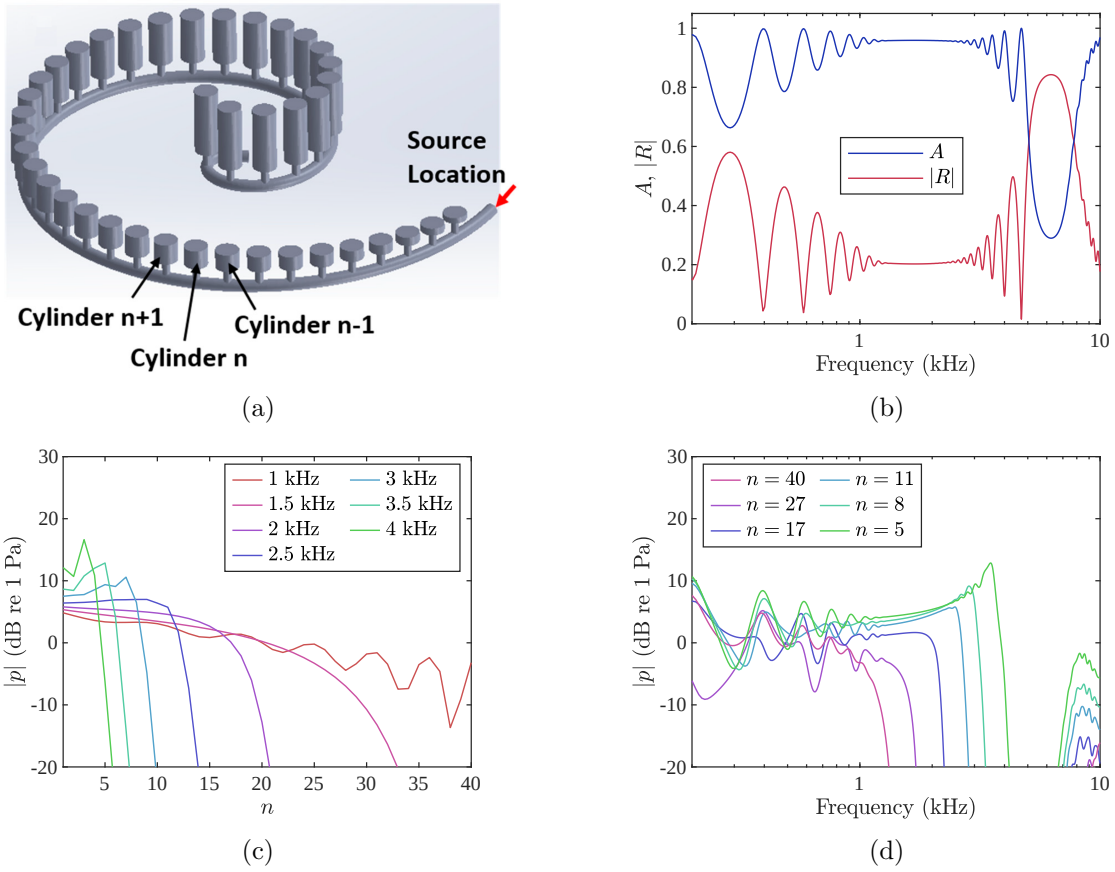

Figure 5.15. (a) Three-dimensional schematic of the system presented in [2]. The image is taken from Figure 1d in [2], which is published in open access under a Creative Commons Attribution 4.0 International License, https://creativecommons.org/licenses/by/4.0/. (b) The calculated absorption and modulus of the reflection coefficient plotted against frequency. (c) Modulus of the pressure at the top of the cavities plotted against the number of element, n, for seven different frequencies. (d) Modulus of the pressure at the top of the cavities plotted as a function of frequency, for six different elements; the natural frequencies are 4.12, 3.43, 3, 2, 2.48 and 1.66 kHz for the 5th, 8th, 11th, 17th, 27th and 40th element, respectively. An excitation volume velocity of $2 \cdot 10^{-8}$ $\mathrm{m}^3 \cdot \mathrm{s}^{-1}$ is used for all simulations.

2.5 kHz, these coefficients also fluctuate up to about 5 kHz, beyond which frequency a band of high reflection is observed. At even higher frequencies, incident waves are again absorbed.

The modulus of the pressure at the top of the cavities is plotted against position for seven different excitation frequencies in Figure 5.15c. At the higher frequencies plotted, the pressure increases up to an element close to the input, which is different for different frequencies, beyond which it rapidly decays. Fluctuations are observed in the modulus of the pressure before the peak, due to reflections. At 1.5 and 2 kHz, the pressure decays rapidly beyond a specific element, without, however, forming a peak before that. At a frequency of 1 kHz, the wave travels all the way to the end of the system, with fluctuations due to reflection and with its amplitude gradually decreasing.

The modulus of the pressure at the top of the cavities is plotted against frequency for six different elements in Figure 5.15d. At lower frequencies, up to about 1.2 kHz, the pressure modulus is seen to fluctuate with frequency. Beyond this frequency, the pressure for the elements closer to the base, that is, with smaller n, increases up to a certain frequency, beyond which it

rapidly decreases. Fluctuations are also observed in the frequency response close to the peak frequency. For the elements closer to the apex, however, the pressure modulus does not form a peak beyond the low-frequency band of fluctuating pressure modulus, only reaching a frequency beyond which the pressure rapidly decays. This unevenness of the frequency response is also shown in Figure 3 of [2], reproduced in Section 1.2 above.

In conclusion, the form of the frequency response does not appear to be suitable for an acoustic 'rainbow' sensor, since the fluctuations near the peak of the frequency response may compromise the efficiency of the respective elements as pass-band filters around the peak frequency. Additionally, a large proportion of the elements towards the apex do not present a frequency response peak.

5.6 Design of an acoustic 'rainbow' sensor with Helmholtz Resonators based on a discrete model of the cochlea

The continuous cochlea can be analysed by a discrete elemental model, which, if only one-dimensional fluid coupling and no longitudinal coupling are assumed, reduces to a Transmission Line model. This is equivalent to the Finite Difference method used in Section 4.3.2 [71]. Therefore, an acoustic system consisting of discrete elements could be designed to reproduce the behaviour of the cochlea, using a Transmission Line model, provided that a sufficiently large number of elements was used. Such systems that aim at imitating the behaviour of the cochlea to a greater or lesser extent are often called 'artificial cochleae' [75]. The geometrical parameters of the elements should vary smoothly, so that adjacent elements can be considered as approximating an array of identical elements. Thus, the analysis of an array of identical Helmholtz Resonators in Section 5.3 can be used on the assumption that the parameters are only changing slowly. However, in the case of spatially varying elements, the coupled characteristic impedance, given by Equation (5.27) for the system with identical resonators, also varies along the system. Therefore, to calculate the reflection coefficient with Equation (5.40), the input impedance needs to be calculated, which can be achieved using Transfer Matrices.

A system consisting of a main duct of constant cross section with Helmholtz-Resonator side branches of varying geometrical properties is shown in Figure 5.16. The aim of the following analysis is to present a physically motivated design for the geometrical properties of the system, so that it manifests the kind of tonotopic mapping present in the cochlea. Additionally, the designed model aims at reproducing the smooth envelope of the coupled cochlear response, both with respect to position and frequency, that is, without having any ripples, which results from the absence of reflections within the cochlea at its normal functioning. In the following analysis, the input position of the system will also be referred to as the base and the terminating position as the apex, and elements in the respective sides will be referred to as basal and apical,

in analogy with the cochlea.

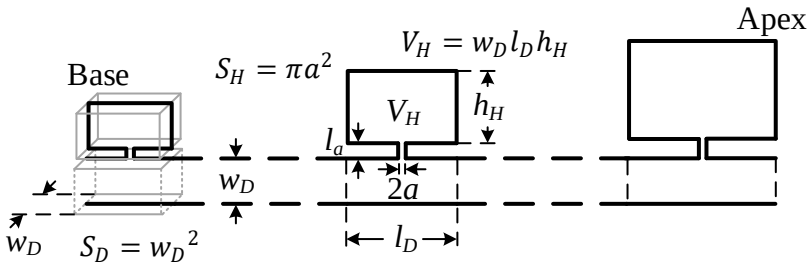

Figure 5.16. Schematic of a longitudinal cross section along the mid-width plane of a square-cross-section duct of side w_D, with side branches consisting of Helmholtz Resonators with varying geometry. The neck radius, a, and length, l_a are shown, along with the cavity volume V_H. Each element of the system consists of a duct segment of length l_D and a Helmholtz Resonator. The length and width of each cavity are the same as those of the corresponding duct segment, and the height of each cavity is denoted by h_H. Formulas for the cross-sectional area of the duct, S_D, and of the neck, S_H, are shown, as well as for the volume of the cavity. The left and right ends of the system correspond to the base and the apex of the cochlea, respectively, as is also noted.

The design of the system by Zhao and Zhou presented in Section 5.5.2 was inspired by the cochlea. In that system, however, only some general characteristics of the design were based on the analogy with the cochlea, so that it failed to reproduce the smooth envelope of the coupled cochlear response. Also, the geometry in the design of Jimenez et al, discussed in Section 5.5.1, was obtained with a numerical optimisation algorithm and so the physical insight into the importance of the various dimensions was lacking. Although the original design of the system presented below was carried out by the author's supervisor, Stephen Elliott, the author further elaborated on some design aspects. The simulations of the designed model and the discussion are entirely the author's work.

5.6.1 Distribution of elements

In the continuous cochlea, the tonotopic mapping of the natural frequency with position on the basilar membrane can be approximated by [13]

$$f_n = f_B \mathrm{e}^{-x/l}, \tag{5.106}$$

where f_B is the natural frequency at the base and l is an exponential decrease length. If an equivalent discrete system with equally spaced elements is considered, then the natural frequency of the n-th element is given by

$$f_n(n) = f_B \mathrm{e}^{-(n-1)\Delta/l}, \tag{5.107}$$

where Δ is the length of each element. The ratio of the natural frequencies of two consecutive elements is given by

$$\frac{f_n(n)}{f_n(n+1)} = \mathrm{e}^{\Delta/l}, \tag{5.108}$$

which is fixed for given Δ. It should be noted that a constant element length is only considered in this section to estimate the distribution of elements per octave; the element length of the designed system is actually varying.

To calculate the number of elements per octave, two elements are considered, where the natural frequency of the more apical element is half that of the more basal element. Using Equation (5.107), the number of elements per octave is calculated as

$$f_n(n_2) = \frac{1}{2} f_n(n_1) \Rightarrow f_B \mathrm{e}^{-(n_2-1)\Delta/l} = \frac{1}{2} f_B \mathrm{e}^{-(n_1-1)\Delta/l} \Rightarrow N_{oct} \approx \frac{0.7l}{\Delta}, \tag{5.109}$$

where $N_{oct} \equiv n_2 - n_1$ is the number of elements per octave. An estimate of an appropriate number of elements per octave can be found by combining two requirements. First, the minimum wavelength should be at least six times larger than the element length, which can conveniently be defined as $\lambda_{min} = 2\pi\Delta$. If the band gap is large, the minimum wavelength is given by Equation (5.39), so that the element length can be written as

$$\Delta = d\sqrt{\frac{2}{Q}}. \tag{5.110}$$

The second requirement is that the number of cycles of phase shift from the base to the characteristic position should be approximately given by the phase-shift parameter introduced in [65], defined as

$$N_c = \frac{l}{4d}, \tag{5.111}$$

which was also discussed in Chapter 4 and shown to be important in achieving the correct shape of frequency response. Combining the result from Equation (5.109) with Equations (5.110) and (5.111), and applying algebraic approximations, gives a relation for the number of elements per octave for given N_c and Q as

$$N_{oct} \approx 2N_c\sqrt{Q}. \tag{5.112}$$

It is thus clear that the choice of the damping in the resonators allows for a trade-off in the design between good frequency selectivity, high Q, and the number of elements required for a given frequency range, low Q. The attenuation per octave in the stop band can then be calculated as

$$\mathrm{Att_{oct}} = \mathrm{e}^{-\Delta N_{oct}/d} \approx \mathrm{e}^{-2.8N_c}, \tag{5.113}$$

where it has been assumed that the decay rate in the stop band is given by d, in accordance with Equation (5.31).

5.6.2 Number of elements

The number of cycles of phase shift has been taken to be $N_c = 2.5$, which is a good approximation for the human cochlea, as can be seen for example in the phase plots in [13]. Therefore, the attenuation per octave, given by Equation (5.113), becomes $\text{Att}_{\text{oct}} \approx 60$ dB/octave. If it is assumed that an attenuation of 30 dB per octave in the stop band is sufficient, then a band gap of at least half an octave should be used, that is,

$$\frac{\omega_2}{\omega_1} \geq \sqrt{2}, \tag{5.114}$$

which, in geometrical terms, implies that $V_H \geq S_D l_D$, according to Equation (5.23).

The system is aimed at working in the standard telecommunications bandwidth of 300 Hz to 3.4 kHz, which is about 3.5 octaves. Therefore, the basal and apical natural frequencies are set to be $f_B = 3.4$ kHz and $f_A = 300$ Hz, respectively. Assuming a neck radius of $a = 0.5$ mm, the quality factor for the first and the last element can be calculated from Equation (5.12), giving $Q_B = 17.5$ and $Q_A = 5.2$ for the basal and apical element. The number of elements per octave, calculated by Equation (5.112) with the respective values for Q for the basal and apical elements, takes approximately the values 21 and 11. On average, it can be assumed that around 15 elements per octave are required, so that for the 3.5 octaves of the considered bandwidth, around 50 elements are required in total.

5.6.3 Design of the first element

For design convenience, a duct of square cross section is used, whose height and width, w_D, is equal to the width of the cavity. The length of each cavity is also assumed to coincide with the length of the corresponding element, l_D, as can be seen in Figure 5.16 in the three-dimensional sketch of the first element. All the geometrical parameters of the Helmholtz Resonators vary for each element, except for the neck radius, which has the value $a = 0.5$ mm for all the resonators, so that the neck cross-sectional area is $S_H = \pi a^2 = 0.25\pi \cdot 10^{-6}$ m^2 for all the resonators. For the design of the system, the effective length of the neck, l_H, which includes end corrections, will be defined first, as this is primarily involved in the physical calculations, rather than the actual neck length, l_a. The latter will be defined from the former afterwards.

The effective neck length is assumed to be $l_H = 2a = 1$ mm for the first element. The volume of the cavity can be calculated from Equation (5.10) for this element, giving

$$V_H = \frac{S_H}{l_H}\left(\frac{c_0}{\omega_B}\right)^2 \approx 2 \cdot 10^{-7} \text{ m}^3, \tag{5.115}$$

where $\omega_B = 2\pi f_B = 2\pi \cdot 3.4$ kHz is the resonance angular frequency of the basal Helmholtz Resonator. The height of the cavity is set to vary according to $h_H = w_D H$, where H is a non-dimensional parameter. The band gap is defined here for convenience, based on

Equation (5.23), as

$$G_s \equiv \frac{\omega_2}{\omega_1} = \left[1 + \frac{C_H}{C_D}\right]^{1/2} = [1 + H]^{1/2}, \tag{5.116}$$

where the subscript s denotes the stop band, and $H = h_H/w_D = V_H/V_D = C_H/C_D$, where the volume of the cavity is given by $V_H = l_D w_D h_H = H l_D S_D$, and $V_D = l_D S_D = l_D w_D^2$ is the volume of the duct segment of the basal element. To keep the volume of the cavity as small as possible relative to the volume of the duct of the same element, the smallest value required for the band gap, as defined by Equation (5.114), is chosen, that is, $G_s = \sqrt{2}$ in Equation (5.114). Therefore, it follows from Equation (5.116) that $H = 1$ and, therefore, $V_H = V_D$ and $h_H = w_D$ for this first element.

In the analysis of the system with the identical resonators in Section 5.3, it was assumed that the band gap is large. This assumption led to the specific forms for Equations (5.34), (5.38), (5.39) and, consequently, for Equation (5.41). Here the band gap has the value $\sqrt{2}$, so that the approximations applied for these equations are not necessarily justified. In particular, the decay length, defined in (5.32), using Equations (5.23) and (5.33), now takes the form $d = l_D\sqrt{\mu/2}$. If it is assumed that Equation (5.39) is still valid for $G_s = \sqrt{2}$, the ratio of the minimum wavelength to the element length is now given by

$$\frac{\lambda_{min}}{l_D} = 2\pi\sqrt{\frac{\mu}{Q}}. \tag{5.117}$$

For this ratio to be equal to 2π, the inertance ratio has to be equal to the quality factor, $\mu = Q$. Using the relation $V_H = V_D = l_D S_D$ and the definition of the inertance ratio in Equation (5.33), the cross-sectional area of the duct is calculated as

$$S_D = \sqrt{\frac{Q_B V_H S_H}{l_H}} = 5.2 \cdot 10^{-5}\ \mathrm{m}^2, \tag{5.118}$$

where $Q_B = 17.5$, as mentioned in Section 5.6.2. Therefore, the width of the square-cross-section duct is $w_D = \sqrt{S_D} = 7.2$ mm, and so is the height of the basal cavity, $h_H = 7.2$ mm. The element length can then be calculated as $l_D = V_H/S_D = 3.8$ mm.

5.6.4 Design of the last element

The neck radius and, therefore, the neck cross-sectional area are kept constant for all elements. The width of the duct is also constant for all elements and so it is the same as that calculated above for the first element, $w_D = 7.2$ mm. The quality factor for the apical element has already been calculated in Section 5.6.2 as $Q_A = 5.2$. If it assumed that the volume of the cavity of the apical element is much larger than the volume of the respective duct segment, or, equivalently, that $H \gg 1$, then it follows from Equation (5.41) that the inertance ratio has to be $\mu = Q_A/2$ for the ratio of the minimum wavelength over the element length to be 2π.

Using the definition of the inertance ratio in Equation (5.33) and the requirement that

$\mu = Q_A/2$, the element length can be expressed as

$$l_D = \frac{2 l_H S_D}{S_H Q_A}. \tag{5.119}$$

From Equation (5.10), the neck effective length can be expressed as

$$l_H = \frac{S_H}{H l_D S_D} \left(\frac{c_0}{\omega_A} \right)^2. \tag{5.120}$$

Substituting Equation (5.120) into Equation (5.119) and solving for l_D gives

$$l_D = \frac{c_0}{\omega_A} \sqrt{\frac{2}{H Q_A}}. \tag{5.121}$$

Assuming that $H = 4$, the height of the apical element takes the value $h_H = H w_D = 29$ mm, and the element length is calculated to be $l_D = 56$ mm. The neck effective length is calculated from Equation (5.120) and is found to be $l_H = 2.2$ mm.

It should be noted that the thickness of the wall between adjacent cavities has not been taken into account in this initial design, since the inner length of an element cavity is assumed to be equal to the length of the duct segment of the same element. If the wall thickness is subtracted from the length of the cavity, its height could be adjusted to keep the volume unaltered.

5.6.5 Scaling of parameters along the system

Once the parameters of the first and last elements have been defined, the parameters of the intermediate elements can be derived by scaling according to the exponential decay of parameters observed in the cochlea. In analogy with the exponential variation of the natural frequency in the cochlea with position, given by Equation (5.106), it is assumed that the natural frequency in the system under design varies exponentially with the order of element, n,

$$f_n(n) = f_B \left(\frac{f_B}{f_A} \right)^{\frac{1-n}{N-1}}, \tag{5.122}$$

where N is the total number of elements. From Equations (5.12) and (5.122), the quality factor of each resonator can readily be calculated as

$$Q(n) = 600(a/\mathrm{m}) \sqrt{f_n(n)/\mathrm{Hz}}. \tag{5.123}$$

It can also be derived from Equation (5.122) that $f_n(n+1) = f_n(n)(f_B/f_A)^{-1/(N-1)}$, which, for $f_B = 3.4$ kHz, $f_A = 300$ Hz and $N = 50$, gives $f_n(n+1) \approx 0.95 f_n(n)$, that is, the natural frequency of each element is about 95% of that of the previous element.

The scaling parameter of the cavity height is assumed to also vary exponentially,

$$H(n) = 4^{\frac{n-1}{N-1}}. \tag{5.124}$$

For the scaling of the other parameters, another non-dimensional parameter is defined as

$$E(n) = 2^{\frac{n-1}{N-1}}. \tag{5.125}$$

It can be seen that $H(n) = E^2(n)$. The inertance ratio varies from $\mu(1) = Q(1)$ to $\mu(N) = Q(N)/2$, so that, if it is assumed to vary exponentially with the order of element, it can be expressed as

$$\mu = \frac{Q}{E}, \tag{5.126}$$

where the argument notation has been omitted for convenience, as is also done in subsequent expressions.

n	f_n (Hz)	Q	H	E	l_D (mm)	h_H (mm)	l_a (mm)	l_H (mm)	μ	G_s
1	3400	17.5	1	1	3.8	7.2	0.31 (0.3)	1	17.5	1.4
25	1035	9.7	2	1.4	14.3	14.2	0.74 (0.7)	1.5	6.9	1.7
50	300	5.2	4	2	56	29	1.44 (1.4)	2.2	2.5	2.2

Table 5.1. Designed properties of the first, twenty-fifth and fiftieth element of a system with an array of Helmholtz Resonators of varying geometry. The values in parentheses for the actual neck length, l_a, are rounded to a precision of 0.1 mm to comply with restrictions in additive manufacturing [1].

From Equations (5.10), (5.33) and (5.126), also using that $V_H = l_D S_D H$, $H = E^2$ and $\omega_n = 2\pi f_n$, the element length can be expressed as

$$l_D = \frac{c_0}{2\pi f_n}\sqrt{\frac{1}{EQ}}. \tag{5.127}$$

The effective neck length can be calculated from Equations (5.33), (5.126) and (5.127), giving

$$l_H = \frac{c_0 S_H}{2\pi f_n S_D}\frac{1}{E}\sqrt{\frac{Q}{E}}. \tag{5.128}$$

The actual neck length can be calculated as $l_a = l_H - l_{cor}$, where the correction length is calculated either with the simple form of Equation (5.13) or with the more accurate forms of Equations (5.63) and (5.64). The total length of the structure is calculated as

$$l_{tot} = \sum_{n=1}^{N} n l_D \approx 1 \text{ m}. \tag{5.129}$$

Table 5.1 indicatively shows the parameters for the first, twenty-fifth and fiftieth element, as calculated with Equations (5.122) to (5.128) and Equation (5.116), and with $h_H = H w_D$ and

$l_a = l_H - l_{cor}$, where the end corrections are calculated with Equations (5.63) and (5.64). Values for the actual neck length rounded to a precision of 0.1 mm are also shown in parentheses, to comply with restrictions in additive manufacturing precision [1].

5.7 Results from simulations

A set of results is first presented for a matched termination, using Transmission Matrices, as presented in Section 5.4.2. The end correction is calculated as the sum of the two end corrections given by Equations (5.63) and (5.64), and losses are included by using the wavenumbers and characteristic impedances given by Equations (5.60) and (5.61) for the various parts of the system in the Transmission Matrices. The input of the system is a constant volume velocity at the left side of the first element. An input volume velocity of $q_{in} = 2 \cdot 10^{-7}$ $\mathrm{m^3 \cdot s^{-1}}$ is used, which produces pressures close to 1 Pa at lower frequencies.

5.7.1 Wavenumber, propagation velocity and effective length results

The real and imaginary parts of the wavenumber, calculated with Equation (5.73), the wavelength and the phase and group velocities, calculated from the wavenumber, are plotted in Figure 5.17, both against the element number, n, and against frequency. The plots against n correspond to an excitation frequency of 1 kHz, and the plots against frequency correspond to the 26th element, whose resonance frequency is 985 Hz.

It can be seen that the frequency plots for the wavenumber and the wavelength, and those for the propagation velocities, shown in Figures 5.17b and 5.17d, are similar to the corresponding ones for the array of identical Helmholtz Resonators, shown in Figures 5.4a and 5.4b. However, there is a shift in the correspondence with the resonance frequency, f_1, and the upper pass-band cut-on frequency, f_2, of the considered resonator. This results from the fact that the wavenumber here is calculated with Equation (5.73) using the loss model of Equations (5.60) and (5.61), whereas for the array of identical resonators, the wavenumber, plotted in Figure 5.4a, is calculated with Equation (5.26), which uses the lumped-parameter loss model given in Section 5.2. Since the frequencies f_1 and f_2 are calculated with the lumped-parameter analysis, better correspondence between these frequencies and the wavenumber and propagation velocities is observed in the case of the lumped-parameter analysis of Section 5.3 than with those plotted here.

The spatial variation of the wavenumber and of the propagation velocities in Figures 5.17a and 5.17c is similar to their spectral variation in Figures 5.17b and 5.17d. The spatial response of the system for a given frequency implies that the wave slows down at an element slightly basal to the element of resonance, beyond which it is greatly attenuated, as indicated by the imaginary wavenumber. The very large phase velocity and negative group velocity, indicative of the wave nearly halting [48] and of strong 'pulse reshaping' [83], respectively, are observed

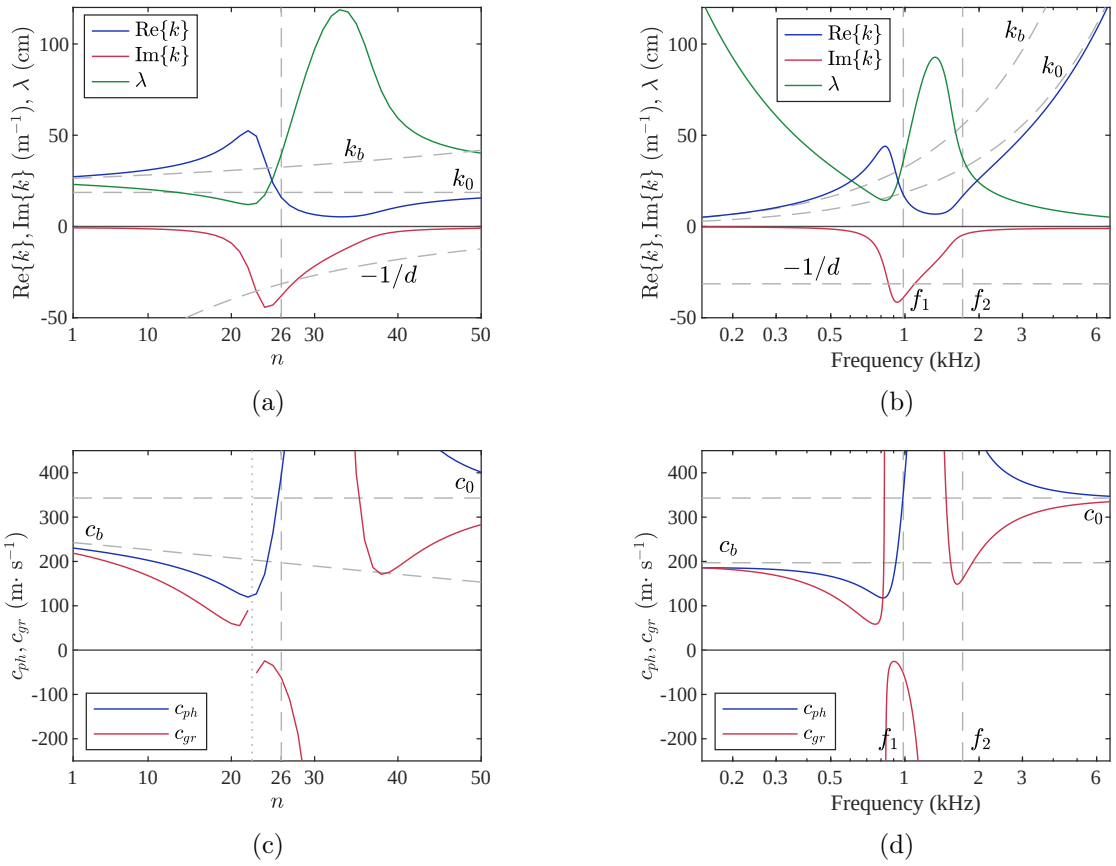

Figure 5.17. Simulations of the new design of 'rainbow' sensor using the detailed Transmission Matrix model terminated with a matched load; the impedance of the Helmholtz Resonators is calculated by the detailed form of Equation (5.57), the end corrections for the necks are calculated by Equations (5.63) and (5.64) and duct and cavity losses are included. (a) Real and imaginary parts of the wavenumber and local wavelength plotted against the number of element, n, for an excitation frequency of 1 kHz. (b) Real and imaginary parts of the wavenumber and local wavelength plotted against frequency, for the 26th element; wavelengths are plotted in cm. (c) Phase and group velocity plotted against n at 1 kHz. (d) Phase and group velocity plotted against frequency for $n = 26$. The dashed vertical lines in the plots against n denote the element used, and in the frequency plots the frequency of Helmholtz resonance, f_1, at the specified element and the cut-on frequency of the second pass-band, f_2. The dotted vertical line in (c) denotes the discontinuity of the group velocity from positive to negative values.

both in the spatial and spectral plots in Figures 5.17c and 5.17d, respectively, so that, apart from the stop band observed in frequency, a corresponding stop region in space also appears.

The normalised effective length, given by Equation (5.75), is plotted in Figure 5.18. The spectrum within the band of high absorption, defined by the vertical dotted lines, as discussed later, and slightly above this band is shown, as results for the effective length are not accurate outside this band, due to the minimum of the group velocity not being well defined there. It can be seen that the normalised effective length is larger than one in this frequency band. Therefore, the effective length is larger that the length of a waveguide whose elements are the same as the basal element and whose length is equal to the length from the base to the position of the first minimum of the group velocity of the considered system, which is at the 21st element for the example of Figure 5.17c. This means that the side branches of varying Helmholtz Resonators effectively lengthen the system, as they cause a wave pulse to slow down as it propagates through it. The ripples in the plot of Figure 5.18 are due to the discrete nature of the system.

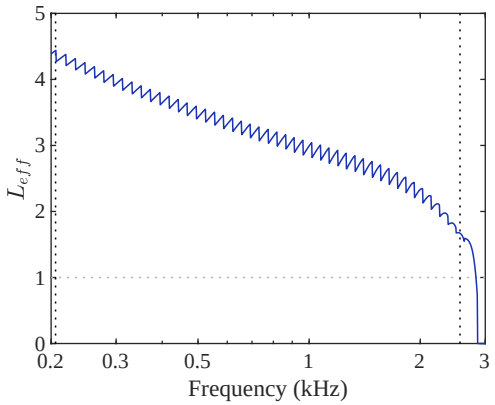

Figure 5.18. Frequency variation of the normalised effective length of the designed 'rainbow' sensor. The dotted vertical lines define the frequency band of high absorption, as can be seen in Figure 5.22.

5.7.2 Acoustic pressure results

The predicted variation of the modulus of the acoustic pressure along the waveguide, both in the cavities and in the main duct, is plotted against the element number, n, in Figure 5.19a, for three different frequencies. It can be seen that the pressure in the cavities, plotted with solid lines, builds up smoothly along the waveguide, reaching a peak at a specific element, after which it decreases rapidly. This variational pattern closely resembles the coupled response of the cochlea for the transverse velocity of the basilar membrane, as seen in Figure 4.7a.

The phase of the pressure along the waveguide is plotted in Figure 5.19c. It can be seen that the rate of decrease of the phase becomes greater at the location of the peak of the pressure modulus, after which it again starts decreasing more slowly. The larger phase shift at further positions is less important, since the response has already decreased to very small values there. The phase variation is also similar to that in the cochlea, plotted in Figures 4.6c and 4.7c. The phase in the cavities can be seen to drop more than that in the duct around the peak region, as was also observed for the phase in the basilar membrane velocity compared to the phase of the pressure in the cochlea.

It would be expected for the phase to lag by about N_c cycles at the peak position, where the phase-shift parameter was taken to be $N_c = 2.5$ when designing the system. It can be seen, however, that the phase shift from base to peak does not reach that value, although at the lowest frequency plotted, that is, at 0.5 kHz, the phase shift approaches it. The fact that at higher frequencies the phase shift from base to peak is less than that at lower frequencies may be attributed to the fact that it takes a considerable number of elements for the phase to accumulate, which is prevented at high frequencies by the small number of elements involved. This result agrees qualitatively with the behaviour of the cochlea, where the total phase shift is smaller at higher frequencies [13], as was also observed in the simulations in Section 4.4.

The modulus and phase of the pressure are plotted against frequency in Figures 5.19b and 5.19d for three different elements. The specified elements have resonance frequencies that

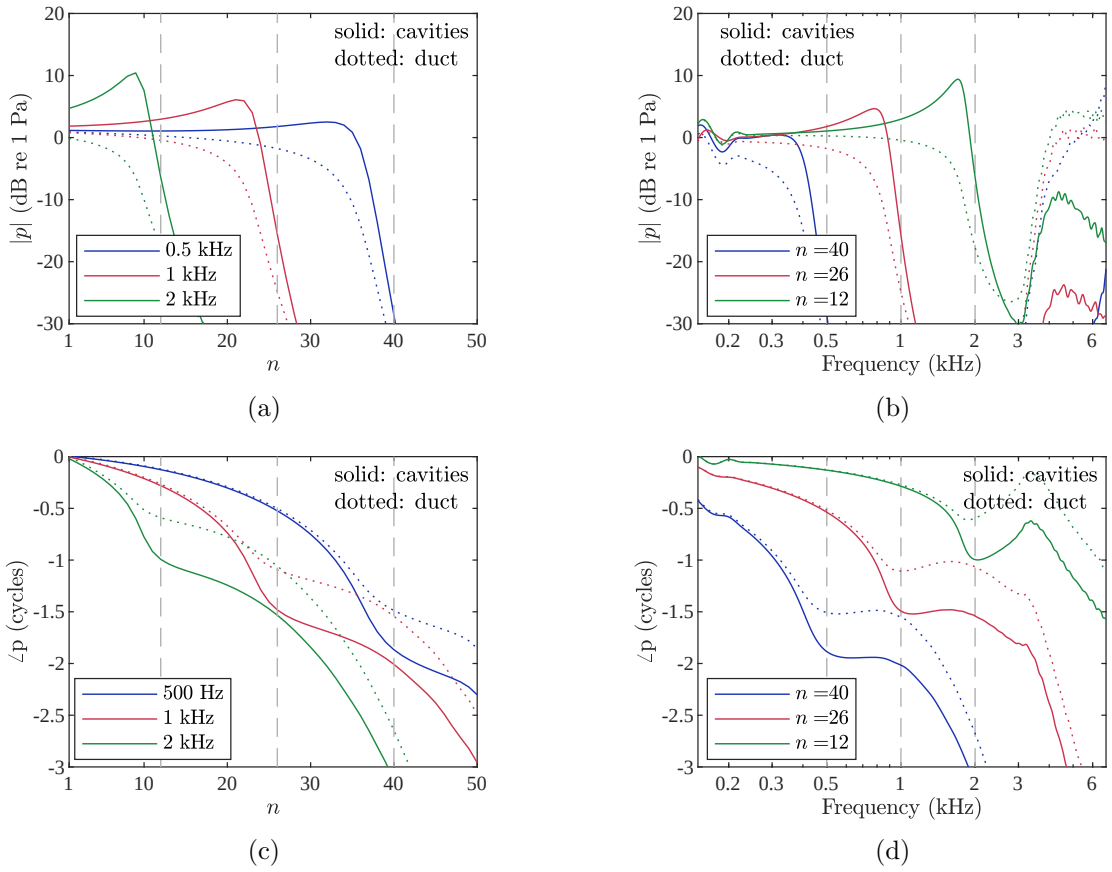

Figure 5.19. Pressure plots for a waveguide with matched load, using the specifications stated in the caption of Figure 5.17. (a) Modulus of the pressure plotted against the number of element, n, for three different excitation frequencies. (b) Modulus of the pressure plotted against frequency for three different elements. (c) Phase of the pressure plotted against n for three different excitation frequencies. (d) Phase of the pressure plotted against frequency for three different elements. In all plots, the solid lines correspond to the pressure in the cavities and the dotted lines to the pressure in the duct. In (a) and (c), the vertical lines correspond to the elements whose resonance frequency is the closest to the respective input frequency. In (b) and (d), the vertical lines correspond to the resonance frequencies of the elements used.

are the closest to the three excitation frequencies used in the plots against n. Specifically, elements 12, 26 and 40 have resonance frequencies 1.97 kHz, 985 Hz and 492 Hz, respectively. It can be seen that within the spectrum defined by the basal and apical resonance frequencies, that is, between 0.3 and 3.4 kHz, the pressure in the cavity of a specific element smoothly increases and peaks at a specific frequency, similarly to the cochlea. The peaks of the cavity pressures occur at lower frequencies compared to the corresponding resonance frequencies, denoted by the grey vertical dashed lines in Figures 5.19b and 5.19d, due to the presence of damping. At lower frequencies, damping is more prominent, since the quality factor is smaller towards the apex. Therefore, for the element which is closer to the apex among those plotted in Figure 5.19b, that is, for $n = 40$, the peak of the coupled response appears to be low.

Outside the spectrum defined by the resonance frequencies of the first and last element, some anomalies appear in the response with respect to frequency, as can be seen in Figures 5.19c and 5.19d. At lower frequencies, fluctuations occur both in modulus and phase, and at higher frequencies, the modulus of the pressure starts to increase with frequency. The increasing

modulus at higher frequencies is due to the presence of the second pass band.

The pressure modulus plots in Figures 5.19a and 5.19b demonstrate that the designed system can be used as an acoustic 'rainbow' sensor, where different frequency components are filtered at different positions, since the frequency response of a given element acts as a pass band filter centred at a different frequency. The different frequency components could be captured by introducing small microphones in the cavities of the Helmholtz Resonators. It should be noted, however, that at apical elements, the coupled frequency response resembles more a low pass filter, if the frequencies below the working spectrum are neglected, rather than a pass band filter. This may limit the performance of the 'rainbow' sensor at low frequencies.

The 3-dB quality factor of the frequency response of the coupled system is defined as [42]

$$Q_c = \frac{f_{peak}}{f_h - f_l}, \tag{5.130}$$

where f_l and f_h are the frequencies where the coupled response drops by 3 dB below and above the peak frequency, respectively. This quality factor is plotted against the element number in Figure 5.20 along with the quality factor of each separate element, given by Equation (5.123). It can be seen that the coupled quality factor for a given element is significantly smaller than the quality factor of the resonance of the same element, as was also observed for the cochlea. As n gets larger, the response peak gets smaller, as can be seen in Figure 5.19b, and beyond some element, the 31st in this case, the response does not drop enough to reach a point 3 dB smaller than the peak towards lower frequencies. Therefore, the 3-dB quality factor is not defined there, and is therefore not plotted in Figure 5.20 for elements beyond the 31st.

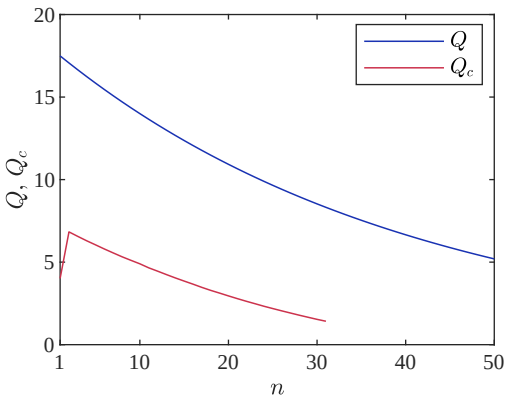

Figure 5.20. 3-dB quality factor of each separate element, Q, and 3-dB quality factor of the coupled system, Q_c, plotted against the number of element, n. Beyond the 31st element, the coupled response does not fall down to 3 dB from the peak towards lower frequencies, as can be seen for example for $n = 40$ in Figure 5.19b, and therefore the 3-dB quality factor cannot be defined there.

A set of plots for the modulus and phase of the pressure is given in Figure 5.21, both against the number of element and against position, for a system whose actual neck lengths are rounded to a precision of 0.1 mm, to comply with restrictions in additive manufacturing [1]. The other geometrical design properties are already rounded to this precision, as can be seen in Table 5.1.

It can be seen that this rounding causes ripples in the coupled response of the system, though relatively shallow ones. Therefore, the smoothness of the response is expected to be somewhat compromised by the imposed manufacturing restriction.

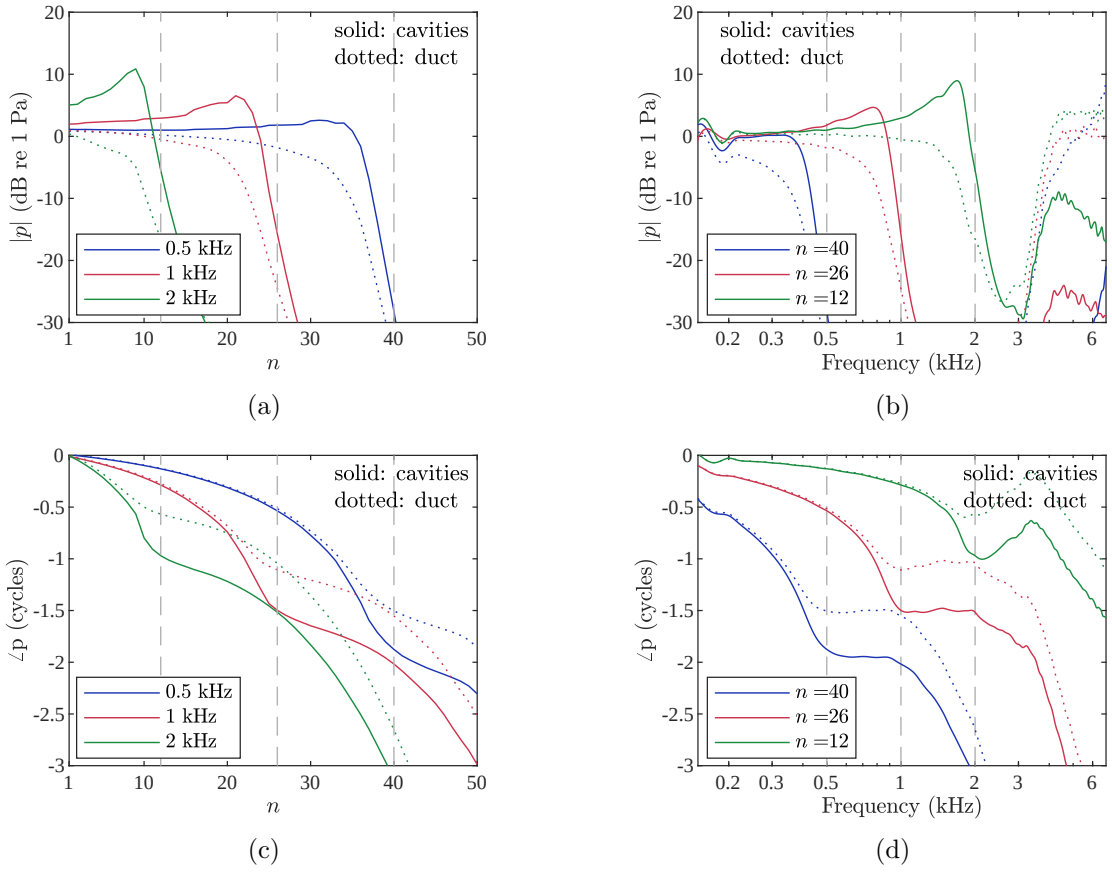

Figure 5.21. Modulus and phase of the pressure plotted against the number of element and against frequency, with the actual length of the necks rounded to a precision of 0.1 mm given in parentheses in Table 5.1. All other configurations are the same as for the plots in Figure 5.19.

5.7.3 Absorption, reflection and transmission results

The absorption coefficient and the modulus of the reflection and transmission coefficients are plotted against frequency in Figure 5.22a, for a waveguide with a matched termination. The absorption coefficient represents the ratio of absorbed power, whereas the reflection and transmission coefficients are ratios of amplitudes of reflected and transmitted pressures, respectively, to the incident pressure, so that all three coefficients are related by Equation (5.90) for a matched termination. It can be seen that within the region defined by the lowest and highest resonance frequencies, practically no transmission occurs; incident waves are either reflected or absorbed. The reflection coefficient retains small values in a great part of this frequency band, around 0.2, so that incident power is mainly absorbed, as can be seen by the part of the absorption coefficient plot above the horizontal line, which corresponds to values of absorption greater than 0.9.

As in the case of the pressure plots of Figures 5.19b and 5.19d, fluctuations can also be

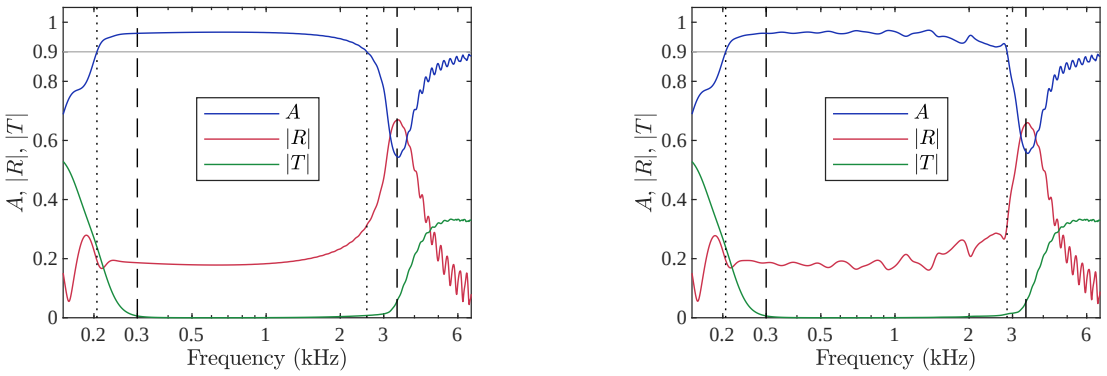

Figure 5.22. Absorption coefficient and modulus of the reflection and transmission coefficients for a waveguide with matched termination, (a) using the specifications stated in the caption of Figure 5.17 and(b) with the neck length rounded to a precision of 0.1 mm. The dashed vertical lines correspond to the highest and lowest resonance frequencies, the horizontal line denotes the value 0.9, and the dotted vertical lines are defined by the intersection of the absorption coefficient with the 0.9 line.

observed for the absorption coefficient outside the frequency band defined by the lowest and highest resonance frequencies. It can also be seen that absorption is actually highest over a frequency band which is shifted downwards compared to the band defined by the two extreme resonance frequencies. Therefore, the designed system behaves more effectively as an absorber over a frequency band which can be defined, for example, by an absorption coefficient greater than 0.9, as defined by the dotted vertical lines in Figure 5.22a.

The frequency band defined by an absorption coefficient above 0.9 also seems to match better with the spectrum over which the pressure frequency response is smooth and free of ripples, as observed in Figures 5.19b and 5.19d. Therefore, this band appears to be a better choice for the working spectrum of the system. If the system is to be used only as a 'rainbow' sensor, so that high absorption is not necessary, the working spectrum can retain its upper limit as defined by the resonance frequency at the base.

The absorption, reflection and transmission coefficients for a system whose geometrical properties are rounded to a precision of 0.1 mm are plotted in Figure 5.22b. It can be seen that the rounding causes ripples in the reflection and absorption coefficients within the band of high absorption, especially at higher frequencies. Nevertheless, the general level of absorption is not significantly affected.

5.7.4 Simulations with different modelling configurations

Figure 5.23 shows the pressure frequency response and the absorption characteristics for a matched termination impedance, as in Sections 5.7.2 and 5.7.3, and for a rigid termination. It can be seen that the pressure coupled response is practically the same in the spectrum defined by the lowest and highest resonance frequencies. Differences occur outside this spectrum, with the rigid termination producing greater fluctuations in the modulus of the pressure. If the system

is to be used as an absorber, then the rigid termination is predicted to retain high absorption values at lower frequencies compared to the matched termination.

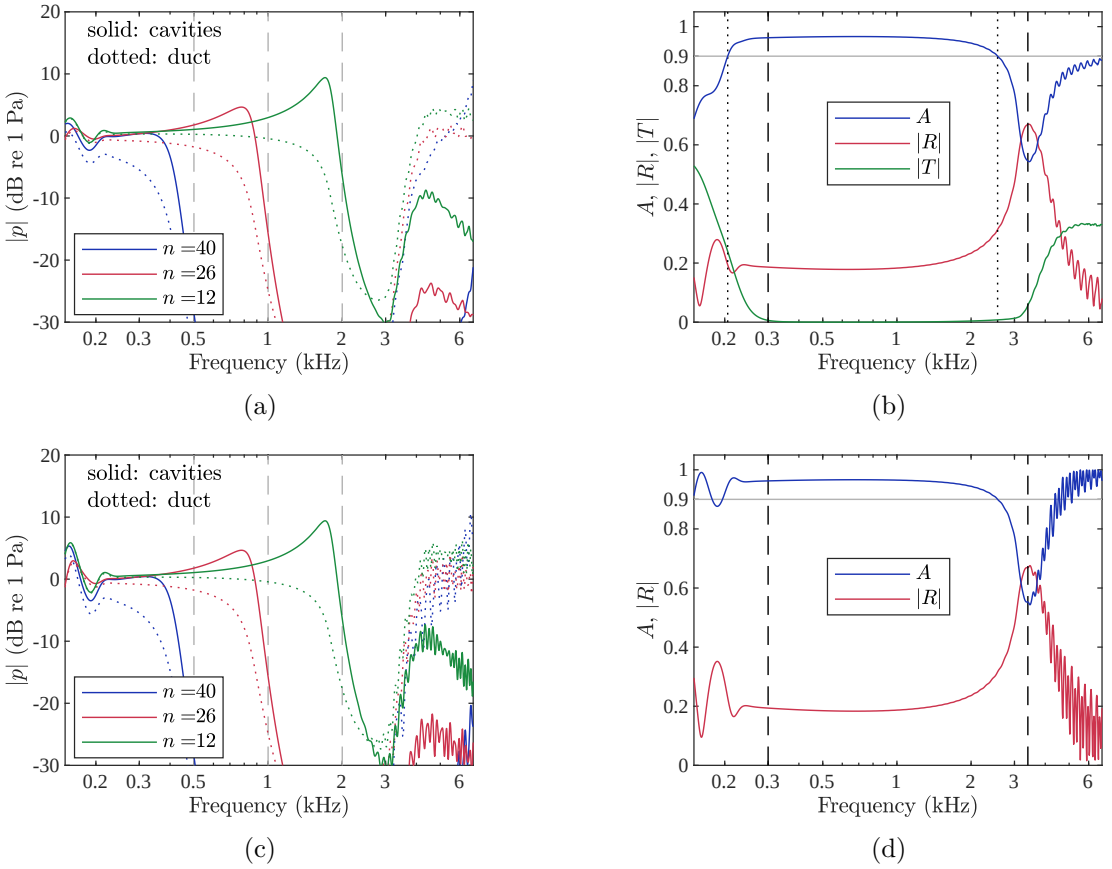

Figure 5.23. (a) Frequency response of the pressure modulus and (b) absorption, reflection and transmission coefficients, with a matched termination. (c) Frequency response of the pressure modulus and (d) absorption and reflection coefficients with a rigid termination. The meaning of the vertical lines in (a) and (v) is given in the caption of Figure 5.19, and the meaning of the vertical lines in (b) and (d) is given in the caption of Figure 5.22.

A set of plots in terms of the pressure modulus frequency response and of the absorption behaviour for various different modelling configurations is given in Figure 5.24. Plots on the same row correspond to the same configuration and for each configuration a specific modelling aspect is changed from the default configuration, as used in Figures 5.23a and 5.23b. In Figures 5.24a and 5.24b, losses in the main duct and in the resonator cavities are not accounted for. This exclusion gives more prominent peaks, as can be seen by comparing Figure 5.24a with Figure 5.23a. Therefore, although the necks of the resonators are the dominant source of losses, the other components of the system are also found to contribute to the losses.

A Transmission Line approximation is used in Figures 5.24c and 5.24d, where the transmission along the main duct and the impedance of the Helmholtz Resonators are calculated using lumped parameters. It can be seen that fluctuations appear at high frequencies, both in the absorption spectrum and in the pressure response. It can also be observed that the pressure peaks are more pronounced compared to the ones in Figure 5.23a for the respective element numbers. Both of these discrepancies can be attributed to the simpler loss model used for the

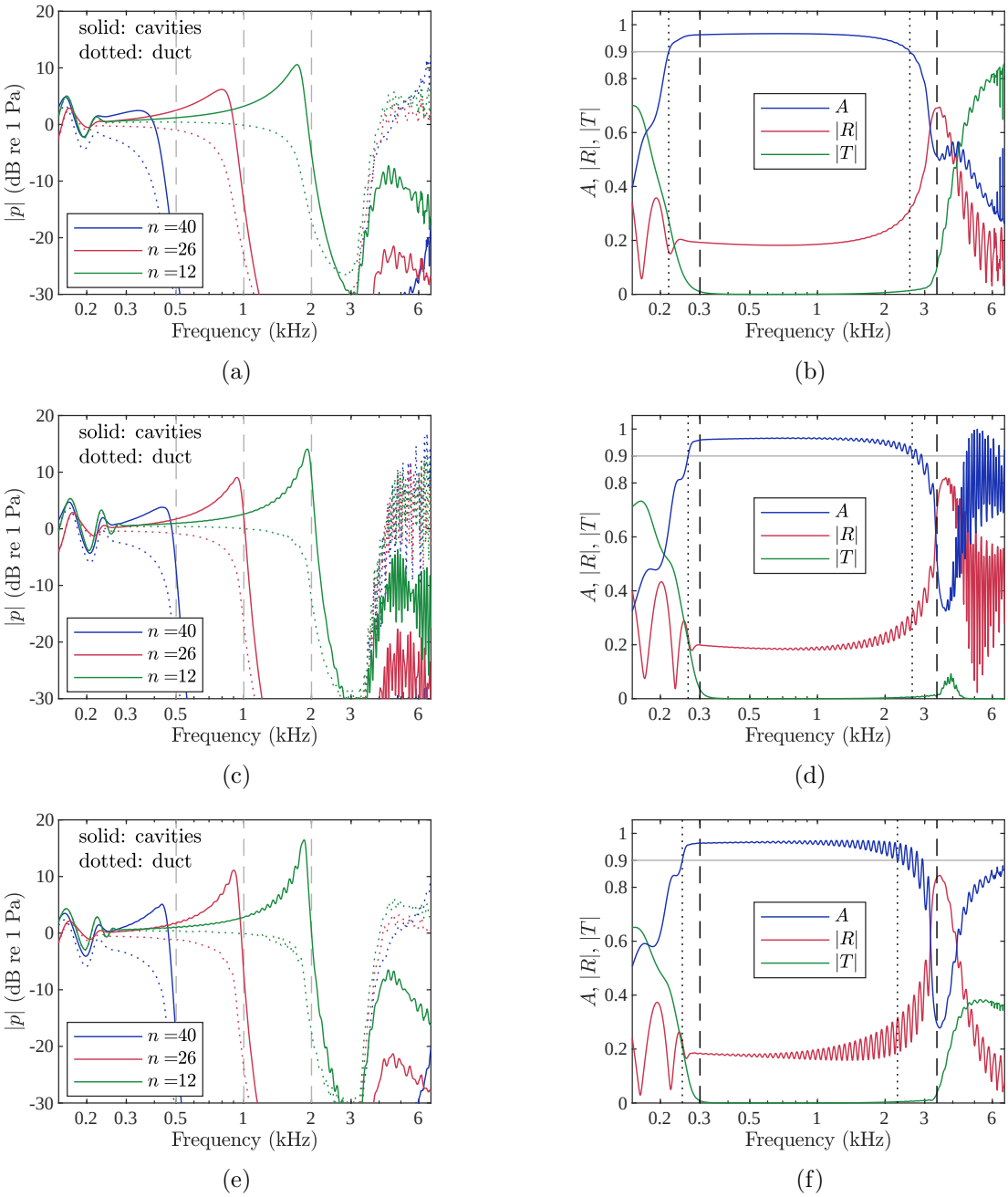

Figure 5.24. Frequency variation of (a) the pressure modulus and (b) the absorption, reflection and transmission coefficients, without losses in the main duct and in the cavities. Frequency variation of (c) the pressure modulus and (d) the absorption, reflection and transmission coefficients, for the lumped-parameter model for the calculation of the Helmholtz Resonator input impedance, Z_H, according to Equation (5.8), where the lumped parameters are calculated with Equation (5.9) and the loss coefficient is calculated with Equation (5.7), and for the lumped parameter Transfer Matrix, which corresponds to a Transmission Line approximation, whose elements are given by Equation (5.65). Frequency variation of (e) the pressure modulus and (f) the absorption, reflection and transmission coefficients, using the loss model given by Equations (5.93) to (5.96).

lumper-parameter calculation of Z_H. The large discrepancies at very high frequencies, beyond 3.4 kHz, may be attributed to the deteriorating validity of the lumped parameter assumption with increasing frequency.

In Figures 5.24e and 5.24f, the loss model given by Equations (5.93) to (5.96) is used, which involves a complex density and a complex bulk modulus for the calculation of the complex wavenumber and characteristic impedance. It can be seen that this loss model produces more prominent peaks and greater fluctuations in the coupled response. Therefore, it underestimates the losses compared to the loss model with Equations (5.60) and (5.61), which has been used for the reference simulations, as was also observed in Figure 5.13 for the system presented in [1].

5.8 Summary and conclusions

A new design procedure for systems that act as acoustic 'rainbow' sensors has been presented, consisting of a main duct with side branches of Helmholtz Resonators. Such a system enhances and absorbs incident waves at different positions for different frequencies. An analysis of a system consisting of a main duct with an infinite array of side branches of identical Helmholtz Resonators was first carried out, based on a Transmission Line approximation. A Transfer Matrix method for analysing a system with a finite number of Helmholtz Resonators of varying geometrical properties was then presented.

The response of two systems from the literature which use arrays of varying Helmholtz Resonators has been calculated. Simulations showed that the system in [1], for which the cross section of the main duct varies for different elements, apart from acting effectively as an absorber, also produces a tonotopic mapping as a by-product and has a smooth frequency response of the coupled pressure modulus inside the cavities of the resonators. Therefore, this system acts as an acoustic 'rainbow' sensor. For the system designed in [2], however, it was shown that its use as a 'rainbow' sensor is limited since the frequency response was not smooth.

The new design of an acoustic system consisting of a main duct of constant cross section with a finite number of side branches of Helmholtz Resonators whose geometry varies along the system was then presented. The main performance characteristics of the designed system were based on a correspondence with the cochlea. Simulations based on the Transmission Matrix method showed that the pressure in the cavities of the Helmholtz Resonators for a given frequency increases smoothly as the acoustic wave travels along the system, until it reaches a maximum at a specific Helmholtz Resonator, beyond which it quickly decreases to very small values. Higher frequencies peak towards the base while lower frequencies peak towards the apex of the system.

The frequency response for the pressure in a specific Helmholtz Resonator follows a similar behaviour, where, within a certain bandwidth, the pressure increases smoothly with frequency until it reaches a peak at a specific frequency, beyond which it quickly decreases to very

small values. Therefore, the response of the system in terms of the pressure in the cavities is qualitatively similar to the coupled response of the cochlea in terms of the transverse velocity of the basilar membrane, so that the presented system may be used as an acoustic 'rainbow' sensor, that is, as a spatial spectrum analyser. The designed 'rainbow' sensor also behaves as an acoustic absorber, with different frequency components being absorbed around their corresponding peak positions. The main characteristics of the previous systems and the current design are shown in Table 5.2.

	Freq. range octaves	Number of elements	Smooth freq. response	Design procedure	Average Q
Jimenez et al. [1]	2	9	Yes	Numerical optimisation	8
Zhao and Zhou [2]	2	40	No	Ad hoc	21
Current design	3.5	50	Yes	Physically based	10

Table 5.2. Main characteristics of previous 'rainbow' sensors and the current design.

One of the advantages of the current design is that the parameter choices are clearly based on the physical principles of the coupled system. The choice of the damping in the resonator, for example, is seen to involve a trade-off between the frequency selectivity, high Q, and limiting the number of elements, low Q. Unfortunately, time did not permit the construction and practical testing of the current design, so its advantages over previous systems are still to be proven.

Chapter 6

Conclusions and suggestions for future work

In this thesis, a number of non-uniform waveguides that have focusing and absorbing properties have been studied. Different response aspects have been highlighted for each system. The conclusions for the type of system studied in each chapter are summarised in Section 6.1. A discussion on the similarities and differences of the response characteristics of the different systems is then given in Section 6.2. Suggestions for future work are given in Section 6.3.

6.1 Summary of conclusions for the studied non-uniform waveguides

6.1.1 Tapered elastic wedges

Elastic wedges terminating a uniform plate cause incident flexural waves to slow down and to be significantly absorbed towards their edge. They have been analysed using an analytical method based on the WKB approximation method with different orders of approximation. Different thickness variation profiles were considered, all of which cause incident waves to slow down and undergo significant absorption towards the edge. Results from the analytical method for the total reflection coefficient were compared with results from Finite Element models, and it was shown that the analytical method provides accurate predictions over a significant part of the spectrum in which the wedge behaves effectively as a vibration absorber, provided that higher orders of WKB approximation are used. It was shown that the typically used first-order WKB approximation only predicts the general level of reflection, failing in general to predict the details of the fluctuations of the reflection coefficient with frequency. Among the different profiles considered, the exponential was found to give the lowest reflection.

The presented analytical method also allows for the calculation of the reflection coefficients due to the junction and due to the edge truncation. The fluctuations in the total reflection

coefficient are primarily due to the interference of the waves reflected from the end and from the junction, for wedges whose thickness changes more rapidly close to the junction. These fluctuations are more pronounced when these reflected waves are of similar amplitude.

The accuracy of the WKB method was assessed by examining the behaviour of the WKB validity condition. It was shown that there is a correspondence between the accuracy of the analytical results and the satisfaction of the WKB validity condition, although it is not apparent how quantitative predictions of the accuracy of the analytical method could be obtained from the WKB validity condition. The WKB method was shown to generally fail for wedges whose thickness varies little at the junction but varies considerably within the wedge, since the method does not account for reflections away from the junction and the edge.

6.1.2 Absorbing acoustic waveguides with fitted rings

Waveguides with fitted rigid rings were studied as acoustic absorbers, where the inner radius of the rings follows either a linear or a quadratic taper. An approximate continuous analytical model, taken from the literature, was used to illustrate the general characteristics of the system, where acoustic waves slow down as they travel along the waveguide, reaching a small propagation velocity close to the end, where they are significantly attenuated. The analytical model was shown to only give accurate predictions for waveguides with a very large number of very thin rings.

A Transfer Function method was also formulated, which can account for the discrete rings and cavities. Two different geometrical approaches for modelling the main core and the cavities were followed, where these are modelled either with respect to cylinders, as has been done previously, or with respect to truncated cones. A Transmission Line model was also formulated, which uses lumped acoustic parameters and forms a low-frequency approximation of the Transfer Function method, and its limitations with respect to frequency and the number of rings were illustrated.

Numerical results from the Transfer Function method were compared with experimental results from the literature for a linear and a quadratic waveguide. The numerical results with the conical approach gave a good prediction of the reflection coefficient of the linear waveguide in a large part of the spectrum, although they deviated significantly at lower frequencies. For the quadratic waveguide, only the general characteristics of the frequency variation of the reflection coefficient were predicted.

6.1.3 The cochlea as a non-uniform waveguide

Wave propagation in the cochlea was studied using a one-dimensional model of the passive cochlea with single-degree-of-freedom micromechanics. The cochlear wave equation was solved both with the Finite Difference method and with the WKB method to provide the coupled

response. It was shown that the WKB method provides accurate results for the coupled response over a large part of the working frequency range of the cochlea and over most of its length.

A parametric analysis was conducted for the variation of the coupled response with respect to a number of non-dimensional parameters. The local quality factor of the basilar membrane was varied, and it was shown that even with very little damping no significant reflections occur at the point of maximum response. The form of the coupled response was found to depend on the values of the mass ratio and the phase-shift parameter, with a symmetric response occurring for a certain high value of mass ratio and a corresponding low value of the phase-shift parameter. It was shown, however, that if the phase-shift parameter is not changed and the characteristic length and the cochlear length are allowed to vary, in order to keep the working spectrum of the model intact, varying the mass ratio does not affect the form of the coupled response, apart from causing a change in amplitude. Therefore, the symmetry of the frequency-domain coupled resonance is seen to depend only on the value of the phase-shift parameter.

The accuracy of the Finite Difference cochlear model with respect to the spatial resolution was also assessed, and it was shown that for a small number of elements per wavelength, the Finite Difference model predicts reflections. It was shown, in general, that six elements per minimum wavelength provide reasonably accurate results, a condition that was then used in the design of acoustic 'rainbow' sensors.

6.1.4 Acoustic 'rainbow' sensors

A new design of an acoustic 'rainbow' sensor was presented, whose properties were based on the characteristics of the cochlea. The system comprises a main duct of constant cross section and a number of side branches consisting of Helmholtz Resonators. A duct with an array of identical Helmholtz Resonators was first examined using a Transmission Line model, illustrating the general wave propagation characteristics in such a system, where there are two pass bands and a stop band between them. The choice of the damping in the resonators is found to allow for a trade-off between frequency selectivity and the number of elements.

The Transfer Matrix method was then presented, which accounts for wave propagation in the various parts of a system consisting of a main duct with Helmholtz-Resonator side branches. Simulations showed that the pressure in the cavities of the Helmholtz Resonators increases up to a specific frequency-dependent position, or up to a specific position-dependent frequency, where it peaks, beyond which it rapidly decays. Therefore, the system presents a tonotopic mapping, similarly to the cochlea. The quality factor of the coupled response was found to be different from the quality factor of the Helmholtz Resonators, as was also observed for the cochlea. In contrast to some previous designs in the literature, the response of the designed system was predicted to vary smoothly with respect to position and frequency. It was also predicted that the system presents broadband high absorption.

6.2 Comparison of the different systems

In this section, the different types of non-uniform waveguides are compared with each other to highlight similarities and differences between them. Some of these comparative aspects have been pointed out within the main chapters of the thesis, while some additional ones are presented here. The normalised effective lengths, defined in the respective chapters for the different types of waveguide, are shown in Figure 6.1. It can be seen that within the respective working frequency ranges, the normalised effective length is larger than one for all the waveguides, which implies that these systems cause waves to slow down as they propagate through them, as expected, so that an equivalent uniform waveguide would have to be longer for the waves to travel from its input to its end in the same time.

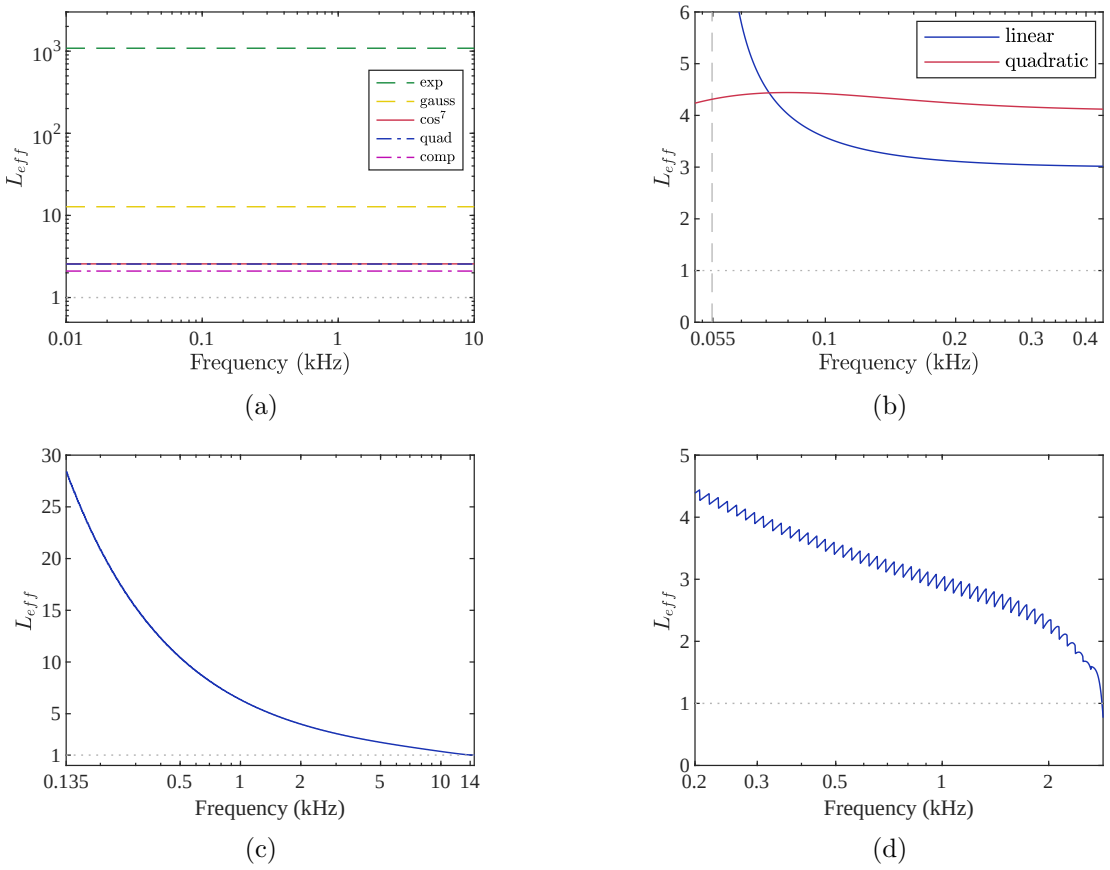

Figure 6.1. Normalised effective length plotted against frequency for (a) elastic wedges of different profiles, (b) linear and quadratic acoustic waveguides with fitted rings, (c) the cochlea and (d) the acoustic 'rainbow' sensor. The normalised effective number of elements is also plotted in (d). In (b), the dashed vertical line denotes the cut-off frequency for the linear waveguide. The dotted horizontal lines in all graphs pass from 1.

The effective length of the wedge is constant with frequency for a given thickness profile, but different profiles have different effective lengths, with the exponential having the largest effective length, as can be seen in Figure 6.1a. In the acoustic waveguide with fitted rings, the effective length varies little along its working frequency range in Figure 6.1b, and for the most part it is larger for the quadratic waveguide than for the linear one. In the cochlear model and in the acoustic 'rainbow' sensor, the effective length, plotted in Figures 6.1c and 6.1d, decreases

with frequency.

6.2.1 Elastic wedges and acoustic waveguides with fitted rings as absorbers

The elastic wedge and the acoustic waveguide with fitted rings are both presented as terminating uniform flexural and acoustic waveguides, respectively, to provide low reflection of the corresponding incident waves. The flexural waves that travel along the wedge result from the interaction between the density and the Young's modulus of the material of the wedge, whereas the acoustic waves that travel along the waveguide with rings result from the interaction between the inertance of the air mainly in the core of the waveguide and the compressibility of the air both in the core and in the lateral cavities.

In both of these systems, the propagation velocity starts from a high value at their input and decreases to a small value at their end, as can be seen for the group velocity in Figure 6.2a. A quadratic wedge and a linear waveguide with fitted rings are chosen, whose velocities decrease linearly. Since the velocity at the far end of the system has a non-zero, although relatively small, value, and since the waves are not completely absorbed along its length, a part of the waves travelling through the system reach the end and are reflected. These reflected waves then travel back to the input boundary of the waveguides, where the discontinuity with the uniform input waveguide causes partial reflection and partial transmission back into the input waveguide. Reflections may also occur from the discrete rings along the acoustic waveguide and along the wedge due to its tapering. At different frequencies, these internal reflections match or mismatch in phase, leading to fluctuations in the reflection coefficient, as can be seen in Figure 6.2b for both waveguides. The losses are larger at higher frequencies, as can be deduced from the frequency dependence of the wavenumber for the two waveguides, as presented in Chapters 2 and 3. Therefore, the reflection coefficient follows a generally decreasing trend with increasing frequency, as can also be seen in Figure 6.2b.

The responses of the vibration displacement in the elastic wedge and the pressure in the acoustic absorber are plotted in Figures 6.2c and 6.2d against normalised position for three different frequencies. It can be seen that in both waveguides, the response builds up as it travels with decreasing speed, reaching its maximum value at the end. The maximum displacement at the wedge occurs at its free vibrating end, and the maximum pressure in the waveguide with rings occurs at its rigid end, as would also be observed in uniform flexural and acoustic waveguides with respective boundary conditions at the end. The value of the response at the end of both waveguides is seen to decrease with frequency, since the losses increase with frequency.

6.2.2 The cochlea and the acoustic 'rainbow' sensor

The cochlea and the acoustic 'rainbow' sensor presented in Section 5.6 form waveguides that focus incident waves of different frequencies at different positions along their length, around

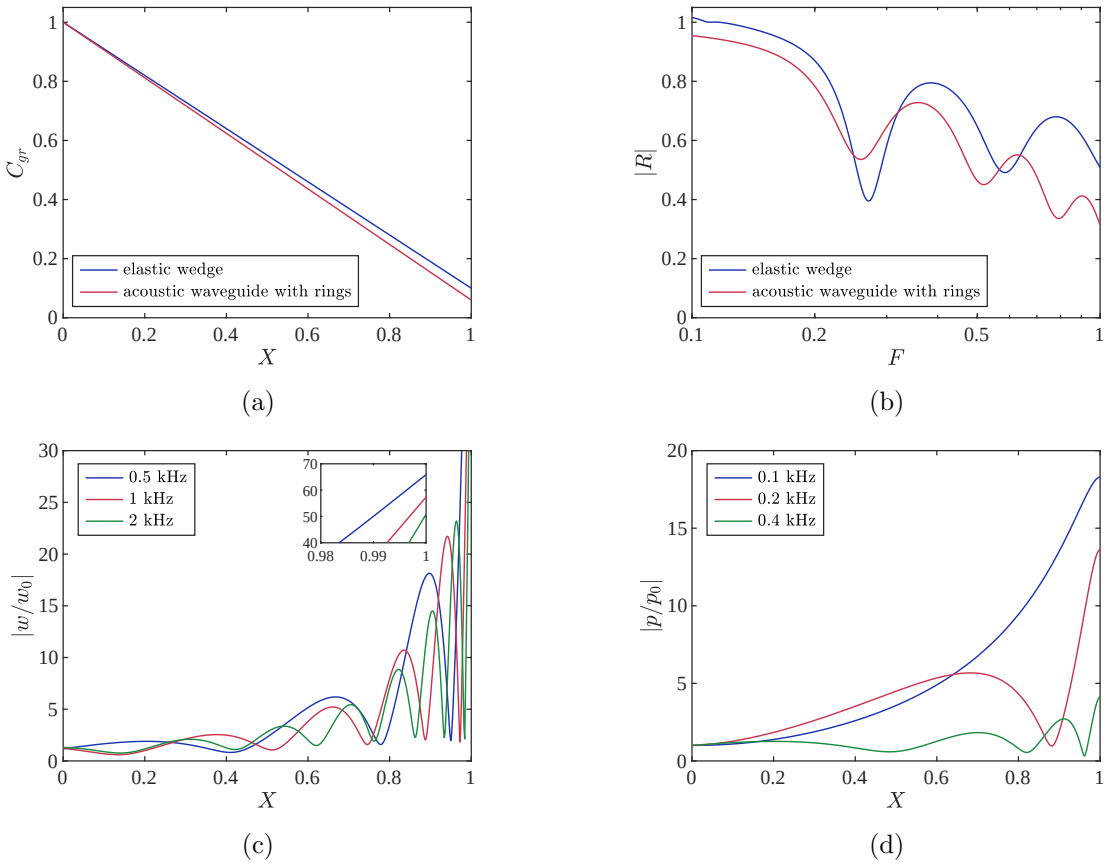

Figure 6.2. Properties of a quadratic elastic wedge and of a linear acoustic waveguide with fitted rings. (a) Normalised group velocity, C_{gr}, plotted against normalised position, X, at a high working frequency. The group velocities are normalised with respect to the group velocity at the input boundary of the two waveguides. (b) Modulus of the total reflection coefficient of the wedge and the reflection coefficient of the waveguide with fitted rings, plotted against normalised frequency. The frequency is normalised with respect to the highest working frequency of the waveguide with rings, that is, $f = 437$ Hz, for both waveguides, for ease of comparison, although this frequency is low within the working frequency range of the wedge. (c) Modulus of the displacement of a wedge, normalised with respect to the incident displacement amplitude, plotted against normalised position, for three different frequencies. A small detail plot is included, showing the response near the end of the waveguide. (d) Modulus of the pressure in an acoustic waveguide with rings, normalised with respect to the pressure at its input, plotted against normalised position, for three different frequencies. The results for the wedge are calculated with the second-order WKB approximation, and for the waveguide with rings they are calculated with the analytical method. In (a), (c) and (d), the position is normalised with respect to the length of each waveguide. In (a), (b) and (c), a large damping factor of $\eta = 0.1$ has been used for the wedge, for ease of comparison with the waveguide with fitted rings.

which positions the waves are absorbed, and beyond which they rapidly decay. A symmetry between position and frequency is observed in both systems, so that results with respect to one variable can be used to draw conclusions with respect to the other variable.

A set of corresponding plots against frequency for the two systems is given in Figure 6.3, where the plots in the left column correspond to the cochlea and the plots in the right column correspond to the 'rainbow' sensor. The plots can be used for drawing conclusions also with respect to the spatial variation of the responses. The real and imaginary parts of the wavenumber are plotted in Figures 6.3a and 6.3b. Similar behaviour of the real and imaginary parts of the wavenumber is observed up to the natural frequency, f_n, at a given position along the cochlea, and up to the resonance frequency of a given Helmholtz Resonator, f_1.

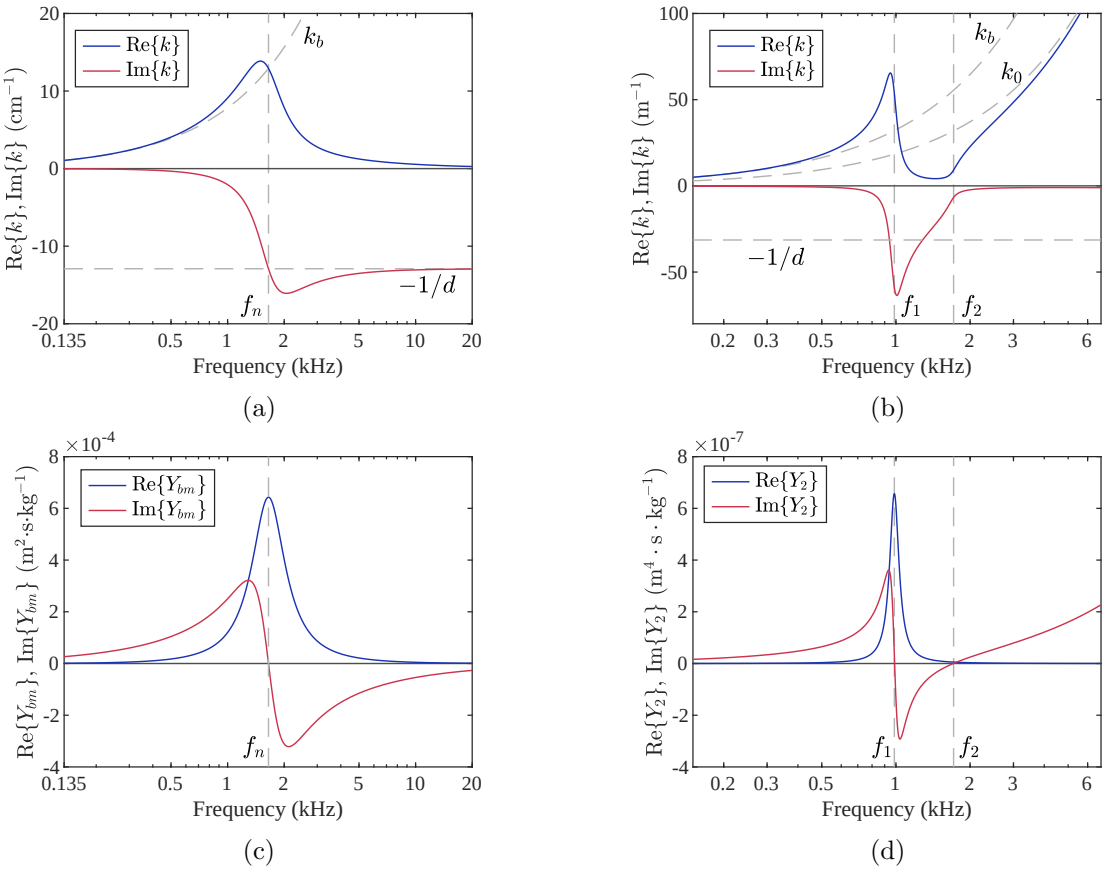

Figure 6.3. Real and imaginary parts of the wavenumber plotted against frequency, for (a) the cochlea at $x = 17.5$ cm and (b) the acoustic 'rainbow' sensor at $n = 26$. Real and imaginary parts of (c) the basilar membrane admittance and (d) the shunt admittance of the 'rainbow' sensor, plotted against frequency. The vertical dashed lines in (a) and (c) correspond to the natural frequency of the specified position, and in (b) and (d) they correspond to the frequencies of resonance, f_1 and cut-on, f_2, for the specified element. The other dashed lines in (a) and (b) correspond to asymptotic behaviours, except for the horizontal line in (b), which approximately corresponds to the imaginary part of the wavenumber in the middle of the stop band.

In the 'rainbow' sensor, it can be seen that for a given Helmholtz Resonator a limited stop band of high absorption, that is, large negative imaginary part of the wavenumber, is formed, which occurs between frequencies that are a bit below the resonance frequency, f_1, of the considered resonator and a bit below the frequency of antiresonance of the characteristic impedance, f_2, as presented in Section 5.3.3. Below and above the stop band, there are pass bands of low absorption. In the cochlea, however, the wavenumber has large values throughout the spectrum beyond the natural frequency, so that at a given position only one pass band is present, in the lower part of the working spectrum, and the stop band extends throughout the upper part of the working spectrum.

In both systems, waves result from the interaction of a series inertive element with a shunt compliant, or flexible, element. In the cochlea, the series element is the fluid moving longitudinally in the chambers and the shunt element is the basilar membrane, including the load of the fluid above it. In the 'rainbow' sensor, the series element is the inertia of the air in the duct and the shunt element in the compliance of the duct in parallel with the Helmholtz

Resonator. Wave propagation is only possible when the shunt element is compliant, whereas when it is inertive, the waves are evanescent.

To illustrate the relation of the behaviour of the two systems in the different frequency bands, the admittance of their respective shunt elements is shown in Figures 6.3c and 6.3d. The real and imaginary parts of the basilar membrane admittance given by Equation (4.14) are plotted in Figure 6.3c. At low frequencies, well below the natural frequency, the basilar membrane admittance is approximately given by $Y_{bm} \approx \mathrm{i}\omega/m_0\omega_n^2$, that is, it is approximately positive imaginary, and, therefore, it is stiffness-dominated. At high frequencies, however, well above the natural frequency, the basilar membrane admittance is approximately given by $Y_{bm} \approx -\mathrm{i}/\omega m_0$, that is, it is approximately negative imaginary, and, therefore, it is mass-dominated.

An expression for the shunt admittance of the n-th element of the 'rainbow' sensor, $Y_2(n)$, which is the reciprocal of the element shunt impedance, $Z_2(n)$, can be derived using Equations (5.14), (5.15), (5.20) and (5.27), giving

$$Y_2(n) = Y_{C_D}(n)\frac{\omega_2^2(n) + \mathrm{i}\frac{\omega\omega_2(n)}{Q_2(n)} - \omega^2}{\omega_1^2(n) + \mathrm{i}\frac{\omega\omega_1(n)}{Q_1(n)} - \omega^2}, \tag{6.1}$$

where $Y_{C_D}(n) = 1/Z_{C_D}(n)$, where $Z_{C_D}(n)$ is the impedance due to the duct compliance and is given by Equation (5.17); the notation (n) is omitted in the discussion below for convenience. At low frequencies, well below the natural frequency of the Helmholtz Resonator of a given element, the shunt admittance is approximately given by $Y_2 \approx Y_{C_D} + Y_{C_H}$, where $Y_{C_H} = 1/Z_{C_H}$, where Z_{C_H} is the impedance due to the cavity compliance and is given by Equation (5.19). This means that the shunt admittance is approximately positive imaginary, and, therefore, it is compliant. The imaginary part of the shunt admittance is negative within the stop band, since for $\omega_1 \ll \omega \ll \omega_2$, the shunt admittance is approximately given by $Y_2 \approx Y_{L_H}(1 + Y_{C_D}/Y_{C_H})$, that is, it is approximately negative imaginary like the inertive admittance Y_{L_H}.

At high frequencies, well above the cut-on angular frequency, ω_2, the shunt admittance is approximately given by $Y_2 \approx Y_{C_D}$, that is, it is approximately positive imaginary, and, therefore, the shunt admittance is again compliant. The real and imaginary parts of the shunt admittance are plotted in Figure 6.3d. Therefore, in the 'rainbow' sensor there are two pass bands and a stop band between them.

The fact that in the 'rainbow' sensor there is a stop band of limited bandwidth compared to the extended stop band in the cochlea results from the discretisation of the 'rainbow' sensor, where each element has a non-zero length. If the 'rainbow' sensor were discretised to elements of infinitesimal length, then the cut-on frequency, given by Equation (5.23), would become infinite and for $\omega_1 \ll \omega$, the shunt admittance would be approximately $Y_2 \approx Y_{L_H}$. Therefore, a 'rainbow' sensor with very fine discretisation would have only one pass band and an extended stop band, as observed in the cochlea.

The correspondence of the coupled response between the two systems is illustrated in Figure 6.4, where the coupled responses of the cochlea and of the 'rainbow' sensor are re-plotted. The upper limit of the pass band in the 'rainbow' sensor can be observed, beyond which the modulus of the response starts increasing again, and the lack of a second pass band in the cochlea is also apparent, where the response continues to decay rapidly throughout the upper part of the spectrum. The correspondence between the pressure in the cochlea and the pressure in the main duct of the 'rainbow' sensor on one hand, and between the basilar membrane velocity and the pressure in the cavities of the Helmholtz Resonators on the other, can also be observed, where the former quantities correspond to the series elements and the latter quantities correspond to the shunt elements of the respective systems.

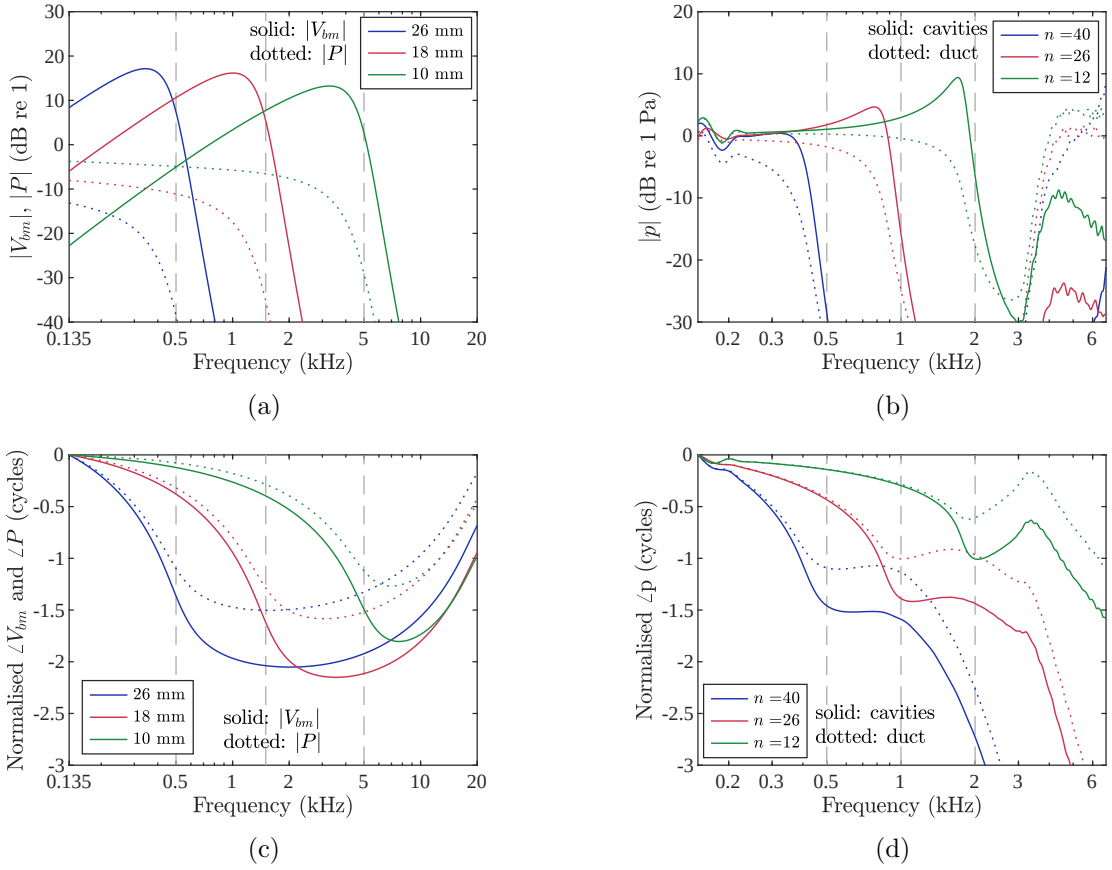

Figure 6.4. (a) Modulus of the normalised basilar membrane velocity and pressure in the cochlea plotted against frequency for three different positions. (b) Modulus of the pressure at the top of the cavities and in the main duct of the acoustic 'rainbow' sensor plotted against frequency for three different positions. (c) Phase of the normalised basilar membrane velocity and pressure in the cochlea plotted against frequency for three different positions. (d) Phase of the pressure at the top of the cavities and in the main duct of the acoustic 'rainbow' sensor, normalised with respect to the respective phase at the lowest shown frequency, plotted against frequency for three different positions. The vertical dashed lines correspond to the natural frequencies of the specified positions for the cochlea and to the natural frequencies of the specified elements for the 'rainbow' sensor.

6.2.3 Comparison of the elastic wedge with the cochlea

The elastic wedge and the acoustic waveguide with rings can be regarded as a single set of systems with similar response characteristics, and can be compared to the cochlea and the

acoustic 'rainbow' sensor, also regarded collectively. For this comparison, the wedge and the cochlea can be considered as representative of the respective types of system. A fundamental difference between the response of the wedge and that of the cochlea is that in the wedge, the response always peaks at the end regardless of frequency, as observed in Figure 6.2c, whereas in the cochlea, the coupled response peaks at different positions for different frequencies, as observed in Figure 4.7a. Therefore, the cochlea can be considered as an 'Acoustic Black Hole' of different length for different frequencies. This interpretation was implied in [64] in 1980, before the concept was introduced for elastic wedges in [7], where the word 'hole' was used for the position where the cochlear wave is focused and absorbed.

Another difference is that in the wedge, even for very high damping, fluctuations due to reflections appear in the response along its length, as seen for the light-coloured plots in Figure 6.2c. In the cochlea, however, no reflections occur. The reflections in the wedge are due to the fact that even though the waves slow down towards its end, they actually reach it with a non-zero velocity, so that they are reflected at the free boundary. In the cochlea, however, and for frequencies that are not close to the low end of the working spectrum, the waves are greatly attenuated around and beyond the peak position, which lies within its length before the helicotrema, so that they are completely absorbed before they reach the boundary of the helicotrema.

6.3 Suggestions for future work

A number of directions for future work on the different types of non-uniform waveguides studied in this thesis are suggested below.

Relationship between the WKB validity conditions and the actual error in the WKB solutions

It has been shown in this thesis, as has also been shown in the literature, that the WKB method can provide accurate solutions even when the commonly used WKB validity condition is violated. Also, more validity conditions need to be satisfied for the WKB solution to asymptotically approach the exact solution, as discussed in Appendix C. It is not clear, however, how the WKB validity conditions relate to the actual error in the WKB approximation, so that further work needs to be done for the estimation of the error from the validity conditions.

Further theoretical investigation of the reflection coefficient in the elastic wedge

It is not well understood how the thickness variation of a wedge terminating a uniform plate results in the fluctuations of a specific magnitude and at specific frequencies in the reflection coefficient. Some insights were given in this thesis, using the effective length and through the analysis of the widening of the dips, and also through the analysis of multiple internal reflections

given in Appendix F. However, further modelling is required to understand the processes that lead to the observed form of the modulus of the reflection coefficient, so that wedges can be designed to give desired levels of absorption at specific frequencies.

Simulations and experiments on wedges with different profiles with damping layers

It is well known that, in practice, truncated wedges are effective as vibration absorbers only when thin damping layers are applied to them. This thesis has only focused on the reflection properties due to the thickness variation. It would, therefore, be of interest to examine the response of wedges of different profiles with damping layers applied to them, both with simulations and experimentally. The exponential wedge presents particular interest, as it was predicted to give the lowest reflection among the considered profiles.

Further modelling of an acoustic waveguide with fitted rings

It was pointed out in the analysis of a waveguide with fitted rings that the Transfer Function method used here has limited accuracy. More accurate models therefore need to be implemented and validated with experiments to facilitate improving the design of such waveguides, such as the more detailed Transfer Matrix method used in [51], which explicitly accounts for the losses in the cavities and for the radiation between consecutive rings. During this PhD programme, Finite Element models for the linear and quadratic waveguides with fitted rings were implemented, but the resulting reflection coefficients were very different from both those experimentally measured, taken from the literature, and from those calculated with the Transfer Function method, as is presented in Appendix K. It is not clear why the Finite Element models give results which are so different from the theoretical and experimental results and this requires further investigation.

Further investigation of the physical meaning of the phase-shift parameter in cochlear modelling

In [65], the phase-shift parameter was shown to approximately correspond to the number of cycles of phase shift from low to high frequencies. The accuracy of this correspondence, however, was shown in this thesis to vary significantly when the value of the phase-shift parameter is varied or when other parameters of the cochlea are varied. Further research is therefore required for understanding the physical meaning of the phase-shift parameter in a wider context of cochlear modelling.

Further investigation of the different acoustic loss models

In this thesis, different models have been used for calculating the acoustic losses in different systems, each based on different assumptions. It is not clear, however, which loss model is more appropriate for each system. Further work is therefore required to clarify the relation between

the assumptions made by the different loss models and their applicability for different acoustic systems.

Experimental measurement of the response of the new acoustic 'rainbow' sensor

The acoustic 'rainbow' sensor designed in Chapter 5 would need to be experimentally tested to assess its performance. More accurate loss models could then be tried for calculating the response and results from simulations could be compared with experimental results. These loss models would need to be validated with experiments before they could then be used for re-designing the system.

Appendices

A Acoustic horns

A.1 Introduction

Acoustic horns may generally be described as tube-like acoustic waveguides whose cross-sectional area varies along the direction of propagation, usually in a monotonic way. In this sense, a cylindrical pipe may be considered as a degenerate form of a horn with constant cross-sectional area. The study of acoustic horns has concerned various scientists since the 18th century, as has been reviewed in [96]. In this appendix, an analytical approach to analysing wave propagation is described, which is valid for exponential horns, but not for those which flare more rapidly, as for musical horns. The WKB method is severely limited in its application to such horns, as will be discussed in Section C.2.3, and so various numerical techniques will be used for their analysis in later sections.

A wave equation describing the acoustic pressure field in a horn can be derived using a modified equation for the mass conservation to account for the non-uniformity. This is known as Webster's horn equation [6]

$$\frac{\partial^2 p}{\partial x^2} + (\ln S_w)' \frac{\partial p}{\partial x} - \frac{1}{c_0^2} \frac{\partial^2 p}{\partial t^2} = 0, \tag{A.1}$$

where $S_w(x)$ is the longitudinally varying area of a wavefront and c_0 is the speed of sound in free space, and the primes denote differentiation with respect to x. A more general form of the horn equation is derived by Benade and Jansson in [97], accounting for variable density and bulk modulus along the horn. If time-harmonic sound pressure is assumed, varying as $e^{\mathrm{i}\omega t}$, where ω is the angular frequency, Equation (A.1) becomes

$$p'' + (\ln S_w)' p' + k_0^2 p = 0, \tag{A.2}$$

where $k_0 = \omega/c_0$ is the wavenumber in free space and $p(x, \omega)$ is the acoustic pressure, although the notation for the independent variables is omitted for convenience.

The wavefront area in Equation (A.2) varies with position and the free space wavenumber varies with frequency. Whether the pressure wave described by this equation is travelling or

evanescent depends on the relation between the relative rate of change of the wavefront area, $(\ln S_w)'$, and the free space wavenumber, k_0. Therefore, for a given frequency, there may exist a position in the waveguide where a propagating wave undergoes cut-off, so that it becomes evanescent beyond this position. At such a turning point, the travelling wave is reflected. Therefore, in the general case where the rate of change of the wavefront area is variable along the waveguide, reflection may occur at different positions for different frequencies.

Equation (A.2) is analytically solvable only for a few types of cross-sectional profiles [96] or, more accurately, longitudinal variation profiles of the wavefront area, $S_w(x)$, the wavefront being the surface of equal phase. In horns whose cross-sectional area changes slowly, the wavefront is nearly planar, and the wavefront area may be approximated by the cross-sectional area, as is implied for example in the derivation of the horn equation in [48]. Up to Section A.3.6, the plane-wave approximation will be followed, where the wavefront area, $S_w(x)$, is approximated by the cross-sectional area, $S(x)$.

In consequent analysis, propagation of the fundamental mode is considered, that is, the pressure is assumed to be constant over the cross section, based on the assumption that the wavelength is large compared with the diameter of the horn. It should be noted, however, that the Finite Element method produces results which do include the effect of higher-order modes. The problem of higher-order-mode propagation is approached in [98] and in [97, 99].

A.2 Analytical approach

A.2.1 Exponential horn

The exponential horn, that is, with a cross-sectional area varying as $S(x) = S_0 e^{mx}$, is an example of a case where Equation (A.2) is exactly solvable. For such a horn, there is a cut-off frequency below which acoustic waves cannot propagate, as explained for example in [48]. This means that incident waves with frequency below cut-off are reflected at the input boundary of the horn, called the throat, while waves with frequency above cut-off propagate through the horn. It should be noted that the cut-off imposed by the flaring of the horn is different from the one referring to higher-order modes, which will be commented upon in Section A.3.2.

An analysis of the horn equation for an exponential horn reveals its cut-off behaviour. Using the cross-sectional profile of the exponential horn, the horn equation becomes

$$p'' + mp' + k_0^2 p = 0. \tag{A.3}$$

A trial solution for the pressure can be used, similar to that of a uniform waveguide,

$$p(x) = Ae^{\mathrm{i}kx}, \tag{A.4}$$

where A and k are the amplitude and the wavenumber, which in this case are independent of

x. After substituting the trial solution and its derivatives, Equation (A.3) becomes

$$k^2 - \mathrm{i}mk - k_0^2 = 0, \tag{A.5}$$

which means that the pressure of Equation (A.4) satisfies the horn equation (A.3) if the wavenumber satisfies Equation (A.5). Solving the second-order algebraic equation for k gives

$$k = \mathrm{i}\frac{m}{2} \pm k_0\sqrt{1 - \left(\frac{m}{2k_0}\right)^2}. \tag{A.6}$$

The general solution for the pressure can be written as the linear combination of a forward- and a backward-travelling wave as

$$p(x) = e^{-\frac{m}{2}x}\left(Ae^{-\mathrm{i}k_0\sqrt{1-\left(\frac{m}{2k_0}\right)^2}x} + Be^{\mathrm{i}k_0\sqrt{1-\left(\frac{m}{2k_0}\right)^2}x}\right). \tag{A.7}$$

It should be noted that no restriction on the sign of the flare constant, m, is imposed, which may, therefore, be either positive or negative. For a diverging horn, that is, with $m > 0$, the exponential decay towards the flaring positive-x direction reflects the fact that the pressure has to decrease as the horn widens, in order for energy to be conserved [48]. Equivalently, for a converging horn, that is, with $m < 0$, the exponential term is increasing along the direction of propagation, as the pressure wave 'condenses' while propagating into the converging direction.

Propagation of an acoustic wave in the horn occurs on condition that the wavenumber have a real part. Therefore, propagation depends on the sign of the quantity under the square root in Equation (A.6). If the quantity under the root is positive, there exists a non-zero real part of the wavenumber and the wave propagates; if, on the other hand, the quantity is negative, the wavenumber is purely imaginary and the wave is evanescent. Consequently, the condition for propagation is

$$1 > \frac{|m|}{2k_0} \Rightarrow 1 > \frac{|m|c_0}{2\omega} \Rightarrow \omega > \frac{|m|c_0}{2} \Rightarrow \omega > \omega_c,$$

where $\omega_c = |m|c_0/2$. The quantity ω_c is called the cut-off frequency and depends on the flare constant. So, for an exponential horn with given flare, there is a certain frequency below which propagation is not possible. Clearly, larger flare results in higher cut-off frequency.

The real part of the wavenumber, denoted by κ, which exists only in the propagation frequency range, can be written as

$$\kappa = k_0\sqrt{1 - \left(\frac{m}{2k_0}\right)^2} = \frac{1}{c_0}\sqrt{\omega^2 - \omega_c^2}. \tag{A.8}$$

A plot of the real part of the wavenumber as a function of angular frequency within the audible spectrum is given in Figure A.1a, for two different flare constants. It is clear that the horn with larger flare has a higher cut-off frequency. The wavenumber of a uniform waveguide, with

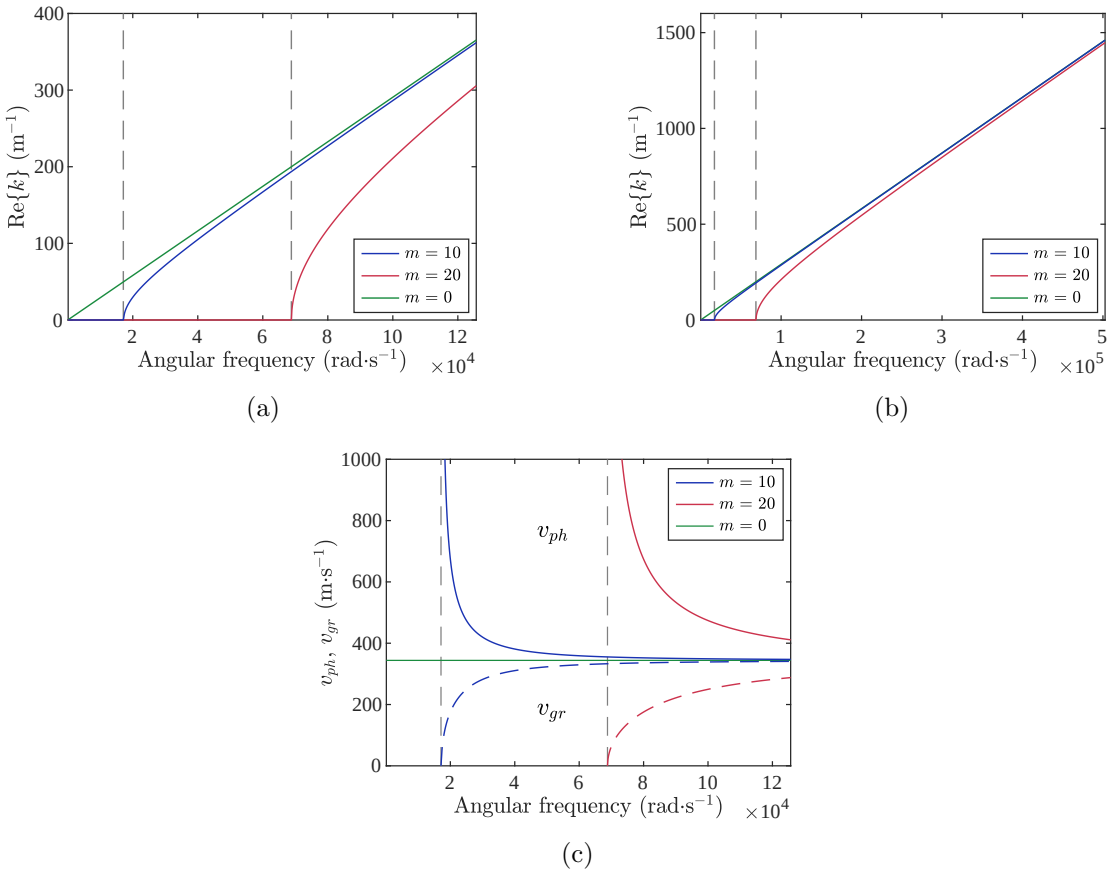

Figure A.1. Frequency dependence of the real part of the wavenumber for two exponential horns with different flare constants. The wavenumber of a uniform waveguide is also plotted: (a) audible spectrum, (b) extended spectrum. (c) Frequency dependence of the phase velocity and group velocity for two exponential horns with different flare.

$m = 0$, is also plotted. Figure A.1b shows the same quantities, but over a wider frequency range. It can be seen that both real wavenumbers asymptote to the wavenumber of a uniform waveguide. This may also be derived by considering the limiting behaviour of the real part of the wavenumber, as given in Equation (A.8), where the constant cut-off frequency is negligible in very high frequencies. From a physical point of view, it can be said that in very high frequencies, the wavelength is so small that the wave does not 'see' the flaring of the horn. It is apparent that a horn with larger flare tends to behave as a uniform tube in higher frequencies compared to one of smaller flare, as can be seen in Figure A.1a.

The phase velocity of the horn is the velocity of propagation of a single frequency, defined as $v_{ph} = \omega/\kappa$, while the group velocity is the velocity at which a wave packet with a certain spectral content propagates, and is defined as $v_{gr} = \mathrm{d}\omega/\mathrm{d}\kappa$. A plot of the two velocities for two exponential horns with different flare is shown in Figure A.1c.

A.2.2 Approximation of higher-order horns as locally exponential horns

Contrary to the exponential horn, for certain cross-sectional profiles, such as in Bessel horns [97], the cut-off frequency varies with position, so that higher frequencies are reflected near the wide

end, called the mouth, while lower frequencies are reflected near the throat of the horn [55]. This property is applied for example in brass musical instruments, facilitating a richer harmonic content compared to uniform tubed instruments [100].

Bessel horns have the advantage of being exactly solvable [96]. In this analysis, however, a different approach is followed for modelling the spatial dependence of the cut-off frequency. The concept of the exponential horn is extended to that of a 'local exponential', where the flare coefficient varies with position along the horn. The cross-sectional area variation can then be written as $S(x) = S_0 e^{m_{eff}(x)x}$, where $m_{eff}(x)$ is the effective flare coefficient. A specific case of flare-coefficient variation is considered, where $m_{eff}(x) = bx^{n-1}$, so that the cross-sectional area takes the form of a 'power exponential', $S(x) = S_0 e^{bx^n}$, with $n > 1$ and $b > 0$.

The propagation characteristics of the 'power-exponential' horn may be investigated by transforming the horn equation (A.2) into Schrödinger's equation, by application of the substitution $p = S^{-1/2}y$ [97, 55], as

$$y'' + \left(k_0^2 - F(x)\right) y = 0, \tag{A.9}$$

where the horn function $F(x)$ is given by

$$F(x) = \frac{S''}{2S} - \frac{S'^2}{4S^2}. \tag{A.10}$$

For the 'power-exponential' horn, the horn function takes the particular form

$$F(x) = \frac{1}{2}bnx^{n-2}\left(\frac{1}{2}bnx^n + n - 1\right). \tag{A.11}$$

In correspondence with the standard Helmholtz equation with constant wavenumber [57],

$$y'' + k^2 y = 0, \tag{A.12}$$

the bracketed quantity in Equation (A.9) can be considered as the square of the spatially varying wavenumber, so that

$$k(x,\omega) = \sqrt{k_0^2 - F(x)} = \sqrt{\left(\frac{\omega}{c_0}\right)^2 - F(x)}. \tag{A.13}$$

The wavenumber at a specific frequency is either purely real or purely imaginary, depending on whether the quantity under the square root is positive or negative, leading to either propagation or evanescence, respectively. Since the rooted quantity depends on position, its sign is also location-dependent, leading to regions where a wave of a certain frequency propagates and regions where it is evanescent.

In an expanding horn, the constant b is positive. Since the horn is located in the positive-x region, the horn function, $F(x)$, is positive throughout; it is reminded that $n > 1$. By inspection

of Equation (A.13) it can be derived that, at any specified position along the horn, there is a frequency for which the wavenumber becomes zero and below which it becomes imaginary. Therefore, for each position along the horn, a certain excitation frequency above the cut-off frequency for that position is required for the wave to propagate.

The cut-off frequency variation with position may be found by setting the wavenumber equal to zero, thus giving

$$\omega_c = c_0\sqrt{F(x)}. \tag{A.14}$$

Three different cases can be considered according to the value of the exponent of x, n. For $1 < n < 2$, the horn function has an infinite positive value at the throat of the horn, and, according to Equation (A.14), an infinite excitation frequency is required for a wave to propagate through the throat. Therefore, such a horn, driven from its throat, is practically useless. For $n = 2$, the horn function acquires the positive value $bn/2$ at the throat and then rises monotonically as the horn flares. Therefore, only frequencies above the cut-off frequency $\omega_c = c_0\sqrt{bn/2}$ may propagate up to some length of the horn. At positions further inside the horn, the horn function has larger values and, accordingly, the cut-off frequency becomes larger, causing waves of different frequencies to be reflected in different positions. For $n > 2$, the horn function becomes zero at the origin and the cut-off frequency is also zero there, increasing monotonically towards the mouth. Consequently, waves of all frequencies can start propagating into the horn from the throat; lower frequencies are reflected near the throat while higher frequencies are reflected near the mouth.

The spatial variation of the effective flare coefficient for $n = 3$ is shown in Figure A.2a and the spatial variation of the cut-off frequency in Figure A.2b. The regions of propagation and evanescence are defined by the intersection of the cut-off frequency variation with the horizontal line of the excitation frequency, as shown in Figure A.2b. The point of transition is usually called a turning point. At all positions to the left of the vertical line passing from the turning point, the excitation frequency is above the cut-off frequency and, therefore, the wave is propagating. On positions to the right of the turning point, however, the frequency is below the cut-off frequency and the wave ceases to propagate.

A corresponding line of thought can be followed to analyse the plot of the effective flare coefficient in Figure A.2a. The excitation frequency defines the turning point, which in turn defines a cut-off effective flare coefficient, denoted by m_c in the figure, which is the effective flare coefficient at the turning point, $m_c = m_{eff}(x_{tp})$. Wave propagation is possible only in the region where the effective flare coefficient is smaller than the cut-off one, that is, to the left of the turning point. This property is also in accordance with the behaviour of the exponential horn. In Figure A.1a, an excitation frequency corresponding, for example, to the cut-off frequency of the exponential horn with $m = 20$ may be considered. It can be seen that, at this frequency, all horns with a flare constant smaller than 20 will have a non-zero real wavenumber and so

will propagate, while all horns with larger flare will have zero real wavenumber and will not propagate.

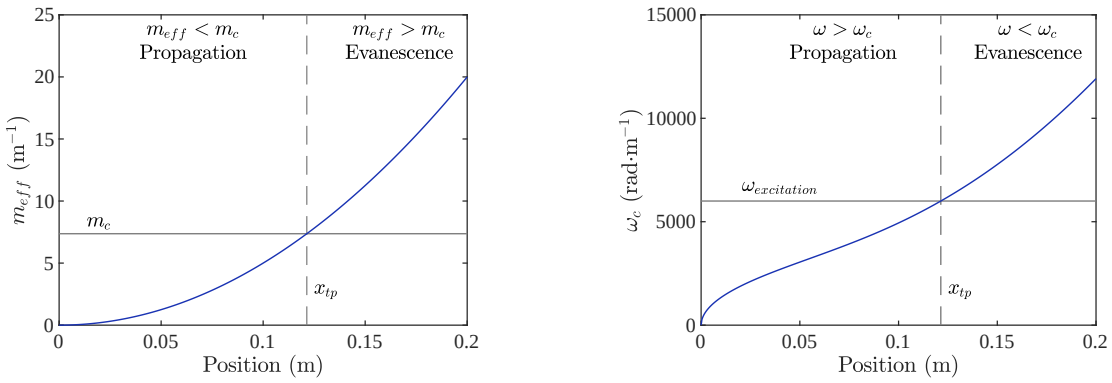

Figure A.2. (a) Spatial variation of the effective flare coefficient of a diverging 'power-exponential' horn. (b) Spatial variation of the cut-off frequency of a diverging 'power-exponential' horn. Geometrical properties: $S(x) = S_0 e^{bx^n}$, $S_0 = \pi a_0^2$, $a_0 = 0.02$ m, $b = 500$ and $n = 3$. In the graphs, x_{tp} is the position of the turning point, m_{eff} the effective flare coefficient, m_c the cut-off effective flare coefficient, ω_c the cut-off frequency and $\omega = \omega_{excitation}$ the excitation frequency. Propagation and evanescence regions for an excitation frequency $\omega = 6 \cdot 10^3$ rad$\cdot$ s^{-1} are noted in both graphs.

A symmetric converging horn is obtained by substitution of x by $l - x$ in the expression for the cross-sectional area, S, where l is the length of the horn. It should be noted that a simple change in the sign of the constant b, or, in general, of the effective flare coefficient, m_{eff}, does not result in a symmetric converging horn. The horn function for the converging horn becomes

$$F(x) = \frac{1}{2} bn(l-x)^{n-2} \left(\frac{1}{2} bn(l-x)^n + n - 1 \right). \tag{A.15}$$

A corresponding set of plots for the converging horn with cross-sectional area variation $S(x) = S_0 e^{b(l-x)^n}$ is given in Figure A.3; the plots are symmetric to those of Figure A.2. S_0 now equals the cross-sectional area at the end of the horn, which is the narrow one. The plots illustrate the fact that the 'power-exponential' horn, when driven from the wide end, allows only waves of frequency higher than the cut-off frequency at the wide end to propagate further; all frequencies below that are promptly reflected. Furthermore, since the cut-off frequency at the wide end is the maximum cut-off frequency in the horn, any wave of higher frequency may propagate throughout the length of the horn. Therefore, such a use of the horn practically imposes only one cut-off frequency. It should be noted that the above conclusions for a converging horn are valid for $n \geq 2$.

The horn equation (A.2) is not known to be analytically solvable for the 'power-exponential' horn, where $S = S_0 e^{bx^n}$, except for $n = 1$, where the horn reduces to an exponential one, and for $b < 0, n = 2$, where the longitudinal variation of the cross-sectional area becomes Gaussian [96]. Therefore, either approximate analytical or numerical methods have to be applied for acquiring the field of such a horn. An approximate analytical solution can be derived for example with

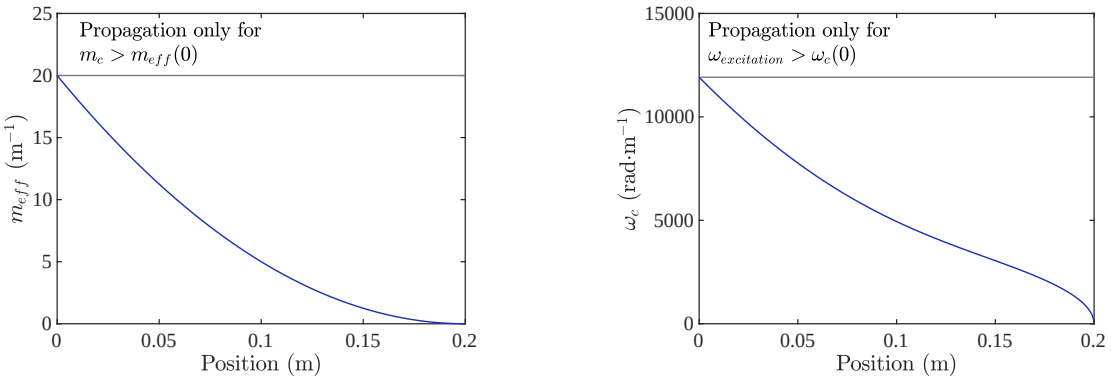

Figure A.3. (a) Spatial variation of the effective flare coefficient of a converging 'power-exponential' horn. (b) Spatial variation of the cut-off frequency of a converging 'power-exponential' horn. Geometrical properties: $S(x) = S_0 e^{b(l-x)^n}$, $S_0 = \pi a_0^2$, $a_0 = 0.02$ m, $b = 500$ and $n = 3$.

perturbation analysis, as in [101]. It should also be noted that Webster's equation describes exactly only the field of a cylindrical tube, a cylindrical sector or a conical horn [102], so it is not exactly descriptive of either the exponential or the 'power-exponential' horn, thus attributing an overall approximate character to the analytical considerations of such horns.

A.2.3 Composite horn model

Apart from the model of a simple flaring horn, the behaviour of a composite horn is also considered, as a simple model of a musical horn. Such a horn comprises a cylindrical tube connected to a 'power-exponential' horn. A composite horn consisting of a tube of radius $a_0 = 0.02$ m and length 0.4 m and a 'power-exponential' horn of length 0.18 m, with cross-sectional area variation $S(x) = S_0 e^{bx^n}$, where $S_0 = \pi a_0^2$, $b = 500$ and $n = 3$, is widely used in consequent simulations. The choice of a length of 0.18 m for the defined values of flare parameters is explained in Section A.3.2. An advantage of such a composite horn is that it allows for resonances and anti-resonances at lower frequencies compared to a purely expanding horn, as will be discussed in Section A.3.4.

The upper half of a longitudinal cross section of the horn is shown in Figure A.4, corresponding to the axial variation of the cross-sectional radius. It should be noted that the 'power-exponential' horn may be smoothly connected to a tube, since its radius is given by $a(x) = a_0 e^{0.5bx^n}$, whose derivative is

$$a' = \frac{1}{2} a_0 b x^{n-1} e^{\frac{1}{2}bx^n}, \tag{A.16}$$

which gives a zero slope at $x = 0$ (for $n > 1$). The cut-off frequency can be calculated by use of Equation (A.14), where, for the part with constant cross section, the horn function and, accordingly, the cut-off frequency, is zero. The spatial variation of the cut-off frequency is shown in Figure A.5a.

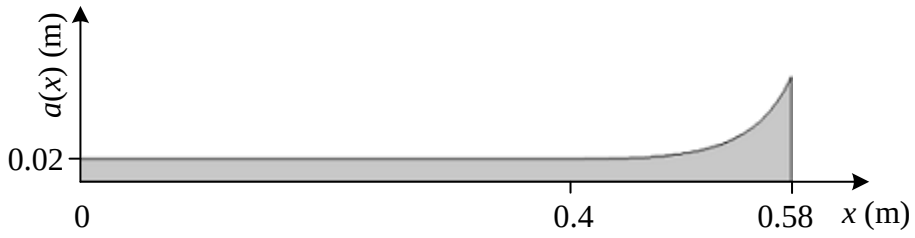

Figure A.4. Composite horn made of a cylindrical pipe connected to a 'power-exponential' horn.

The wavenumber distribution is calculated with Equation (A.13) and plotted in Figure A.5b in terms of its real and imaginary parts, for an excitation frequency of 1 kHz. Throughout the cylindrical tube, the wavenumber has a purely real value, which is that of plane-wave propagation. In the flaring region of the horn, it starts to decrease, until it reaches a turning point where it vanishes; reflection occurs at this point. Beyond the turning point, the wavenumber becomes purely imaginary, implying that waves no longer propagate; they are attenuated exponentially.

A.3 Numerical approach

This section presents two different numerical methods for calculating the field variables of a horn, namely, the Finite Element method and the Transmission Matrix method. The wave equation is not involved in these methods, and, so, they are not limited by its approximations. Other sources of approximation are present, however, for example due to discretisation of the spatial continuum. The two methods are each described in Sections A.3.1 to A.3.4, and the results from them are compared in Section A.3.5.

A.3.1 The Finite Element method

The acoustic horn can be analysed using the Finite Element method, which was briefly presented in Section 2.3.4. In the mesh used for the simulations here, the distance between two consecutive elements on the axis of the horn is about 0.012 m, which means that a minimum wavelength of about 0.072 m can be modelled accurately, if at least six elements per wavelength are used [40]. The smallest local wavelength occurs at the cylindrical section of the horn, where $\lambda_0 = c_0/f = 2\pi/k_0$, as can be seen in Figure A.5c. Mathematically, this occurs from the fact that the horn function of Equations (A.11) and (A.15) is always positive, for $n > 1$, and, therefore, in the region of propagation the following relations hold

$$\frac{2\pi}{\lambda(x,\omega)} = k(x,\omega) = \sqrt{k_0(\omega)^2 - F(x)} < k_0(\omega) = \frac{2\pi}{\lambda_0(\omega)} \Rightarrow \lambda(x,\omega) > \lambda_0(\omega). \tag{A.17}$$

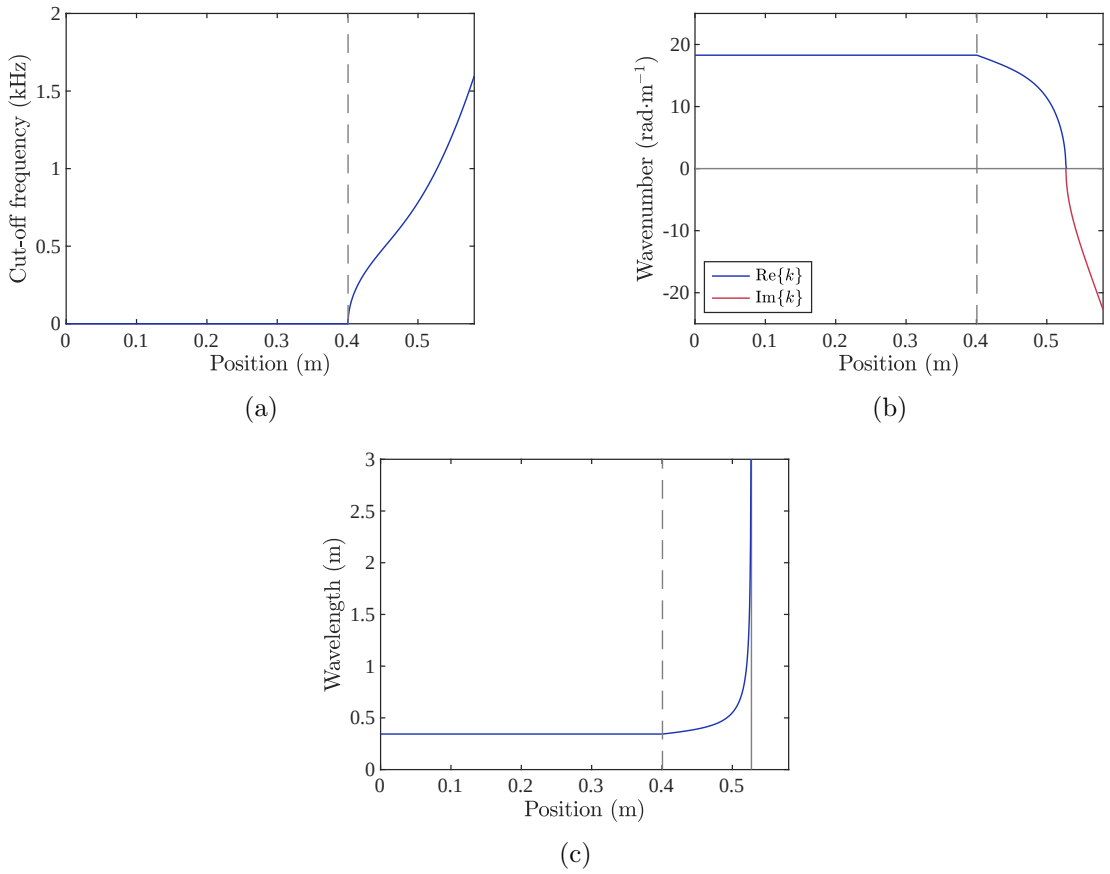

Figure A.5. Spatial variation of (a) the cut-off frequency (b) the real and imaginary parts of the wavenumber and (c) the wavelength in the composite horn of Figure A.4. In (b) and (c), an excitation frequency of 1 kHz has been used. The dashed vertical lines indicate the connection point of the cylindrical tube with the flaring horn and the cut-off location is noted by the solid vertical line in (c).

If the wavelength is calculated at the cylindrical section of the horn, the corresponding high-frequency limit is about $f_{max} = 4.8$ kHz. Therefore, frequencies up to this value will be considered.

A set of three-dimensional plots of Finite Element simulations is given in Figures A.6 to A.8. Figure A.6 shows the sound pressure level in the horn for two different frequencies. It can be seen that the surfaces of constant sound pressure level are generally planar in the uniform tube. Furthermore, in the high frequency plot of Figure A.6b, it can be seen that in the flaring part of the horn the surfaces of constant sound pressure level cease to be planar and then get further distorted towards the mouth. Figures A.7 and A.8 illustrate the surfaces of equal pressure for different frequencies, which will be commented upon in the next section. Numerical results from the Finite Element method are given in Section A.3.5, where they are used as a reference for assessing the Transmission Matrix method.

A.3.2 The Transmission Matrix method

In this section, a numerical solution for the acoustic field of a horn is described, by approximating the horn with a large number of consecutive segments of simpler form and small length. Initially,

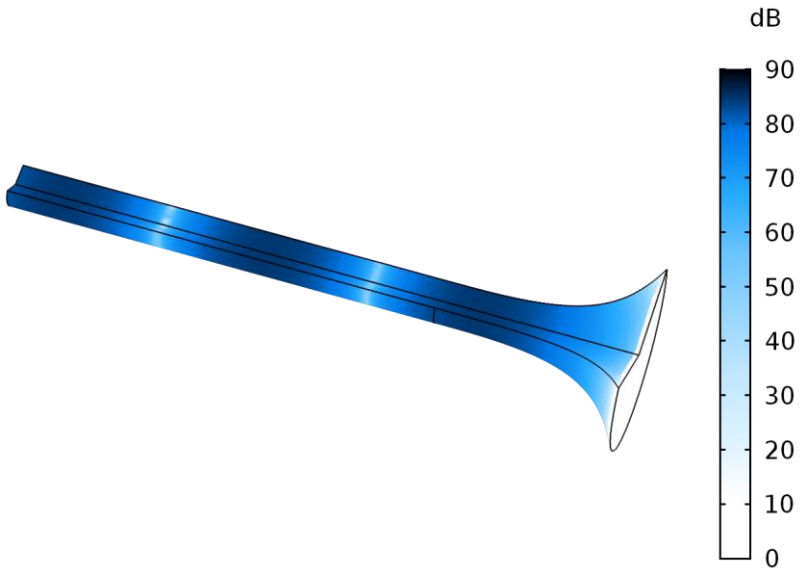

(a)

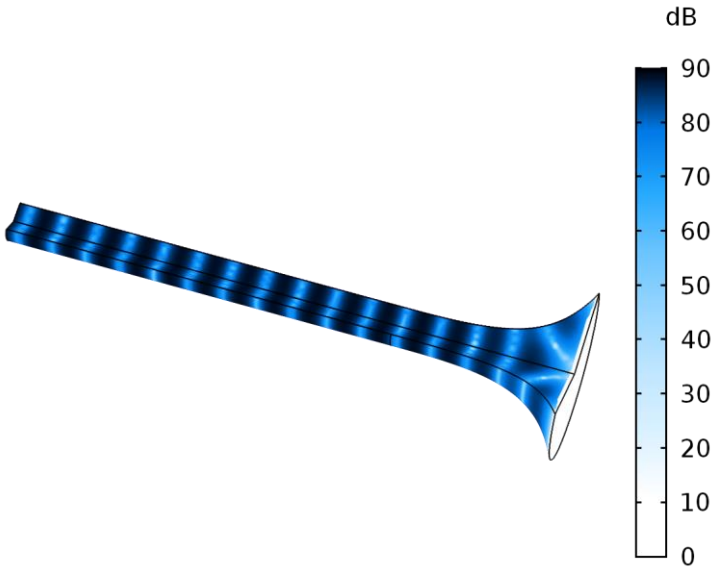

(b)

Figure A.6. Sound pressure level of a 'power-exponential' horn connected to a cylindrical tube, in dB re $2 \cdot 10^{-5}$ Pa, calculated using the Finite Element method. (a) 880 Hz, (b) 4.8 kHz.

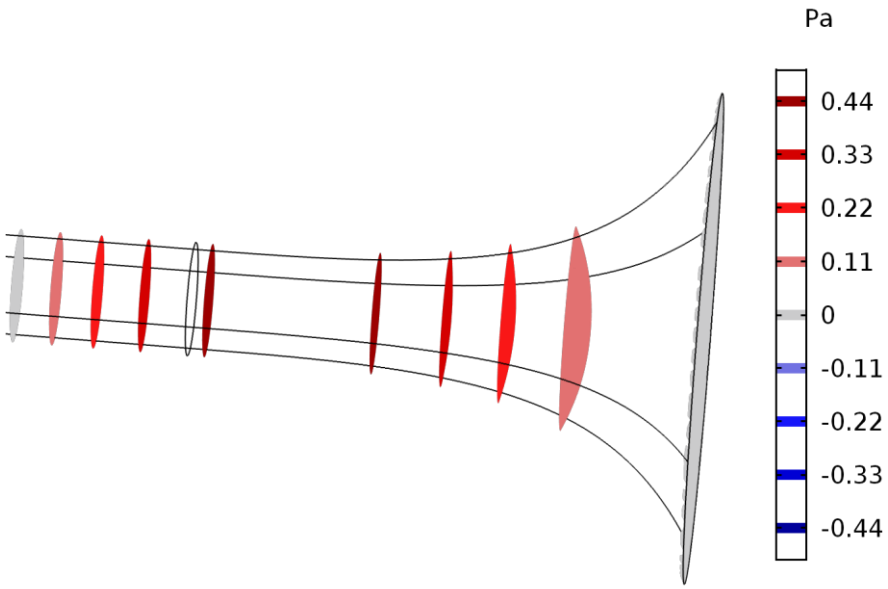

(a)

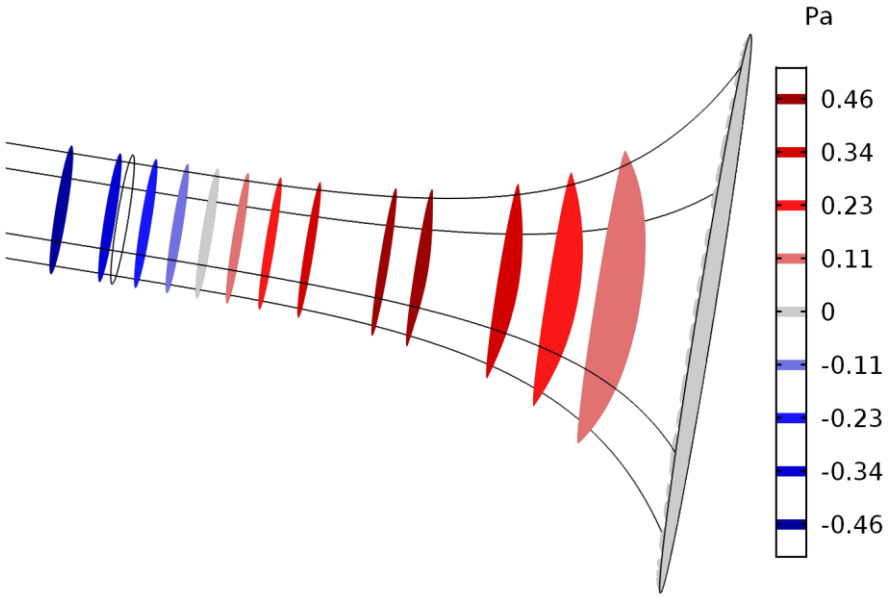

(b)

Figure A.7. Isopressure surfaces in a wide end of a 'power-exponential' horn connected to a cylindrical tube, calculated using the Finite Element method. (a) 880 Hz, (b) 1.32 kHz

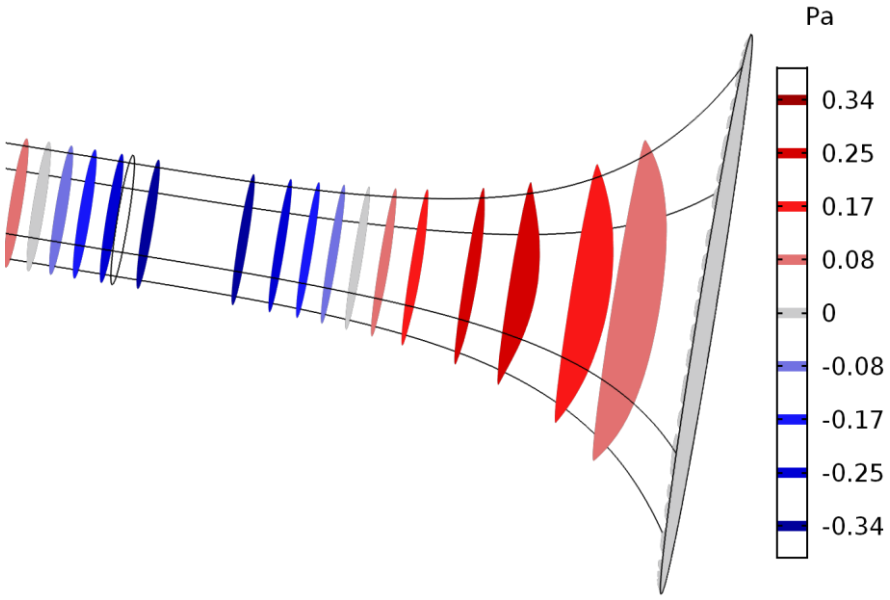

(a)

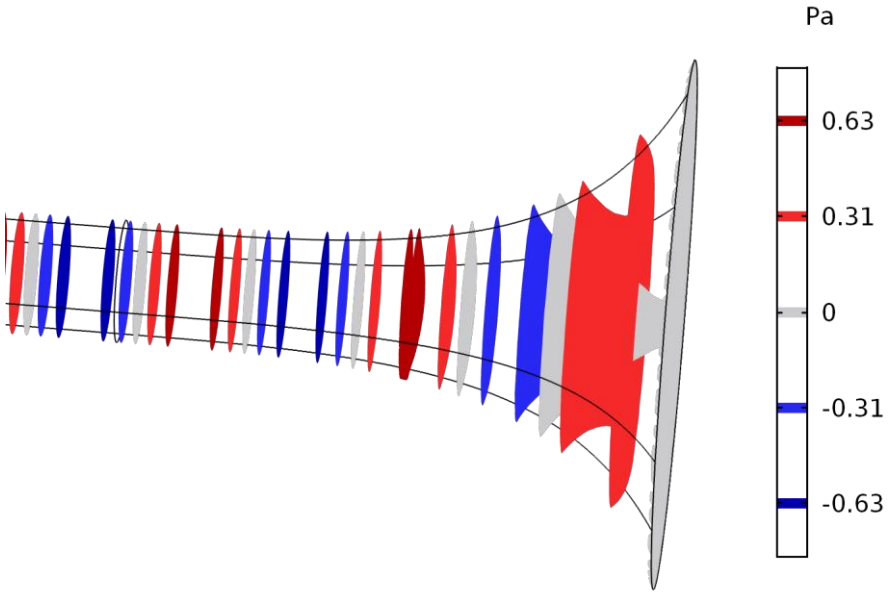

(b)

Figure A.8. Isopressure surfaces in a wide end of a 'power-exponential' horn connected to a cylindrical tube, calculated using the Finite Element method. (a) 1.76 kHz, (b) 4.8 kHz.

the horn is approximated by cylindrical segments, where the segments have progressively larger cross-sectional area as they approach the mouth. A second approximation consists of elementary conical horns, with segments towards the mouth having larger flare, following the correspondent geometry of the initial horn. The distribution of the acoustic variables is calculated by use of the Transmission Matrix. Such methodology has been used widely for modelling acoustic horns, for example in [103, 104].

The Transmission Matrix method is based on the assumption that only the fundamental mode is present in the horn [104]. Therefore, it may be applied up to the cut-off frequency of the first higher-order mode. This limit, for a tube with circular cross section, is given by $f_{c,11} = 0.293c_0/a$, where $f_{c,11}$ is the cut-off frequency of the first higher-order mode and a is the radius of the cross section [57]. For the flare coefficients of a 'power-exponential' horn used in most parts of this analysis, namely, $b = 500$ and $n = 3$, a horn length of 0.2 m results in a maximum radius of 0.148 m, which gives a cut-off frequency of 681 Hz.

The concept of the cut-off frequency of higher-order modes should not be confused with that of the fundamental mode, presented in the analysis of exponential and 'power-exponential' horns. Propagation of higher-order modes depends on the relative magnitude of the local wavelength with respect to the local diameter, while the cut-off of the fundamental mode is due to the flaring of the horn. In case where the cut-off frequency of the fundamental is higher than the cut-off frequency of the first higher-order mode, unimodal propagation is not possible; if a wave of frequency higher than the cut-off frequency of the fundamental mode enters the horn, both the fundamental and the higher-order mode will be present.

A wider spectrum of unimodal propagation is accomplished by use of a shorter horn. In a 'power-exponential' horn of length 0.18 m, the first higher-order mode has a cut-off frequency of 1172 Hz and, therefore, unimodal propagation takes place up to this frequency. In Figure A.5a it can be seen that a flaring horn with the above characteristics imposes cut-off within its length for frequencies up to about 1600 Hz, that is, well into the non-unimodal spectrum. This is found to be convenient for comparisons between different calculation methods. It should be noted, however, that higher-order modes will begin to appear at the mouth of the horn as frequency increases. Therefore, in the narrow part of the horn, the pressure will remain unimodal as long as the frequency is higher than the cut-off frequency of the first higher-order mode at the narrow cylindrical tube, which, with the values used here, gives $f_{c,11} \approx 5$ kHz.

In Figures A.7 and A.8, the isopressure surfaces for different frequencies calculated using the Finite Element method, were shown, which coincide with the wavefronts in the case of unimodal propagation [97]. Most of the uniform part of the horn is not shown, for ease of illustration. It can be seen that the isopressure surfaces are nearly planar in the uniform part even at the high frequency, which complies with the result of the first higher-order mode cut-off frequency for the uniform part being about 5 kHz. Moreover, these surfaces become sphere-like at the flaring part of the horn, thus resembling the wavefronts of a conical horn, as will be presented in

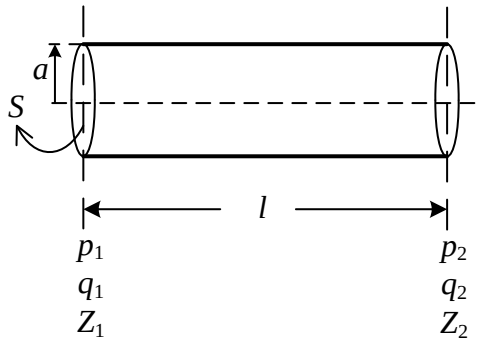

Figure A.9. Schematic of a cylindrical tube.

subsequent sections. In the highest frequency illustrated here, that is, 4.8 kHz, the isopressure surfaces cease to be sphere-like. This indicates the presence of higher-order modes, as would be expected by previous considerations.

A.3.3 Approximation with cylindrical tubes

It will be useful for subsequent analysis to consider the elementary structure of a tube with constant cross section. A convenient way of mathematical representation of such a tube, as the one shown in Figure A.9, in order to associate the values of the acoustic pressure and acoustic volume velocity at its ends, is that of the Transmission Matrix [93],

$$\begin{bmatrix} p_1 \\ q_1 \end{bmatrix} = \begin{bmatrix} \cos k_0 l & \mathrm{i}\frac{\rho_0 c_0}{S} \sin k_0 l \\ \mathrm{i}\frac{S}{\rho_0 c_0} \sin k_0 l & \cos k_0 l \end{bmatrix} \begin{bmatrix} p_2 \\ q_2 \end{bmatrix}, \tag{A.18}$$

where the indices 1 and 2 denote the left and right side of the tube, respectively, l is the length of the tube, k_0 is the wavenumber in free space and S is the cross-sectional area. The pressure and volume velocity are considered to be the state variables of the system. It is also useful to introduce the acoustic impedance, defined as the ratio of the acoustic pressure to acoustic volume velocity, $Z = p/q$. The input impedance is the value of the impedance at the throat of the horn.

An acoustic horn with circular cross section is shown in Figure A.10a. In this analysis, the case where the horn is driven with constant volume velocity, Q, at its narrow end and a pressure release condition holds at its wide end is examined. Again, it should be noted that the equivalence of the cross-sectional area, $S(x)$, to the wavefront area, $S_w(x)$, assumes plane-wave propagation. An approximate correspondence of the two areas requires slow variance in cross section.

The continuously flaring horn may be approximated by a finite number of cylindrical tubes of the same length, geometrically fitted in the horn, as depicted in Figure A.10b. When the

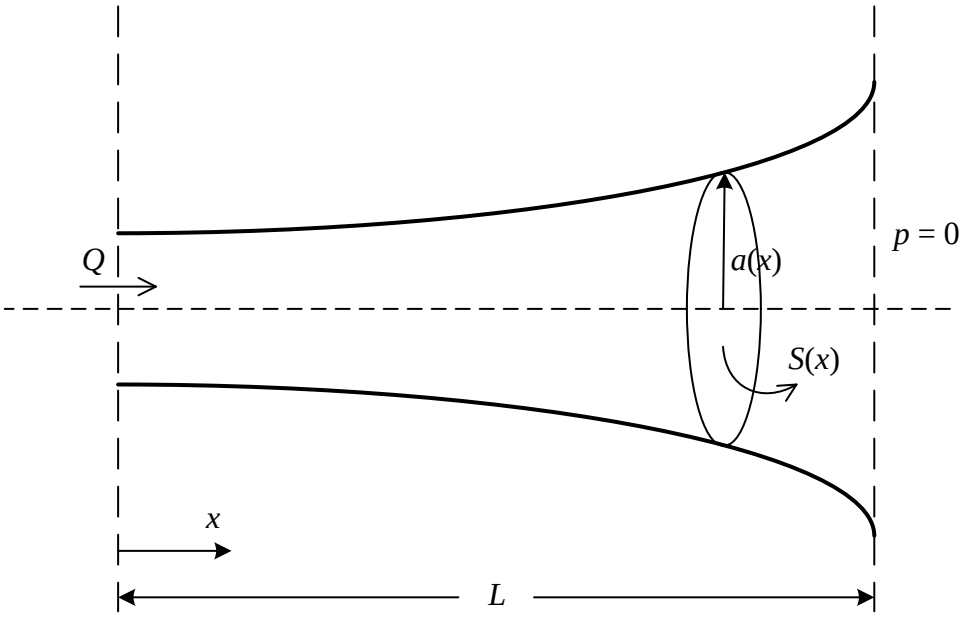

(a)

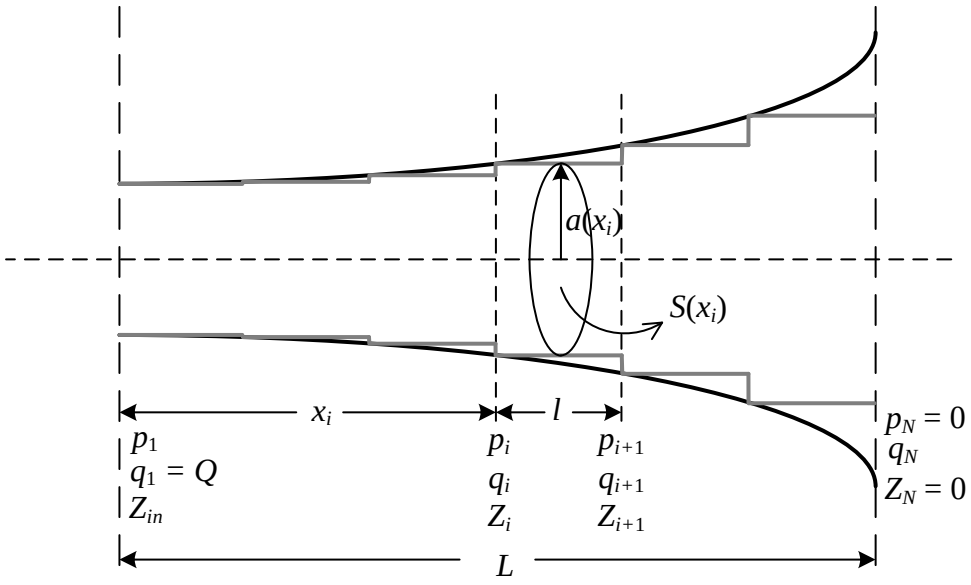

(b)

Figure A.10. (a) Schematic of an acoustic horn with circular cross-section of radius $a(x)$ and cross-sectional area $S(x)$, driven with volume velocity Q at its narrow end. A pressure release condition applies in the wide end. (b) Approximation of the horn with a finite number of cylindrical tubes.

number of the tubes becomes large, the length of each cylinder and the radial step between two adjacent cylinders become small, and the resulting structure approaches the geometry of the horn. In this way, the wave propagation in the horn can be locally approximated by forward- and backward-travelling plane waves with locally constant complex amplitudes within each

cylindrical tube, according to the plane-wave pressure in a tube with constant cross section [57],

$$p_i(x) = A_i \mathrm{e}^{-\mathrm{i}k_0 x} + B_i \mathrm{e}^{\mathrm{i}k_0 x}, \tag{A.19}$$

where $p_i(x)$, A_i and B_i are the acoustic pressure, the forward-travelling-wave amplitude and the backward-travelling-wave amplitude in the i-th cylinder, respectively. The volume velocity has, accordingly, the form [57]

$$q_i(x) = \frac{S_i}{\rho_0 c_0} \left(A_i \mathrm{e}^{-\mathrm{i}k_0 x} - B_i \mathrm{e}^{\mathrm{i}k_0 x} \right), \tag{A.20}$$

where ρ_0 is the ambient density of air, or, in general, of the fluid consisting the medium of propagation.

If a sufficiently fine spatial discretisation of the horn is considered in terms of small-length cylinders, the values of the pressure and volume velocity in the ends of the cylinders may be taken as discrete approximations of the continuous longitudinal variation of the respective physical quantities along the horn. Furthermore, due to the continuity of pressure and volume velocity at the joints of the cylindrical tubes, the right-side pressure and volume velocity of a tube have to be equal to the left-side pressure and velocity of its adjacent tube, respectively [57].

At the specified problem, the Transmission Matrix relation for an arbitrary position along the horn takes the form

$$\begin{bmatrix} p_i \\ q_i \end{bmatrix} = \begin{bmatrix} \cos k_0 l & \mathrm{i}\frac{\rho_0 c_0}{S_i} \sin k_0 l \\ \mathrm{i}\frac{S_i}{\rho_0 c_0} \sin k_0 l & \cos k_0 l \end{bmatrix} \begin{bmatrix} p_{i+1} \\ q_{i+1} \end{bmatrix}, \tag{A.21}$$

where indices denote order of position along the horn. Especially for the cross-sectional area, it should be clarified that $S_i = S(x_i)$, which means that the cross-sectional area of the i-th cylindrical element is that of the original continuously flaring horn at position x_i, as can also be seen in the illustration of Figure A.10b.

In order to acquire the values of the field quantities at the ends of all the elementary cylinders, it is required that both quantities be known at the right end, or mouth, of the horn; the rest of the values can be found by iteratively applying the Transmission Matrix relation of Equation (A.21). Once the pressure, p_N, and volume velocity, q_N, at the mouth are known, the values at the left side of the rightmost cylinder, p_{N-1} and q_{N-1}, can be found, which are equal to the right-side values of the penultimate cylinder, from which the values of the left side of the penultimate cylinder are obtained; this procedure of induction can be continued until the values of the field quantities are obtained throughout the horn.

The pressure at the mouth of the horn is set to zero, expressing the pressure release boundary condition at the mouth; the volume velocity at the mouth then needs to be found. The other

boundary condition is the constant input volume velocity, Q, at the throat. Therefore, the values of the acoustic variables at the throat must be associated directly to the ones at the mouth. For this aim, all intermediate state vectors have to be replaced by the matrix product of all the intermediate Transmission Matrices. At this point, Equation (A.18) is written in compact matrix form for a cylinder of arbitrary order of position, i, in the horn as

$$\mathbf{v}_i = \mathbf{T}_i \mathbf{v}_{i+1}, \tag{A.22}$$

where $\mathbf{v}_i$ and $\mathbf{v}_{i+1}$ are the state vectors at the left side of the tubes of position order i and $i+1$, respectively, and $\mathbf{T}_i$ is the i-th Transmission Matrix. The state vector at position x_{N-1} can then be written as

$$\mathbf{v}_{N-1} = \mathbf{T}_{N-1} \mathbf{v}_N, \tag{A.23}$$

where N is the number of positions where the field is evaluated; it follows that the number of elementrary cylinders used is $N-1$, as can be seen in the illustration of Figure A.10b. The state vector at position x_{N-2} is in turn written as

$$\mathbf{v}_{N-2} = \mathbf{T}_{N-2} \mathbf{v}_{N-1} = \mathbf{T}_{N-2} \mathbf{T}_{N-1} \mathbf{v}_N, \tag{A.24}$$

and, by iteration, the state vector at position $x_1 = 0$, that is, at the throat of the horn, can be written as

$$\mathbf{v}_1 = \mathbf{T}_1 \mathbf{T}_2 ... \mathbf{T}_{N-2} \mathbf{T}_{N-1} \mathbf{v}_N. \tag{A.25}$$

It is noted that all intermediate Transmission Matrices, and, therefore, also their product, can be calculated directly, as can be clearly seen from the form of the elements of the matrix in Equation (A.18). For further manipulation, the state vectors are returned to their expanded form and the Transmission Matrix of the whole horn, consisting of the product of all the intermediate Transmission Matrices, is also written explicitly in terms of its elements as

$$\begin{bmatrix} p_1 \\ q_1 \end{bmatrix} = \begin{bmatrix} T_{11} & T_{12} \\ T_{21} & T_{22} \end{bmatrix} \begin{bmatrix} p_N \\ q_N \end{bmatrix}. \tag{A.26}$$

Substitution of the known values due to the boundary conditions gives

$$\begin{bmatrix} p_1 \\ Q \end{bmatrix} = \begin{bmatrix} T_{11} & T_{12} \\ T_{21} & T_{22} \end{bmatrix} \begin{bmatrix} 0 \\ q_N \end{bmatrix}. \tag{A.27}$$

The values of p_1 and q_N are found by solution of the 2x2 system of equations of the matrix equation (A.27), giving

$$p_1 = \frac{T_{12}}{T_{22}} Q, q_1 = \frac{1}{T_{22}} Q.$$

It is now possible to obtain the values of the state vector, and, therefore, the state variables, at all positions, by iteratively applying Equation (A.22), starting from the mouth of the horn, where $i = N - 1$, and moving step by step backwards up to the throat. It should be made clear that in this procedure a single frequency is considered. The input impedance for a frequency range can be determined by evaluating the ratio of the pressure to the volume velocity at the throat for a set of frequencies across the desired range, as calculated with the above procedure.

If only the impedance is sought, for example in order to acquire the input impedance of the horn over a certain frequency range, it is alternatively possible to use a formula relating the impedance at the left side of each cylinder with the impedance at its right side [54],

$$Z_1 = \frac{\rho_0 c_0}{S}\left(\frac{SZ_2\cos k_0 l + \mathrm{i}\rho_0 c_0 \sin k_0 l}{\mathrm{i}SZ_2 \sin k_0 l + \rho_0 c_0 \cos k_0 l}\right), \tag{A.28}$$

where Z_1 is the impedance at the left side of the cylinder and Z_2 is the impedance at the right side of the cylinder, as shown in Figure A.9. This relation is derived from Equation (A.18), if it is written explicitly as two equations as

$$\begin{aligned} p_1 &= p_2 \cos k_0 l + \mathrm{i}q_2 \frac{\rho_0 c_0}{S} \sin k_0 l, \\ q_1 &= \mathrm{i}p_2 \frac{S}{\rho_0 c_0} \sin k_0 l + q_2 \cos k_0 l; \end{aligned} \tag{A.29}$$

dividing by sides and writing the pressure at the right side as $p_2 = q_2 Z_2$ results in Equation (A.28). For an arbitrary cylindrical segment, Equation (A.28) can be written as

$$Z_i = \frac{\rho_0 c_0}{S_i}\left(\frac{S_i Z_{i+1}\cos k_0 l + \mathrm{i}\rho_0 c_0 \sin k_0 l}{\mathrm{i}S_i Z_{i+1} \sin k_0 l + \rho_0 c_0 \cos k_0 l}\right). \tag{A.30}$$

Starting with the pressure release boundary condition at the mouth, now expressed as $Z_N = 0$, the impedance at the throat, that is, the input impedance, can be found by iteratively using Equation (A.30) step by step towards decreasing position in the horn. No boundary condition at the input end is required in this procedure.

A.3.4 Approximation with conical horns

In the case of a conical horn consisting of a truncated cone, such as the one depicted in Figure A.11, the Transmission Matrix is given by [105]

$$\begin{bmatrix} p_1 \\ q_1 \end{bmatrix} = \frac{x_2}{x_1} \begin{bmatrix} -\frac{\sin(k_0 l - \theta_2)}{\sin\theta_2} & \mathrm{i}\frac{\rho_0 c_0}{S_2}\sin k_0 l \\ \mathrm{i}\frac{S_1}{\rho_0 c_0}\frac{\sin(k_0 l + \theta_1 - \theta_2)}{\sin\theta_1 \sin\theta_2} & \frac{S_1}{S_2}\frac{\sin(k_0 l + \theta_1)}{\sin\theta_1} \end{bmatrix} \begin{bmatrix} p_2 \\ q_2 \end{bmatrix}, \tag{A.31}$$

where $\theta_1 = \tan^{-1} k_0 x_1$ and $\theta_2 = \tan^{-1} k_0 x_2$, and x_1 and x_2 are the axial distances of the two ends of the truncated cone from its geometrical apex. It should be noted that for the conical horn, as is the case for the cylindrical pipe, the wavenumber, k_0, is the constant wavenumber

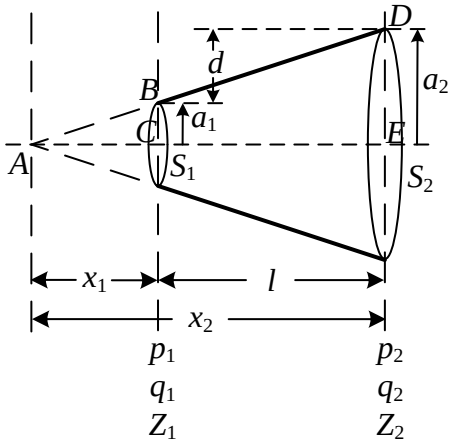

Figure A.11. Schematic of a conical horn.

in free space. This derives from the fact that, for the variation of cross-sectional area of the conical horn, $S = S_0 x^2$, the horn equation (A.2) has the exact solution [48]

$$p = \frac{p_0}{x}\left(A\mathrm{e}^{-\mathrm{i}k_0 x} + B\mathrm{e}^{\mathrm{i}k_0 x}\right), \tag{A.32}$$

consisting of forward-, or outward-, and backward-, or inward-, travelling waves with linear phase $\mp k_0 x$, respectively, where A and B are complex coefficients.

The formulation of the Transmission Matrix of Equation (A.31) is based on a plane-wave assumption, where the pressure is considered as constant over the cross section, and the volume velocity is accordingly defined as the product of the particle velocity with the cross-sectional area. In principle, this assumption is not applicable for wave propagation in a cone, where the wavefront is actually spherical. Different formulations of the Transmission Matrix are also possible, such as in [104]. Further considerations on the wavefront are made in Section A.3.6, providing justification for the the use of the Transmission Matrix method with conical elements.

In a similar way as with the cylindrical segments, the horn can be geometrically approximated by a number of conical horns of small length, whose end circular curves intersect the walls of the original horn exactly, as shown in Figure A.12a. For clarity of illustration, a horn with larger flare is shown here compared to that of Figure A.10, and it is shown as approximated by only four conical horns. Again it becomes clear that as the number of conical horns increases, the resulting shape approaches that of the initial horn.

The geometrical apices of the fitted conical horns of Figure A.12a do not coincide, as can be seen by extending their generating lines, also shown in the drawing. Therefore, it is not helpful to consider the axial distances of the ends of each cone from a specific point; alternatively they can be expressed in terms of the radii of the respective cross sections, which are known at each point from the shape of the initial horn, and of the cone length. This is accomplished

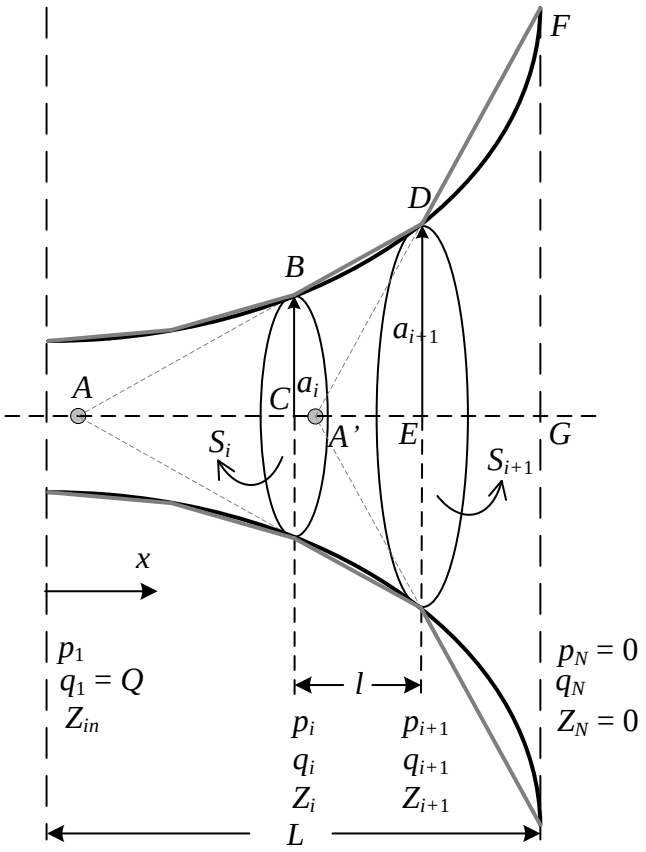

(a)

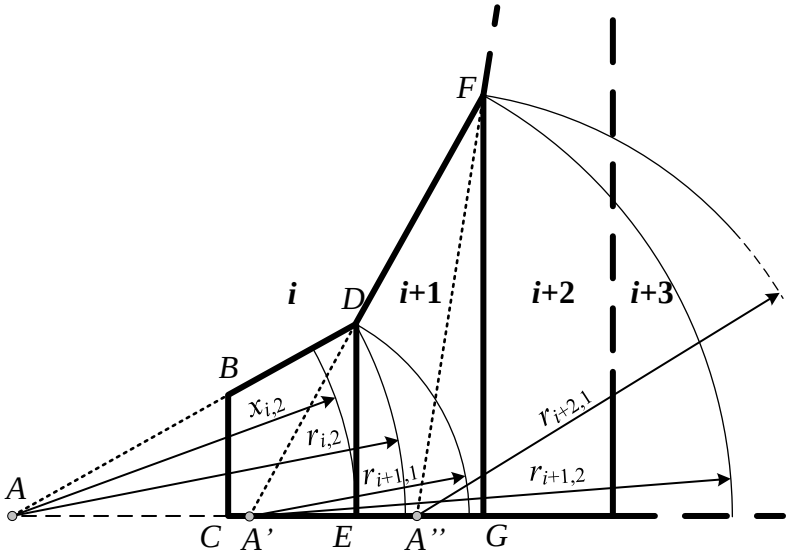

(b)

Figure A.12. (a) Horn approximated by fitted consecutive conical horns. (b) Planar geometrical representation of half a section of consecutive conical segments. Points A, A' and A'' are the apices of the cones i, $i+1$ and $i+2$, respectively.

by inspection of the similar triangles ABC and ADE in Figure A.11, so that $x_1 = a_1 l/d$ and $x_2 = a_2 l/d$, where $d = a_2 - a_1$. If a fitted conical horn of an arbitrary order of position is considered, Equation (A.31) takes the form

$$\begin{bmatrix} p_i \\ q_i \end{bmatrix} = \frac{a_{i+1}}{a_i} \begin{bmatrix} -\frac{\sin(k_0 l - \theta_{i,2})}{\sin\theta_{i,2}} & \mathrm{i}\frac{\rho_0 c_0}{S_{i+1}} \sin k_0 l \\ \mathrm{i}\frac{S_i}{\rho_0 c_0} \frac{\sin(k_0 l + \theta_{i,1} - \theta_{i,2})}{\sin\theta_{i,1}\sin\theta_{i,2}} & \frac{S_i}{S_{i+1}} \frac{\sin(k_0 l + \theta_{i,1})}{\sin\theta_{i,1}} \end{bmatrix} \begin{bmatrix} p_{i+1} \\ q_{i+1} \end{bmatrix}, \tag{A.33}$$

where $\theta_{i,1} = \tan^{-1}(k_0 l a_i/d_i)$ and $\theta_{i,2} = \tan^{-1}(k_0 l a_{i+1}/d_i)$, with $d_i = a_{i+1} - a_i$.

In correspondence with Equation (A.28), a relation expressing the input impedance of a conical horn in terms of its output impedance holds, which, if written for an arbitrary segment, takes the form [54]

$$Z_i = \frac{\rho_0 c_0}{S_i} \left[\frac{\mathrm{i} Z_{i+1} \frac{\sin(k_0 l - \theta_{i,2})}{\sin\theta_{i,2}} + \frac{\rho_0 c_0}{S_{i+1}} \sin k_0 l}{Z_{i+1} \frac{\sin(k_0 l + \theta_{i,1} - \theta_{i,2})}{\sin\theta_{i,1}\sin\theta_{i,2}} - \mathrm{i}\frac{\rho_0 c_0}{S_{i+1}} \frac{\sin(kl + \theta_{i,1})}{\sin\theta_{i,1}}} \right]. \tag{A.34}$$

From a purely geometrical point of view, the conical approximation is better than the cylindrical one, since the cone has a non-zero finite slope, as the original horn, whereas the cascade of cylinders is made of sections of zero slope connected with infinite-slope steps, as can be seen in Figure A.10b. However, simulations carried out show that the two approximations produce almost identical results, even for not very small spatial-meshing segments. In the results shown in Figure A.13 for example, 50 segments were used, which, for a horn with a length of 0.18 m, corresponds to a segment length of 3.6 mm. Figures A.13a and b show the pressure and volume velocity spatial distribution, respectively, for an input frequency of 1 kHz, while Figure A.13c shows the input impedance frequency variation.

Figure A.14 illustrates the effect of the number of elements, with the input impedance evaluated with a simple 'power-exponential' horn approximated with 10 instead of 50 segments. A periodically variable deviation can be observed in the spectrum, with the cylindrical and conical approaches converging in certain frequency bands and diverging in others. A smoother approximation by 200 conical segments is also plotted as a blue line, largely hidden by the conical approximation of 10 segments, justifying the latter as a good approximation for the input impedance of the horn. It should be remembered, however, that the Transmission Matrix method is not valid above the unimodal frequency range, which is up to about 1.2 kHz for the specified horn. Therefore, the current simulation only provides a comparison of the use of cylindrical segments to conical ones, without testing the accuracy of either in terms of the physical problem.

A.3.5 Comparison of the Finite Element and Transmission Matrix methods

The horn used for the comparison of the Finite Element and Transmission Matrix methods is the one illustrated in Figure A.4. Results obtained from a Finite Element analysis are considered

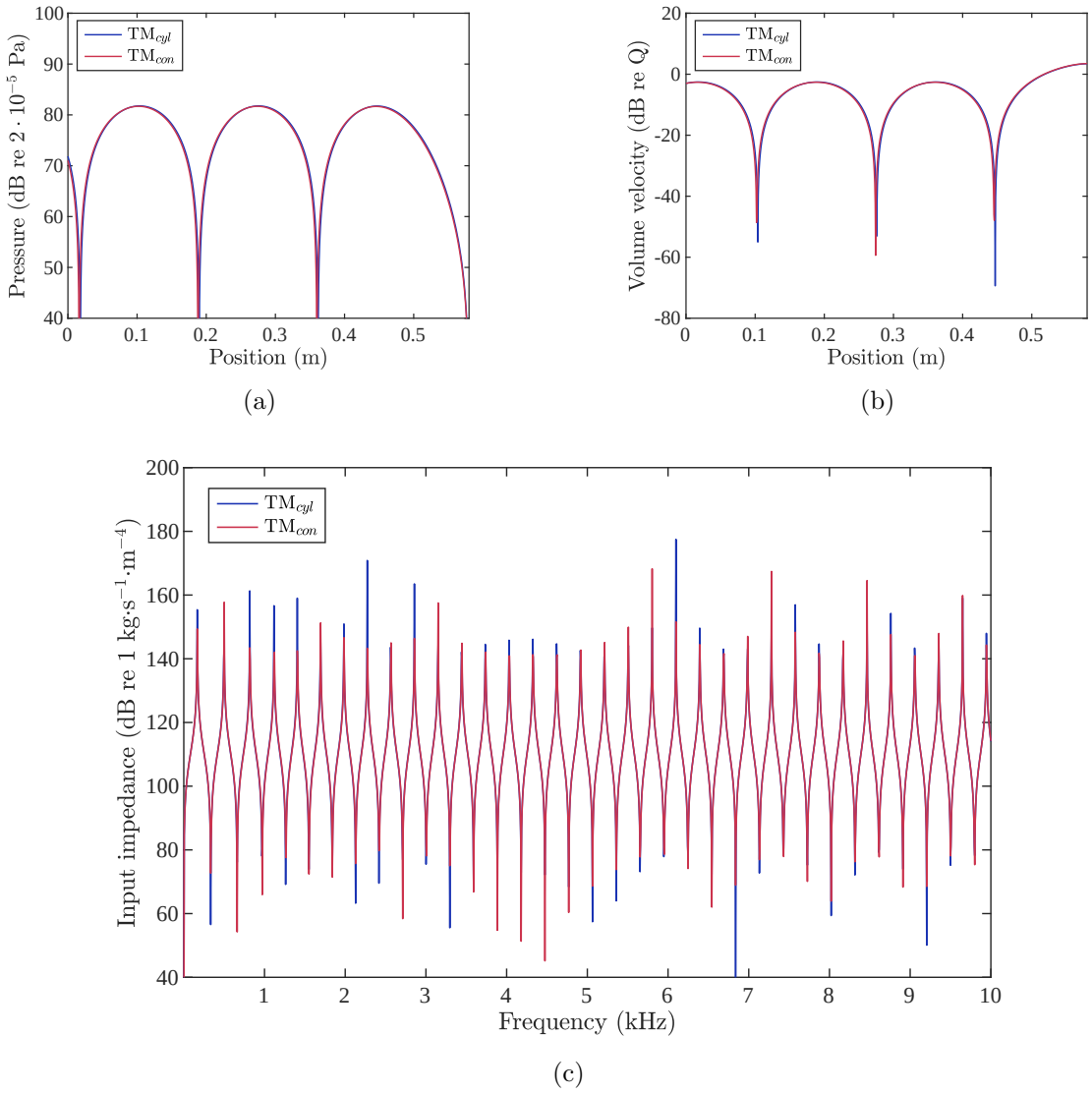

Figure A.13. Comparison of the results of Transmission Matrix simulations using the cylindrical and conical approach of a composite horn, each with 50 segments, consisting of a cylindrical tube of length 0.4 m and a 'power-exponential' horn of length 0.18 m. The cross-sectional area of the flaring part varies as $S = S_0 e^{bx^n}$, where $S_0 = \pi a_0^2$, $a_0 = 0.02$ m $b = 500$ and $n = 3$. Number of segments: 50. Length of segment: 3.6 mm. Input volume velocity: $Q = 10^{-6}$ m^{3}s^{-1}. (a) Pressure spatial distribution for an excitation frequency of 1 kHz. (b) Volume velocity spatial distribution for an excitation frequency of 1 kHz. (c) Input impedance frequency variation.

to be more accurate and are therefore used as a reference for the assessment of the validity of the Transmission Matrix method. In calculations with the Transmission Matrix method, 100 conical segments have been used.

A plot of the input impedance over the range of accuracy of the finite element meshing used, that is, up to about 4.8 Hz, is shown in Figure A.15a. It can be seen that there is a gradual shift towards higher frequencies of the input impedance predicted by use of the Transmission Matrix. Since the cut-off frequency of the first higher-order mode occurs near 1.2 kHz, the Transmission Matrix method is considered to be accurate up to this frequency. A corresponding detail of the input impedance is given in Figure A.15b. Visible deviation occurs towards the high-frequency limit of this spectral region.

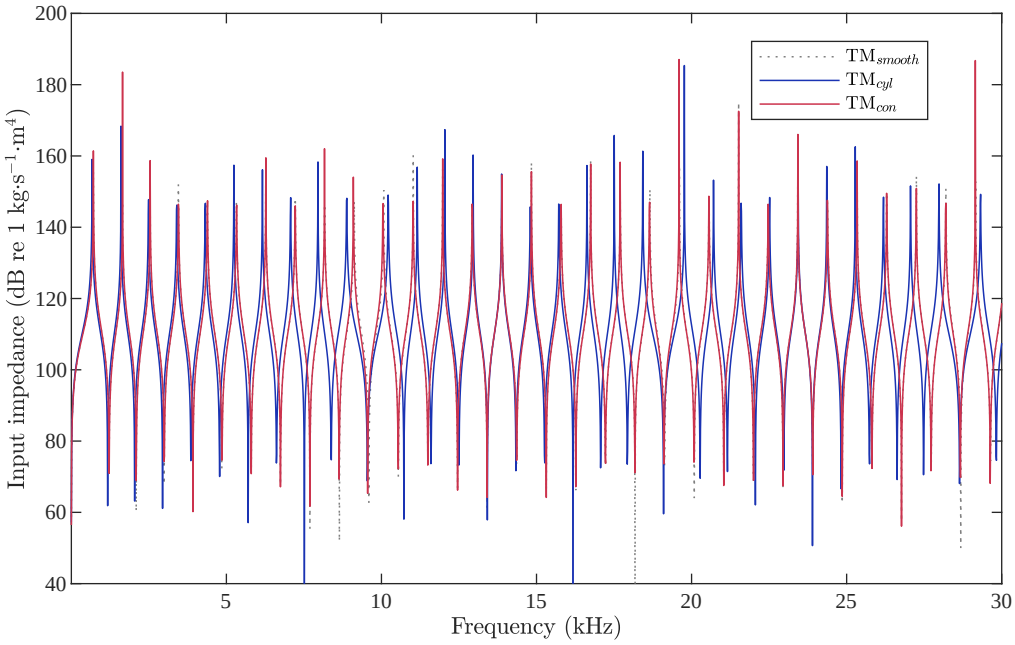

Figure A.14. Input impedance of a simple 'power-exponential' horn of length 0.18 m, approximated by 10 segments, cylindrical, TM$_{cyl}$, and conical, TM$_{con}$. A more accurate approximation by 200 conical segments, TM$_{smooth}$, is also plotted.

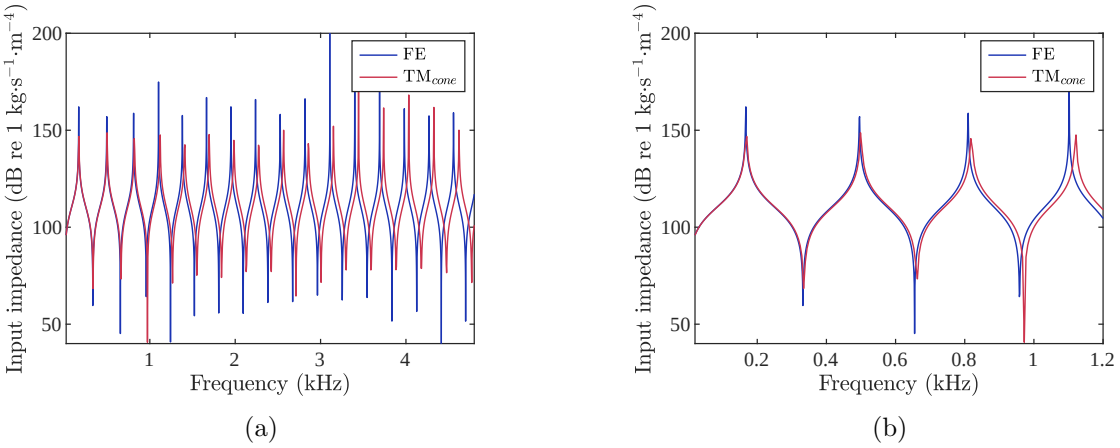

Figure A.15. Input impedance variation of a compound horn with the profile of Figure A.4, calculated with the Finite Element method and the Transmission Matrix method (using 100 conical segments) (a) up to 4.8 kHz, and (b) up to 1.2 kHz.

The relative error of the frequencies of the resonances and anti-resonances calculated with the Transmission Matrix with respect to the corresponding frequencies found with the Finite Element method is calculated by

$$E_f(f_{TM}, f_{FE}) = \frac{f_{TM} - f_{FE}}{f_{FE}} \cdot 100\%, \tag{A.35}$$

where f_{FE} is the frequency in which a resonance or anti-resonance occurs, as calculated with the Finite Element method, and f_{TM} is the corresponding frequency for the same-order resonance or anti-resonance calculated with the Transmission Matrix method. The relative error for the

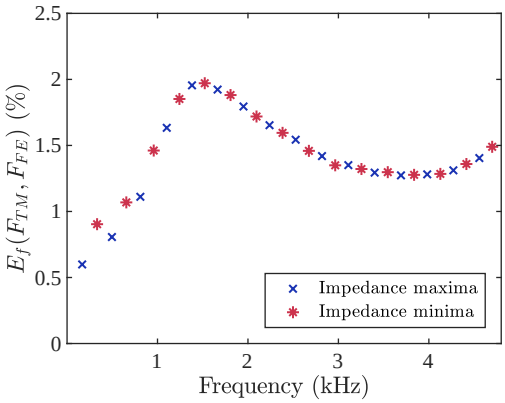

Figure A.16. Relative error of resonance and anti-resonance frequencies calculated with the transmission matrix method, with reference to calculations with the Finite Element method.

32 resonances and anti-resonances occurring up to 4.8 kHz is illustrated in Figure A.16. Firstly, it may be commented that the Transmission Matrix method always overestimates the resonance and anti-resonance frequencies, as can also be seen in Figure A.15a. In low frequencies, the relative error starts from below 1%, reaching a value of 1.1% for the third input impedance maximum, at around 810 Hz. It keeps rising with frequency, up to a value of about 2% at around 1.5 kHz, and then drops to values around 1.5%. It should be noted that in the fourth maximum at around 1.1 kHz, that is, within the range of unimodal propagation, the relative error, about 1.6%, is slightly higher than for frequencies over 2.5 kHz, that is, well into the multimodal spectrum. In general, within the spectrum assessed, the relative error in the estimation of the frequencies of input impedance peaks fluctuates relatively little, around 1.5%.

A set of plots of the spatial variation of the pressure calculated using both the Finite Element and Transmission Matrix methods for different excitation frequencies is given in Figure A.17. In Figure A.17a, which corresponds to an excitation frequency of 220 Hz, little deviation is apparent in the flaring part of the horn. As frequency increases, the spatial pressure distributions calculated by the Transmission Matrix method progressively diverge more. This also reflects the fact that the input impedance of the two methods diverges more as frequency increases, as can be seen in Figure A.15. Since the input volume velocity for the plots of Figure A.17 is constant, the pressure at the origin has to differ for the two calculation methods according to the respective difference of the input impedance at a certain frequency, as is more prominent in the higher-frequency plots of Figure A.17.

A.3.6 Geometrical considerations on the wavefront

The horn equation, either in the form of Equation (A.1) or (A.2), describes the pressure field of a horn exactly only for pressure waves whose wavefronts are parallel planes, coaxial cylinders or concentric spheres, as has been proved in [102]. This means that Webster's equation describes exactly only the acoustic field of a cylindrical tube, a cylindrical sector or a conical horn. The

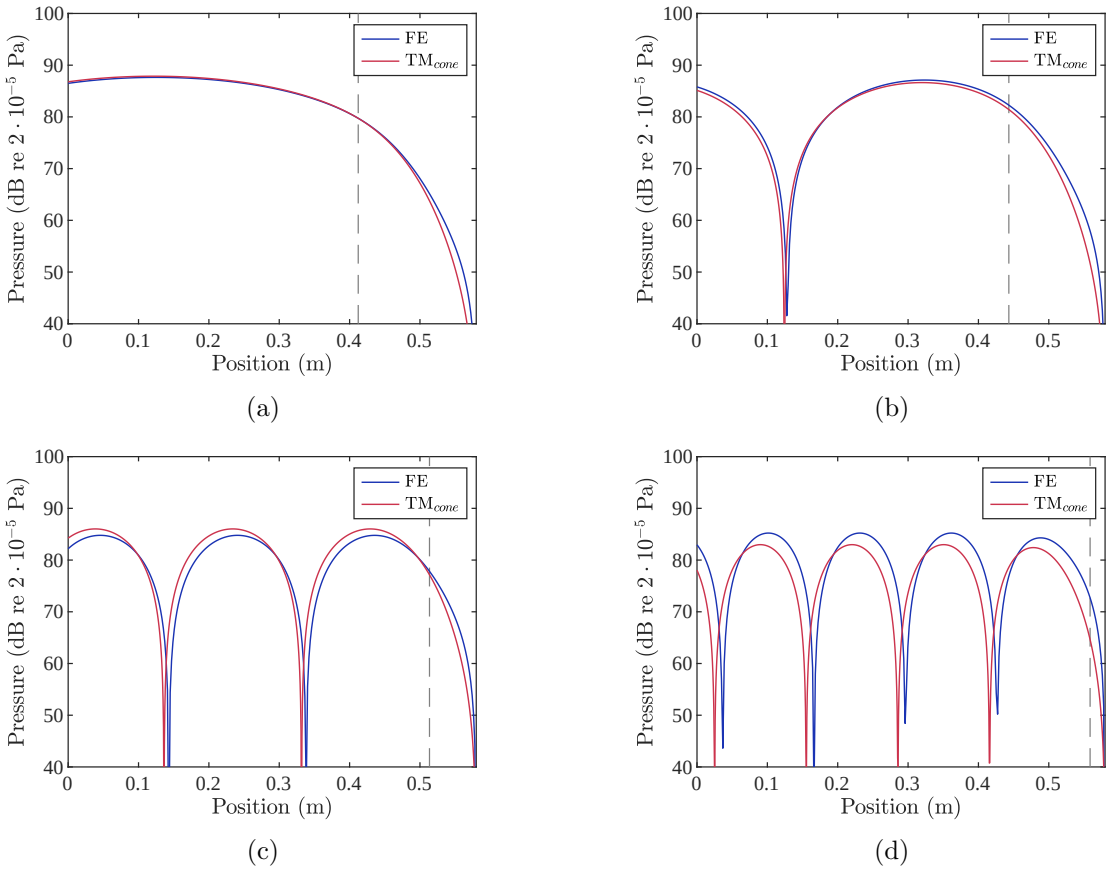

Figure A.17. Sound pressure level spatial variation calculated with the Finite Element method and the Transmission Matrix method (using 100 conical segments), for an input volume velocity of constant amplitude 10^{-6} m$^3 \cdot s^{-1}$ and an excitation frequency of (a) 220 Hz, (b) 440 Hz, (c) 880 Hz and (d) 1.32 kHz.

wavefront area $S_w(x)$ coincides with the cross-sectional area of the horn only in a cylindrical tube, where the wavefronts are planar.

In the case of horns with varying flare that are not exaclty solvable, such as the ones considered in this analysis, where Equation (A.2) is only approximately descriptive of the field, the variable $S_w(x)$ has to be chosen so as to represent an area close to that of the wavefront. In a horn with slowly varying cross-sectional area, the wavefront is nearly planar and $S_w(x)$ may be taken as the cross-sectional area of the horn in good approximation. When the horn cross-sectional area varies rapidly, however, such as near the mouth of a Bessel horn or a 'power-exponential' horn, the plane-wave approximation is far from accurate. The spherical wavefront of a conical horn would seem a better approximation for the area $S_w(x)$ under these conditions. It should be noted that all considerations in this section involve the propagation of the fundamental mode, for which the pressure is constant over the wavefront.

Actually, the wave equation (A.2) for the conical horn and, accordingly, its solution (A.32), should be expressed with respect to a radial coordinate, r, denoting the distance from the apex of the cone, instead of the axial coordinate, x [48]. This means that the pressure is constant over a spherical sector of radius r and not on a plane perpendicular to the axis of the horn at distance x from the apex. Equivalently, it can be said that the wavefronts are spherical surfaces,

such as in waves produced by a pulsating sphere in free space, and not plane waves [48].

The Transmission Matrix formulation of Equation (A.31) is based on a plane-wave approximation for the cone, where the pressure and particle velocity are considered as functions of the axial distance from the apex, x, which means that they are constant in planes of constant x. This is obviously a rough approximation, since the wavefronts inside a conical horn are spherical. If, however, the radial dependence is considered instead, the areas at the two ends of the horn, S_1 and S_2, must be thought of as representing the wavefront areas at those points of the horn. Therefore, the areas of the spherical sectors with radii x_1 and x_2, shown in Figure A.11, could be used instead, representing the areas of the wavefronts intersecting the axis of the horn at its two ends.

In an infinite conical horn, the wavefronts would be parallel spherical surfaces, since the flare of the horn would not change. In consecutive conical horns, however, as depicted in Figure A.12, the problem of the wavefront shape is not well-defined. Figure A.12b in particular illustrates the issue: a spherical wave travelling through a cone of position i along the horn, whose section is $BDEC$, reaches the vertical section DE at its intersection with the horn axis, E, with a radius $x_{i,2}$, since this is the axial distance of the right end of the cone from its apex. This spherical wave then enters the region of the next horn, $DFGE$, denoted by $i+1$. If the wavefront were to continue propagating with a shape corresponding to the cone $BDEC$, that is, with its centre located at A, it would reach the meeting point, D, of the two conical surfaces with radius $r_{i,2}$. If, on the other hand, the wavefront is considered from the point of view of propagation in the second cone, $DFGE$, then, at point D it has a radius of $r_{i+1,1}$, measured from the apex of this cone, A'. It can be seen that the two wavefronts differ, which implies that a transition of the wavefront takes place as the wave propagates through the horn.

Furthermore, if the wavefront in the meeting point of the conical surfaces of cones $i+1$ and $i+2$ is considered in terms of the propagation properties of cone $i+1$, then its radius will be $r_{i+1,2}$, measured from A'. It can be seen that this spherical surface not only differs from the surface with centre A'' and radius $r_{i+2,1}$, corresponding to cone $i+2$, it also enters the region of cone $i+3$, leading to further complication. It can be imagined that in a horn comprising of combined cones of small length, this overlap in regions of propagating wavefronts is extensive. The issue of the shape and area of the wavefronts will not be considered further in this analysis; a more profound examination is carried out in [97], where higher-order-mode propagation is also accounted for.

Returning to the Transmission Matrix of Equation (A.31), it should be considered accurate for transmission between two points inside an infinite conical horn; in a finite one, the area of the wavefront at the ends is not well-defined. Therefore, a choice has to be made for the wavefront areas S_1 and S_2.

A rather simplified geometrical consideration of potential wavefronts can be made by inspection of the drawing in Figure A.18. The area of the spherical surface with radius x_2

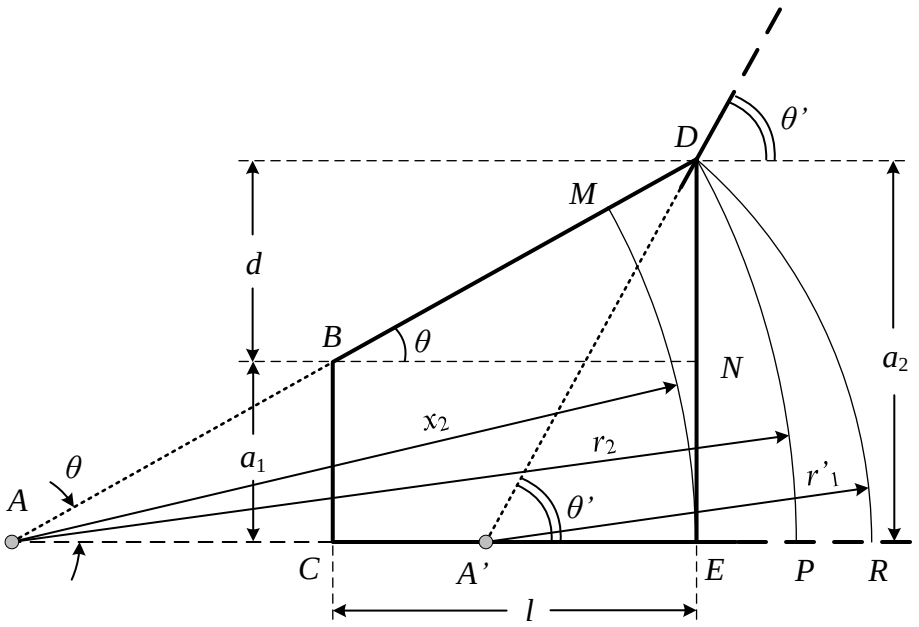

Figure A.18. Geometrical representation of half a conical segment of a conical horn.

and centre A, is given by

$$S_{s,E} = 2\pi x_2^2(1 - \cos\theta), \tag{A.36}$$

where $\cos\theta = l/\sqrt{d^2 + l^2}$, where $d = a_2 - a_1$, and, by similarity of triangles ADE and BDN, $x_2 = la_2/d$. The area of the spherical surface with radius r_2 and centre A, corresponding to the wavefront if the conical segment with side BD were extended further to the right, is given by

$$S_{s,D} = 2\pi r_2^2(1 - \cos\theta), \tag{A.37}$$

where $r_2 = x_2/\cos\theta = a_2\sqrt{d^2 + l^2}/d$. The planar cross-sectional area of the circular disc with radius a_2 is given by

$$S_p = 2\pi a_2^2. \tag{A.38}$$

The area of the spherical surface with radius r_1' and centre A' is also considered, which corresponds to the wavefront if the horn to the right of $BDEC$ were extended from point D towards point A'. This is given by

$$S'_{s,D} = 2\pi r_1'^2(1 - \cos\theta'), \tag{A.39}$$

where $r_1' = a_2\sqrt{d'^2 + l^2}/d'$ and $\cos\theta' = l/\sqrt{d'^2 + l^2}$, where d' is the difference of the big and small cross-sectional radii of the next conical segment. All areas defined by Equations (A.36) to (A.39) are expressed as functions of the chosen length of each segment, l, and the cross-sectional radii a_1 and a_2.

The different areas are plotted in Figures A.19a and b, for a horn with variation of cross-sectional area as given in the caption of Figure A.2. It can be seen that the cross-sectional area S_p is bracketed by the spherical surfaces $S_{s,E}$ and $S_{s,D}$. This can also be derived by inspection of the geometry in Figure A.18. The arc $\widehat{DP}$ is obviously always larger in length than the linear section DE, and the spherical area $S_{s,D}$ generated by rotation of $\widehat{DP}$ around the horn axis, AA', is accordingly always larger than the cross-sectional area S_p with radius a_2.

As for the arc $\widehat{ME}$, some elaboration is required. In the following sequence, y is the length of $\widehat{ME}$,

$$y = x_2\theta \Rightarrow y = \frac{a_2}{\tan\theta}\theta \Rightarrow \frac{y}{a_2} = \frac{\theta}{\tan\theta}.$$

A series expansion of the tangent reveals that it is always larger than its argument angle in the region $[0, 2\pi]$,

$$\tan\theta = \theta + \frac{1}{3}\theta^3 + \frac{2}{15}\theta^5 + \frac{17}{315}\theta^7 + ... \quad .$$

Therefore, the length of $\widehat{ME}$, y, is always smaller that the cross-sectional radius a_2, and, accordingly, the spherical surface $S_{s,E}$ is smaller that S_p.

Finally, the arc $\widehat{DR}$ is even larger than $\widehat{DP}$, which reflects in the respective spherical areas, $S_{s,D}$ and $S'_{s,D}$. This is particularly clear in the plot of Figure A.19a, where a continuously flaring horn is approximated by 10 conical horns. Towards the right end of the horn, where the flare is larger, $S'_{s,D}$ is larger than $S_{s,D}$. In Figure A.19b, however, where the same horn is approximated by 100 conical horns, the two areas are practically indistinguishable. This can be seen by inspection of Figure A.12a. As the number of segments rises and the spatial meshing becomes finer, the right end, D, moves along the initial horn towards the left end, B. Each consecutive cone varies little in flare compared to its previous one, as the flare of the initial horn also varies less over a smaller region. This means that A' approaches A, the angle θ' approaches θ and r'_1 approaches r_2 in Figure A.11. Therefore, $S'_{s,D}$ asymptotes to $S_{s,D}$ as the number of segments becomes very large.

The bracketing of the cross-sectional area by the spherical ones provides a good reason for using the cross-sectional area at the ends of the conical segments in the formulation of the Transmission Matrix. Similar conclusions can be found in the literature, for example in [104].

A.4 Conclusions

Expanding acoustic horns are non-uniform acoustic waveguides in which propagation or evanescence of acoustic waves depends on the flare of the horn and the frequency of the wave. In an exponential horn of a given flare constant, either propagation or evanescence occurs throughout the horn, depending on whether the frequency is above or below the cut-off frequency, respectively, which in turn is defined by the flare constant. In a 'power-exponential' horn, however, in which the effective flare coefficient changes along the length of the horn, the

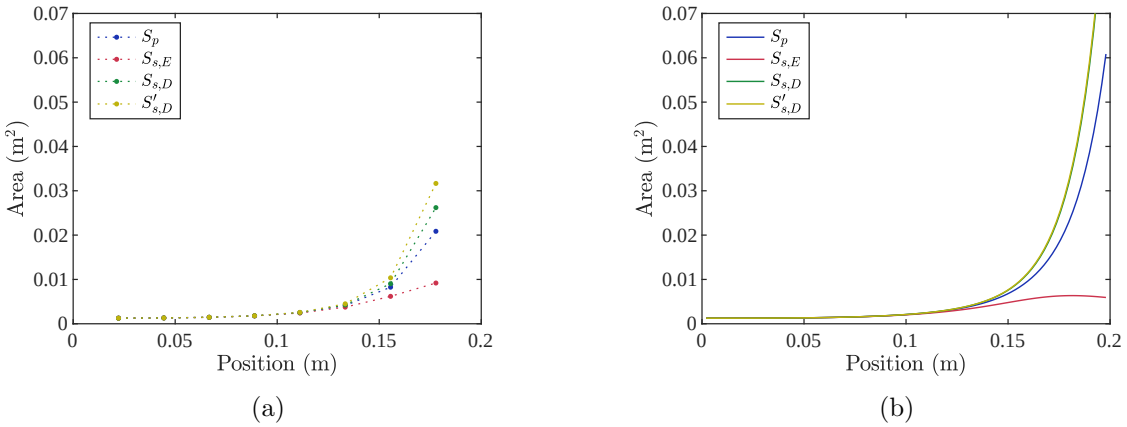

Figure A.19. Comparison of different assumed wavefront areas of a horn made of consecutive cones. The legend follows the definitions of Equations (A.36)-(A.39). The areas are calculated only in the meeting points of segments with changing flare. The left side of the first segment and the right side of the last segment are excluded from the calculations. (a) 10 segments. (b) 100 segments.

cut-off frequency also changes with position. At the position where cut-off occurs, that is, at the turning point, the wavenumber becomes zero and beyond this point it becomes imaginary. Therefore, a wave of given frequency may propagate up to some position in the horn, after which it is exponentially attenuated.

Two numerical methods were employed in order to acquire the response of a 'power-exponential' horn. First, the Transmission Matrix method was formulated, both using cylindrical and conical segments. The Transmission Matrix method assumes unimodal propagation and its use is thus limited by the cut-off frequency of the first higher-order mode. A comparison of the pressure and volume velocity spatial distribution, along with the input impedance spectral variation predicted by the two models, showed that the conical approach gives consistent results using a small number of segments, while using cylindrical segments requires a larger number of segments in order to give consistent results. Nevertheless, both models give similar results above a number of segments, which is not large.

A Finite Element model of the horn was also implemented. Simulations with the Finite Element method include the effect of higher-order modes. The use of this method is only restricted by the relative length of the mesh elements of the model and the local wavelength, imposing an upper frequency limit for a given mesh. Comparison with the Transmission Matrix method shows that the resonances and anti-resonances predicted by the Transmission Matrix method present a gradual upward shift in terms of frequency as frequency increases, with an approximately constant relative difference of about 1.5 %, except for the first few resonances and anti-resonances, where the match with the ones predicted by the Finite Element method is better. The discrepancy in the predicted input impedance may be linked to the fact that higher-order modes start to propagate as frequency increases, which are accounted for in the Finite Element model but not in the Transmission Matrix one.

Some geometrical considerations on the wavefront based on the assumption of unimodal

propagation are also made. It is concluded that, under a rather simplified geometrical approach, the use of the cross-sectional area may be considered a reasonable approximation for the wavefront area, and, therefore, its use within the Tranmission Matrix method with conical segments justified. It is, however, noted that the analysis of the wavefront requires a more thorough examination, especially when higher-order modes are present, as can be found in the literature, for example in [97].

B Modelling the mechanics of the active cochlea

This appendix reports some early work on solutions to the coupled equations that define the cochlear response, when the cochlear partition is active but nonlinear. Although part of this work was published in a conference paper [63], it was not pursued further as the structure of the thesis evolved and so is reported separately from the main text.

B.1 Introduction

It is widely believed that an active mechanism exists inside the cochlea, which provides local amplification to the response of the cochlear partition for low input levels. This 'cochlear amplifier' [62] is nonlinear, since it enhances the low-level response more than the high level response.

The activity of the cochlea is attributed to the outer hair cells, which integrate a mechanism of amplification of the cochlear partition displacement and velocity in low level stimuli. This additional kinetic energy is provided in the expense of electrochemical energy available in the fluid surrounding the organ of Corti, in which the outer hair cells are incorporated [62]. The local character of the activity lies in the fact that energy is provided by the outer hair cells mainly in a certain region of the cochlea's length for a given frequency, that is, in the region of peak response, called the characteristic place for this frequency.

The active cochlea may be modelled as a two-degree-of-freedom system with an additional pressure component generated by a feedback loop, as was done for example by Neely and Kim [4]. In that model, a gain factor was used to control the level of amplification. However, this factor had a global character, which means that its value is constant throughout the length of the cochlea, thus imposing the same amount of amplification at all locations. It is apparent that the initial formulation of this model does not consider the local character of activity.

The nonlinearity of the active mechanism imposes a saturating distortion on the time-domain signal. This presents a difficulty in dealing with this phenomenon, as time-domain formulations are usually more cumbersome in terms of calculations, compared to frequency domain models. Furthermore, time-domain models are not insightful for steady-state analysis.

A way to overcome this difficulty was introduced by Kanis and de Boer [106], where a quasi-linear approach is followed. In this analysis, the quasi-linear procedure is adapted for use with the Neely and Kim micromechanical active model. Initially, a global gain value is applied to all positions of the cochlea and the coupled model is solved, producing a cochlear partition velocity and a corresponding difference of the displacements of the organ of Corti and the tectorial membrane. The nonlinearity is then applied to the time-domain displacement difference. The nonlinearly truncated displacement difference is approximated by its first-order Fourier component and a local distribution of gain is acquired, as the ratio of this quasi-linear displacement difference to the initial frequency-domain displacement difference. Using this

new gain distribution, a modified distribution of cochlear partition impedances is calculated, leading to a modified solution of the coupled model. This iterative procedure is continued until the coupled response settles to a steady value. The quasi-linear model can be viewed as generally linear and frequency-domain based, with a 'window' of time-domain manipulation for the application of the nonlinearity. The resulting gain distribution can be studied as a measure of local activity. The quasi-linear approach thus offers the capability of modelling the steady-state response of a nonlinear, locally active cochlea.

In implementing the quasi-linear method, the wave equation has to be solved for every iteration, using the modified version of the cochlear partition impedance. In the literature, for example in [106], this is usually done with a Finite Difference method, where the continuous length of the cochlea is represented by a certain number of spatially distributed elements, and the wave equation is approximated by its equivalent of finite differences. This approach lacks the clarity offered by an analytical solution. Alternatively, the WKB approximation method can be used, which provides an analytical solution, thus offering insight into the behaviour of the model. This method has been demonstrated to give fairly accurate results, although its validity is theoretically limited by a certain restricting condition [65]. As will be demonstrated below, however, even if this condition ceases to hold, the results obtained with the WKB method are in good accordance with the ones acquired with the Finite Difference method.

A simplification of the method can also be made, if the local gain is replaced by an appropriate global value. It is demonstrated here that this approach seems to give similar results to the ones obtained with distributed gain. It is therefore implied that a number of different gain distributions may all produce similar coupled responses, a conclusion that is supported by the lack of uniqueness in the inverse problem in cochlear mechanics [107].

B.2 The one-dimensional wave equation

Following a number of simplifying assumptions, as presented for example by de Boer [78] and in Chapter 4, the cochlea can be modelled as a fluid-filled parallelepiped box, separated longitudinally by the cochlear partition, as depicted in the one-dimensional 'box model' of Figure B.1. The two chambers thus formed are connected via an opening in the cochlear partition at the apical end of the structure, called the helicotrema. The end of the cochlea at the two windows on the left side of the figure is called the base and the end at the helicotrema is called the apex.

The system is driven by the velocity of the stapes at the oval window, which is situated at the upper basal end. This motion is transferred by the fluid, which is considered to be incompressible, to the basal end of the lower chamber, forcing the round window membrane to vibrate accordingly. The motion of the fluid in the chambers results in a pressure difference across the cochlear partition. The pressure difference is coupled with the mechanical properties

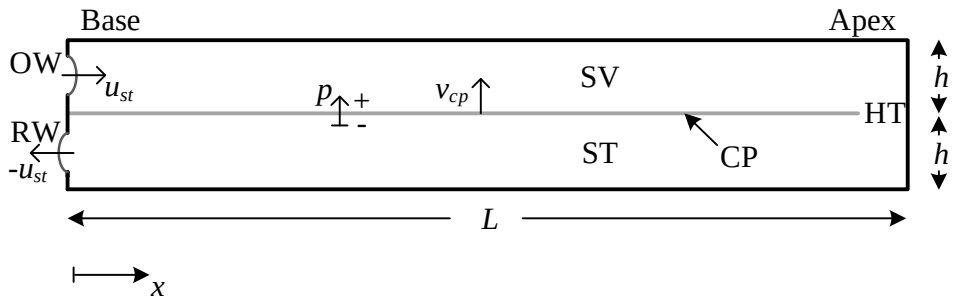

Figure B.1. A one-dimensional 'box model' of the cochlea of length L, with chamber effective height h. The upper chamber (scala vestibuli, SV) and the lower chamber (scala tympani, ST) are separated by the cochlear partition (CP) throughout the length of the cochlea, except for the apical end where they are connected through the helicotrema (HT). The velocity of the stapes, u_{st}, which drives the oval window (OW), and the opposite velocity at the round window (RW) are shown, as well as the vertical velocity of the cochlear partition, v_{cp} and the pressure difference between the two chambers, p.

of the cochlear partition, resulting in a transverse wave of the vibrating cochlear partition travelling in the longitudinal direction.

If harmonic fluctuations are assumed, the pressure difference between the chambers, $p(x,\omega)$, then satisfies the following wave equation [13]

$$p''(x,\omega) - \frac{i2\omega\rho}{hZ_{cp}(x,\omega)}p(x,\omega) = 0, \tag{B.1}$$

where the primes denote differentiation with respect to x, ω is the angular frequency, ρ is the fluid density, h is the effective height of the fluid chambers and $Z_{cp}(x,\omega)$ is the impedance of the locally reacting cochlear partition, defined as the ratio of the pressure across the cochlear partition to its velocity,

$$Z_{cp}(x,\omega) = -\frac{p(x,\omega)}{v_{cp}(x,\omega)}. \tag{B.2}$$

The minus sign accounts for the fact that a positive pressure difference, that is, a higher pressure at the upper chamber, produces a downward velocity for the cochlear partition, while the convention followed here considers the cochlear partition velocity to be positive upwards, as illustrated in Figure B.1. The impedance can take different forms, according to the mechanical model used for the cochlear partition.

Equation (B.1) can be seen as being in the form of a Helmholtz equation

$$p''(x,\omega) + k^2(x,\omega)p(x,\omega) = 0, \tag{B.3}$$

where the wavenumber is represented by the complex wavenumber function $k(x,\omega)$, which varies with location and frequency. The form of the wavenumber function is given by

$$k(x,\omega) = \sqrt{-\frac{\mathrm{i}2\omega\rho}{hZ_{cp}(x,\omega)}}, \tag{B.4}$$

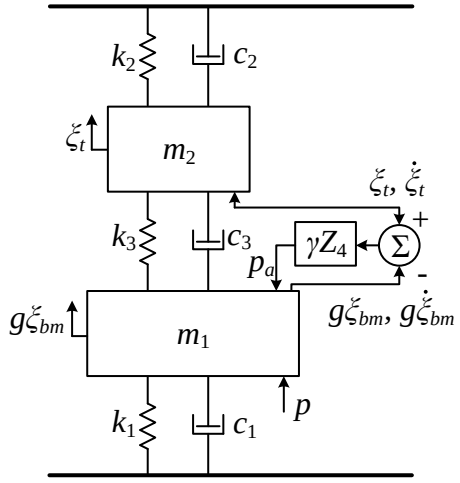

Figure B.2. The Neely and Kim linear active micromechanical model [4].

which, in turn, is formulated according to the specific mechanical model used, due to its dependence on the cochlear partition impedance. The complex wavenumber function can be expressed as the sum of a real and an imaginary part as

$$k(x,\omega) = \kappa(x,\omega) + \mathrm{i}\alpha(x,\omega). \tag{B.5}$$

The real part of the wavenumber represents the spatial angular frequency of the wave, and is equal to 2π over the local wavelength, while the imaginary part holds the role of a gain or attenuation factor [108]. The solution to Equation (B.3) using either the WKB method or the Finite Difference method, with appropriate boundary conditions, is outlined in Chapter 4.

B.3 The Neely and Kim active micromechanical model

In this section, the active micromechanical model of Neely and Kim is briefly presented. In the first subsection, the original linear form is demonstrated, where the velocity difference of the tectorial membrane and basilar membrane is amplified uniformly with respect to input amplitude. In the second subsection, a modified version of the model is given, which includes the nonlinear self-suppressing behaviour of the cochlear amplifier [106].

B.3.1 The linear Neely and Kim active micromechanical model

A two-degree-of-freedom system including an active element was proposed by Neely and Kim [4] to describe the activity of the outer hair cells and the resulting amplification of the coupled response. For the purpose of the presentation of the micromechanics of the model, the notational style of the initial paper is followed, although the indices are modified, where ξ and $\dot{\xi}$ denote displacements and velocities, respectively. A schematic illustration is given in Figure B.2. The

masses m_1 and m_2 represent the organ of Corti and the tectorial membrane, respectively. The two degrees of freedom of the model are the displacement of the basilar membrane, ξ_{bm}, and the radial motion of the tectorial membrane, ξ_t. For the cochlear partition, the average of its displacement is used, and a ratio of the two displacements is defined as

$$b = \frac{\xi_{cp}}{\xi_{bm}}. \tag{B.6}$$

The radial motion of the reticular lamina is also considered, as the product of the basilar membrane displacement and a lever gain. With this, the difference in the radial displacement of the reticular lamina and the tectorial membrane is formed, henceforth to be called the displacement difference, which acts as the input to the cochlear amplifier, and is given by

$$\xi_d = g\xi_{bm} - \xi_t, \tag{B.7}$$

where g is the lever gain between the reticular lamina and the organ of Corti.

The active pressure, p_a, represents the pressure produced by the cochlear amplifier, which corresponds to the velocity difference, directly derived from Equation (B.7), amplified by the feedback gain factor γ and multiplied by the impedance Z_4,

$$p_a = -\gamma Z_4 \dot{\xi}_d. \tag{B.8}$$

The cochlear partition impedance of the Neely and Kim model is given by

$$Z_{cp} = \frac{g}{b}\left(Z_1 + Z_2\frac{Z_3 - \gamma Z_4}{Z_2 + Z_3}\right), \tag{B.9}$$

where $Z_1 = k_1/\mathrm{i}\omega + c_1 + \mathrm{i}\omega m_1$, $Z_2 = k_2/\mathrm{i}\omega + c_2 + \mathrm{i}\omega m_2$, $Z_3 = k_3/\mathrm{i}\omega + c_3$ and $Z_4 = k_4/\mathrm{i}\omega + c_4$.

The relation of the displacement difference to the displacement of the cochlear partition is also given, which will be useful for subsequent analysis,

$$\xi_d = \frac{g}{b}\frac{Z_2}{Z_2 + Z_3}\xi_{cp}. \tag{B.10}$$

The dependence with respect to space and frequency is omitted in the above expressions, for convenience. The mechanical parameters of the model, that is, the stiffness and damping coefficients, vary with location. Values and formulas of the parameters used in the following simulations are shown in Table B.1.

A set of plots of the coupled response of the cochlea, calculated using the WKB method, are shown in Figure B.3 for uniform, or global, activity such that γ is independent of x. The graphs were produced with the WKB method, as described in Section B.5, for different global gain values. The gradual enhancement of the coupled response at the characteristic place

Quantity	Formula / Value	Quantity	Formula / Value
$k_1(x)$	$1.1 \cdot 10^{10} \mathrm{e}^{-400x}$ N $\cdot$ m^{-3}	$c_4(x)$	$10400 \cdot \mathrm{e}^{-200x}$ N $\cdot$ s $\cdot$ m^{-3}
$c_1(x)$	$200 + 15 \cdot 10^3 \cdot \mathrm{e}^{-200x}$ N $\cdot$ s $\cdot$ m^{-3}	k_m	$2.1 \cdot 10^6$ N $\cdot$ m^{-3}
m_1	$3 \cdot 10^{-2}$ kg $\cdot$ m^{-2}	c_m	$4 \cdot 10^3$ N $\cdot$ s $\cdot$ m^{-3}
$k_2(x)$	$7 \cdot 10^7 \mathrm{e}^{-440x}$ N $\cdot$ m^{-3}	m_m	$4.5 \cdot 10^{-3}$ kg $\cdot$ m^{-2}
$c_2(x)$	$100 \cdot \mathrm{e}^{-220x}$ N $\cdot$ s $\cdot$ m^{-3}	ρ	10^{-3} kg $\cdot$ m^{-3}
m_2	$5 \cdot 10^{-3}$ kg $\cdot$ m^{-2}	g	1
$k_3(x)$	$10^8 \mathrm{e}^{-400x}$ N $\cdot$ m^{-3}	b	0.4
$c_3(x)$	$20 \cdot \mathrm{e}^{-80x}$ N $\cdot$ s $\cdot$ m^{-3}	l	$2 \cdot 10^{-2}$ m
$k_4(x)$	$6.15 \cdot 10^9 \cdot \mathrm{e}^{-400x}$ N $\cdot$ m^{-3}	h	$2 \cdot 10^{-3}$ m

Table B.1. Parameters of a cat cochlea according to the Neely and Kim model [4]. Values were converted to SI and corrected according to [109], with a few further modifications.

as the feedback gain increases is clearly seen in the basilar membrane velocity modulus plot, Figure B.3a. Furthermore, the phase of the basilar membrane velocity plotted in Figure B.3b can be seen to halt in a small region basal to the peak, and it even slightly increases in this region for a global gain value of 0.7 before starting to decrease again. The modulus and the phase of the admittance, which is equal to the reciprocal of the impedance, are plotted in Figures B.3c and B.3d, respectively.

B.3.2 The nonlinear version of the Neely and Kim active micromechanical model

The linear active model of Neely and Kim can be changed to incorporate the nonlinear saturating effect of the outer hair cells, by introducing a nonlinear function of an appropriate form adjacent to the cochlear amplifier [109]. This function nonlinearly distorts the time-domain displacement difference of the two masses of the model, which drives the cochlear amplifier, for input levels above some threshold, thus accounting for the fact that the response of the cochlea is found to be active for low level stimuli, while it gradually turns to passive for high level stimuli. The nonlinear version of the model is shown in Figure B.4.

The saturating function used in this analysis is a first-order asymmetric Boltzmann function, taken from [110], where it was formed based on [111]

$$F(x,t) = \delta(x) \left(\frac{1}{1 + \beta \mathrm{e}^{\frac{u(x,t)}{\eta(x)}}} - \frac{1}{1+\beta} \right). \tag{B.11}$$

It is plotted in Figure B.5a. In Equation (B.11), $u(x,t)$ is the input displacement difference of the two masses of the model, β is a constant that controls the asymmetricity of the function, given here a value of 3, $\delta(x)$ defines the saturating point and $\eta(x)$ determines the slope. It has to be mentioned that the form of the nonlinearity is chosen to be asymmetric to be consistent with measurements [112]. It should be noted that $\delta(x)$ varies across the length of the cochlea, to produce a similar saturating effect in different positions, by counterbalancing the varying

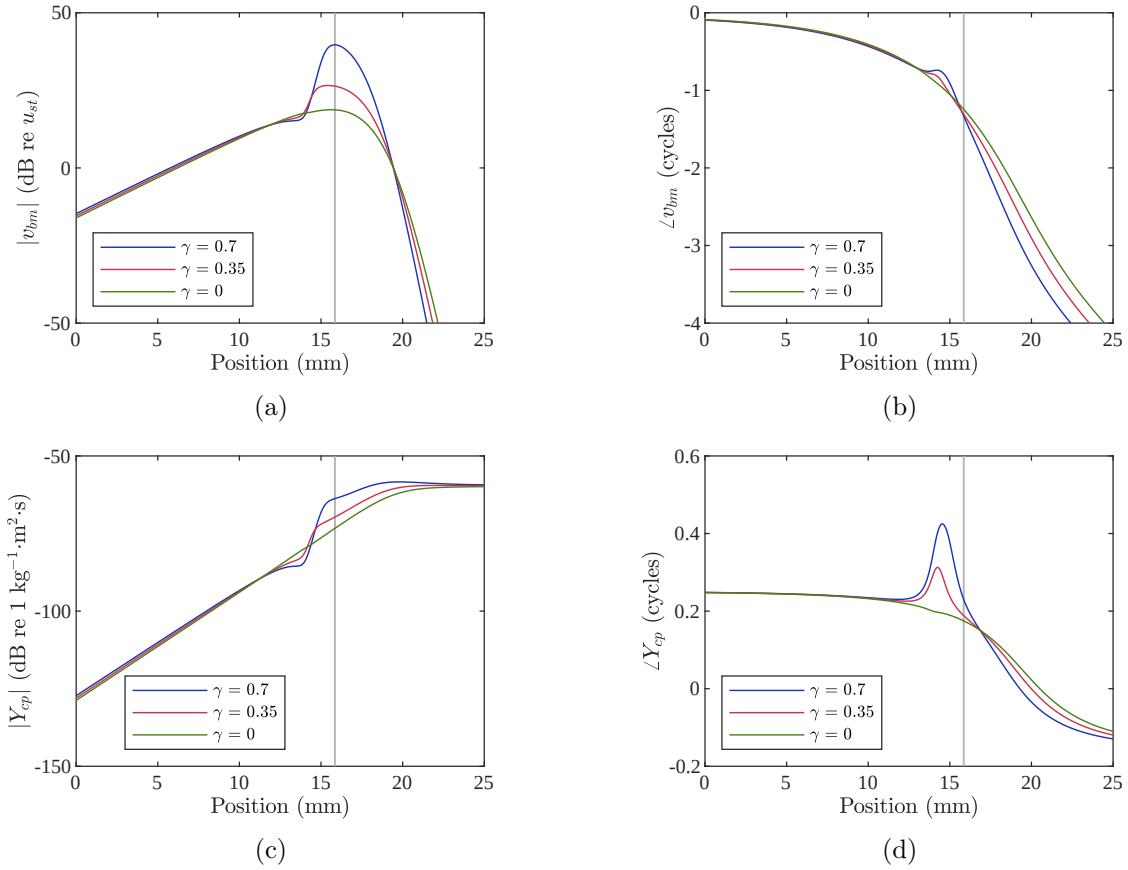

Figure B.3. Coupled response and admittance of the linear Neely and Kim model for three different gain values, from passive ($\gamma = 0$) to fully active ($\gamma = 0.7$): (a) WKB basilar membrane velocity coupled response modulus and (b) corresponding phase. (c) Modulus of the admittance and (d) phase of the admittance. Basilar membrane velocities are normalised with respect to the stapes velocity.

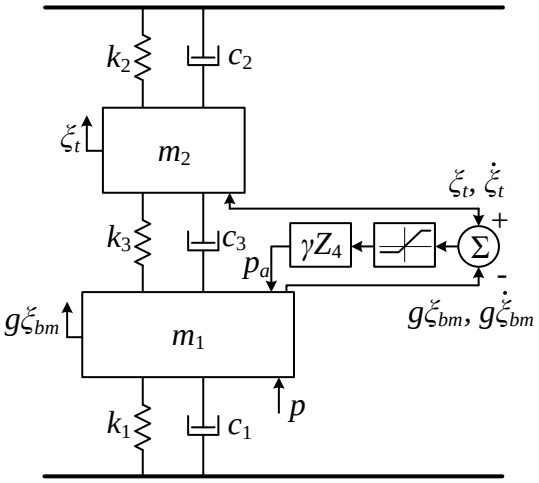

Figure B.4. The nonlinear version of the Neely and Kim active micromechanical model. The nonlinearity is represented by a saturating function being applied at the input of the cochlear amplifier.

mechanical parameters [110]. Its assumed variation is plotted in Figure B.5b. In the plot of Figure B.5a, the value of $\delta(x)$ at the basal region has been used.

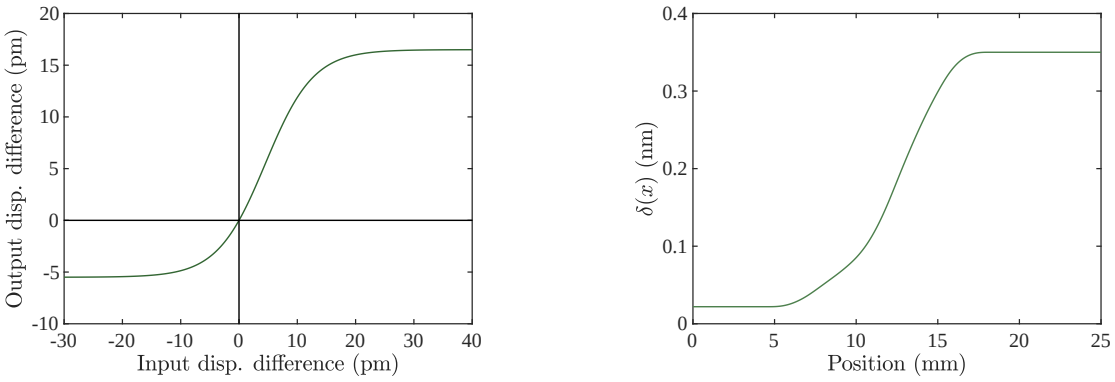

(a) (b)

Figure B.5. (a) First-order Boltzmann function, representing the nonlinear saturation of the cochlear amplifier. The value of $\delta(x)$ at the basal region of the cochlea was used. Input and output displacements are in pm ($10^{-12}m$). (b) Spatial distribution of the saturation coefficient, $\delta(x)$, in nm.

The slope-determining parameter $\eta(x)$ is defined so that the function has a slope of unity at the origin. Therefore, the form of $\eta(x)$ is found by differentiating Equation (B.11) with respect to the input function $u(x,t)$ and setting it equal to one for zero input, which gives

$$\eta(x) = \frac{\delta(x)\beta}{(1+\beta)^2}. \tag{B.12}$$

B.4 The quasi-linear approach

In this section, the quasi-linear approach is briefly outlined, where the original concept of Kanis and de Boer [106] is adapted to the Neely and Kim active micromechanical model [4]. Initially, the algorithmic procedure is used to obtain the longitudinally varying distribution of the gain factor $\gamma(x)$. In section B.4.2, a simplifying approach of global gain is presented, where γ is independent of x.

B.4.1 The locally active case

Starting with a global value for the gain factor in the cochlear partition impedance, that is, imposing the same amount of activity at all positions along the cochlea, the wave equation (B.1) can be solved. For this, either a Finite Difference discrete-space approximation can be used as in the original Kanis and de Boer formulation [106], or the WKB analytical approximation, which will be used in the following section. An initial pressure distribution is therefore obtained, and, by means of Equations (B.2) and (B.9), a cochlear partition velocity distribution. It should be noted that, in all implementations, an initial global maximum value of 0.7 for γ was used for the 0 dB input Sound Pressure Level (SPL). For every consequent level, the final gain distribution of its previous SPL was used as a starting point, to improve convergence.

The next step of the procedure consists in the application of the nonlinearity. For this aim, the time-domain signal of the displacement difference, defined in Equation (B.10), is formed as

$$\xi_{d,t}(x,t) = |\xi_d(x)| \cos\left(\omega t + \phi_d(x)\right), \tag{B.13}$$

where $\phi_d(x)$ corresponds to the phase of the displacement difference. The time signal of Equation (B.13) forms the input to the nonlinear function, which represents the saturating effect of the outer hair cell motion as the relative displacement of the outer hair cells with respect to the tectorial membrane increases. The output of the nonlinearity can be expressed as

$$\xi_{d,t}^{NL}(x,t) = F\left[\xi_{d,t}(x,t)\right]. \tag{B.14}$$

In the above expression, F is the saturating filtering function of Equation (B.11). At this point, the first Fourier component of the displacement difference is acquired,

$$\xi_d^{QL}(x) = \frac{2}{T}\int_0^T \xi_{d,t}^{NL}(x,t)\mathrm{e}^{-\mathrm{i}\omega t}\mathrm{d}t, \tag{B.15}$$

where T is the period corresponding to the fundamental frequency. This fundamental component is used as a frequency-domain approximation of the nonlinearly filtered displacement difference. The ratio of the quasi-linear displacement difference with respect to the displacement difference prior to the nonlinearity gives a scaling factor that is spatially distributed and represents the magnitude of attenuation due to the saturating effect of the nonlinear function on different locations along the cochlea, given by

$$S = \frac{\xi_d^{QL}(x)}{\xi_d(x)}. \tag{B.16}$$

It is worth noting that the quasi-linear procedure does not affect the phase of its input, that is, it does not shift the signal in time. Therefore, the quotient of Equation (B.16) is real and equal to the ratio of the moduli of its components. It should also be noted that the values of the scaling factor are between zero and unity, since the nonlinear function either leaves its input unaffected, for low stimuli, or reduces its amplitude, for higher inputs; it does not amplify the signal.

A quasi-linear gain distribution can be defined as

$$\gamma_{QL} = S\gamma. \tag{B.17}$$

This scaled gain distribution has values between zero and the maximum global gain that was initially imposed, and forms a measure of the local activity of the cochlear amplifier. It can be said that the effect of the nonlinearity has been passed on to the distribution of the gain.

Using the quasi-linear gain distribution of Equation (B.17), the cochlear partition impedance

of Equation (B.9) is modified. Consequently, the wavenumber function of Equation (B.4) is also altered. Therefore, a new version of the solution for the cochlear partition velocity is obtained, which gives a corresponding cochlear partition displacement distribution, by dividing by $\mathrm{i}\omega$. This cochlear partition displacement gives a new displacement difference, according to Equation (B.10), which initiates a new cycle of the iterative quasi-linear procedure. The iteration can be stopped when the output ceases to change significantly. It should be mentioned that, for better convergence, the gain distribution at the end of each cycle is averaged as a weighted linear combination of the last obtained distribution and its previous one.

The output of the system is usually considered to be the velocity of the basilar membrane, which for the Neely and Kim model is given by

$$\dot{\xi}_{bm}(x) = \frac{\dot{\xi}_{cp}(x)}{b}. \tag{B.18}$$

B.4.2 The globally active case

The above procedure can be simplified by imposing a single, global, value for the gain factor at all locations, at the end of each iteration. This value is chosen to be the value of the gain at the position where the response is maximum, resulting in different levels of global activity for different input SPLs. The validity of the global gain is assessed in Section B.6.

B.5 The WKB approximation method

B.5.1 The WKB solutions in cochlear mechanics

The WKB approximation method is an analytical approximation method for equations that can be written in the form [27]

$$p''(x) + k^2(x)p(x) = 0. \tag{B.19}$$

A derivation of the WKB solution for one-dimensional cochlear mechanics is given, for example, in [13]. In the cochlear case, both the pressure difference field and the wavenumber function are dependent on frequency. However, this dependence does not affect the form of the solution, since the differential equation is only with respect to the spatial independent variable.

As noted in Chapter 4, the WKB solution to Equation (B.19) is a pressure difference distribution of the form

$$p(x) = Ak^{-1/2}(x)\mathrm{e}^{-\mathrm{i}\int_0^x k(\tilde{x})\mathrm{d}\tilde{x}}, \tag{B.20}$$

where A is a complex coefficient. A form of the cochlear partition velocity can be obtained by substituting Equation (B.2) into (B.4) and solving for the cochlear partition velocity, while using the WKB pressure difference waveform of Equation (B.20). The cochlear partition velocity can

then be found to be

$$v_{cp}(x) = Bk^{3/2}(x)\mathrm{e}^{-\mathrm{i}\int_0^x k(\tilde{x})\mathrm{d}\tilde{x}}, \tag{B.21}$$

where the cochlear partition velocity is noted by $v_{cp}(x)$ instead of $\dot{\xi}_{cp}(x)$ for notational convenience and the complex coefficient B is given by

$$B = \frac{hA}{\mathrm{i}2\omega\rho}. \tag{B.22}$$

Only a forward-travelling, that is, towards the positive-x direction, wave has been considered, as is expressed by the minus sign on the exponent. The general solution contains also a backward-travelling wave, but this has been neglected, accounting for the fact that in the general case no significant reflections occur inside the cochlea [78].

The amplitude coefficient A is found by use of the boundary condition at the base. The condition at the helicotrema can be neglected, as the wave is excessively attenuated for locations after the characteristic place, and, even for low frequencies resonating near the apex, no significant reflections seem to occur [78]. The boundary condition at the stapes is written as

$$p'(0) = -\mathrm{i}2\omega\rho u_{st}. \tag{B.23}$$

For further elaboration, the stapes velocity is written in the form

$$u_{st} = u_{st,0} - \frac{p(0)}{Z_m}, \tag{B.24}$$

where $u_{st,0}$ is the component of the stapes velocity due to the external acoustic pressure, whose value is given by

$$u_{st,0} = \frac{g_m p_0}{Z_m}, \tag{B.25}$$

and Z_m is the mechanical impedance of the middle ear, given by

$$Z_m = \frac{k_m}{\mathrm{i}\omega} + c_m + \mathrm{i}\omega m_m. \tag{B.26}$$

The assumed values of the mechanical properties of the middle ear are shown in Table B.1. In the implementation of the calculation code for this analysis, a more complicated model of the middle ear and ear canal has been used for the component of the stapes velocity due to external excitation, as presented in [110].

The spatial derivative of the WKB pressure difference, as shown in Equation (B.20), is derived to be

$$p'(x) = -A\left(\frac{1}{2}k^{-3/2}(x)k'(x) + \mathrm{i}k^{1/2}(x)\right)\mathrm{e}^{-\int_0^x k(\tilde{x})\mathrm{d}\tilde{x}}. \tag{B.27}$$

Therefore, if the value of the derivative at the basal boundary is taken for the left-hand side of the boundary condition (B.23), and the stapes velocity of Equation (B.24) is used, also

substituting the pressure difference at the base, that is, for $x = 0$, from Equation (B.20), then the boundary condition (B.23) takes the form

$$-A\left(\frac{1}{2}k^{-3/2}(0)k'(0)+\mathrm{i}k^{1/2}(0)\right)=-\mathrm{i}2\omega\rho\left(u_{st,0}-\frac{1}{Z_m}Ak^{-1/2}(0)\right). \tag{B.28}$$

Finally, the amplitude coefficient of the pressure difference, A, can be written as

$$A=\frac{\mathrm{i}2\omega\rho u_{st,0}}{\frac{1}{2}k^{-3/2}(0)k'(0)+\mathrm{i}k^{1/2}(0)+\mathrm{i}2\omega\rho\frac{1}{Z_m}k^{-1/2}(0)}, \tag{B.29}$$

and the coefficient of the cochlear partition velocity, B, is accordingly written as

$$B=\frac{u_{st,0}}{h\left(\frac{1}{2}k^{-3/2}(0)k'(0)+\mathrm{i}k^{1/2}(0)+\mathrm{i}2\omega\rho\frac{1}{Z_m}k^{-1/2}(0)\right)}. \tag{B.30}$$

The basilar membrane velocity can then be calculated from Equation (B.21) using Equation (B.18). It is reminded that v_{cp} is equivalent to $\dot{\xi}_{cp}$, and v_{bm} is used to represent the basilar membrane velocity instead of $\dot{\xi}_{bm}$.

B.5.2 Components and form of the WKB velocity

In this section, the form of the WKB solution is used to gain insight into the form of the coupled cochlear response, in particular to show that the magnitude and phase of the coupled response are mainly governed by different components of the WKB solution. The form of the solution can be written, assuming for simplicity that B is equal to unity, as

$$v_0(x)=k^{3/2}(x)\mathrm{e}^{-\mathrm{i}\phi(x)}, \tag{B.31}$$

where the phase function is defined by

$$\phi(x)=\int_0^x k(\tilde{x})\mathrm{d}\tilde{x}. \tag{B.32}$$

For notational convenience, the dependence of the terms on frequency has been neglected.

The solution in the form of (B.31), representing the normalised coupled velocity response, can be seen as consisting of two components: the wavenumber function raised to the power 3/2, which will be referred to as the wavenumber factor or the local factor, and an exponential term, henceforth to be called the exponential or global term, which has the complex exponent $-\mathrm{i}\phi(x)$. It is apparent from Equation (B.32) that the phase function is directly dependent on the wavenumber function, which is written again here in terms of its real and imaginary parts as

$$k(x)=\kappa(x)+\mathrm{i}\alpha(x). \tag{B.33}$$

It is reminded that the real part of the wavenumber, or real wavenumber, is equal to 2π over the

local wavelength. The imaginary part of the wavenumber will be called imaginary wavenumber hereafter for convenience, although its characterisation as attenuation/amplification factor would be more physically enlightening, as will be commented later. The phase function can then be written accordingly as

$$\phi(x) = \phi_R(x) + \mathrm{i}\phi_I(x), \tag{B.34}$$

where

$$\begin{aligned} \phi_R(x) &= \int_0^x \kappa(\tilde{x})\mathrm{d}\tilde{x}, \\ \phi_I(x) &= \int_0^x \alpha(\tilde{x})\mathrm{d}\tilde{x}. \end{aligned} \tag{B.35}$$

Some elaboration can be made on the exponential term to demonstrate the explicit relation between its modulus and phase on one side and the real and imaginary parts of the wavenumber on the other. For this aim, the exponential term is written analytically, with the use of Equations (B.33) and (B.34), as

$$\mathrm{e}^{-\mathrm{i}\phi(x)} = \mathrm{e}^{\phi_I(x)}\mathrm{e}^{-\mathrm{i}\phi_R(x)}. \tag{B.36}$$

It can clearly be seen from the form of the phase function that the modulus of the exponential factor only depends on the imaginary wavenumber, whereas its phase only depends on the real wavenumber. As regards the wavenumber factor, its modulus and phase are the modulus of the wavenumber raised to the power 3/2 and the phase of the wavenumber multiplied by a factor of 3/2, respectively. In the previous analysis, the term 'phase' for the phase function should be considered in a loose sense following the general form of the solution (B.31), where $\phi(x)$ would correspond to a phase function if it was purely real. It is apparent, though, that since the phase function is complex, it leads to both an amplitude and a phase term for the exponential, as can be seen in Equation (B.36). A set of plots of the wavenumber and the moduli and phases of the WKB components is given in Figure B.6.

An examination of the moduli of the components plotted in dB in Figure B.6b reveals how the coupled response in the form of the WKB solution is formed by its varying factors, which are shown as coloured lines in the plot. A globally active case is chosen for presentational reasons, providing a prominent peak at the maximum response. The blue line shows the spatial variance of the wavenumber term and the red line represents the exponential term. Three regions are defined here by the form of the overall response. In the basal region, the exponential term is almost constant throughout, and close to zero; it actually reaches a minimum value of -1.4 dB near the boundary with the peak region. Therefore, the total response modulus remains largely unaffected by the global term and closely follows the spatial pattern of the local term.

However, in the relatively narrow region that is called here the peak region, the exponential term presents a bell-shaped form, reaching a peak near the maximum of the response and

then quickly falling off. The boundaries of the peak region are defined by the zero crossings of the overall coupled response. In this region, the local term increases monotonically. As a consequence of the forms of the two components, the shape of the overall response follows the resonance-like ascent and descent of the exponential term. Therefore, the shape of the coupled response in this region is largely formed by the global term, whereas its order of magnitude follows that of the local term. In the apical region, the exponential term continues to fall off quickly and the overall response varies accordingly, regardless of the continued increase and stabilisation of the wavenumber term. It can, therefore, be concluded that the modulus of the coupled response is largely formed by the modulus of the global term.

If another step backwards is taken, the form of the modulus of the exponential term, considering Equations (B.35) and (B.36), provides a link between the imaginary wavenumber and the total response. Specifically, the modulus of the exponential term is the exponential of the integral of the imaginary wavenumber. By inspecting Figure B.6a, it can be seen that in the basal region the imaginary wavenumber is generally close to zero. Therefore, the exponential term is in general close to one in this region. In roughly the right half of the basal region, the imaginary wavenumber is slightly negative, resulting in a small decline of the exponential term. Just before the peak region, the imaginary wavenumber becomes positive and ascending.

In the peak region, the imaginary wavenumber ascends to a peak and then starts descending, passes through zero and keeps descending. The modulus of the exponential factor, that is, the exponentiated integral of the imaginary wavenumber, takes the bell shape illustrated in Figure B.6b, with its peak at the point where the imaginary wavenumber is zero.

In the apical region the imaginary wavenumber further descends and the modulus of the exponential vanishes accordingly. Therefore, a correspondence of the total response to the imaginary wavenumber can be considered. In the basal region, the imaginary wavenumber is roughly zero and the total response follows the local term. In the peak region, the wavenumber increases, forms a peak, then decreases, passes through zero and continues to decrease in the negative realm, causing a bell-shaped resonance form for the total response, with a peak near the zero-crossing of the imaginary wavenumber. In the apical region, the imaginary wavenumber continues to decline and the total response quickly vanishes.

The characterisation of the imaginary part of the wavenumber as an attenuation/amplification factor is also demonstrated by the previous analysis. As long as its value is zero, the response is equal to the wavenumber term, which is then only defined by the real wavenumber. When the imaginary wavenumber is positive, the response is amplified, mainly by the exponential term (although the modulus of the wavenumber term is also increased). Hence its characterisation as an amplification factor. When the imaginary wavenumber becomes negative, the response is attenuated, by the decay of the exponential term, even though the wavenumber term still increases. This justifies its characterisation as an attenuation factor.

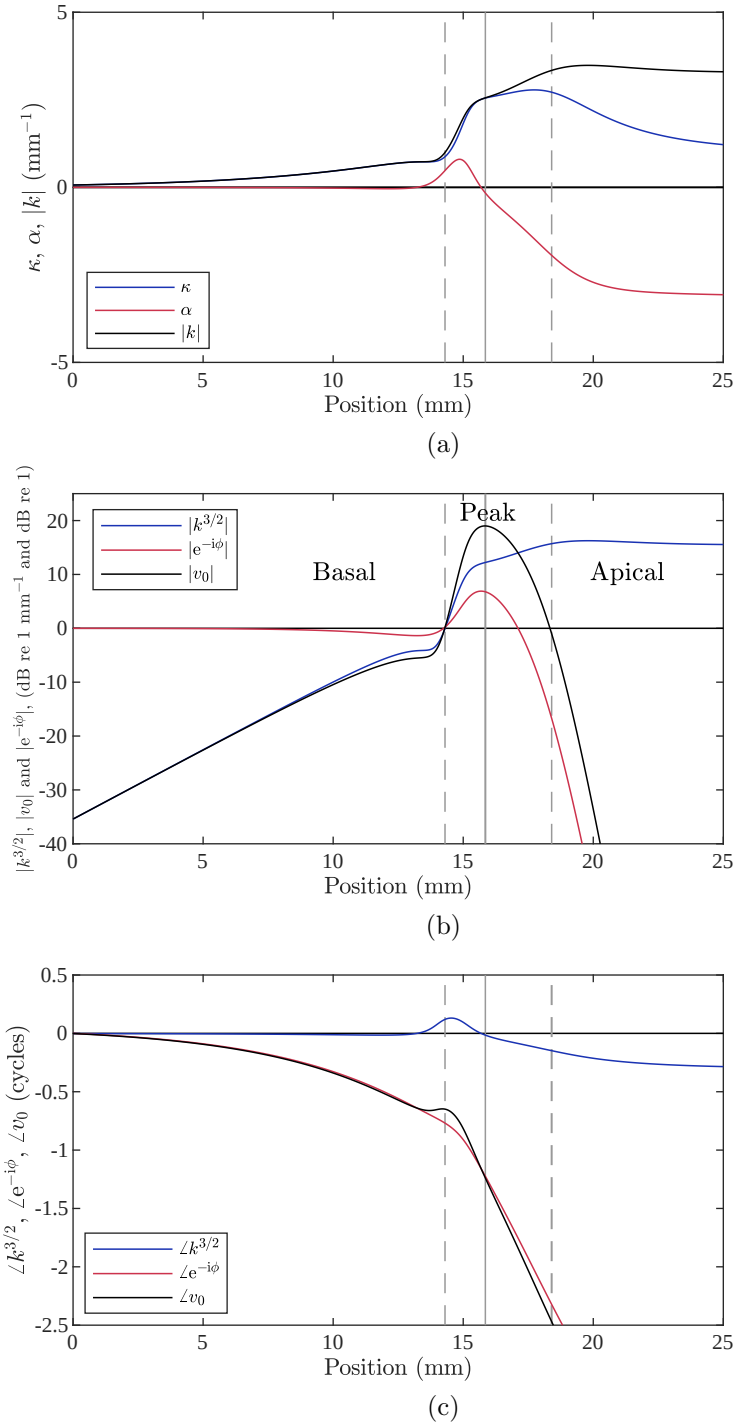

Figure B.6. (a) Real (blue line) and imaginary (red line) parts of the wavenumber and modulus (black line) of the wavenumber. Vertical lines according to (b). (b) Moduli of the components of the WKB velocity of the Neely and Kim model in dB: the local wavenumber term (blue line), the exponential global term (red line) and overall coupled response (black line). The dashed vertical lines cross the overall coupled response at its zero crossings, thus defining three regions, named here basal, peak and apical. The solid vertical line passes through the maximum overall coupled response, that is, the peak of the black line. (c) Phases of the components of the WKB solution: the local wavenumber term (blue line), the exponential term (red line) and the overall response (black line). A global gain value of 0.7 is used.

A plot of the phases of the components is given in Figure B.6c. The phase of the total response is the sum of the phases of the two components of the WKB velocity solution (B.31). It can be seen that the phase of the total response mainly follows that of the exponential factor, which, according to Equations (B.35) and (B.36), is equal to the opposite of the integral of the real wavenumber. The phase of the exponential is monotonically decreasing, since the real wavenumber is positive throughout. The phase of the wavenumber term, however, is close to zero for the most part of the basal region, but, as it approaches the peak region, it start to rise. In the left side of the peak region, it increases to a small peak, then gradually falls to zero and continues to decrease. In the apical region, the phase of the local term keeps decreasing at a slower rate, until it nearly stabilises.

The phase of the local term, when added, gives the phase of the overall response its characteristic deviation from the phase of the global term: a small peak at the boundary of the first two regions and a higher rate of decrease mainly in the apical region. However, since the variation of the phase of the local term is relatively small compared to the phase of the global term, the phase of the overall response generally follows the latter, as was previously mentioned. In correspondence with the moduli, a link between the variation of the real wavenumber and the phase of the response can be made: the phase is mainly dependent on the accumulating real wavenumber as it is spatially integrated.

B.5.3 Validity of the WKB method

The validity of the WKB method, and, therefore, the accuracy of the solutions it provides, is defined by a limiting condition, given for example in [13], which can be expressed as

$$\left|\frac{k'(x)}{k^2(x)}\right| \ll 1. \tag{B.37}$$

This condition can be described as a limitation on how quickly, in terms of length across the cochlea, the wavenumber function varies. It imposes that the wavenumber function vary slowly in the longitudinal direction, compared to the local wavelength of the cochlear wave, for the method to be accurate. This statement is equivalent to absence of reflections of the propagating wave [78]. It was shown, however, in [64], using a simpler cochlear model, that even if the properties of the model vary rapidly, as is the case near the peak with very small damping, still practically no reflections occur.

A plot of the left-hand side of the WKB condition is shown in Figure B.7. It can be seen that the condition is strongly violated in the basal region and in the region adjacent and basal to the characteristic place. Despite this fact, acquired results using this method are fairly accurate even at these regions. This is demonstrated in Figure B.8, where the moduli and phases of the basilar membrane velocity using the Neely and Kim linear micromechanical model are plotted, calculated both with the WKB and Finite Difference methods. Maximum

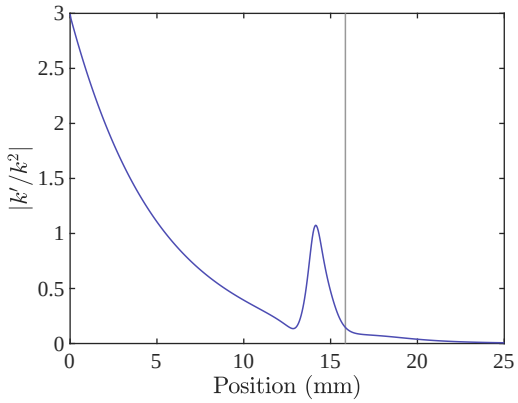

Figure B.7. The WKB condition for the fully active Neely and Kim model, at 1600 Hz. The characteristic place is noted by the vertical line at 15.9 mm.

differences between moduli for the two calculating methods are about 2 dB for both the passive and the active case, while, for the phases, maximum differences are less than 1/10 of a cycle. It is therefore confirmed, as has been shown in the literature, for example in [65], that the WKB can be considered as an accurate approximation method for one-dimensional cochlear mechanics. Similar results have been obtained also for higher-order fluid coupling, for example in [66] for a two-dimensional model. It is again stressed that this holds despite the violation of the mathematically imposed limiting condition of Equation (B.37).

B.6 Results and Discussion

The quasi-linear version of the Neely and Kim active cochlear model presented previously was solved for a single excitation frequency of 1600 Hz, and corresponding results were obtained. All results presented in the following analysis were obtained using a 512-sample spatial integrating efficiency for the WKB method. It should be mentioned that both for the Finite Difference and the WKB method, a value of 1024 spatial elements was also tried, giving almost identical results for each method, and therefore demonstrating that the value of 512 provides accurate calculations.

An assessment of the two calculating methods in the context of the quasi-linear model was made with the local gain implementation. The greatest differences between coupled responses corresponding to the same excitation level were found for medium external SPLs. In Figure B.9, the moduli, phases and gain distributions for 50 dB and 70 dB external SPL are plotted. It can be seen that, even for medium stimulus levels, the WKB coupled response is similar to the one acquired with the Finite Difference method. The 50 dB SPL has been chosen here because it forms the input level for which the difference of the velocity modulus at the peak for the two calculating methods is greatest, as will be discussed later. Maximum differences are found to be compatible with the comparison of the WKB and Finite Difference methods in the previous section, using the linear model. It is therefore demonstrated that the quasi-linear procedure

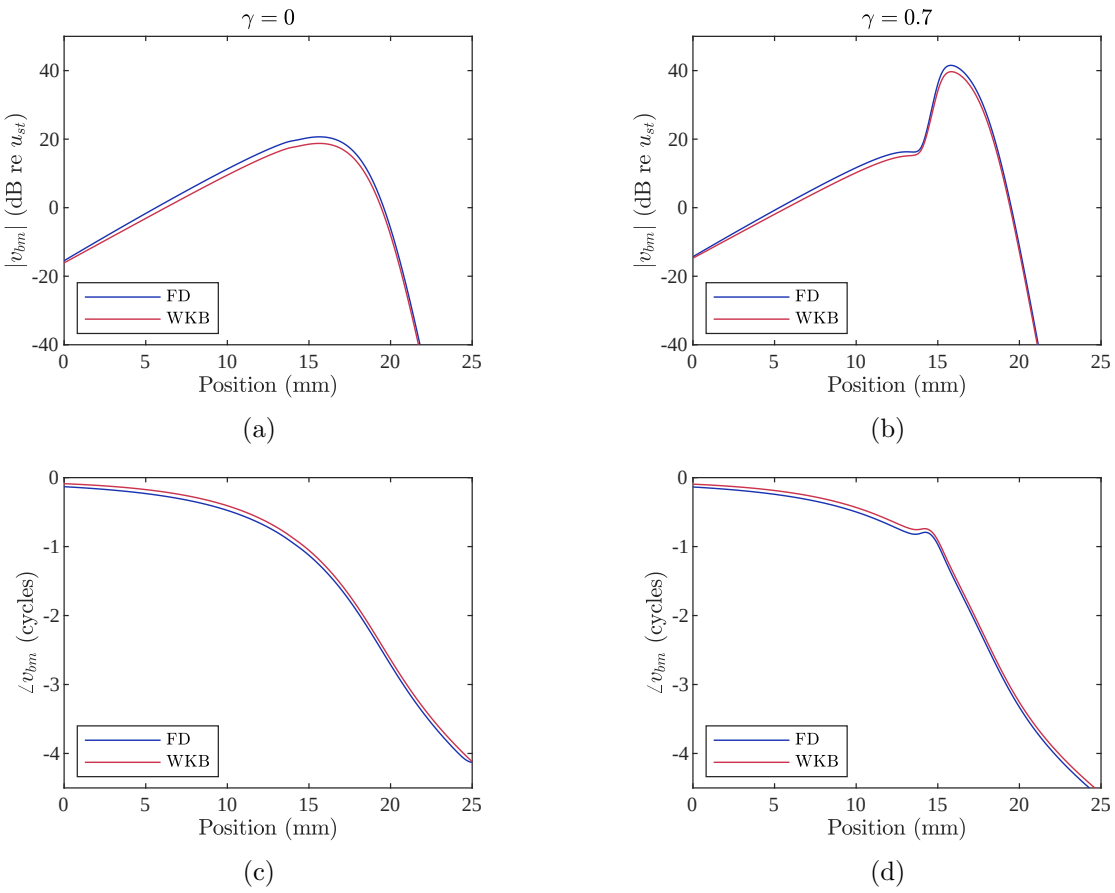

Figure B.8. Comparison of the basilar membrane coupled response of the linear Neely and Kim model, using the Finite Difference and WKB methods, for the passive case (modulus (a) and phase (b)) and for a global feedback gain factor of 0.7 (modulus (c) and phase (d)). Frequency: 1600 Hz.

does not impose limitations to the use of the WKB method. The 70 dB SPL is also displayed on the same figure, to illustrate that greatly different gain distributions produce similar results. In fact, the gain distributions for the two methods are much more different at 70 dB compared to 50 dB, but the resulting coupled responses are more consistent in 70 dB. This is an indication of the 'ill-posed' inverse problem and regional sensitivity, which will be discussed later.

The quasi-linear procedure was also implemented for global gains at different levels of excitation, so that γ was calculated at the position of peak response using the method outlined in Section B.4.1, but then applied at all positions along the cochlea, as mentioned in Section B.4.2, using the WKB method, for single-frequency excitation at 1600 Hz. A corresponding set of graphs for the modulus of the basilar membrane velocity coupled response, Figure B.10a, phase, Figure B.10b, and gains, Figure B.10c, is presented, where the global gain results are plotted along with the ones obtained with distributed gains. It can be seen that for input levels up to 40 dB, where the model is almost fully active, the gains are almost constant and therefore the global response is practically indistinguishable from the local one. However, for medium input levels, namely, 60 and 80 dB in this case, where the effect of the nonlinearity is more apparent and the local implementation of the model produces gains with notable longitudinal variations, there seems to be some difference, especially in the modulus of the coupled response. In the

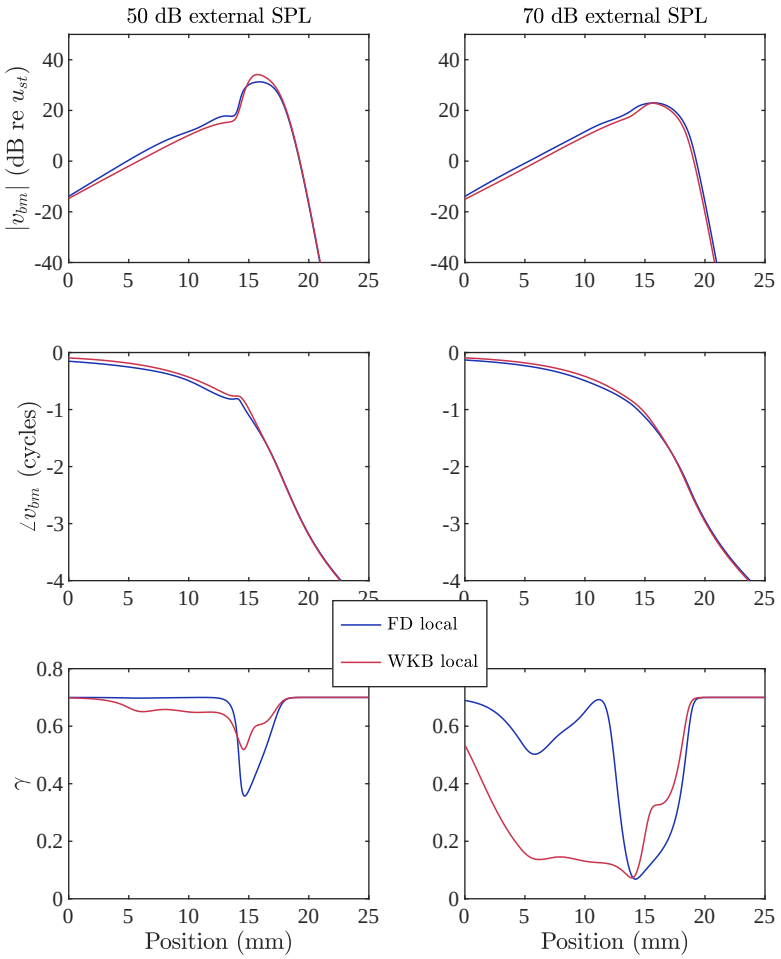

Figure B.9. Finite Difference local and WKB local coupled response for an external SPL of 50 dB (left) and 70 dB (right), at a frequency of 1600 Hz. Moduli (upper), phases (middle) and gain distributions (lower).

peak region, this difference is less than 2 dB, but in the apical region there is an evident shift of the global response. However, since the coupled response falls quickly to small values in the apical region, this difference is not so important. In the almost passive case of 100 dB SPL input, the global response matches well the local one.

By inspection of the gain distributions in Figure B.10c, it can be commented that greatly varying distributions result in quite similar coupled responses. It is reminded that the global gain is chosen to be equal to the local gain at the location of maximum response, during the iterative procedure presented in Section B.4.1. The fact that the global and local gain lines do not intersect exactly at the characteristic place, as can be seen in the 40 dB graph of Figure B.10c, is due to two reasons. First, the vertical line corresponds to the maximum response of the local implementation of the model, which does not occur at the same location as the maximum response of the global implementation. Second, at each iteration of the global model, the global gain is assigned the value of an intermediate local gain produced by the model, at the location of the maximum response; this intermediate local gain distribution is not the

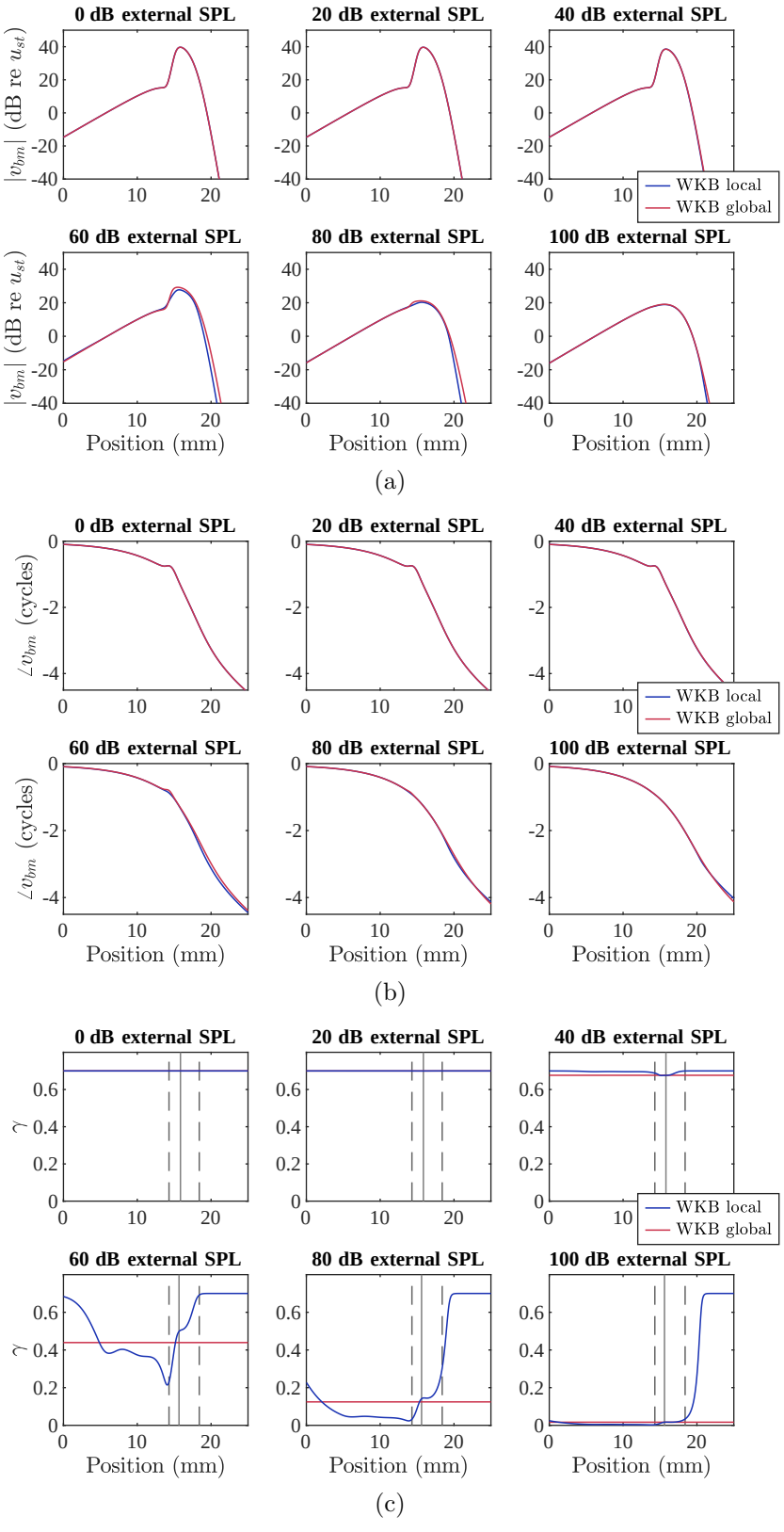

Figure B.10. Comparison of the cochlear coupled response for the locally active and the globally active case, for six different input levels, at 1600 Hz. Calculations were made with the WKB method. (a) Modulus of the basilar membrane velocity normalised with respect to the stapes velocity. (b) Phase of the basilar membrane velocity with respect to the phase of the stapes velocity. (c) Gain distributions. Vertical lines plotted according to Figure B.6b.

same as the final gain distribution of the local implementation of the model plotted here. It can be seen that the variation of the gain at the apical region does not noticeably affect the coupled response. This is especially illustrated by the fact that in the case of 100 dB SPL, the global response is almost the same as the local one, despite the fact that the local model seems to be almost fully active in the apical region, where the global one is almost fully passive, as seen in the lower right graph of Figure B.10c. This implies that for 60 and 80 dB SPL, shown in the lower left and lower middle graphs of Figure B.10c, where greater differences in the coupled response are observed, these are probably due to the differences in gain in the basal and/or peak regions. It should be emphasised that this global gain approach is valid for single-tone excitation and cannot be applied in general, for example when the cochlea excitation is due to the interaction between two tones [113, 114].

In order to further assess the sensitivity of the coupled response to gain variation in different locations, the Normalised Mean Square Error can be used. The formula used here is given by

$$\mathrm{NMSE}(\tilde{x}) = \frac{\sum\limits_{x} |v_{bm}(x) - \hat{v}_{bm}(\tilde{x}, x)|^2}{\sum\limits_{x} |v_{bm}(x)|^2}. \tag{B.38}$$

In the above equation, $v_{bm}(x)$ is the basilar membrane velocity distribution with an unperturbed global gain and $\hat{v}_{bm}(\tilde{x}, x)$ is the basilar membrane velocity distribution with a perturbation of gain in longitudinal location $\tilde{x}$. Therefore, $\mathrm{NMSE}(\tilde{x})$ is the Normalised Mean Square Error corresponding to a perturbation applied at length $\tilde{x}$ of the cochlea. A plot of the Normalised Mean Square Error, further normalised by the value of gain perturbation, is shown in Figure B.11. It is apparent that the sensitivity of the model to gain perturbation is 'densely' concentrated around the characteristic place, since the Normalised Mean Square Error falls rapidly as the perturbation is applied to locations away from the peak. It can therefore be concluded that the differences in the response of the global gain formulation are due to differences in gain in the peak region, while differences in both the basal and the apical regions do not significantly affect the coupled response.

The loose relation between gain distributions and responses presented previously implies that many different distributions may result in similar coupled responses. This implication is directly related to the non-uniqueness of the so-called 'inverse problem' in cochlear mechanics, as reviewed for example by de Boer in [107]. The inverse problem consists in obtaining model parameters by use of response data, mainly measured ones, but also model-produced data for validation purposes of the inverse method used. These model parameters can for example be the cochlear partition impedance or the functions that form the real and imaginary parts of the wavenumber [81]. In the current analysis, the gain distribution can be considered as a characteristic property of the model, directly linked to the cochlear partition impedance through Equation (B.9). It has been demonstrated, for example in [107] and [81], that the

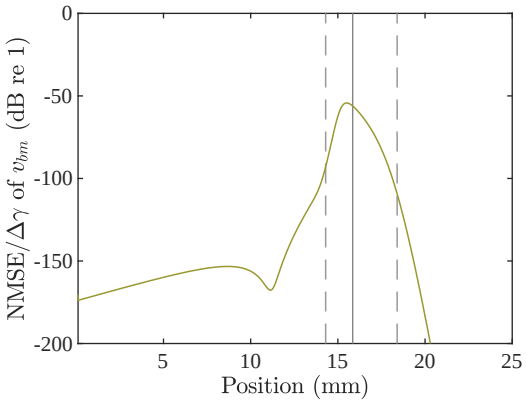

Figure B.11. Normalised Mean Square Error of the basilar membrane velocity divided by the gain perturbation, with a perturbed gain of 0.69 ($\Delta\gamma = 0.01$) applied at different locations along the cochlea. The vertical lines are plotted according to Figure B.6b.

inverse problem is 'ill-posed', as it has been characterised, due to the fact that similar responses may be produced by models with very different properties. Moreover, it can be said that a specific solution may result in different inversely acquired model parameters, depending on the inverse method used.

The nonlinear behaviour of the model can be demonstrated by plotting its maximum coupled response at different excitation levels. This is done in Figure B.12, where the coupled response is represented by the displacement of the basilar membrane. The WKB method responses for both the locally and globally active cases have been plotted against the locally active case calculated with the Finite Difference method. It can first be commented that the WKB globally active response curve only slightly diverges from the WKB locally active one, and only in a small input level region. This is in accordance with the previous discussion. It can further be observed that the WKB and Finite Difference methods behave similarly in the two end regions, that is, for input levels below about 30 dB, where the amplifier is almost fully active, and above about 80 dB, where the cochlea is almost passive. However, in the middle region, between about 40 and 70 dB, there seems to be some deviation. Specifically, for a 50 dB input level, the WKB local gain implementation gives about 3.5 dB higher maximum response compared to that calculated with the Finite Difference method. With global gains this error is slightly greater. These error values are higher than the ones of the linear model presented in Section B.5.3. Nevertheless, the WKB coupled response can still be considered to follow that calculated with the Finite Difference method fairly well, as can be seen in the upper left graph of Figure B.9. It is also worth noting that the dynamic range of the response is practically the same for both methods.

A comparison of the global gain approach for the two calculation methods in the context of the quasi-linear model is illustrated in Figure B.13a. It can be seen that in the fully active region up to about 25 dB SPL, the two methods behave similarly. However, for higher stimuli, the WKB method seems to give significantly greater values of global gain. Specifically, for

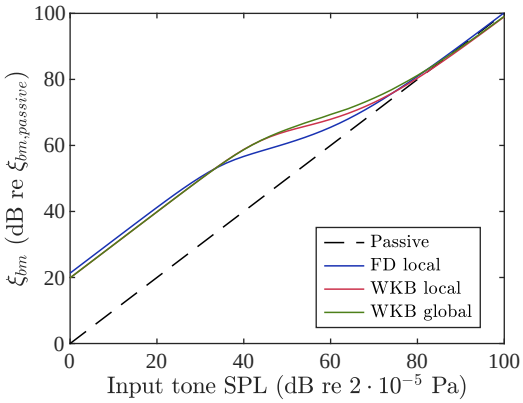

Figure B.12. Input/output functions of the Neely and Kim active model with distributed and global gain, using the quasi-linear approach. Peak values of the basilar membrane displacement were calculated for input SPLs between 0 dB and 100 dB with a step of 2 dB, at a frequency of 1600 Hz. Finite Difference local, WKB local and WKB global responses are plotted, all of which are offset with respect to the passive response (dashed line) for ease of assessment in terms of amplification. The passive response line was produced as the asymptote of the Finite Difference local case for high level input.

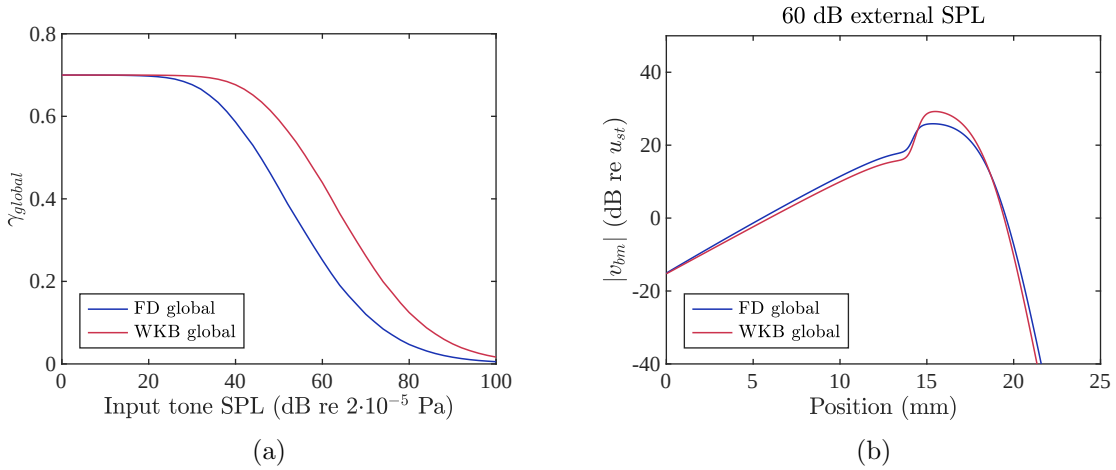

Figure B.13. (a) Variation of the global gain factor with respect to input SPL for the Finite Difference and WKB methods in the quasi-linear Neely and Kim model. (b) Basilar membrane velocity coupled response at 60 dB SPL, 1600 Hz, for the Finite Difference global and WKB global cases.

60 dB input SPL, the WKB global gain is 75% greater than the corresponding value calculated with the Finite Difference method. Respectively, the coupled response of the basilar membrane velocity, shown in the Figure B.13b, has a maximum difference of less than 3.5 dB near the peak. It can be seen that the coupled response is mainly affected in the peak region, where the activity of the cochlear amplifier is prominent. Expectedly, the lower global gain of the Finite Difference method results in a less active coupled response and, therefore, in a less prominent peak. It can be commented that even with a big difference in global gain, the two methods give fairly similar results for the quasi-linear model.

B.7 Conclusions

The quasi-linear approach to calculating the steady-state response in the nonlinear cochlea has been modified to use the WKB approximation method to calculate the coupled response. It has

been demonstrated that the WKB method provides an accurate approximation for the solution of the quasi-linear approach for the cochlear amplifier. An analysis of the components of the WKB solution has shown that the magnitude of the coupled velocity response is shaped by the exponential term of the solution, whose amplitude is formed by the integral of the imaginary wavenumber, while its phase is the integrated real wavenumber.

It has further been shown that a global gain may be used instead of a spatially varying one, providing a good approximation for the cochlear coupled response. The WKB and Finite Difference methods were found to behave slightly differently in the global implementation of the quasi-linear approach, without, however, loss of general consistency. Moreover, the variation of the gain distribution in locations away enough from the peak seems to have a negligible effect on the overall response. The most important conclusion is thus that many, apparently rather different, distributions of feedback gain can give very similar coupled responses in the cochlea. This is highlighted by the differences in the local feedback gain distributions in Figure B.9 and the global feedback gains in Figure B.10, all of which give similar coupled responses for the active cochlea.

C The WKB approximation method

C.1 Introduction

The WKB approximation method, named after physicists Wentzel, Kramers and Brillouin, is a method within perturbation theory, which gives approximate analytical solutions to differential equations [27]. It is also known as the WKBJ, JWKB, where J stands for Jeffreys, or the Liouville-Green, LG, method. The method is particularly useful for obtaining analytical solutions for differential equations which are not analytically solvable. Analytical solutions have two main advantages compared to numerically obtained results: first, they can be easily manipulated mathematically, and second, their components may be interpreted in physical terms, thus providing insight to the corresponding physical problem. A general presentation of the WKB method is given in this appendix, based on the formal analysis in [27, 115, 28], focusing on the second-order wave equation for acoustic waves in a horn and on the fourth-order wave equation for flexural waves on an elastic wedge.

The WKB method is applied to differential equations of the form

$$f\left(\epsilon^{\nu_\kappa}\frac{\mathrm{d}^\kappa y}{\mathrm{d}x^\kappa}, \epsilon^{\nu_{\kappa-1}}\frac{\mathrm{d}^{\kappa-1} y}{\mathrm{d}x^{\kappa-1}}, ..., \epsilon^{\nu_1}\frac{\mathrm{d}y}{\mathrm{d}x}, \epsilon^{\nu_0} y\right) = 0, \tag{C.1}$$

where f is a linear function of its arguments and ϵ is a perturbation factor. Usually, the exponent of the perturbation factor multiplying the highest-order derivative is equal to the order of the derivative, $\nu_\kappa = \kappa$. The formulation of the solution is based on an exponential trial solution of the form

$$y = \mathrm{e}^{\epsilon^{-1}\sum_{n=0}^{\infty} S_n \epsilon^n}, \epsilon \to 0, \tag{C.2}$$

where the functions S_n are arbitrary functions of x. In strict mathematical terms, the above relation forms an asymptotic solution to the differential equation as the perturbation factor tends to zero, and, therefore, the equal sign should be replaced by $\sim$; a looser notation is followed throughout this analysis.

Once all the derivatives appearing in Equation (C.1) have been calculated for the trial solution given in (C.2), they may be substituted, along with the trial solution, into the differential equation. The resulting terms may be arranged in the form of a polynomial equation for the perturbation factor, ϵ, as

$$g_0(A)\epsilon^0 + g_1(A)\epsilon^1 + g_2(A)\epsilon^2 + ... = 0, \tag{C.3}$$

where A is the set of the derivatives of all orders of the functions S_n appearing in the exponent of the trial solution. In order for Equation (C.3) to hold for all ϵ, all the coefficients of ϵ must

be equal to zero, thus yielding an infinite set of equations,

$$\begin{aligned} g_0(A) &= 0, \\ g_1(A) &= 0, \\ g_2(A) &= 0, \\ &\dots . \end{aligned} \tag{C.4}$$

Each one of Equations (C.4) for $g_n(A)$ involves derivatives of up to the function S_n. That is, the first equation, $g_0(A) = 0$, involves only the derivative of the zeroth-order function S_0, the second equation, $g_1(A) = 0$, involves only derivatives of S_0 and S_1 and so on. Therefore, all these equations may be solved successively starting from the zeroth-order one, so as to obtain, by means of integration, the sought-after S_n functions. A WKB approximation of order n is obtained by including up to the function S_n in Equation (C.2).

In practice, the perturbation factor appearing in a differential equation describing a specific physical system may not be tending to zero; it could actually have high values, for example $\epsilon = 1$. In this case, the relation of the form of Equation (C.2) is not an asymptotic solution to the differential equation (C.1). Even so, the WKB approximation may give results of high accuracy, as is demonstrated in [27]. Another cause of error of the approximation is the order of the solution used, that is, the order of the highest-order S function used, after which the solution is truncated. A commonly used WKB approximation for many applications is the first-order one, where the solution is written as

$$y = \mathrm{e}^{\epsilon^{-1}S_0+S_1}. \tag{C.5}$$

In order for the WKB solution given in Equation (C.2) to be an asymptotic solution to Equation (C.1), the following set of conditions have to be satisfied [27],

$$|\epsilon S_{n+1}(x)| \ll |S_n(x)| \Rightarrow \left|\epsilon \frac{S_{n+1}(x)}{S_n(x)}\right| \ll 1, \epsilon \to 0, n \geq 0. \tag{C.6}$$

These correspond to an infinite set of relations, comparing each two consecutive S functions. Additionally, in order for the Nth-order WKB solution to be an accurate approximation of the solution, the following condition also has to hold [27],

$$\left|\epsilon^N S_{N+1}(x)\right| \ll 1, \epsilon \to 0. \tag{C.7}$$

The above conditions are given here for completeness; they are discussed further in the specific examples presented in the next sections.

C.2 Second-order wave equation

C.2.1 Derivation of the first-order WKB approximation for Schrödinger's equation

A differential equation appearing in various non-uniform systems is Schrödinger's equation,

$$y'' + k^2(x)y = 0, \tag{C.8}$$

where the prime notation denotes differentiation with respect to x of the same order as the number of primes. Equation (C.8) is similar to the Helmholtz equation [57], the difference being that, in the former, the wavenumber is a non-consant function of x. This second order equation describes, for example, the harmonic acoustic pressure along an acoustic horn normalised with respect to the cross-sectional radius, as is presented in Appendix A. It also describes the spatial distribution of the pressure difference across the cochlear partition in the cochlea along its length, again for harmonic excitation. Equation (C.8) is often called 'the wave equation' for the corresponding system, although in a rather abusive manner, since the actual wave equation is a partial differential equation with respect both to space and time, whereas in Equation (C.8), the time dependence has been dropped due to harmonic time dependence of the sought-after function y.

Equation (C.8) is solvable only for a limited number of forms of the wavenumber function [96]. Therefore, in general, it either has to be solved numerically or an analytical approximation has to be found. The WKB method may be employed in order to provide such an analytical approximation. The second-order wave equation (C.8) may be written in the form of Equation (C.1) by including a perturbation factor, ϵ, multiplying the highest-order derivative, raised to the power of this derivative,

$$\epsilon^2 y'' + k^2(x)y = 0. \tag{C.9}$$

It can be seen that the initial equation (C.8) corresponds to the perturbed equation (C.9) with the perturbation factor being equal to one. The WKB solution may be found for the perturbed equation (C.9), and the particular value of one for the perturbation factor may be applied afterwards.

The general WKB solution is

$$y = \mathrm{e}^{\epsilon^{-1}\sum_{n=0}^{\infty} S_n \epsilon^n}, \epsilon \to 0. \tag{C.10}$$

Differentiating twice yields the second derivative

$$y'' = \left[\epsilon^{-1}\sum_{n=0}^{\infty} S_n''\epsilon^n + \left(\epsilon^{-1}\sum_{n=0}^{\infty} S_n'\epsilon^n\right)^2\right] y. \tag{C.11}$$

Substituting into Equation (C.9) and neglecting the trivial solution, $y = 0$, gives

$$\epsilon^{-1}\sum_{n=0}^{\infty} S_n''\epsilon^n + \left(\epsilon^{-1}\sum_{n=0}^{\infty} S_n'\epsilon^n\right)^2 + k^2 = 0. \tag{C.12}$$

This equation may be re-arranged as a polynomial of ϵ as

$$\left(S_0'^2 + k^2\right)\epsilon^0 + \left(S_0'' + 2S_0'S_1'\right)\epsilon^1 + \left(S_1'' + S_1^2 + 2S_0'S_2'\right)\epsilon^2 + ... = 0. \tag{C.13}$$

In order for this equation to hold for all values of ϵ, the coefficients of all its powers must be zero. Therefore, an infinite set of equations is obtained, the first three of which are

$$\epsilon^0 : S_0'^2 = -k^2, \tag{C.14}$$

$$\epsilon^1 : S_1' = -\frac{S_0''}{2S_0'}, \tag{C.15}$$

and

$$\epsilon^2 : S_2' = -\frac{1}{2}\left(\frac{S_1''}{S_0'} + \frac{S_1'^2}{S_0'}\right) = \frac{S_0'''}{4S_0'^2} - \frac{3S_0''^2}{8S_0'^3}. \tag{C.16}$$

Equations (C.14) and (C.15) are also called the 'eikonal' equation and the 'transport' equation, respectively. The solution of the eikonal is

$$S_0' = \pm \mathrm{i}k, \tag{C.17}$$

which, by integration, yields

$$S_0 = \pm \mathrm{i}\int_0^x k(\tilde{x})\mathrm{d}\tilde{x}. \tag{C.18}$$

Consequently, the transport equation becomes

$$S_1' = -\frac{k'}{2k}, \tag{C.19}$$

which, by integration, gives

$$S_1 = \frac{1}{2}\ln\left(\frac{k_{in}}{k}\right), \tag{C.20}$$

where k_{in} is the wavenumber at the input boundary of the waveguide. The first-order WKB approximation may then be obtained by taking only the first two terms in the exponential of

the general solution, Equation (C.10), and taking ϵ to be equal to one, giving

$$y = \left(\frac{k_{in}}{k}\right)^{1/2} \mathrm{e}^{\pm \mathrm{i} \int_0^x k(\tilde{x}) \mathrm{d}\tilde{x}}. \tag{C.21}$$

It should be noted that no particular assumption about the wavenumber function has been made, which may in general be complex. Therefore, the above solution, corresponding to two linearly independent solutions, represents either a travelling or an evanescent wave, or a combination of the two types of waves, depending on whether the real and imaginary parts of the wavenumber are zero or not. Specifically, if the wavenumber is real, Equation (C.21) represents a travelling wave, whereas if the wavenumber is imaginary, it represents an evanescent wave. Moreover, if the resulting sign in the exponent is negative, the wave either travels or attenuates towards positive x, while if the sign is positive, it either travels or attenuates towards negative x. The general first-order WKB solution is a linear combination of the two linearly independent solutions, which may be written as

$$y = Ak^{-1/2} \mathrm{e}^{-\mathrm{i} \int_0^x k(\tilde{x}) \mathrm{d}\tilde{x}} + Bk^{-1/2} e^{\mathrm{i} \int_0^x k(\tilde{x}) \mathrm{d}\tilde{x}}, \tag{C.22}$$

where the factor due to k_{in} has been absorbed into the arbitrary complex constants A and B.

C.2.2 The WKB approximation for an acoustic horn

In order to provide a concrete example of a system obeying a second-order wave equation, sound propagation in an acoustic horn will be considered. The acoustic pressure in an acoustic horn may be reduced, by an appropriate variable substitution, to the wave equation (C.8), as is presented in Appendix A. The wavenumber in a horn takes the form [97, 55]

$$k = \pm\sqrt{k_0^2 - F(x)}, \tag{C.23}$$

where k_0 is the free space wavenumber, given by $k_0 = \omega/c_0$, where ω is the angular frequency of the wave and c_0 is the speed of sound in free space, and $F(x)$ is called the horn function, which, for a horn of circular cross section, is given by

$$F(x) = \frac{r''}{r}, \tag{C.24}$$

where $r(x)$ is the radius of the cross section and r'' its second spatial derivative.

It should be noted that no losses have been included in this analysis. If losses were included, for example by incorporating an imaginary part for the speed of sound, the quantity under the square root in Equation (C.23) would be complex, as would the wavenumber function. In the case, however, where losses are excluded, it can be seen that the wavenumber may be either purely real or purely imaginary, since the argument of the square root in Equation (C.23)

is purely real. Therefore, the wave may be either purely propagating or purely evanescent, according to the wavenumber being real or imaginary, respectively.

In general, the wavenumber may become zero for an appropriate combination of the frequency-dependent free space wavenumber and the spatially-dependent horn function. Therefore, for a given horn function, the wavenumber may become zero for different frequencies in different positions along the horn, leading to a qualitative change of the character of the wave from travelling to evanescent. The vanishing of the wavenumber introduces a singularity in the WKB solution, as is apparent from the form of Equation (C.22), where the wavenumber appears in the denominator due to the factor $k^{-1/2}$. Such a singularity is called a turning point or cut-off point, defining the border between the regions of propagation and evanescence. Consequently, the WKB method is not applicable in a turning point. In order for the WKB to be applied throughout the horn, including turning points, a procedure known as asymptotic matching needs to be followed, as presented for example in [27] and [115].

C.2.3 Validity of the WKB approximation for an acoustic horn

The validity of the approximation of the WKB method is determined by the satisfaction of certain conditions. In the strict mathematical formulation of the method, as presented in [27], two different types of conditions have to hold. Firstly, every WKB function multiplied by the perturbation factor must be much smaller than the previous WKB function in absolute terms, as the perturbation factor tends to zero, so that

$$\text{WKB}_{a,n+1}\text{:}\ \ |\epsilon S_{n+1}(x)| \ll |S_n(x)| \Rightarrow \left|\epsilon \frac{S_{n+1}(x)}{S_n(x)}\right| \ll 1, \epsilon \to 0, n \geq 0, \tag{C.25}$$

which means that each term in the exponent of the WKB solution, as given in Equation (C.10), must be much smaller than the previous one. Additionally, for the solution to be accurate if truncated at the term of order N, the first term to be neglected must be much smaller than one,

$$\text{WKB}_{b,N+1}\text{:}\ \ \left|\epsilon^N S_{N+1}(x)\right| \ll 1, \epsilon \to 0. \tag{C.26}$$

It is important to note that the above relations, as well as all consequent relations where a comparison of "much smaller than one" or "much larger than one" is involved, should not be considered as a comparison of the respective left-hand-side term with unity. Instead, the comparison should be considered with respect to order of magnitude, so that the left-hand-side terms should have an order of magnitude much less than the order of magnitude of one in order for the respective conditions to be satisfied.

An equivalent rigorous formulation of the WKB solution is presented in [28], but with the

WKB functions explicitly expressed as integrands as

$$y = \mathrm{e}^{\epsilon^{-1}\int_0^x d\tilde{x}\sum_{n=0}^{\infty} s_n \epsilon^n}, \tag{C.27}$$

where $s_n = S_n'$ and S_n are the WKB functions as defined previously. According to this formulation, the requirement that progressive terms get much smaller can be expressed in terms of the integrand functions s_n as

$$\mathrm{WKB}_{a,n+1}\text{:}\ \ |\epsilon s_{n+1}(x)| \ll |s_n(x)| \Rightarrow \left|\epsilon \frac{s_{n+1}(x)}{s_n(x)}\right| \ll 1. \tag{C.28}$$

In view of Equations (C.17) and (C.19), the validity condition $\mathrm{WKB}_{a,1}$ becomes

$$\left|\frac{k'}{2k^2}\right| \ll 1. \tag{C.29}$$

Equations (C.28) may be obtained by differentiating both sides in the first expression of the conditions in (C.25). In general, differentiation cannot be applied to an inequality. However, since integration takes place in a finite interval, in this case between 0 and x, and a relation of "much smaller than" is involved, implying, in the strict sense, a difference of many orders of magnitude, relations (C.25) and (C.28) equivalently express the requirement that each WKB term is much smaller than the previous one.

In the engineering literature, only condition (C.29) is typically used, as, for example, in [116] and [65]. Its derivation is usually based on a physical line of thought, requiring that the relative variation of the wavenumber over the length of the order of a wavelength be negligible, which can be expressed as

$$\left|\frac{k'}{k}\lambda\right| \ll 1. \tag{C.30}$$

Since, in the absence of losses, the wavelength is $\lambda = 2\pi/k$, the validity condition takes the more popular form [8, 7]

$$\mathrm{WKB}_c\text{:}\ \ \left|\frac{k'}{k^2}\right| \ll 1, \tag{C.31}$$

where the subscript c stands for common. The factor 2π has been neglected as being of the order of 1, something which may be done if the term on the left side of the inequality is many orders of magnitude smaller than one. If this is not the case, however, and a quantitative measure of validity is desired, then, if such constant terms are of the same order of magnitude as the left side of inequality (C.31), their exclusion may significantly affect the assessment of validity, as will be discussed later.

The validity condition in the form of relation (C.31) may also be obtained by requiring that the relative spatial variation of the coefficients of the differential equation be negligible within the length of the order of a wavelength. In Equation (C.8), the only variable coefficient is k^2.

Therefore, the above requirement may be expressed mathematically as

$$\left|\frac{\left(k^2\right)'}{k^2}\frac{1}{k}\right| \ll 1 \Rightarrow \left|\frac{2k'}{k^2}\right| \ll 1, \tag{C.32}$$

which is the same as condition (C.31), except for a constant factor of 2. This approach is followed for example in [11].

The first two validity conditions (C.25), by use of Equations (C.18) and (C.20), take the form

$$\text{WKB}_{a,1}\text{:}\ \left|\frac{S_1(x)}{S_0(x)}\right| \ll 1 \Rightarrow \left|\frac{\frac{1}{2}\ln\frac{k_{in}}{k(x)}}{\int_0^x k(\tilde{x})\mathrm{d}\tilde{x}}\right| \ll 1, \tag{C.33}$$

$$\text{WKB}_{a,2}\text{:}\ \left|\frac{S_2(x)}{S_1(x)}\right| \ll 1 \Rightarrow \left|\frac{\int_0^x \left(-\frac{k''(\tilde{x})}{4k^2(\tilde{x})}+\frac{3k'^2(\tilde{x})}{8k^3(\tilde{x})}\right)\mathrm{d}\tilde{x}}{\frac{1}{2}\ln\frac{k_{in}}{k(\tilde{x})}}\right| \ll 1, \tag{C.34}$$

and the condition due to the truncation of the solution after the second WKB term takes the form

$$\text{WKB}_{b,2}\text{:}\ |S_2(x)| \ll 1 \Rightarrow \left|\int_0^x \left(-\frac{k''(\tilde{x})}{4k^2(\tilde{x})}+\frac{3k'^2(\tilde{x})}{8k^3(\tilde{x})}\right)\mathrm{d}\tilde{x}\right| \ll 1. \tag{C.35}$$

An illustration of the four validity conditions of relations (C.33), (C.34), (C.35) and (C.31) at a frequency of 1 kHz is given in Figure C.1b, for a horn whose wavenumber distribution at 1 kHz is shown in Figure C.1a. Firstly, it can be observed that the conditions involving the second-order WKB term, S_2, are strongly violated when approaching the turning point from the region of propagation, that is, where the wavenumber is real, and throughout the region of evanescence. The terms evaluating the validity of these conditions actually take very high values, of the order of 10^4, not shown here for illustrational purposes.

As regards the commonly used WKB condition, WKB_c, this is strongly violated over a relatively wide region around the turning point. It is expected that the terms for these three conditions will become large at least at the turning point, since they all involve terms with the wavenumber at the denominator, which vanishes at the turning point. Only the term of the $\text{WKB}_{a,1}$ condition retains relatively small values throughout the horn, even at the turning point, where it is close to unity. Nevertheless, it should be pointed out that, even at the positions of the horn where some of the terms of the conditions have relatively small values, these are still comparable to unity and, therefore, the conditions cannot be considered to be strictly satisfied, since the requirement calls for a 'much less' comparative relation. This is also expected, since, for the strict WKB formulation, the validity conditions also require that the perturbation factor, ϵ, tends to zero, whereas, in the case examined here, it actually has a value of one.

The WKB conditions presented do not seem to give a clear indication of the validity of the solution, since they do not agree in the same regions. Specifically, two conditions are very strongly violated throughout the evanescent region, another one is violated clearly around the turning point and a fourth one seems to have relatively small values throughout the horn.

Therefore, in order to assess the proximity of the WKB solution to the actual solution of the problem, comparison with numerical methods has to be made. At least for the case where a turning point is included in the system, that is, for frequencies for which cut-off occurs at some location inside the horn, the WKB solution is expected to diverge significantly from a more accurate numerical solution at the region of the turning point, due to the existence of the singularity in Equation (C.22).

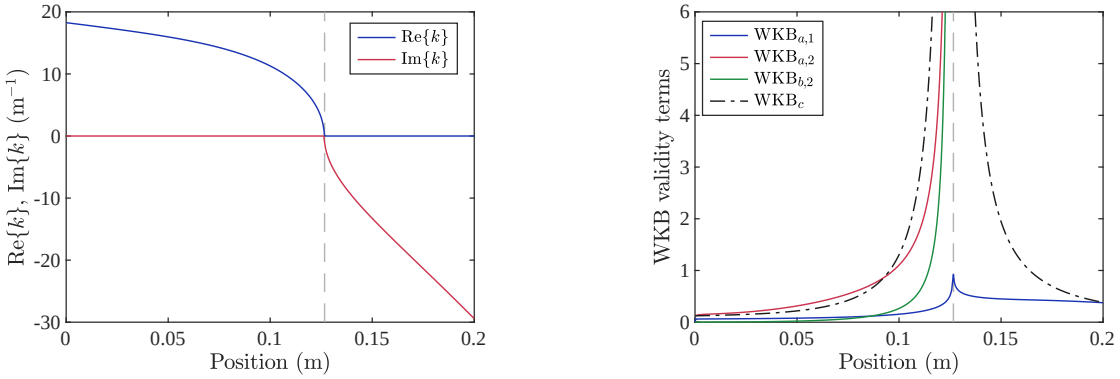

(a) (b)

Figure C.1. (a) Spatial variation of the real and imaginary parts of the wavenumber in a horn with radius $r = 0.02\exp\{250x^3\}$. (b) Spatial variation of the different WKB validity terms.

C.3 Fourth-order wave equation

C.3.1 Derivation of the first-order WKB approximation for a non-uniform plate

In this section, the WKB solution for the vertical harmonic displacement of a non-uniform plate in bending is derived, based on the method presented in [27]. A derivation of the WKB solution for a non-uniform beam and a non-uniform plate was presented by Pierce in [5]. A more standard approach is followed here, which is similar to that in [34].

The equation of motion for a non-uniform plate in bending is first re-written, with the prime notation corresponding to differentiation with respect to the axial coordinate, x,

$$\left(Dw''\right)'' - \omega^2 \rho h w = 0, \tag{C.36}$$

where $D = \rho c_p^2 h^3/12$, ρ is the density of the material of the plate and $h(x)$ is the spatially varying thickness of the plate. A perturbation factor may be introduced by setting $\omega = \epsilon^{-2}$, on the grounds that very low frequencies are not so important in the practical consideration of the system. Therefore, the perturbation parameter, ϵ, will in general have small values; let it be noted that ϵ cannot become zero, since frequency can only take finite values. Consequently, the equation of motion becomes

$$\epsilon^4 \left(Dw''\right)'' - \rho h w = 0. \tag{C.37}$$

The starting point for the WKB solution is the general formula

$$w = \mathrm{e}^{\epsilon^{-1}\sum_{n=0}^{\infty} S_n \epsilon^n}, \epsilon \to 0. \tag{C.38}$$

By taking the derivatives of w and substituting into Equation (C.37), also dividing by the exponential, which appears in all terms, the following equation is obtained

$$\begin{aligned}\epsilon^4 \Bigg\{ D \Bigg[\sum_{n=0}^{\infty} S_n''' \epsilon^{n-1} + 4 \left(\sum_{n=0}^{\infty} S_n''' \epsilon^{n-1} \right) \left(\sum_{n=0}^{\infty} S_n' \epsilon^{n-1} \right) + 3 \left(\sum_{n=0}^{\infty} S_n'' \epsilon^{n-1} \right)^2 + \\ +6 \left(\sum_{n=0}^{\infty} S_n' \epsilon^{n-1} \right)^2 \left(\sum_{n=0}^{\infty} S_n'' \epsilon^{n-1} \right) + \left(\sum_{n=0}^{\infty} S_n' \epsilon^{n-1} \right)^4 \Bigg] + \\ +2D' \Bigg[\sum_{n=0}^{\infty} S_n''' \epsilon^{n-1} + 3 \left(\sum_{n=0}^{\infty} S_n' \epsilon^{n-1} \right) \left(\sum_{n=0}^{\infty} S_n'' \epsilon^{n-1} \right) + \left(\sum_{n=0}^{\infty} S_n' \epsilon^{n-1} \right)^3 \Bigg] + \\ +D'' \Bigg[\sum_{n=0}^{\infty} S_n'' \epsilon^{n-1} + \left(\sum_{n=0}^{\infty} S_n' \epsilon^{n-1} \right)^2 \Bigg] \Bigg\} - \rho h = 0.\end{aligned} \tag{C.39}$$

By re-arranging the left side as a polynomial of ϵ, that is, gathering equal powers of ϵ, and setting all the coefficients of the powers of ϵ equal to zero, so that the equation holds for all values of ϵ, an infinite set of equations is obtained. The first three are

$$\epsilon^0 : S_0'^4 = \frac{\rho h}{D} = \frac{12}{c_p^2 h^2}, \tag{C.40}$$

$$\epsilon^1 : S_1' = -\frac{3}{2}\frac{S_0''}{S_0'} - \frac{1}{2}\frac{D'}{D}, \tag{C.41}$$

and

$$\epsilon^2 : S_2' = -\frac{3}{2}\frac{S_1'^2}{S_0'} - \frac{3}{2}\frac{S_1''}{S_0'} - 3\frac{S_0'' S_1'}{S_0'^2} - \frac{S_0'''}{S_0'^2} - \frac{3}{4}\frac{S_0''^2}{S_0'^3} - \frac{3}{2}\frac{D'}{D}\frac{S_1'}{S_0'} - \frac{1}{4}\frac{D''}{D}\frac{1}{S_0'} - \frac{3}{2}\frac{D'}{D}\frac{S_0''}{S_0'^2}. \tag{C.42}$$

Equation (C.40), the eikonal equation, has four roots,

$$S_0' = \{\pm 1, \pm \mathrm{i}\} \left(\frac{\rho h}{D} \right)^{1/4} = \{\pm 1, \pm \mathrm{i}\} \frac{12^{1/4}}{c_p^{1/2} h^{1/2}}, \tag{C.43}$$

where the four factors in curly brackets correspond to the factors multiplying each separate solution. By integration of Equation (C.43), the four different forms of S_0 are found to be

$$S_0 = \{\pm 1, \pm \mathrm{i}\} \int_0^x \frac{12^{1/4}}{c_p^{1/2} h^{1/2}(\tilde{x})} \mathrm{d}\tilde{x}, \tag{C.44}$$

where the lower limit of integration has been chosen to be the input boundary of the waveguide for convenience.

Since the four S_0 functions differ only by a constant factor, Equation (C.41), that is, the transport equation, has the same form for all solutions of Equation (C.40), as the factors of each S_0 function cancel out in the first fraction. Substituting Equation (C.44) into Equation (C.41), and also using the relation $D = \rho c_p^2 h^3/12$, gives

$$S_1' = -\frac{3}{4}\frac{h'}{h}, \tag{C.45}$$

which, by integration, yields

$$S_1 = \frac{3}{4}\ln\left(\frac{h_0}{h}\right), \tag{C.46}$$

where $h_0 = h(0)$ is the thickness at the input boundary. By substitution of Equations (C.44) and (C.46) into the general form of the solution, Equation (C.38), and neglecting higher-order terms, the first-order WKB approximation is obtained

$$w = \left(\frac{h_0}{h}\right)^{3/4} \mathrm{e}^{\{\pm 1, \pm \mathrm{i}\}\int_0^x k(\tilde{x})\mathrm{d}\tilde{x}}, \tag{C.47}$$

where

$$k = \frac{12^{1/4}\omega^{1/2}}{c_p^{1/2}h^{1/2}}. \tag{C.48}$$

The general solution using the first-order WKB approximation is writen as

$$w = \left(\frac{h_0}{h}\right)^{3/4} \left[A_1\mathrm{e}^{-\mathrm{i}\phi} + A_2\mathrm{e}^{\mathrm{i}\phi} + A_3\mathrm{e}^{-\phi} + A_4\mathrm{e}^{\phi}\right], \tag{C.49}$$

where A_1, A_2, A_3 and A_4 are complex constants.

C.3.2 Validity of the WKB approximation for a non-uniform plate

The validity conditions of the WKB approximation are re-written here for ease of reference,

$$\mathrm{WKB}_{a,n+1}\text{:}\ \ |\epsilon S_{n+1}(x)| \ll |S_n(x)| \Rightarrow \left|\epsilon\frac{S_{n+1}(x)}{S_n(x)}\right| \ll 1, \epsilon \to 0, n \geq 0, \tag{C.50}$$

$$\mathrm{WKB}_{b,N+1}\text{:}\ \ \left|\epsilon^N S_{N+1}(x)\right| \ll 1, \epsilon \to 0. \tag{C.51}$$

The WKB condition commonly found in the literature is also re-written,

$$\mathrm{WKB}_{c}\text{:}\ \ \left|\frac{k'}{k^2}\right| \ll 1. \tag{C.52}$$

If the approach with integrand functions is followed, as was done for the second-order equation according to the analysis in [28], this condition takes the form

$$\left|\frac{3}{4}\frac{k'}{k^2}\right| \ll 1, \tag{C.53}$$

which is equivalent to the commonly used form in relation (C.52) if the constant factor is neglected.

Similarly to the case of the second-order equation, the validity condition of relation (C.52) may be obtained also for the fourth-order equation of flexural vibrations by requiring that the relative variation of each of the coefficients of the differential equation over the length of the order of a wavelength be negligible, as is done for example in [117]. In this sense, the waveguide may be regarded as having slowly varying geometrical parameters along the direction of propagation. For this aim, the fourth-order differential equation (C.36) is expanded as

$$Dw'''' + 2D'w''' + D''w'' - \omega^2\rho h w = 0. \tag{C.54}$$

The four resulting conditions are expressed as

$$\left|\frac{C_j'}{C_j}\frac{1}{k}\right| \ll 1, \tag{C.55}$$

where $C_1 = D$, $C_2 = 2D'$, $C_3 = D''$ and $C_4 = -\omega^2\rho h$; all four conditions have to be satisfied for the waveguide to be considered slowly varying. The conditions (C.55) can be expressed in terms of the wavenumber and its derivatives. If the derivatives of the wavenumber of order higher than one are neglected, in compliance with the slowly varying assumption and the first-order approximation, all four conditions result in the form of (C.52), only differing by constant factors.

A number of issues arise in the assessment of the validity of the WKB approximation by use of the various conditions. Firstly, the conditions $\mathrm{WKB}_{a,n+1}$ and $\mathrm{WKB}_{b,N+1}$ are required to hold in the formal vanishing limit of the perturbation factor for the WKB approximation to be accurate. In the WKB formulation presented in the previous section, the perturbation factor is defined in terms of the angular frequency as $\epsilon = \omega^{-1/2}$, so that the limiting case corresponds to frequency tending to infinity. The first WKB_a condition, that is, $\mathrm{WKB}_{a,1}$, is written as

$$\mathrm{WKB}_{a,1}\text{:}\quad \left|\frac{S_1(x)}{\omega^{1/2}S_0(x)}\right| \ll 1 \Rightarrow \left|\frac{\frac{3}{4}\ln\left(\frac{h_0}{h(x)}\right)}{\int_0^x k(\tilde{x},\omega)\mathrm{d}\tilde{x}}\right| \ll 1, \omega \to \infty. \tag{C.56}$$

It can be seen that this condition is satisfied as the frequency tends to infinity, since the wavenumber is proportional to the square root of the angular frequency, as long as the thickness of the waveguide is not zero. In fact, all conditions of Equation (C.50) are satisfied in the strict requirement of infinite frequency, as long as the involved S functions are finite non-zero functions of x.

In special cases, such as if the thickness tends to zero, indefiniteness may occur and further investigation may be required in order to define the behaviour of the fraction in Equation (C.56). It should also be noted that all of these conditions are violated in the low-frequency limit, a point that considerably affects the accuracy of the method at low frequencies. It can be deduced

that the common validity condition of Equation (C.52) is also satisfied as frequency tends to infinity, in light of Equation (C.48), under the same restrictions for the thickness as for the WKB_a condition; it also fails as frequency approaches zero.

In a physical context, frequencies are of finite magnitude and for many useful cases have values towards the lower end of the spectrum. Therefore, even if the approximation is found to be accurate in the limiting high-frequency case, a quantitative assessment of the conditions along the useful frequency spectrum needs to be made. Furthermore, there exists an intrinsic arbitrariness in what is considered to be accurate when an inequality involving a "much larger / smaller than" relation is used as a criterion, so that some acceptable threshold value for the quantities compared to one in the given relations has to be defined. Similarly, the low-frequency region is arbitrary and has to be defined according to some threshold value for the quantity of the condition.

The second type of condition, WKB_b, expressed in Equation (C.51), is also satisfied in the high-frequency limit, as long as the corresponding S_{N+1} function is a finite function of x; in the low-frequency limit it is violated. Again, the left-hand side of the expression has to be calculated within the useful frequency spectrum, in order to check the extent to which the condition is satisfied or violated. If the WKB solution is truncated after the first-order term, $N = 1$, the first term to be neglected in the exponent of the solution is ϵS_2, where S_2 is calculated by integrating Equation (C.42). The corresponding condition is then written as

$$\text{WKB}_{b,2}\text{:}\ \ |\epsilon S_2(x)| \ll 1, \epsilon \to 0. \tag{C.57}$$

Contrary to functions S_0 and S_1, whose modulus is independent of the particular solution of the eikonal equation (C.40), the second-order function S_2, that is, the integral of Equation (C.42), corresponds to four different functions, depending on which one of the four solutions of the eikonal equation is used. It is reminded that the solutions of the eikonal equation are distinguished by factors $+1$, -1, $+\text{i}$ and $-\text{i}$, according to Equations (C.43). Actually, due to the form of the various terms of S_2, the two imaginary roots, which correspond to the two travelling waves of the general solution, have S_2 functions with identical modulus. Therefore, three distinct conditions occur. The same plurality of conditions holds for higher-order WKB_a conditions, such as for $\text{WKB}_{a,2}$, which also involves S_2.

A position of special interest, as is made clear in the analysis in Chapter 2, is at the input end where the non-uniform plate has its maximum thickness, h_0, which corresponds to spatial coordinate $x = 0$. Condition $\text{WKB}_{a,2}$ is written as

$$\text{WKB}_{a,2}\text{:}\ \ \left|\frac{S_2(x)}{\omega^{1/2} S_1(x)}\right| \ll 1. \tag{C.58}$$

At this thick end, the first-order function vanishes, $S_1(0) = 0$. A study of the corresponding

behaviour of the second-order function is thus required. It can be shown that for a wedge of power-law profile of order higher than 2, S_2 also tends to zero at the thick end. Once the indefiniteness is raised, the limiting behaviour of the $\mathrm{WKB}_{a,2}$ condition is found to give a finite value at the thick end of the waveguide.

For other thickness profiles, however, such as the power-cosine wedges, S_2 is not zero at $x = 0$ and the condition is strongly violated. In such a case, the first truncated term, ϵS_2, is infinitely greater than the previous one, S_1, which is zero at this position, independently of frequency. Even though this result seems to invalidate the approximation, it should be observed that the function S_0 is still present in the solution and it may hold that $|\epsilon S_2| \ll |\epsilon^{-1} S_0|$, that is, the first term in the exponent of the WKB solution may be much larger than the third term. Therefore, despite the violation of this validity condition at the thick end of the waveguide, the resulting solution may still be a good approximation.

C.3.3 Summary and conclusions

The WKB method provides approximate analytical solutions to differential equations in the form of an exponential power series with respect to a perturbation factor. The corresponding solutions were obtained by application of the WKB method to the second-order wave equation with variable wavenumber and to the fourth-order equation of flexural vibration in non-uniform plates. In most cases, the first-order solution is used, that is, only the first two WKB terms are used. Higher-order approximations up to a certain order improve the accuracy, although the corresponding mathematical expressions become increasingly cumbersome. Beyond some order of approximation, however, the series of the WKB functions diverges and the accuracy deteriorates [45, 46].

In the strict formulation of the WKB approximation, a whole set of conditions has to be satisfied. The validity conditions for the first-order WKB solution of the second-order wave equation for an expanding acoustic horn are in general strongly violated in the region of the turning point. Furthermore, conditions involving the second-order WKB term are also violated in the evanescent region. As regards the first-order approximation for the one-dimensional flexural vibration of a non-uniform plate, the validity conditions are generally satisfied for high frequencies and violated for low frequencies, although these characterisations are of a quite arbitrary qualitative nature. Nevertheless, some conditions may be strongly violated in certain locations for all frequencies.

The set of conditions for the relation between any two consecutive terms of the WKB solution have a different form depending on whether the integrand functions or the integral ones are used for the comparison. Even though both sets of equations express the requirement that each WKB term be much smaller than the previous one, the actual mathematical expressions that are compared to unity for the assessment of the condition are different. Therefore, even though

these expressions are supposed to represent the same requirement, their values do not coincide, and, consequently, they are not equivalent as quantitative measures of validity. Moreover, the omission of constant factors of the order of one from the validity conditions, while applicable in the high-frequency case, may introduce further ambiguity in the use of the various conditions for validity assessment. The cause of this ambiguity lies in the fact that comparison with unity in the various conditions should not be taken as an actual comparison of the values of the condition terms with unity, but rather as a comparison of order of magnitude. For these reasons, the solutions resulting from the WKB method need to be compared with models which do not make the assumptions of the WKB method.

It should also be noted that, even though some of the apparent validity conditions may be violated, this does not necessarily lead to large errors in the solution. These errors have been estimated in [27, 115] and further work is required to apply this analysis in the cases considered here.

D Reflection coefficient from a free end of a uniform plate

A schematic of a semi-infinite uniform plate with a free termination is shown in Figure D.1. The displacement is given by

$$w = w_i + w_r + w_{rn} = A\mathrm{e}^{-\mathrm{i}kx} + B\mathrm{e}^{\mathrm{i}kx} + C\mathrm{e}^{kx}, \tag{D.1}$$

where k is the constant wavenumber in the uniform plate, and A, B and C are complex constants. The boundary conditions at the free end are [16]

$$w''(0) = 0 \text{ and } w'''(0) = 0, \tag{D.2}$$

where the origin is set to be at the free end.

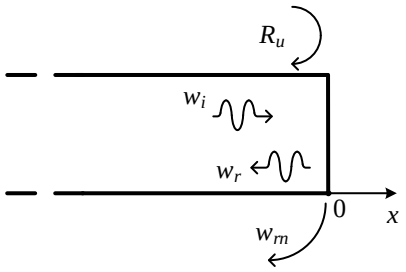

Figure D.1. Schematic of a longitudinal cross section of a semi-infinite uniform plate with a free termination. The wave components are shown, along with the reflection coefficient related to the reflected travelling wave.

The reflection coefficient related to the reflected travelling wave is defined as

$$R_u = \frac{w_r(0)}{w_i(0)} = \frac{B}{A}. \tag{D.3}$$

Calculating up to the third derivative of the displacement and substituting appropriately into the boundary conditions expressed in Equations (D.2) yields the equations

$$-Ak^2 - Bk^2 + Ck^2 = 0 \tag{D.4}$$

and

$$\mathrm{i}Ak^2 - \mathrm{i}Bk^2 + Ck^2 = 0. \tag{D.5}$$

Eliminating C from Equations (D.4) and (D.5) and solving for B/A gives

$$R_u = -\mathrm{i}. \tag{D.6}$$

E Matrix equations for truncated and ideally tapered wedges

The matrix equation for a truncated wedge is written as

$$\begin{bmatrix} M_{11} & M_{12} & M_{13} & M_{14} & M_{15} & M_{16} \\ M_{21} & M_{22} & M_{23} & M_{24} & M_{25} & M_{26} \\ M_{31} & M_{32} & M_{33} & M_{34} & M_{35} & M_{36} \\ M_{41} & M_{42} & M_{43} & M_{44} & M_{45} & M_{46} \\ M_{51} & M_{52} & M_{53} & M_{54} & M_{55} & M_{56} \\ M_{61} & M_{62} & M_{63} & M_{64} & M_{65} & M_{66} \end{bmatrix} \begin{bmatrix} R_{tot} \\ R_n \\ T \\ T_n \\ \tilde{R}_{end} \\ R_{nw} \end{bmatrix} = \begin{bmatrix} 0 \\ 0 \\ -1 \\ \mathrm{i}k_u \\ k_u^2 \\ -\mathrm{i}k_u^3 \end{bmatrix}, \tag{E.1}$$

where the system matrix elements are

$$\begin{aligned}
&M_{11} = 0,\ M_{12} = 0,\ M_{13} = \left(\psi_t''(x_1) + \psi_t'^2(x_1)\right) \mathrm{e}^{\psi_t(x_1)},\ M_{14} = \left(\psi_{tn}''(x_1) + \psi_{tn}'^2(x_1)\right) \mathrm{e}^{\psi_{tn}(x_1)}, \\
&M_{15} = \left(\psi_{rw}''(x_1) + \psi_{rw}'^2(x_1)\right) \mathrm{e}^{\psi_{rw}(x_1)},\ M_{16} = \left(\psi_{rnw}''(x_1) + \psi_{rnw}'^2(x_1)\right) \mathrm{e}^{\psi_{rnw}(x_1)}, \\
&M_{21} = 0,\ M_{22} = 0,\ M_{23} = \left(\psi_t'''(x_1) + 3\psi_t'(x_1)\psi_t''(x_1) + \psi_t'^3(x_1)\right) \mathrm{e}^{\psi_t(x_1)}, \\
&M_{24} = \left(\psi_{tn}'''(x_1) + 3\psi_{tn}'(x_1)\psi_{tn}''(x_1) + \psi_{tn}'^3(x_1)\right) \mathrm{e}^{\psi_{tn}(x_1)}, \\
&M_{25} = \left(\psi_{rw}'''(x_1) + 3\psi_{rw}'(x_1)\psi_{rw}''(x_1) + \psi_{rw}'^3(x_1)\right) \mathrm{e}^{\psi_{rw}(x_1)}, \\
&M_{26} = \left(\psi_{rnw}'''(x_1) + 3\psi_{rnw}'(x_1)\psi_{rnw}''(x_1) + \psi_{rnw}'^3(x_1)\right) \mathrm{e}^{\psi_{rnw}(x_1)}, \\
&M_{31} = 1,\ M_{32} = 1,\ M_{33} = -1,\ M_{34} = -1,\ M_{35} = -1,\ M_{36} = -1, \\
&M_{41} = \mathrm{i}k_u,\ M_{42} = k_u,\ M_{43} = -\psi_t'(0),\ M_{44} = -\psi_{tn}'(0),\ M_{45} = -\psi_{rw}'(0),\ M_{46} = -\psi_{rnw}'(0), \\
&M_{51} = -k_u^2,\ M_{52} = k_u^2,\ M_{53} = -\psi_t''(0) - \psi_t'^2(0),\ M_{54} = -\psi_{tn}''(0) - \psi_{tn}'^2(0), \\
&M_{55} = -\psi_{rw}''(0) - \psi_{rw}'^2(0),\ M_{56} = -\psi_{rnw}''(0) - \psi_{rnw}'^2(0),\ M_{61} = -\mathrm{i}k_u^3,\ M_{62} = k_u^3, \\
&M_{63} = -\psi_t'''(0) - 3\psi_t'(0)\psi_t''(0) - \psi_t'^3(0) - \frac{3h'(0)}{h_0}\left(\psi_t''(0) + \psi_t'^2(0)\right), \\
&M_{64} = -\psi_{tn}'''(0) - 3\psi_{tn}'(0)\psi_{tn}''(0) - \psi_{tn}'^3(0) - \frac{3h'(0)}{h_0}\left(\psi_{tn}''(0) + \psi_{tn}'^2(0)\right), \\
&M_{65} = -\psi_{rw}'''(0) - 3\psi_{rw}'(0)\psi_{rw}''(0) - \psi_{rw}'^3(0) - \frac{3h'(0)}{h_0}\left(\psi_{rw}''(0) + \psi_{rw}'^2(0)\right), \\
&M_{66} = -\psi_{rnw}'''(0) - 3\psi_{rnw}'(0)\psi_{rnw}''(0) - \psi_{rnw}'^3(0) - \frac{3h'(0)}{h_0}\left(\psi_{rnw}''(0) + \psi_{rnw}'^2(0)\right).
\end{aligned} \tag{E.2}$$

The ψ functions correspond to the exponent of the WKB solution, given in Equation (2.11). The subscript of each of these functions defines the corresponding type of wave, as explained in the caption of Figure 2.3, which, in turn, defines which of the four constant factors has to be used for the solution, Equation (2.12), of the eikonal equation.

For an ideally tapered wedge driven from a uniform plate, the matrix equation is written as

$$\begin{bmatrix} 1 & 1 & -1 & -1 \\ \mathrm{i}k_u & k_u & -\psi_t'(0) & -\psi_{tn}'(0) \\ -k_u^2 & k_u^2 & -\left(\psi_t''(0)+\psi_t'^2(0)\right) & -\left(\psi_{tn}''(0)+\psi_{tn}'^2(0)\right) \\ -\mathrm{i}k_u^3 & k_u^3 & -\left[\frac{3h'(0)}{h_0}\left(\psi_t''(0)+\psi_t'^2(0)\right)+\psi_t'''(0)+3\psi_t'(0)\psi_t''(0)+\psi_t'^3(0)\right] & -\left[\frac{3h'(0)}{h_0}\left(\psi_{tn}''(0)+\psi_{tn}'^2(0)\right)+\psi_{tn}'''(0)+3\psi_{tn}'(0)\psi_{tn}''(0)+\psi_{tn}'^3(0)\right] \end{bmatrix} \begin{bmatrix} R_{jun,f} \\ R_{jn,f} \\ T_{jun,f} \\ T_{jn,f} \end{bmatrix} = \begin{bmatrix} -1 \\ \mathrm{i}k_u \\ k_u^2 \\ -\mathrm{i}k_u^3 \end{bmatrix}, \tag{E.3}$$

where

$$R_{jun,f} = \frac{w_{r,f}(0)}{w_{i,f}(0)},\ R_{jn,f} = \frac{w_{rn,f}(0)}{w_{i,f}(0)},\ T_{jun,f} = \frac{w_{t,f}(0)}{w_{i,f}(0)},\ T_{jn,f} = \frac{w_{tn,f}(0)}{w_{i,f}(0)}. \tag{E.4}$$

For an ideally tapered wedge driven from inside the wedge, the matrix equation is written as

$$\begin{bmatrix} 1 & 1 & -1 & -1 \\ \psi_r'(0) & \psi_{rn}'(0) & -\mathrm{i}k_u & -k_u \\ \psi_r''(0)+\psi_r'^2(0) & \psi_{rn}''(0)+\psi_{rn}'^2(0) & k_u^2 & -k_u^2 \\ \frac{3h'(0)}{h_0}\left(\psi_r''(0)+\psi_r'^2(0)\right)+\psi_r'''(0)+3\psi_r'(0)\psi_r''(0)+\psi_r'^3(0) & \frac{3h'(0)}{h_0}\left(\psi_{rn}''(0)+\psi_{rn}'^2(0)\right)+\psi_{rn}'''(0)+3\psi_{rn}'(0)\psi_{rn}''(0)+\psi_{rn}'^3(0) & \mathrm{i}k_u^3 & -k_u^3 \end{bmatrix} \mathbf{r} = \begin{bmatrix} -1 \\ -\psi_i'(0) \\ -\psi_i''(0)-\psi_i'^2(0) \\ -\frac{3h'(0)}{h_0}\left(\psi_i''(0)+\psi_i'^2(0)\right)-\psi_i'''(0)-3\psi_i'(0)\psi_i''(0)-\psi_i'^3(0) \end{bmatrix}, \tag{E.5}$$

where $\mathbf{r} = [R_{jun,r}\ R_{jn,r}\ T_{jun,r}\ T_{jn,r}]^{\mathrm{T}}$, where

$$R_{jun,r} = \frac{w_{r,r}(0)}{w_{i,r}(0)},\ R_{jn,r} = \frac{w_{rn,r}(0)}{w_{i,r}(0)},\ T_{jun,r} = \frac{w_{t,r}(0)}{w_{i,r}(0)},\ T_{jn,r} = \frac{w_{tn,r}(0)}{w_{i,r}(0)}. \tag{E.6}$$

In Equations (E.3) and (E.5), as well as in the definitions (E.4) and (E.6), in the subscripts of the reflection and transmission coefficients, jun denotes reflection and transmission coefficients at the junction that are ratios of a travelling wave over the incident wave, while jn denotes reflection and transmission coefficients at the junction that are ratios of a nearfield wave over the incident wave.

Both in the reflection and transmission coefficients and in the wave components, the subscript f after the comma corresponds to forward excitation, that is, from the uniform plate, and the subscript r after the comma corresponds to reverse excitation, that is, from inside the wedge; the latter subscript should not be confused with the r appearing in the various reflected waves as a first subscript. For the system driven from inside the wedge, the direction of incidence is taken to be towards negative x, as shown in Figure F.1c, so that the incident and transmitted waves are directed towards negative x while reflected waves are directed towards positive x; a corresponding figure for a forward-driven ideal wedge is shown in Figure F.1b. It should be noted that only travelling waves are shown in Figure F.1 for convenience.

F Analysis of multiple internal reflections

A wavefront of a harmonic wave w_i travelling from a uniform plate towards a truncated elastic wedge may be considered, as depicted in Figure F.1a; the total and end reflection coefficients are also shown. By following the consecutive reflections and transmissions of the incident wavefront at the junction and at the truncation, a relation for the total reflection coefficient with respect to the reflection and transmission coefficients at the junction and with respect to the reflection coefficient due to the truncation may be found.

Reflections and transmissions at the junction are expressed using the corresponding coefficients from the analysis of the ideally tapered wedge, in which no other source of reflection is present. Therefore, the various travelling waves when the wedge is ideally tapered, along with the reflection and transmission coefficients at the junction, are needed; they are shown in Figure F.1b and Figure F.1c, when the system is driven from the uniform plate and when it is driven from inside the wedge, respectively. In this analysis, all the coefficients are ratios of travelling waves, and, therefore, the nearfield waves are omitted from Figure F.1. It should be pointed out that all the wave components are evaluated at the junction, $x = 0$; the notation (0) is omitted in this section for convenience.

The various coefficients shown in Figure F.1 are defined as

$$R_{tot} = \frac{w_r}{w_i},\ R_{end} = \frac{w_{rw}}{w_t},\ R_{jun,f} = \frac{w_{r,f}}{w_{i,f}},\ T_{jun,f} = \frac{w_{t,f}}{w_{i,f}},\ R_{jun,r} = \frac{w_{r,r}}{w_{i,r}},\ T_{jun,r} = \frac{w_{t,r}}{w_{i,r}}, \quad \text{(F.1)}$$

where the subscripts are explained in Appendix E. The consecutive reflections and transmissions of the incident wave are shown in the lower part of Figure F.1a. It should be pointed out that the reflected waves inside the wedge, denoted by w_{rw}, are evaluated at the junction, even though they are shown towards the right side of the figure for presentational clarity.

The first cycle along the truncated wedge, starting inversely from the reflected wave in the uniform plate, w_r, up to the incident wave, w_i, also using the definitions in Equations (F.1), leads to the following relations

$$w_{r,1} = T_{jun,r} w_{rw,1} = T_{jun,r} R_{end} w_{t,1} = T_{jun,r} R_{end} T_{jun,f} w_i, \quad \text{(F.2)}$$

where the subscript 1 denotes the order of the cycle. Accordingly, the second cycle gives

$$w_{r,2} = T_{jun,r} w_{rw,2} = T_{jun,r} R_{end} w_{t,2} = T_{jun,r} R_{end} R_{jun,r} w_{rw,1} = T_{jun,r} R_{end}^2 T_{jun,f} R_{jun,r} w_i, \quad \text{(F.3)}$$

since $w_{t,2} = R_{jun,r} w_{rw,1}$. Similarly, for the m-th cycle,

$$w_{r,m} = T_{jun,r} w_{rw,m} = T_{jun,r} R_{end} w_{t,m} = T_{jun,r} R_{end} R_{jun,r}^{m-1} w_{rw,1} = T_{jun,r} R_{end}^m T_{jun,f} R_{jun,r}^{m-1} w_i. \quad \text{(F.4)}$$

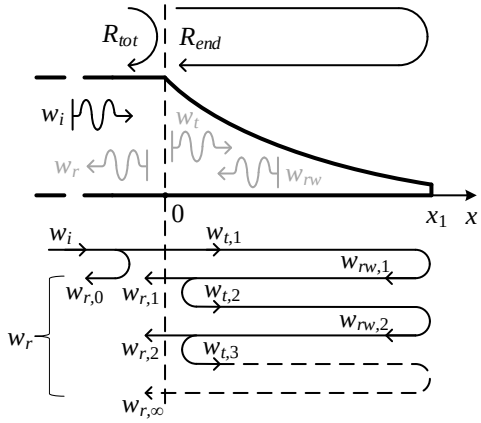

(a)

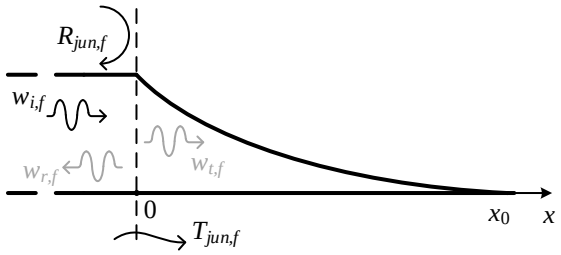

(b)

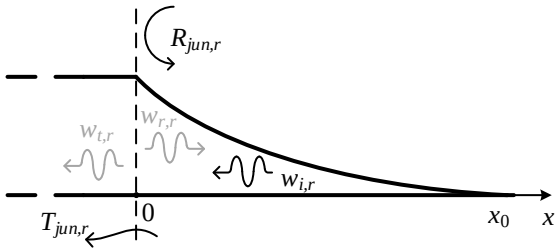

(c)

Figure F.1. (a) Total and end reflection coefficients of a truncated wedge driven from a uniform plate. A vertical line in the schematic of the waves is used to represent a single wavefront. The procedure of internal reflections is also depicted. Reflection and transmission coefficients due to the junction of an ideally tapered wedge, driven (b) from the uniform plate and (c) from inside the wedge. The incident, reflected and transmitted travelling waves for each case are also shown; the incident wave is shown in black whereas the rest wave components are shown in grey. The second subscript in variables in (b) and (c) stands for either forward or reverse.

After an infinite amount of cycles of transmission and reflection, the resulting wave is given by

$$\tilde{w}_r = T_{jun,r}T_{jun,f}w_i \sum_{m=1}^{\infty} R_{end}^m R_{jun,r}^{m-1} = T_{jun,r}T_{jun,f}R_{end}w_i \sum_{m=0}^{\infty} R_{end}^m R_{jun,r}^m = \frac{T_{jun,f}R_{end}T_{jun,r}}{1 - R_{end}R_{jun,r}}w_i, \tag{F.5}$$

where the formula for an infinite geometric series whose ratio is absolutely smaller that 1 has been used. Considering the steady state of a harmonic incident wave, where the infinite internal reflections are established in time, and also including the wave which is promptly reflected at the junction upon the initial incidence, the reflected wave may be written as

$$w_r = \tilde{w}_r + w_{r,0} = \tilde{w}_r + R_{jun,f}w_i = \left(R_{jun,f} + \frac{T_{jun,f}R_{end}T_{jun,r}}{1 - R_{end}R_{jun,r}}\right)w_i, \tag{F.6}$$

so that the total reflection coefficient is expressed as

$$R_{tot} = \frac{R_{jun,f}\left(1 - R_{end}R_{jun,r}\right) + T_{jun,f}R_{end}T_{jun,r}}{1 - R_{end}R_{jun,r}}. \tag{F.7}$$

By expanding Equation (F.7) using the moduli and phases of the various reflection and transmission coefficients, the total reflection coefficient is written in terms of its real and imaginary part as

$$R_{tot} = \mathrm{Re}\{R_{tot}\} + \mathrm{iIm}\{R_{tot}\}, \tag{F.8}$$

where,

$$\mathrm{Re}\{R_{tot}\} = \frac{\begin{array}{c}\left|R_{jun,f}\right|\cos\phi_a\left(1+\left|R_{end}R_{jun,r}\right|^2-2\left|R_{end}R_{jun,r}\right|\cos\phi_0\right)+\\ \left|T_{jun,f}R_{end}T_{jun,r}\right|\left(\cos(\phi_b+\phi_d+\phi_e)-\left|R_{end}R_{jun,r}\right|\cos(\phi_c-\phi_d-\phi_e)\right)\end{array}}{1+\left|R_{end}R_{jun,r}\right|^2-2\left|R_{end}R_{jun,r}\right|\cos\phi_0} \tag{F.9}$$

and

$$\mathrm{Im}\{R_{tot}\} = \frac{\begin{array}{c}\left|R_{jun,f}\right|\sin\phi_a\left(1+\left|R_{end}R_{jun,r}\right|^2-2\left|R_{end}R_{jun,r}\right|\cos\phi_0\right)+\\ \left|T_{jun,f}R_{end}T_{jun,r}\right|\left(\sin(\phi_b+\phi_d+\phi_e)-\left|R_{end}R_{jun,r}\right|\sin(\phi_c-\phi_d-\phi_e)\right)\end{array}}{1+\left|R_{end}R_{jun,r}\right|^2-2\left|R_{end}R_{jun,r}\right|\cos\phi_0}, \tag{F.10}$$

where $\phi_a = \angle R_{jun,f}$, $\phi_b = \angle R_{end}$, $\phi_c = \angle R_{jun,r}$, $\phi_d = \angle T_{jun,f}$, $\phi_e = \angle T_{jun,r}$ and $\phi_0 = \phi_b + \phi_c$. The modulus of the total reflection coefficient, after algebraic manipulations, takes the form

$$\left|R_{tot}\right| = \Big[\left|R_{jun,f}\right|^2 + \frac{\left|T_{jun,f}R_{end}T_{jun,r}\right|^2 + 2\left|R_{jun,f}T_{jun,f}R_{end}T_{jun,r}\right|\left(\cos\phi_1 - \left|R_{end}R_{jun,r}\right|\cos\left(\phi_0+\phi_1\right)\right)}{1+\left|R_{end}R_{jun,r}\right|^2-2\left|R_{end}R_{jun,r}\right|\cos\phi_0}\Big]^{1/2}, \tag{F.11}$$

where $\phi_1 = \phi_a - \phi_b - \phi_d - \phi_e$.

Simulations with the WKB method for the various thickness profiles that are considered in Chapter 2 have shown that the phase $\phi_0 + \phi_1$ is roughly equal to $-\pi$ over the frequency range in which the total reflection coefficient is consistently smaller than one, that is, where energy conservation is not violated, which occurs above a specific frequency for a given profile and a

given order of WKB approximation, as is shown in Section 2.6. This result may also be written as

$$\angle R_{jun,f} + \angle R_{jun,r} = \angle T_{jun,f} + \angle T_{jun,r} - \pi, \tag{F.12}$$

that is, the sum of the phases of the reflection coefficients at the junction differs from the sum of the transmission coefficients by half a cycle. If frequencies below that limit are neglected, as conservation of energy is violated there and the analytical results cannot be regarded as accurate, Equation (F.11) takes the form

$$|R_{tot}| = \Big[|R_{jun,f}|^2 + |T_{jun,f}R_{end}T_{jun,r}| \frac{|T_{jun,f}R_{end}T_{jun,r}| + 2\,|R_{jun,f}R_{end}R_{jun,r}| - 2\,|R_{jun,f}|\cos\phi_0}{1 + |R_{end}R_{jun,r}|^2 - 2\,|R_{end}R_{jun,r}|\cos\phi_0}\Big]^{1/2}. \tag{F.13}$$

Considering also that $|R_{jun,f}| \approx |R_{jun,r}|$, as mentioned in Section 2.3.3, Equation (F.13) can be further simplified to

$$|R_{tot}| = \left[|R_{jun}|^2 + |T_{jun,f}R_{end}T_{jun,r}| \frac{|T_{jun,f}R_{end}T_{jun,r}| + 2\left|R_{jun}^2 R_{end}\right| - 2\,|R_{jun}|\cos\phi_0}{1 + |R_{end}R_{jun}|^2 - 2\,|R_{end}R_{jun}|\cos\phi_0}\right]^{1/2}, \tag{F.14}$$

where $|R_{jun}|$ has replaced both $|R_{jun,f}|$ and $|R_{jun,r}|$.

G Exponential thickness profile as the limit of a power-law profile

Two families of wedge are shown representatively in Figure G.1: the power-law wedge, with thickness profile $h_p = h_0 \left(1 - x/x_0\right)^n$, where x_0 is the position where the thickness becomes zero, and the exponential wedge, with thickness profile $h_e = h_0 e^{-\beta x}$, $\beta > 0$. It should be clarified that the family of power-law profiles considered are the ones that meet the x axis tangentially, that is, the ones without any constant offset from the x axis. Correspondingly, the family of exponential profiles considered are the ones with zero limit as x approaches infinity. It will be shown that, for wedges passing from two given points, $(0, h_0)$ and (x_1, h_1), the limit of the power-law profile when the order of power tends to infinity is the exponential profile

$$\lim_{n\to\infty} h_p = h_e. \tag{G.1}$$

The two profiles are expressed as Maclaurin series, that is, in the form

$$f(x) = \sum_{k=0}^{\infty} \frac{f^{(k)}(0)}{k!} x^k, \tag{G.2}$$

where $f^{(k)}(0)$ is the k-th-order derivative of f with respect to x, evaluated at $x = 0$. For the power-law profile, it can be found that the k-th derivative has the form

$$h_p^{(k)} = (-1)^k \frac{n!}{(n-k)!} \frac{1}{x_0^k} \left(1 - \frac{x}{x_0}\right)^{n-k}, \tag{G.3}$$

which, when evaluated at $x = 0$, becomes

$$h_p^{(k)}(0) = (-1)^k \frac{n!}{(n-k)!} \frac{1}{x_0^k}. \tag{G.4}$$

The Maclaurin series of the power-law profile can then be written as

$$h_p = h_0 \sum_{k=0}^{\infty} (-1)^k \frac{n!}{(n-k)!k!} \frac{x^k}{x_0^k} \left(1 - \frac{x}{x_0}\right)^{n-k}. \tag{G.5}$$

The Maclaurin series of the exponential profile is, accordingly, written as

$$h_e = h_0 \sum_{k=0}^{\infty} (-1)^k \beta^k \frac{x^k}{k!}. \tag{G.6}$$

In order to proceed further, it should be observed that the position x_0 where the power-law profile tangentially intersects the x axis is variable, depending on the order of the profile; as the order increases, x_0 also increases. It should therefore be expressed with respect to given quantities. For this aim, the coordinates of the second point which satisfy the equation of the

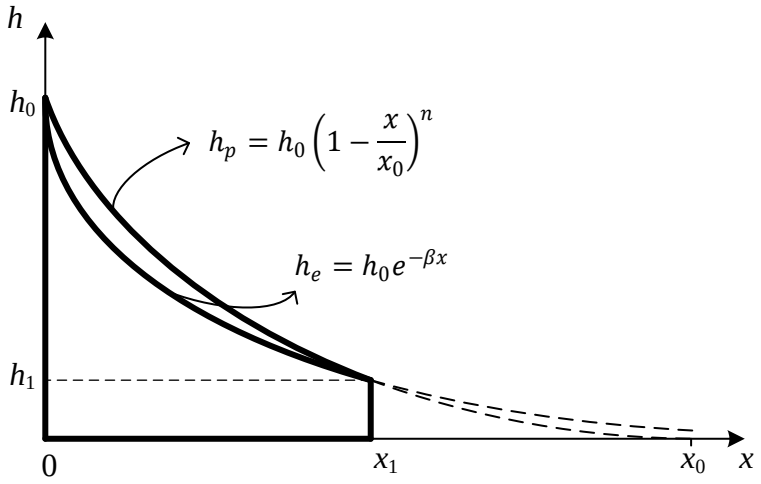

Figure G.1. Power-law and exponential profile with two common fixed points.

profile are substituted into the relation of the profile, giving successively

$$h_1 = h_0 \left(1 - \frac{x}{x_0}\right)^n \Rightarrow H^{1/n} = 1 - \frac{x_1}{x_0} \Rightarrow x_0 = \frac{x_1}{1 - H^{1/n}}. \tag{G.7}$$

The rate of exponential decay, β, is also expressed with respect to given quantities

$$h_1 = h_0 e^{-\beta x_1} \Rightarrow -\beta x_1 = \ln H \Rightarrow \beta = \frac{1}{x_1} \ln \frac{1}{H}. \tag{G.8}$$

Consequently, the Maclaurin series for the two profiles become

$$h_p = h_0 \sum_{k=0}^{\infty} (-1)^k \frac{n!}{(n-k)!k!} \left(1 - H^{1/n}\right)^k \frac{x^k}{x_1^k} \tag{G.9}$$

and

$$h_e = h_0 \sum_{k=0}^{\infty} \frac{(-1)^k}{x_1^k} \frac{x^k}{k!} \left(\ln \frac{1}{H}\right)^k. \tag{G.10}$$

The limit of the power-law profile as the order of power tends to infinity is expressed as

$$\lim_{n\to\infty} h_p = h_0 \sum_{k=0}^{\infty} \frac{(-1)^k}{x_1^k} \frac{x^k}{k!} \lim_{n\to\infty} \frac{n!}{(n-k)!} \left(1 - H^{1/n}\right)^k, \tag{G.11}$$

where the limit has been entered into the sum, encompassing all the terms that involve n. It can be seen from Equations (G.10) and (G.11) that, in order for the right-hand sides to be equal, it has to hold that

$$\lim_{n\to\infty} \frac{n!}{(n-k)!} \left(1 - H^{1/n}\right)^k = \left(\ln \frac{1}{H}\right)^k. \tag{G.12}$$

Equation (G.12) can be proved by mathematical induction. For $k = 0$, both sides of the

equation equal one. It is then supposed that Equation (G.12) holds for an arbitrary k and the relation of the two sides for $k+1$ is examined. The left-hand side is written successively as

$$\begin{gathered}\lim_{n\to\infty}\frac{n!}{(n-k-1)!}\left(1-H^{1/n}\right)^{k+1}= \\ \lim_{n\to\infty}\frac{n!}{(n-k)!}(n-k)\left(1-H^{1/n}\right)^{k}\left(1-H^{1/n}\right)= \\ \lim_{n\to\infty}\frac{n!}{(n-k)!}\left(1-H^{1/n}\right)^{k}\lim_{n\to\infty}(n-k)\left(1-H^{1/n}\right)= \\ \left(\ln\frac{1}{H}\right)^{k}\lim_{n\to\infty}(n-k)\left(1-H^{1/n}\right).\end{gathered} \tag{G.13}$$

For the evaluation of the remaining limit, the substitution $m=1/n$ is applied. The limit then becomes

$$\begin{gathered}\lim_{m\to0}\left(\frac{1}{m}-k\right)\left(1-H^{m}\right)=\lim_{m\to0}\frac{(1-mk)\left(1-H^{m}\right)}{m}= \\ \lim_{m\to0}\frac{1-mk-H^{m}+mkH^{m}}{m}.\end{gathered} \tag{G.14}$$

The above limit is indefinite of type $0/0$. Without loss of generality, it can be assumed that m is real, so that L' Hospital's rule can be applied, yielding

$$\begin{gathered}\lim_{m\to0}\left(\frac{1}{m}-k\right)\left(1-H^{m}\right)= \\ \lim_{m\to0}\frac{0-k-H^{m}\ln H+kH^{m}+kmH^{m}\ln H}{1}=-k-\ln H+k=\ln\frac{1}{H}.\end{gathered} \tag{G.15}$$

Substituting this result into Equation (G.13) gives

$$\lim_{n\to\infty}\frac{n!}{(n-k-1)!}\left(1-H^{1/n}\right)^{k+1}=\left(\ln\frac{1}{H}\right)^{k+1}. \tag{G.16}$$

It has therefore been shown that, if Equation (G.12) holds for an arbitrary value of k, it also holds for $k+1$, and, since it holds for $k=0$, it also holds for all $k\geq0$. Consequently, the series expression of Equation (G.11) for the limit of the power-law profile as the order of the profile tends to infinity is equal to the series expression for the exponential profile, given in Equation (G.10). Hence the exponential profile forms the limit of the power-law profile as the order of power tends to infinity.

It will also be shown that a power-law wedge of certain order always has smaller thickness than a power-law wedge of lower order in the interval $0<x<x_1$. In the two ends of the interval the thickness of the two profiles coincide, in accordance with the definition of the wedges considered. Therefore, it will be concluded that the exponential profile, which forms the high-order limit of the power-law profile, always has smaller thickness between its two ends than a power-law wedge of any given order.

The sought-after inequality can be written in the form

$$\begin{gathered}\left(1-\frac{x}{x_{0,n}}\right)^n > \left(1-\frac{x}{x_{0,n+1}}\right)^{n+1} \Longleftrightarrow \\ \left[1-\frac{x}{x_1}\left(1-H^{1/n}\right)\right]^n > \left[1-\frac{x}{x_1}\left(1-H^{1/(n+1)}\right)\right]^{n+1}.\end{gathered} \tag{G.17}$$

This inequality shall be constructed from elementary relations of its parts. Initially, the relation of the thickness at the two ends is considered, for which, by the definition of the system,

$$h_1 < h_0 \Rightarrow H < 1. \tag{G.18}$$

Additionally, for two successive orders of power it holds that

$$n < n+1 \Rightarrow \frac{1}{n} > \frac{1}{n+1}. \tag{G.19}$$

By considering the fact that the exponential function $f(n) = a^n$ is strictly decreasing for $0 < a < 1$, it follows from inequalities (G.18) and (G.19) that

$$H^{1/n} < H^{1/(n+1)}. \tag{G.20}$$

This relation leads to the following successive inequalities

$$\begin{gathered}H^{1/n} < H^{1/(n+1)} \Rightarrow \\ 1-H^{1/n} > 1-H^{1/(n+1)} \Rightarrow \\ 1-\frac{x}{x_1}\left(1-H^{1/n}\right) < 1-\frac{x}{x_1}\left(1-H^{1/(n+1)}\right),\end{gathered} \tag{G.21}$$

where the direction of the inequality is inverted each time the sign of the two sides is inverted. In order to reach relation (G.17), the two left and right sides of the last of relations (G.21) have to be raised to powers n and $n+1$, respectively. For the relation of the resulting expressions to be known, it is required that the magnitude of two sides of the last of relations (G.21) be known compared to one. Successively, it holds that

$$H < 1 \Rightarrow H^{1/n} < 1 \Rightarrow 1-H^{1/n} > 0 \Rightarrow 1-\frac{x}{x_1}\left(1-H^{1/n}\right) < 1. \tag{G.22}$$

A similar relation can be produced for an exponent of $1/(n+1)$. It is therefore shown that both sides of the last of relations (G.21) are less than one. Again, using the fact that the exponential function with base less than one is strictly decreasing yields

$$\left[1-\frac{x}{x_1}\left(1-H^{1/n}\right)\right]^n > \left[1-\frac{x}{x_1}\left(1-H^{1/(n+1)}\right)\right]^n. \tag{G.23}$$

Multiplying the right-hand side of this inequality by a factor of $\left[1-(x/x_1)\left(1-H^{1/(n+1)}\right)\right]$, which was previously shown to be smaller than one, finally gives

$$\left[1-\frac{x}{x_1}\left(1-H^{1/n}\right)\right]^n > \left[1-\frac{x}{x_1}\left(1-H^{1/(n+1)}\right)\right]^{n+1}. \tag{G.24}$$

In conclusion, every higher-order power-law thickness profile is smaller than the lower-order ones in the interval $0 < x < x_1$, and, since the exponential is the limiting case for the order of power tending to infinity, the exponential wedge has a thickness which is always smaller than any power-law wedge in the interval $0 < x < x_1$.

H Wedges of different lengths

The thickness variation of three quadratic wedges of the same input and end thickness are is shown in Figure H.1. The modulus of the total reflection coefficient of these wedges is plotted in Figures H.2a and H.2c, calculated with the Finite Element method and with the analytical method using the second-order WKB approximation, respectively. It can be seen that when the length of the wedge shifts, while the input and end thickness remains unchanged, the reflection coefficient plotted against logarithmic frequency only shifts along the spectrum, without changing its form. This can also be seen in Figures H.2b and H.2d, where the reflection coefficients of the shorter and longer wedges match with the wedge of median length, when shifted in frequency by a factor of $(x_{1,a}/x_{1,b})^2$ and $(x_{1,c}/x_{1,b})^2$, respectively.

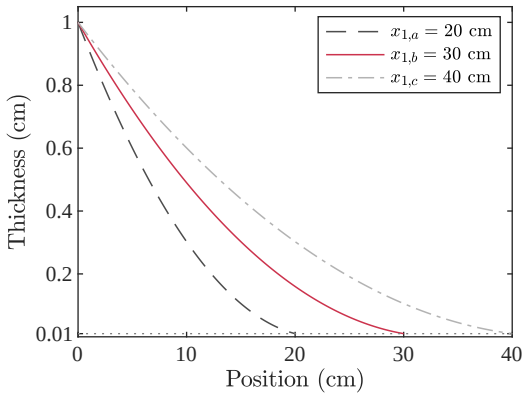

Figure H.1. Thickness profiles of three quadratic wedges with the same junction and end thickness and different lengths.

In the results with the Finite Element method a small deviation is observed, which may be due to the fact that the Finite Element method captures more complicated frequency-dependent phenomena, thus affecting the calculated response at different frequencies. In the results with the WKB method, the shifted reflection coefficients match perfectly. The matching with shifting in frequency according to the length ratio holds for all the different profiles presented in Section 2.5, although only results for the quadratic are shown here. It is not apparent from the WKB analysis presented in Sections 2.2 and 2.3 how the matching occurs when the reflection coefficient is shifted in frequency by the ratio of the lengths squared.

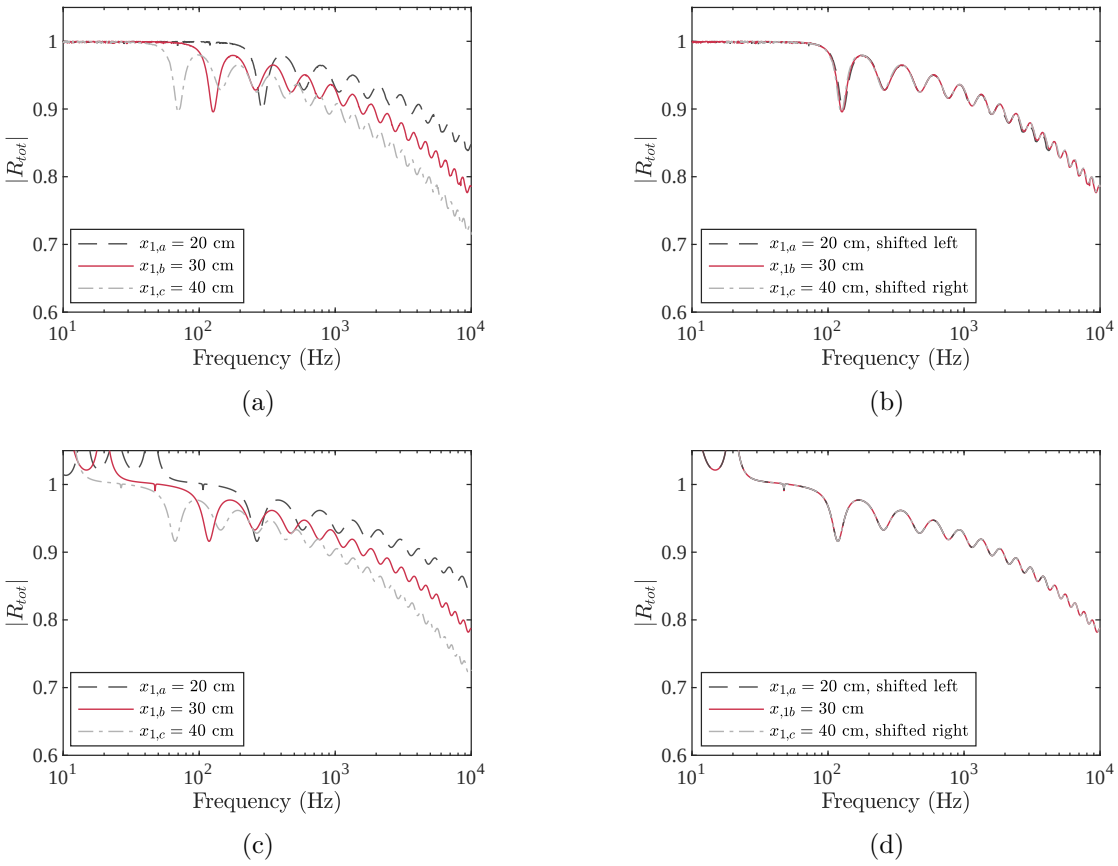

Figure H.2. Modulus of the total reflection coefficient calculated with (a) the Finite Element method and (c) the second-order WKB approximation. In (b) and (d), the grey lines of (a) and (c), respectively, are shifted in frequency by a factor of $(x_{1,i}/x_{1,b})^2$, where i is either a or c.

I End reflection coefficient of a power-law wedge with increasing power

It was shown in Appendix G that the thickness of a power-law wedge of a given order is smaller than the thickness of a power-law wedge of a lower order, except from the edges, where the thickness is fixed. This result may be written as

$$h_{n+1} < h_n, \text{ , } n \geq 2 \text{ for } 0 < x < x_1, \tag{I.1}$$

where the order of power, n, should not be confused with the thickness at the endpoints, h_0 and h_1. The zeroth-order end reflection coefficient, given in Equation (2.37), is re-written here for convenience,

$$|R_{end}| = \mathrm{e}^{2\int_0^{x_1} \mathrm{Im}\{k(x)\}\mathrm{d}x}, \tag{I.2}$$

where the imaginary part of the wavenumber is written according to Equation (2.16) as

$$\mathrm{Im}\{k\} = -\frac{12^{1/4}\omega^{1/2}\eta}{4c_p^{1/2}h^{1/2}}. \tag{I.3}$$

Successive manipulation of the inequality in Equation (I.1) gives

$$\begin{aligned} h_{n+1}^{-1/2} > h_n^{-1/2} \Rightarrow \mathrm{Im}\{k_{n+1}\} < \mathrm{Im}\{k_n\} \Rightarrow \\ \int_0^{x_1} \mathrm{Im}\{k_{n+1}(x)\}dx < \int_0^{x_1} \mathrm{Im}\{k_n(x)\}dx \Rightarrow \\ \mathrm{e}^{2\int_0^{x_1} \mathrm{Im}\{k_{n+1}(x)\}dx} < \mathrm{e}^{2\int_0^{x_1} \mathrm{Im}\{k_n(x)\}dx} \Rightarrow \\ |R_{end,n+1}| < |R_{end,n}|, \end{aligned} \tag{I.4}$$

where the subscripts denote the order of power and should not be confused with the similar notation for the order of WKB approximation used in Sections 2.3.1 and 2.4.2. Therefore, the end reflection coefficient of a power-law wedge always improves throughout the frequency spectrum as the order of power increases.

The zeroth-order WKB approximations for the quadratic and exponential wedges take the explicit forms

$$|R_{end}|_q = H^{\frac{12^{1/4}\eta x_1}{4c_p^{1/2}\left(h_0^{1/2}-h_1^{1/2}\right)}\omega^{1/2}} \tag{I.5}$$

and

$$|R_{end}|_e = \mathrm{e}^{\frac{12^{1/4}\eta x_1\left(1-H^{1/2}\right)}{c_p^{1/2}h_1^{1/2}\ln H}\omega^{1/2}}, \tag{I.6}$$

respectively, and they are plotted in Figure I.1. Since the end reflection coefficient decreases with increasing power, and since the thickness of the exponential wedge forms the limit of the thickness of a power-law wedge as the order of power tends to infinity, as shown in Appendix G,

it follows that the exponential wedge has smaller end reflection coefficient than any power-law wedge with the same end points at a given frequency.

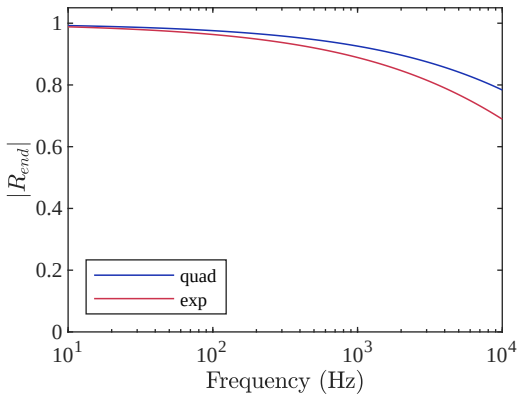

Figure I.1. Modulus of the end reflection coefficient of a quadratic and an exponential wedge, calculated with the zeroth-order WKB approximation.

The fact that the limit of the modulus of the end reflection coefficient of a power-law wedge coincides with that of an exponential wedge can also be shown by taking the relation for the former with $n > 2$, which is calculated from Equations (I.2) and (I.3) with $h = h_0(1 - x/x_0)^n$, $n > 2$, and is expressed as

$$|R_{end}|_{pl} = \mathrm{e}^{\frac{12^{1/4}\eta x_1\left(H^{1/n-1/2}-1\right)}{c_p^{1/2}h_1^{1/2}(2-n)H^{-1/2}\left(1-H^{1/n}\right)}\omega^{1/2}}, \tag{I.7}$$

and then taking the limit for $n \to \infty$, which also leads to Equation (I.6). Consequently, the two frequency variations of the end reflection coefficient shown in Figure I.1 form the limit cases of wedges of power-law profile that can be used as vibration absorbers, where the low-order limit corresponds to the quadratic wedge, that is, with $n = 2$, and the high-order limit, that is, for $n \to \infty$, coincides with the exponential wedge.

J Relation of the effective length of a linear acoustic waveguide with fitted rings with its actual length

The normalised effective length of a waveguide with fitted rings of linearly tapered inner radius is given by Equation (3.24), which can also be written as

$$L_{eff} = \left(1 + \frac{1}{L_{1,tr}}\right) \frac{\ln(1 + L_{1,tr})}{\sqrt{1 - \left(\frac{c_0}{4\pi f l_0}\right)^2}}. \tag{J.1}$$

where $L_{1,tr} = l_1/l_{tr}$, where l_1 is the actual length and l_{tr} is the truncation length. The limiting value of the normalised effective length at high frequencies is given by

$$L_{eff,hf} = \lim_{f \to \infty} L_{eff} = \left(1 + \frac{1}{L_{1,tr}}\right) \ln(1 + L_{1,tr}). \tag{J.2}$$

The non-dimensional ratio $L_{1,tr}$ takes values from zero, when the actual length of the waveguide is zero, to infinity, when the truncation length is zero. At the limit when $L_{1,tr}$ tends to zero, the high-frequency normalised effective length is written as

$$\lim_{L_{1,tr} \to 0} L_{eff,hf} = \frac{\ln(1 + L_{1,tr})}{\frac{L_{1,tr}}{1+L_{1,tr}}}. \tag{J.3}$$

This limit is indefinite of the type $0/0$, so that L'Hôpital's rule can be applied, giving

$$\lim_{L_{1,tr} \to 0} L_{eff,hf} = \frac{\frac{1}{1+L_{1,tr}}}{\frac{1}{(1+L_{1,tr})^2}} = 1. \tag{J.4}$$

Therefore, at the limit of $l_1 \to 0$, the high-frequency limit of the normalised effective length is one. The monotonicity of $L_{eff,hf}$ as a function of $L_{1,tr}$ can be inspected by taking its respective derivative,

$$\frac{\mathrm{d}L_{eff,hf}}{\mathrm{d}L_{1,tr}} = \frac{1}{L_{1,tr}} \left[1 + \frac{\ln(1 - L_{1,tr})}{L_{1,tr}}\right]. \tag{J.5}$$

The factor $1/L_{1,tr}$ is positive for positive $L_{1,tr}$, and it can be shown that the factor in square brackets is also positive for positive $L_{1,tr}$. Therefore, the high-frequency limit of L_{eff} is one for $L_{1,tr} \to 0$ and greater than one for $L_{1,tr} > 0$. It can also be seen in Equation (J.1) that for $f > c_0/4\pi l_0$, the normalised effective length decreases with increasing frequency. Since its high-frequency limit is greater than one, the normalised effective length is greater than one at all frequencies above cut-off.

K Finite Element modelling for comparison with experimental results for an absorbing acoustic waveguide with fitted rings

A linear and a quadratic two-dimensional axisymmetric Finite Element model were implemented in COMSOL Multiphysics 5.3a to simulate the experimental models of [3], as shown in Figure K.1. Figure K.1a shows the whole linear model, including the uniform tube, while Figures K.1b and K.1c show only the non-uniform part of the system for the linear and quadratic case, respectively. The linear model has 18 rings while the quadratic one has 15 rings. The design details of the non-uniform parts of the two models are given in Section 3.5.

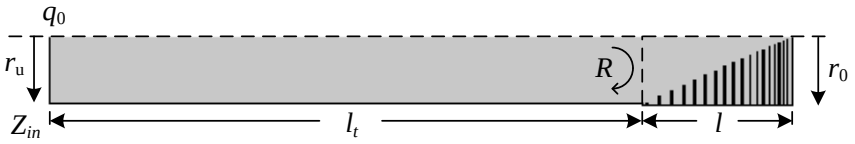

(a)

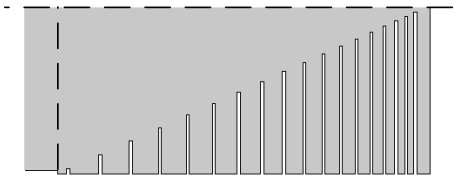

(b)

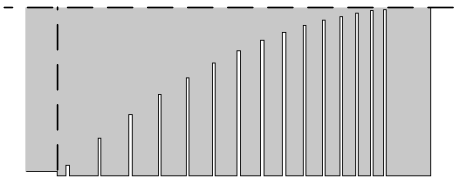

(c)

Figure K.1. Geometry of the Finite Element model based on [3]. A half cross-section is used, due to rotational symmetry, where the horizontal dashed line is the axis of revolution. (a) The non-uniform waveguide of length l with fitted rings is connected to a uniform tube of length l_t, which is acoustically driven by a constant volume velocity q_0 for the left-end boundary. The input impedance is also shown, along with the reflection coefficient at the junction of the non-uniform waveguide with the uniform tube. The uniform and non-uniform parts have slightly different tube radii, which are denoted by r_u and r_0, respectively. (b) Detail of the non-uniform waveguide with linear inner-radius variation. (c) Detail of the non-uniform waveguide with quadratic inner-radius variation. The vertical dashed line in (b) and (c) designates the boundary of the uniform and non-uniform parts.

The Thermoviscous Acoustics module in COMSOL Multiphysics was used for the non-uniform part to calculate viscous and thermal losses in the boundary layers of the inter-ring cavities. Six elements were used across the boundary layer, but more elements were also tried. The model boundary layer thickness was taken to be that of the viscous boundary layer, given by $\delta_v \approx \sqrt{2\eta/(\omega\rho)}$ for air, where η is the dynamic viscosity of air [42], which is $\eta \approx 1.8{\cdot}10^{-5}$ m$^2{\cdot}$s at 20 °C. For the uniform tube, the Pressure Acoustics module in COMSOL Mulitphysics was used, with no losses included.

The system is driven by the left boundary of the uniform tube, which vibrates like a piston with a constant volume velocity q_0. The pressure at this input boundary, p_0, is calculated with the Finite Element model, thus giving the input impedance, $Z_{in} = p_0/q_0$. The modulus of the

reflection coefficient is then calculated by [48]

$$|R| = \left| \frac{Z_{in} - Z_0}{Z_{in} + Z_0} \right|, \tag{K.1}$$

where $Z_0 = \rho c_0 / S_u$, where $S_u = \pi r_u^2$ is the cross-sectional area of the input tube. Since the model assumes no losses in the uniform tube, the modulus of the reflection coefficient calculated by Equation (K.1) is equal to the modulus of the reflection coefficient which corresponds to the input of the non-uniform part, denoted by R in Figure K.1a. In other words, the phase of the reflection coefficient is not considered, so that the phase shift along the length of the uniform tube, l_t, can be neglected. The uniform tube is set to be $h_t = 1$ m, which is long enough for the nearfield waves arising from the interaction of the generated plane wave with the rings to have decayed before reaching back to the left end of the tube.

The experimental results, taken from [3], are shown in Figures K.2a and K.2b for the linear and quadratic waveguide, respectively, along with the results from the Finite Element models. The modulus of the reflection coefficient obtained from the experiment shows a fluctuating pattern, with the general level of reflection decreasing with increasing frequency in the considered spectrum. It can be seen that the Finite Element results diverge significantly from the experimental ones for both geometries. The modulus of the reflection coefficient calculated with the Finite Element models appears to follow an increasing trend above some frequency, which is around 430 Hz for the linear and around 270 Hz for the quadratic waveguide, even though the experimental data show a clear decreasing trend for the general level of the reflection coefficient.

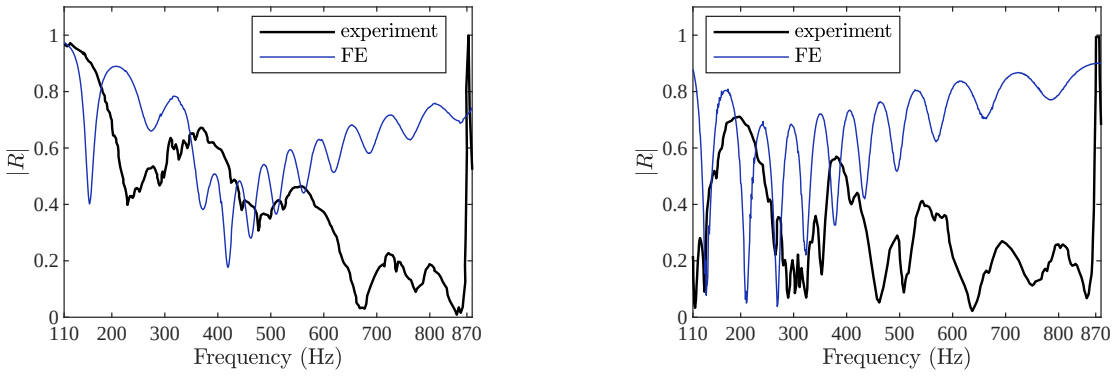

Figure K.2. Modulus of the reflection coefficient of the model used by El Ouahabi et al. in [3], for (a) a linear and (b) a quadratic non-uniform termination, where the experimental results are taken from [3] and the Finite Element results were produced with the models shown in Figure K.1.

It is apparent from the presented results that the implemented Finite Element models do not represent the physical ones well. An alternative method was also used for obtaining the reflection coefficient, consisting in two-point pressure measurements along the uniform duct, and an incident pressure plane wave was also tried as an alternative input boundary condition.

However, the results from the Finite Element analysis were very similar in all these cases, which are qualitatively very different from the experimental ones. Further investigation of the details of the Finite Element models is required to achieve better correspondence with the physical models.

L Ratios of the dimensions of the acoustic 'rainbow' sensor over the wavelength

The applicability of the Transmission Line approximation requires that the dimensions of elements that are modelled with lumped parameters are much smaller than the free-space wavelength. Since the pressure response is strongly attenuated beyond a frequency which is smaller than the resonance frequency for a given element number, n, as can be seen in Figure 5.19b, it is justified to assume that the dimensions of a given element have to be much smaller than the free-space wavelength which corresponds to the resonance frequency of the Helmholtz resonator of the element. This resonance wavelength can be calculated by $\lambda_{r,n} = c_0/f_n$, where the resonance frequency is calculated by Equation (5.122).

The ratios of the various element dimensions of the system over the local resonance wavelength is plotted with coloured lines in Figure L.1. It can be seen that all dimensions are less than 10% of the local wavelength, so that it can be said that the Transmission Line approximation can be used with quite good accuracy. It should be noted, however, that this only holds up to highest resonance frequency. Beyond that, the pressure response again increases, as can be seen in Figure 5.19b, so that the element dimensions would have to be compared with much smaller wavelengths, corresponding to the upper end of the plotted spectrum.

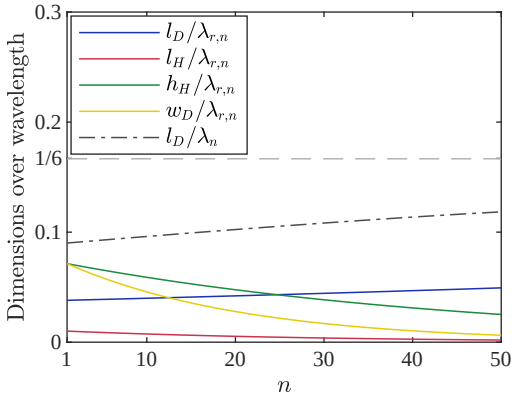

Figure L.1. Element dimensions over the free-space wavelength corresponding to the resonance frequency of each resonator, $\lambda_{r,n}$, plotted against the order of element, n. The ratio of the element length over the slow-wave wavelength as calculated for the n-th element, λ_n, is also plotted.

Another requirement for the designed discrete model to approximate the response of the continuous cochlea, regardless of the modelling approach for the Transfer Matrix, is that there have to be at least six elements per local wavelength. The local wavelength of the system is calculated by $\lambda_n = 2\pi/k_n$, where the local wavenumber is calculated by Equation (5.73). The ratio of the local element length over the local wavelength is also plotted in Figure L.1 as a grey dash-dotted line. This ratio is smaller that 1/6 throughout the system, so that the condition of six elements per local wavelength is satisfied.

Bibliography

[1] N. Jimenez, V. Romero-Garcia, V. Pagneux, and J. P. Groby. Rainbow-trapping absorbers: Broadband, perfect and asymmetric sound absorption by subwavelength panels for transmission problems. *Sci Rep*, 7(1):13595, 2017.

[2] L. Zhao and S. Zhou. Compact acoustic rainbow trapping in a bioinspired spiral array of graded locally resonant metamaterials. *Sensors (Basel)*, 19(4), 2019.

[3] A. Azbaid El-Ouahabi, V. V. Krylov, and D. J. O'Boy. Investigation of the acoustic black hole termination for sound waves propagating in cylindrical waveguides. In *44th International Congress and Exposition on Noise Control Engineering*, 2015.

[4] S. T. Neely and D. O. Kim. A model for active elements in cochlear biomechanics. *J Acoust Soc Am*, 79(5):1472–1480, 1986.

[5] A. D. Pierce. Physical interpretation of the WKB or eikonal approximation for waves and vibrations in inhomogeneous beams and plates. *The Journal of the Acoustical Society of America*, 48(1B):275–284, 1970.

[6] A. G Webster. Acoustical impedance and the theory of horns and of the phonograph. *Proc. Natl. Acad. Sci.*, 5:275–282, 1919.

[7] M. A. Mironov. Propagation of a flexural wave in a plate whose thickness decreases smoothly to zero in a finite interval. *Soviet Physics: Acoustics*, 34(3):318–319, 1988.

[8] V. V. Krylov and F. J. B. S. Tilman. Acoustic 'black holes' for flexural waves as effective vibration dampers. *Journal of Sound and Vibration*, 274(3-5):605–619, 2004.

[9] B. M. P. Chong, L. B. Tan, K. M. Lim, and H. P. Lee. A review on acoustic black-holes (abh) and the experimental and numerical study of abh-featured 3d printed beams. *International Journal of Applied Mechanics*, 9(6), 2017.

[10] V. B. Georgiev, J. Cuenca, F. Gautier, L. Simon, and V. V. Krylov. Damping of structural vibrations in beams and elliptical plates using the acoustic black hole effect. *Journal of Sound and Vibration*, 330(11):2497–2508, 2011.

[11] M. A. Mironov and V. V. Pislyakov. One-dimensional acoustic waves in retarding structures with propagation velocity tending to zero. *Acoustical Physics*, 48(3):347–352, 2002.

[12] O. Guasch, M. Arnela, and P. Sánchez-Martín. Transfer matrices to characterize linear and quadratic acoustic black holes in duct terminations. *Journal of Sound and Vibration*, 395:65–79, 2017.

[13] E. de Boer. Auditory Physics. Physical principles in hearing theory. I. *Phys. Rep.*, 62(2):87–174, 1980.

[14] S. J. Elliott and C. A. Shera. The cochlea as a smart structure. *Smart Mater Struct*, 21(6):64001, 2012.

[15] J. Zhu, Y. Chen, X. Zhu, F. J. Garcia-Vidal, X. Yin, W. Zhang, and X. Zhang. Acoustic rainbow trapping. *Scientific Reports*, 3(1), 2013.

[16] L. Cremer, M. Heckl, and B. A. T. Petersson. *Structure-Borne Sound: Structural Vibrations and Sound Radiation at Audio Frequencies*. Springer-Verlag, Germany, 2005.

[17] V. V. Krylov and A. L. Shuvalov. Propagation of localised flexural vibrations along plate edges described by a power law. *Proceedings of the Institute of Acoustics*, 22(2):263–270, 2000.

[18] M. A. Mironov. Discrete vibrational black holes. In *INTER-NOISE 2019, The 49-th International Congress and Exhibition on Noise Control Engineering*, 2019.

[19] V. V. Krylov and R. E. T. B. Winward. Experimental investigation of the acoustic black hole effect for flexural waves in tapered plates. *Journal of Sound and Vibration*, 300(1-2):43–49, 2007.

[20] V. V. Krylov. Propagation of plate bending waves in the vicinity of one- and two-dimensional acoustic 'black holes'. In *ECCOMAS Thematic Conference on Computational Methods In Structural Dynamics and Earthquake Engineering*, 2007.

[21] E. P. Bowyer, D. J. O'Boy, V. V. Krylov, and F. Gautier. Experimental investigation of damping flexural vibrations in plates containing tapered indentations of power-law profile. *Applied Acoustics*, 74(4):553–560, 2013.

[22] V. Denis, F. Gautier, A. Pelat, and J. Poittevin. Measurement and modelling of the reflection coefficient of an acoustic black hole termination. *Journal of Sound and Vibration*, 349:67–79, 2015.

[23] V. Denis, A. Pelat, and F. Gautier. Scattering effects induced by imperfections on an acoustic black hole placed at a structural waveguide termination. *Journal of Sound and Vibration*, 362:56–71, 2016.

[24] K. Hook, J. Cheer, and S. Daley. A parametric study of an acoustic black hole on a beam. *The Journal of the Acoustical Society of America*, 145(6):3488–3498, 2019.

[25] L. Tang, L. Cheng, H. Ji, and J. Qiu. Characterization of acoustic black hole effect using a one-dimensional fully-coupled and wavelet-decomposed semi-analytical model. *Journal of Sound and Vibration*, 374:172–184, 2016.

[26] D. J. O'Boy, V. V. Krylov, and V. Kralovic. Damping of flexural vibrations in rectangular plates using the acoustic black hole effect. *Journal of Sound and Vibration*, 329(22):4672–4688, 2010.

[27] C. M. Bender and S. A. Orszag. *Advanced mathematical methods for scientists and engineers*. McGraw-Hill, New York, 1978.

[28] N. Fröman and P. O. Fröman. *JWKB Approximation. Contributions to the Theory*. North-Holland Publishing Company, Belgium, 1965.

[29] P. A. Feurtado and S. C. Conlon. Investigation of boundary-taper reflection for acoustic black hole design. *Noise Control Engineering Journal*, 63(5):460–466, 2015.

[30] R. Nielsen and S. Sorokin. The WKB approximation for analysis of wave propagation in curved rods of slowly varying diameter. *Proceedings of the Royal Society A: Mathematical, Physical and Engineering Sciences*, 470(2167):20130718–20130718, 2014.

[31] A. Karlos, S. J. Elliott, and J. Cheer. Higher-order WKB analysis of reflection from tapered elastic wedges. *Journal of Sound and Vibration*, 449:368–388, 2019.

[32] A. Karlos, S. Elliott, and J. Cheer. Reflection from elastic wedges of different thickness profiles. In *ISMA2018 and USD2018*, pages 4571–4584, Leuven, Belgium, 17-19 September, 2018.

[33] J. Y. Lee and W. Jeon. Exact solution of euler-bernoulli equation for acoustic black holes via generalized hypergeometric differential equation. *Journal of Sound and Vibration*, 452:191–204, 2019.

[34] R. D. Firouz-Abadi, H. Haddadpour, and A. B. Novinzadeh. An asymptotic solution to transverse free vibrations of variable-section beams. *Journal of Sound and Vibration*, 304(3-5):530–540, 2007.

[35] S. Chakraverty. *Vibration of Plates*. CRC Press, Taylor & Francis Group, United States of America, 2009.

[36] A. W. Leissa. *Vibration of plates.* NASA, USA, 1969.

[37] *MATLAB R2016a and R2019a.* The MathWorks, Inc., Natick, Massachusetts, United States of America.

[38] K. C. Rockey. *The finite element method: a basic introduction.* Crosby Lockwood Staples, London, 1975.

[39] D. H. Norrie and G. de Vries. *An introduction to finite element analysis.* Academic Press, New York, 1978.

[40] S. Marburg. Six boundary elements per wavelength: is that enough? *Journal for Computational Acoustics*, 10(1):25–51, 2002.

[41] *COMSOL Multiphysics v. 5.3.* COMSOL AB, Stockholm, Sweden.

[42] L. E. Kinsler, A. R. Frey, A. B. Coppens, and J. V. Sanders. *Fundamentals of Acoustics, 4th Edition.* Wiley-VCH, United States of America, 1999.

[43] M. R. Shepherd, P. A. Feurtado, and S. C. Conlon. Multi-objective optimization of acoustic black hole vibration absorbers. *J Acoust Soc Am*, 140(3):EL227, 2016.

[44] *Maple 2017.* Maplesoft, a division of Waterloo Maple Inc., Waterloo, Ontario, Canada.

[45] A. H. Nayfeh. *Introduction to Perturbation Techniques.* John Wiley & Sons , Inc., United States of America, 1981.

[46] M. Van Dyke. *Perturbation Methods in Fluid Mechanics.* Academic Press, Inc., United States of America, 1964.

[47] V. Krylov. Acoustic black holes: recent developments in the theory and applications. *IEEE Trans Ultrason Ferroelectr Freq Control*, 61(8):1296–306, 2014.

[48] D. T. Blackstock. *Fundamentals of Physical Acoustics.* Wiley and Sons Ltd, New York, 2000.

[49] A. Azbaid El Ouahabi, V. V. Krylov, and D. J. O'Boy. Experimental investigation of the acoustic black hole for sound absorption in air. In *Proceedings of the 22nd International Congress of Sound and Vibration*, 2015.

[50] N. Sharma, O. Umnova, and A. T. Moorhouse. Analysis of a low frequency muffler based on the acoustic black hole effect. *Proceedings of the Institute of Acoustics*, 38(1):149–155, 2016.

[51] N. Sharma, O. Umnova, and A. T. Moorhouse. Low frequency sound absorption through a muffler with metamaterial lining. In *24th International Congress on Sound and Vibration*, 2017.

[52] N. Sharma and O. Umnova. Study of sound absorption capability of silencers based on the acoustic black hole effect. In *ISMA2018 and USD2018*, pages 1121–1126, 2018.

[53] A. Karlos and S. J. Elliott. Reflection from a non-uniform acoustic waveguide with fitted rigid rings using a Transfer Function method. In *26th Internation Congress on Sound and Vibration*, Montreal, Canada, 7-11 July, 2019.

[54] H. F. Olson. *Acoustical Engineering*. D. Van Nostrand Company, Inc., USA, 1957.

[55] N. H. Fletcher and T. D. Rossing. *The Physics of Musical Instruments*. Springer-Verlag, New York, 2nd edition, 1998.

[56] R. H. Ghose. *Microwave Circuit Theory and Analysis*. McGraw-Hill Book Company, Inc., United States of America, 1963.

[57] A. D. Pierce. *Acoustics: An Introduction to its Physical Principles and Applications*. McGraw-Hill, United States of America, 1981.

[58] ISO 10534-2. Acoustics - Determination of sound absorption coefficient and impedance in impedance tube - Part 2: Transfer-function method. 1998.

[59] V. V. Krylov. Personal communication. March 2019.

[60] G. von Békésy. *Experiments in Hearing*. McGraw-Hill, New York, 1960.

[61] D. L. Frear, X. Guan, C. Stieger, J. J. Rosowski, and H. H. Nakajima. Impedances of the inner and middle ear estimated from intracochlear sound pressures in normal human temporal bones. *Hear Res*, 367:17–31, 2018.

[62] H. Davis. An active process in cochlear mechanics. *Hearing research*, 9(1):79–90, 1983.

[63] A. Karlos, D. Vignali, B. Lineton, and S. Elliott. Quasi-linear modelling of the coupled cochlea using the WKB method. In *Mechanics of Hearing*, volume 1965. American Institute of Physics, Brock University, Canada, 19-24 June, 2017.

[64] E. de Boer and R. MacKay. Reflections on reflections. *J Acoust Soc Am*, 67(3):882–890, 1980.

[65] G. Zweig, R. Lipes, and J. R. Pierce. The cochlear compromise. *The Journal of the Acoustical Society of America*, 59(4):975–982, 1976.

[66] C. R. Steele and L. A. Taber. Comparison of WKB and finite difference calculations for a twodimensional cochlear model. *The Journal of the Acoustical Society of America*, 65(4):1001–1006, 1979.

[67] Lim K.-M. and Steele C. R. A three-dimensional nonlinear active cochlear model analyzed by the WKB-numeric method. *Hearing Research*, 170:190–205, 2002.

[68] B. P. Peterson, L. C.; Bogert. A dynamical theory of the cochlea. *J Acoust Soc Am*, 22(3):369–380, 1950.

[69] C. A. Shera and G. Zweig. A symmetry suppresses the cochlear catastrophe. *J. Acoust. Soc. Am.*, 89(3):1276–1289, 1991.

[70] S. T. Neely. Finite difference solution of a two-dimensional mathematical model of the cochlea. *J Acoust Soc Am*, 69(5):1386–91, 1981.

[71] S. J. Elliott and G. Ni. An elemental approach to modelling the mechanics of the cochlea. *Hear Res*, 360:14–24, 2018.

[72] F. Böhnke and W. Arnold. 3D-Finite Element Model of the Human Cochlea Including Fluid-Structure Couplings. *ORL*, 61(5):305–310, 1999.

[73] S. J. Elliott, G. Ni, B. R. Mace, and B. Lineton. A wave finite element analysis of the passive cochlea. *J Acoust Soc Am*, 133(3):1535–45, 2013.

[74] Y. Jung, J.-H. Kwak, H. Kang, W. Kim, and S. Hur. *Development of Piezoelectric Artificial Cochlea Inspired by Human Hearing Organ*, book section Chapter 15, pages 145–152. Lecture Notes in Computer Science. 2015.

[75] S. Foucaud, G. Michon, Y. Gourinat, A. Pelat, and F. Gautier. Artificial cochlea and acoustic black hole travelling waves observation: Model and experimental results. *Journal of Sound and Vibration*, 333(15):3428–3439, 2014.

[76] L. Chittka and A. Brockmann. Perception space–the final frontier. *PLoS Biol*, 3(4):e137, 2005.

[77] C. A. Peckens and J. P. Lynch. Utilizing the cochlea as a bio-inspired compressive sensing technique. *Smart Materials and Structures*, 22(10), 2013.

[78] E. de Boer. *Mechanics of the Cochlea: Modelling efforts (Chapter: The Cochlea)*, volume 3, pages 258–317. 1996.

[79] S. T. Neely. Mathematical modeling of cochlear mechanics. *J. Acoust. Soc. Am.*, 78(1):345–352, 1985.

[80] S. J. Elliott, B. Lineton, and G. Ni. Fluid coupling in a discrete model of cochlear mechanics. *J Acoust Soc Am*, 130(3):1441–51, 2011.

[81] C. A. Shera. Laser amplification with a twist: traveling-wave propagation and gain functions from throughout the cochlea. *J Acoust Soc Am*, 122(5):2738–58, 2007.

[82] L. Robles and M. A. Ruggero. Mechanics of the mammalian cochlea. *Physiol Rev*, 81(3):1305–52, 2001.

[83] C. Croënne, E. J. S. Lee, Hefei Hu, and J. H. Page. Band gaps in phononic crystals: Generation mechanisms and interaction effects. *AIP Advances*, 1(4), 2011.

[84] M. Sebawe Abdalla and H. Eleuch. Exact analytic solutions of the schrdinger equations for some modified q-deformed potentials. *Journal of Applied Physics*, 115(23), 2014.

[85] C. R. Steele. *Application of the WKB method in solid mechanics*, volume 3, pages 243–295. Pergamon Press, New York, 1976.

[86] R. Marrocchio. Personal communication. May 2019.

[87] M. J. Rapson, T. J. Hamilton, and J. C. Tapson. On the fluid-structure interaction in the cochlea. *J Acoust Soc Am*, 136(1):284–300, 2014.

[88] F. Zangeneh-Nejad and R. Fleury. Active times for acoustic metamaterials. *Reviews in Physics*, 4, 2019.

[89] Y. Chen, H. Liu, M. Reilly, H. Bae, and M. Yu. Enhanced acoustic sensing through wave compression and pressure amplification in anisotropic metamaterials. *Nat Commun*, 5:5247, 2014.

[90] T. Liu, S. Liang, F. Chen, and J. Zhu. Inherent losses induced absorptive acoustic rainbow trapping with a gradient metasurface. *Journal of Applied Physics*, 123(9), 2018.

[91] L. L. Beranek. *Acoustics*. American Institute of Physics, New York, 1954.

[92] G. Theocharis, O. Richoux, V. R. García, A. Merkel, and V. Tournat. Limits of slow sound propagation and transparency in lossy, locally resonant periodic structures. *New Journal of Physics*, 16(9), 2014.

[93] M. L. Munjal. *Acoustics of ducts and mufflers with application to exhaust and ventilation system design*. John Wiley & Sons, Inc, 1987.

[94] O. Richoux and V. Pagneux. Acoustic characterization of the Hofstadter butterfly with resonant scatterers. *Europhysics Letters*, 59(1):34–40, 2002.

[95] M. R. Stinson. The propagation of plane sound waves in narrow and wide circular tubes, and generalization to uniform tubes of arbitrary cross-sectional shape. *J. Acoust. Soc. Am.*, 89(2):550–558, 1991.

[96] E. Eisner. Complete solutions of the "Webster" horn equation. *The Journal of the Acoustical Society of America*, 41(4B):1126–1146, 1967.

[97] A. H. Benade and E. V. Jansson. On plane and spherical waves in horns with nonuniform flare I. theory of radiation, resonance frequencies, and mode conversion. *Acustica*, 31(2):79–98, 1974.

[98] A. F. Stevenson. Exact and approximate equations for wave propagation in acoustic horns. *Journal of Applied Physics*, 22(12):1461–1463, 1951.

[99] E. V. Jansson and A. H. Benade. On plane and spherical waves in horns with nonuniform flare II. prediction and measurements of resonance frequencies and radiation losses. *Acustica*, 31(4):185–202, 1974.

[100] A. H. Benade. The physics of brasses. *Scientific American*, 229(1):24–35, 1973.

[101] R. S. Langley. Wave evolution, reflection, and transmission along inhomogeneous waveguides. *Journal of Sound and Vibration*, 227(1):131–158, 1999.

[102] G. R. Putland. Every one-parameter acoustic field obeys webster's horn equation. *J. Audio Eng. Soc.*, 41(6):435–451, 1993.

[103] P. Eveno, J. P. Dalmont, R. Causs, and J. Gilbert. Wave propagation and radiation in a horn: Comparisons between models and measurements. *Acta Acustica united with Acustica*, 98(1):158–165, 2012.

[104] D. Mapes-Riordan. Horn modeling with conical and cylindrical transmission line elements. *J. Audio Eng. Soc.*, 41(6):471–484, 1993.

[105] Y. Kulik. Transfer matrix of conical waveguides with any geometric parameters for increased precision in computer modeling. *J Acoust Soc Am*, 122(5):EL179–84, 2007.

[106] L. J. Kanis and E. de Boer. Self-suppression in a locally active nonlinear model of the cochlea: A quasilinear approach. *J Acoust Soc Am*, 94(6):3199–3206, 1993.

[107] E. de Boer. The "inverse problem" solved for a threedimensional model of the cochlea. i. analysis. *The Journal of the Acoustical Society of America*, 98(2):896–903, 1995.

[108] P. Dallos, Arthur N. P., and R. R. Fay. *The cochlea*, volume 8. Springer Science & Business Media, 1996.

[109] S. J. Elliott, E. M. Ku, and B. Lineton. A state space model for cochlear mechanics. *J Acoust Soc Am*, 122(5):2759–71, 2007.

[110] E. M. Ku. *Modelling the human cochlea.* Phd thesis, 2008.

[111] C. J. Kros, A Rüsch, and G. P. Richardson. Mechano-electrical transducer currents in hair cells of the cultured neonatal mouse cochlea. *Proc. R. Soc.*, 249:185–193, 1992.

[112] N. P. Cooper. Harmonic distortion on the basilar membrane in the basal turn of the guinea-pig cochlea. *Journal of Physiology*, 509(1):277–288, 1998.

[113] L. J. Kanis and E. de Boer. Two-tone suppression in a locally active nonlinear model of the cochlea. *The Journal of the Acoustical Society of America*, 96(4):2156–2165, 1994.

[114] Y. W. Liu and T. C. Liu. Quasilinear reflection as a possible mechanism for suppressor-induced otoacoustic emission. *J Acoust Soc Am*, 140(6):4193, 2016.

[115] J. A. Murdock. *Perturbations: theory and methods*. Classics in Applied Mathematics. SIAM, Philadelphia, USA, 1999.

[116] D. H. Keefe and A. Barjau. Acoustic Propagation in Flaring, Axisymmetric Horns: II. Numerical Results, WKB Theory, and Viscothermal Effects. *Acustica - acta acustica*, 85:285–293, 1999.

[117] V. V. Tyutekin and A. P. Shkvarnikov. Propagation of flexural waves in an inhomogeneous plate with smoothly varying parameters. *Soviet Physics - Acoustics*, 10(4):402–406, 1965.